Integrated structural analysis and multiaxial fatigue assessment of a barge-type 15 MW FOWT

European Wind Energy Master (EWEM) thesis

Fotios Theodorakis

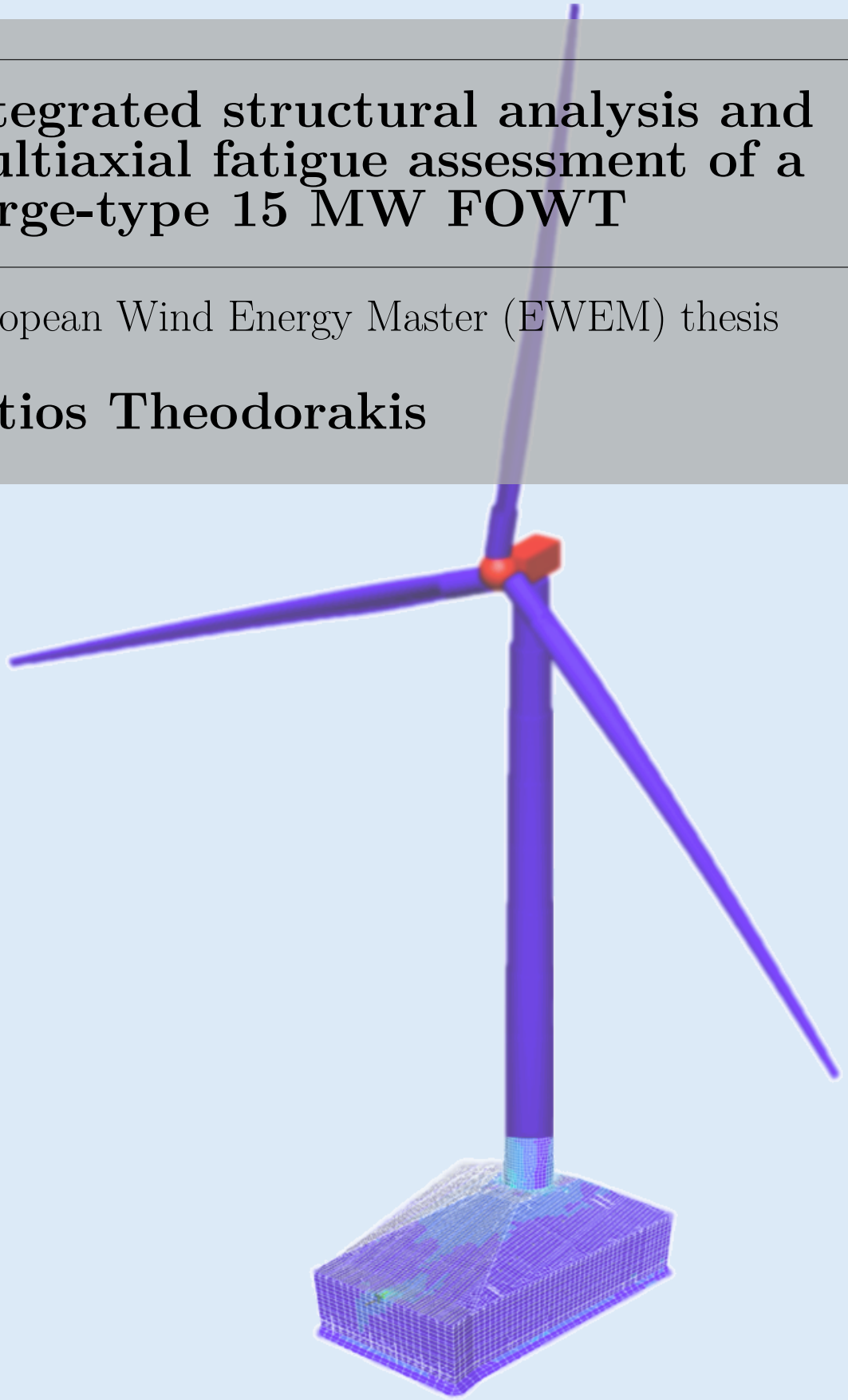

EWEM

TU Delft

NTNU

GFMS

Integrated structural analysis and multiaxial fatigue assessment of a barge-type 15 MW FOWT.

Design considerations of the inner structure and fatigue evaluation of the tower transition region.

by

Fotios Theodorakis

Student number

6071732 TU Delft
123747 NTNU

Thesis duration: January 6, 2025 - June 11, 2025
Language Check: Grammarly [1]

Supervisors

Dr.ir. J.H. den Besten (Henk)	Assistant Professor	TU Delft
Dr. Mojtaba Mokhtari	Associate Professor	NTNU
Dr. Jørgen Ranum Krokstad	GFMS General Manager	

Committee

Dr.ir. J.H. den Besten (Henk)	Chair of TU Delft committee, NTNU committee
Dr.ir. X.L. Jiang (Xiaoli)	TU Delft committee
Dr. Erin Bachynski-Polić	NTNU committee
R.L.G. (Ruben) Slange	TU Delft committee

Public defence: 3rd of July, 2025

Preface

This master's thesis was conducted to fulfill the requirements for the European Wind Energy Master (EWEM) in the offshore engineering track. It is a joint double-degree master's programme from the Delft University of Technology (TU Delft) and the Norwegian University of Science and Technology (NTNU), with one semester also at the Technical University of Denmark (DTU). A master's degree in Offshore Engineering is obtained from TU Delft, and a master's degree in Technology-Wind Energy is obtained from NTNU.

It was done in collaboration with Green Floating Marine Structures (GFMS), utilizing their innovative concept WindBarge, which is a low-draft barge-type floating wind turbine with a single mooring line layout. I want to express my gratitude to Dr. Jørgen Ranum Krokstad, founder and general manager of GFMS, for introducing this concept to me and providing an initial model and background material (the WindBarge project), as well as for the numerous discussions we had and the expertise he shared with me. I learned a lot about floaters and the process of designing something new with this work. Also, I would like to thank Norconsult, GFMS partner, for providing an office to work on my thesis, a nice environment, and a place to have regular meetings.

I would also like to express my thanks to my supervisors for their regular guidance. Professor Mojtaba Mokhtari at NTNU provided significant feedback in every step of my work, and through the fruitful discussions every week, I had a deeper look at the theory and my approaches. He has also been my supervisor for the pre-thesis course "TMR4590 - Wind Turbine Energy - Offshore Engineering, Specialization Project" which resulted partially in the research questions of this study. Professor Henk den Besten at TU Delft inspired me to examine the multiaxiality, extending my research from the common uniaxial approach for fatigue, and with his guidance and feedback to work on my research questions. Additionally, I would like to thank Professor Erin Bachynski-Polić for establishing contact with GFMS and her course "TMR03 Integrated dynamic analysis of wind turbines" with which I got familiar with the software SIMA. Finally, DNV customer support has been crucial to overcoming issues with the different software packages that I used.

I want to extend my thanks to those who helped me make this learning journey abroad a reality. Many thanks to HELLENiQ ENERGY for their recognition of my competencies and their scholarship for the tuition fees of this master's. Also, my thanks to the Union of Greek Shipowners for recognising my excellence from my mechanical engineering studies and their scholarship for continuing with my master's studies abroad. Finally, I would like to thank EMISIA SA, my previous employer, for continuing our cooperation for some period after initiating my master's.

Lastly, I would like to express my warm gratitude to my parents for their love, trust, and support throughout my whole life and with my decision to study abroad. I'm in general very grateful for the chance that I was given to live briefly in three different countries (Denmark, the Netherlands, and Norway), the people who accompanied me on this journey, the friends that I made, and the experiences that will always be a part of me. To the next adventures that life brings upon my way.

Fotios Theodorakis
Trondheim, June 2025

Abstract

The exploitation of the wind as a renewable energy source has increased over the last years. Transitioning to offshore wind means an increased wind energy potential. Bottom-founded wind turbines are suitable for shallow waters, but floating solutions are needed for greater water depths. Barge-type floating wind turbines can offer advantages compared to other competing alternatives in terms of manufacturability, logistics, and installation in shallower water depths. Combining the barge with a single mooring line layout enables a reduction in material costs, utilizing the weathervane principle, and decreasing the wake effects in the wind farm, therefore increasing power output. The WindBarge from Green Floating Marine Structures (GFMS) was studied in this thesis, which integrates, as a first design approach, a 15 MW upwind turbine on a barge-type structure with vertical side walls, horizontal bottom, and one mooring line including internal redundance.

Few floating wind turbine designs exist with a barge-type floater, and the design of the inner structure has not been investigated thoroughly in academic research. The inner design of the WindBarge is established by the WindBarge project, however, further modifications of the inner structure are proposed in this study. Its structural response is associated with the external loading and eigenfrequencies, providing an insight into the stress field of the inner structure for these types of structures based on ultimate limit state load cases. The simulation procedure using DNV's software suite SESAM was implemented.

Apart from extreme loads, fatigue can be a driving design factor due to the dynamic wind and wave loading. A focus was given on the tower transition region in this study. The external loading and the complex geometry can lead to a multiaxial stress state, and only a few studies in academic research have addressed this topic for floating wind turbines. A multiaxial screening method was utilized based on the 2-dimensional stress space representation and a minimum volume enclosed ellipse (MVEE) to identify the level of non-proportionality. Multiaxial conditions were observed at the deck, and the fatigue damage was calculated based on fatigue limit state load cases.

Three different approaches were implemented and compared for the fatigue assessment: the nominal uniaxial fatigue based on the forces/moments from the beam model of the tower, the hot spot plate fatigue, and the hot spot plate multidirectional fatigue, based on an effective stress according to DNVGL-RP-C203. The multidirectional approach considers different stress directions, therefore, different crack planes to identify the critical plane. For the fatigue damage calculation using the shell model of the floater, the response reconstruction method with SESAM Core was utilized.

Supplementary studies were carried out on how to reduce the observed difference in fatigue damage around the tower base caused by the roll motions, focusing on the cause of these motions, the coupling of the different degrees of freedom of the floater, and the effect of increased damping, roll stiffness, and the yaw controller. A conclusion is made that the design of such a floater is mainly fatigue rather than ultimate limit state driven.

Keywords: floating wind turbine, barge, tower transition region, fatigue, multiaxiality, non-proportionality.

Grading note

A pre-thesis study was conducted at NTNU with the course "TMR4590 - Wind Turbine Energy - Offshore Engineering, Specialization Project (15 ECTS)" and it was titled "Structural assessment methods for a barge-type floating wind turbine". The model of the WindBarge, the hydro-aero-servo analysis theory for floating wind turbines, and the simulation procedures using DNV's SESAM software suite were studied. Also, decay tests in SIMA, a frequency domain analysis of the floater, and an initial time domain analysis without including the tower and mooring loads were conducted as a learning process.

The introduction about the WindBarge (section 1.3), the theory about the hydro-aero-servo and time domain analysis (section 2.1.3 and Appendix A), the methods for internal loads in offshore platforms (Appendix B), and the frequency and time domain analysis procedure (section 3.1.2) are included from the pre-thesis report for completeness, after being revised. The initial model of the WindBarge and the controllers, without the part of the tower but with the compartments, were also presented in the pre-thesis. The tower addition, the internal structure modification, and the rest of the sections about the environment, the design load cases, fatigue, multiaxiality, the ultimate and fatigue limit state study, and the supplementary studies have been a sole outcome of this thesis work.

Contents

List of Figures

List of Tables

List of Symbols

Hydrodynamic loads

ρ_{w} density of the water

ρ density of the air

g acceleration of gravity

μ dynamic viscosity

ν kinematic viscosity

p pressure

$\boldsymbol{u}$ velocity vector of fluid

∇ vector of partial derivatives

ϕ velocity potential

ζ free-surface elevation

ζ_α wave amplitude

ω wave frequency or turbine rotational speed

T_{w} wave period

h water depth

λ_{w} wavelength

D horizontal dimension

C_{s} slamming coefficient

U water velocity

W effective width of the structure

l slamming impact height

Aerodynamic loads

α angle of attack

ϕ flow angle

θ (θ_{p}) pitch angle

a axial induction factor

a' tangential induction factor

T Thrust

P Power

C_{T} Thrust coefficient

C_{P} Power coefficient

A Rotor area

c Chord length

p_{N} Normal force per length

p_{T} Tangential force per length

C_{N} Normal force coefficient

p_{N} Tangential force coefficient

B Number of planes

r Radial position

R Wind turbine radius

λ Tip speed ratio

W_{qs} Quasi-static induced velocity

W_{int} Intermediate induced velocity

W Filtered induced velocity

τ_1, τ_2 Time constants

k Parameter

f_{s} Degree of stall

$C_{\mathrm{l,inv}}$ Lift coefficient without separation

$C_{\mathrm{l,fs}}$ Lift coefficient with full separation

χ Wake skew angle

Ψ Azimuth angle

D_{tow} Local tower diameter

b Bak coefficient

Control systems

J_{R} Drivetrain inertia

M_{aero} Aerodynamic torque

M_{g} Generator torque

Ω Shaft rotational speed

β Blade pitch angle

Dynamic time domain analysis

$\mathbf{M}$ Frequency-dependent mass matrix

$\mathbf{m}$ Body mass matrix

$\mathbf{D}_1$ Linear damping matrix

$\mathbf{D}_1$ Quadratic damping matrix

$\mathbf{x}$ Position vector

$\mathbf{q}$ Excitation force vector

$\mathbf{M}^{\mathrm{S}}$ Structural mass matrix

$\mathbf{M}^{\mathrm{H}}$ Hydrodynamic mass (added mass) matrix

$\mathbf{C}^{\mathrm{S}}$ Structural damping matrix

$\mathbf{C}^{\mathrm{H}}$ Hydrodynamic damping (linear and quadratic) matrix

$\mathbf{K}$ Stiffness matrix

$\mathbf{R}^{\mathrm{E}}$ External force vector

$\mathbf{r}$ Displacement vector

$\dot{\mathbf{r}}$ Velocity vector

$\ddot{\mathbf{r}}$ Acceleration vector

$\mathbf{M}_{\mathrm{t}}$ Tangential mass matrix

$\mathbf{K}_{\mathrm{t}}$ Tangential stiffness matrix

Environment and Design Load Cases

H_{s} Significant wave height

T_{p} Wave period

S_{U} Spectral density of the wind speed

σ_{U} Standard deviation of the wind speed

U_{10} 10-min mean wind speed

L_{k} Integral scale parameter for the Kaimal spectrum

H Reference height in the power law for the wind speed profile

α Power law exponent

$S_{\zeta}^{+}(\omega)$ Spectral density of the wave elevation

α Spectral parameter

ω_{p} Peak frequency

γ Peakedness parameter

β Form parameter

σ Spectral parameter

$S_{\omega,\theta}$ Total wave spectrum

S_{ω} Wave spectrum without directionality

D_{θ} Directional wave spectrum

θ Wave direction

$\bar{\theta}$ Mean wave direction

$\theta_{\max}$ Max wave direction

s Wave spreading parameter

C Normalizing constant

U_{W} Mean wind speed

$f_{\mathrm{U_W,H_S,T_P}}$ Joint probability density function of U_w, H_s, T_p

$f_{\mathrm{U_W}}$ Probability density function of U_w

$f_{\mathrm{H_S|U_W}}$ Probability density function of H_s for a given U_w

$f_{\mathrm{T_P|U_W,H_S}}$ Probability density function of T_p for a given U_w and H_s

Element stresses

σ_{x} Normal stress in the direction of the x-axis

σ_{y} Normal stress in the direction of the y-axis

σ_{z} Normal stress in the direction of the z-axis

τ_{xy} Shear stress in the direction of the y-axis in a plane normal to the x-axis

τ_{xz} Shear stress in the direction of the z-axis in a plane normal to the x-axis

τ_{yz} Shear stress in the direction of the z-axis in a plane normal to the y-axis

$\sigma_{\mathrm{vonMises}}$ vonMises stress

P_1 First principal stress

P_2 Second principal stress

$\{\mathbf{u}\}_i$ Nodal displacement vector

$\{\mathbf{F}^{\mathrm{e}}\}_i$ Element nodal force vector

$\mathbf{K}^{\mathrm{e}}$ Element stiffness matrix

F_i Balanced element nodal force

f_i Line force

M_i Balanced element nodal moment

m_i Line force

t Element thickness

σ_{s} Normal structural stress

τ_{s} Shear structural stress

τ_z Transverse shear structural stress

σ_m Membrane component of the normal structural stress

σ_b Bending component of the normal structural stress

τ_m Membrane component of the shear structural stress

τ_b Bending component of the shear structural stress

$f_{x'}$ Line force in x' direction

$f_{y'}$ Line force in y' direction

$f_{z'}$ Line force in z' direction

$m_{x'}$ Line moment in x' direction

$m_{y'}$ Line moment in y' direction

$m_{z'}$ Line moment in z' direction

Fatigue

N_z Axial force

A Cross-sectional area

θ Angle around tower base

I_y Sectional area moment over the y-axis

I_x Sectional area moment over the x-axis

M_y Bending moment over the y-axis

M_x Bending moment over the x-axis

M_z Torsion over the z-axis

J Polar moment of inertia of the section

F_x Shear force in the x-axis

F_y Shear force in the y-axis

$\Delta\sigma$ Stress range

N Number of cycles to failure for the stress range $\Delta\sigma$

m Negative inverse slope of the S-N curve

$log\bar{a}$ Intercept on the log N-axis of the S-N curve

t_{ref} Reference thickness equal to 25 mm for no tubular joints

t Thickness where the crack develops

K Thickness exponent

f_m Stress reduction factor

σ_t Maximum tension stress (positive)

σ_c Maximum compression stress (negative)

σ^{RF} Corrected stress range for Goodman correction

σ^{R} Stress range for Goodman correction

σ^{M} Mean stress for Goodman correction

σ^{MF} Fixed mean stress of the time series for Goodman correction

σ^{ult} Ultimate stress before failure

$\Delta\sigma_{Eff}$ Effective stress range

$\Delta\sigma_1$ First principal stress range

$\Delta\sigma_2$ Second principal stress range

$\Delta\sigma_\perp$ Normal stress range perpendicular to the weld toe

$\Delta\sigma_\parallel$ Parallel stress range parallel to the weld toe

$\Delta\tau_\parallel$ Shear stress range parallel to the weld toe

γ Factor for non-proportionality

$D_\perp$ Perpendicular damage

$D_\parallel$ Parallel damage

G_{NP} Level of non-proportionality

R_{minor} Radii of ellipse's minor axis

R_{major} Radii of ellipse's major axis

$\Delta\sigma_E$ Maximum stress range

D_{imp} Fatigue damage importance

$\Delta S_e^{(i)}$ Path length for the ith reference stress range

D_P Proportional damage

D_{NP} Non proportional damage

g_{NP} Dimensionless damage due to the non-proportionality

α Material-dependent non-proportionality sensitivity parameter

$\Delta\sigma_e$ Effective stress range

$\Delta\sigma_{NP}$ Non proportional effective stress range

$\Delta\sigma_{eq,IIW}$ Equivalent stress range according to IIW

$\Delta\sigma_{i,\mathbf{S,d}}$ Stress range from the rainflow counting method above the knee point of the S-N curve

$\Delta\sigma_{j,\mathbf{S,d}}$ Stress range from the rainflow counting method below the knee point of the S-N curve

$\Delta\sigma_{\mathbf{L,d}}$ Stress range from the rainflow counting method at the knee point of the S-N curve

$\Delta\sigma_{\mathrm{eq,EC3}}$ Equivalent stress range according to Eurocode 3

λ_i Factor for the stress range from Eurocode 3 that depend on the load

$\Delta\sigma_{\mathrm{LM}}$ Stress range from the rainflow counting method based on the load model according to Eurocode 3

$\Delta\sigma_{\mathrm{R}}$ Normal stress fatigue strength respectively for a given number of cycles

$\Delta\tau_{\mathrm{R}}$ Shear stress fatigue strength respectively for a given number of cycles

SF Safety factor

D_{EC3} Damage sum for Eurocode 3

SF Comparison value for IIW

$\Delta\sigma_{\mathrm{IIW}}$ Equivalent stress range that refers to normal stress S-N curves

k Factor that depends on the fatigue strengths and the number of cycles

D_σ Damage for normal stress

D_τ Damage for shear stress

Abbreviations

GFMS	Green Floating Marine Structure
ULS	Ultimate Limit State
CFD	Computational Fluid Dynamics
BVP	Boundary Value Problem
WADAM	Wave Analysis by Diffraction and Radiation Analysis Method
WAMIT	Wave Analysis by the Method of Integral Equations
BEM	Boundary Element Method
RAO	Response Amplitude Operator
SIMA	Simulation of Marine Applications
DOF	Degree of Freedom
COG	Center of Gravity
FOWT	Floating Offshore Wind Turbines
QTF	Quadratic Transfer Functions
SLM	Single Line Mooring
TSR	Tip Speed Ratio
CPC	Collective Pitch Controller
IPC	Individual Pitch Controller
MPPT	Maximum Power Point Tracking
PID	Proportional-Integral-Derivative
PI	Proportional-Integral
LQR	Linear Quadratic Regulator
MPC	Model Predictive Controller
FEM	Finite Element Model
FEA	Finite Element Analysis
DNV	DET NORSKE VERITAS
ABS	American Bureau of Shipping
SWL	Sea Water Level
IRF	Impulse Response Function
TLP	Tension Leg Platform
ULS	Ultimate Limit State
FLS	Fatigue Limit State
ALS	Accidental Limit State
SLS	Serviceability Limit State
NTM	Normal Turbulence Model
ETM	Extreme Turbulence Model
EWM	Extreme Wind Speed Model
DLC	Design Load Case
PDF	Probability Density Function
SCF	Stress Concentration Factor
FPSO	Floating Production Storage and Offloading
MVEE	Minimum Volume Enclosed Ellipse
SVD	Singular Value Decomposition

1 Introduction

1.1 Floating offshore wind turbines (FOWT)

The deployment of offshore wind turbines has increased over the last years to achieve the net-zero targets and increase energy security. Floating wind turbines allow for greater water depths, where an increased wind energy potential is available, and for locations without shallow waters.

Various designs and concepts have been proposed, but none of them prevails. Material availability, cost, sea conditions, and knowledge highly affect the decision of the floater type.

According to the categorization in [2] regarding the stability, the following types exist:

- **Ballast stabilized**: Spar platform. It resembles the monopile, but instead, it has a heavy ballast at the lowest part for increased stability, shifting the metacenter as high as possible.
- **Mooring stabilized**: Tension leg platform (TLP), where vertical taut mooring lines stabilize the floater.
- **Buoyancy stabilized**: Barge and semi-submersible platforms. A large waterplane area provides the restoring moment for stability, with the metacenter located above the center of gravity.

Spars have a large draft, so they are more suited for deep waters. Semi-submersibles and TLPs are suitable for a wider range of water depths. Barges can be used at shallower water depths than semi-submersible or other floaters due to a low draft. They can also replace monopiles, allowing for easier installation with towing. Also, they don't disturb the seabed during installation as monopiles do and they are suitable for various seabed conditions.

In addition, barge-type floating wind concepts can offer advantages compared to other competing alternatives in terms of manufacturability due to a simple structure that allows for easy yard fabrication. Combining the barge with a single mooring line layout enables a reduction in material costs, utilizing the weathervane principle, and decreasing the wake effects in the wind farm.

An overview of the main FOWT floater types is presented Figure 1, where their design characteristics are displayed.

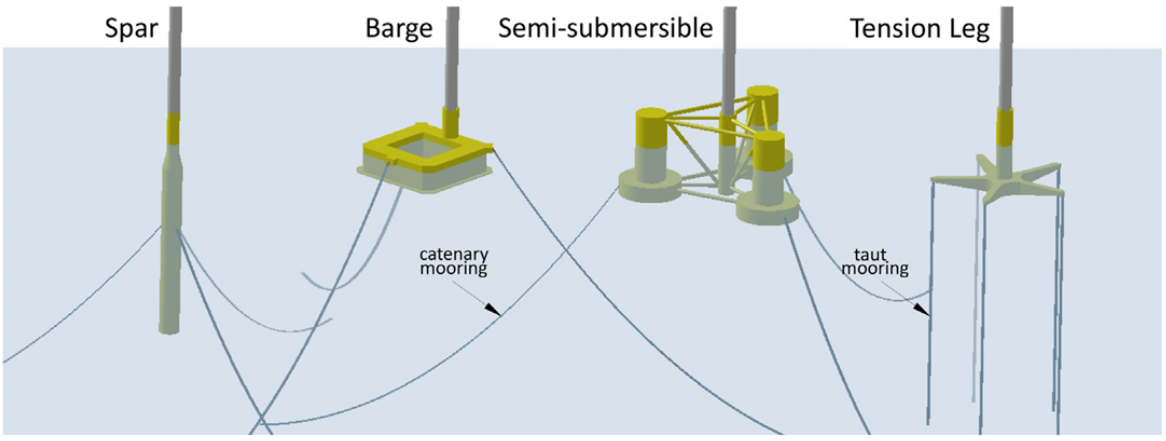

Figure 1: Types of FOWT floaters [3].

Typical values for the natural periods of the different types of floaters are presented in Table 1. TLPs have the smallest natural periods in heave, roll, and pitch due to the vertical taut lines that increase the stiffness. Surge, sway, and yaw have, in general, a high natural period, due to lower mooring stiffness in these directions. The larger waterplane area of semi-submersibles leads to an increased stiffness; therefore, the natural period in roll and pitch is lower than in the spar. Overall, the size (external dimensions) and the mooring layout significantly affect the natural periods of the floater. Therefore,

different behavior and motions are expected from the various designs, so different water depths are more suitable for every configuration.

Table 1: Typical natural periods [s] for floaters [4]

Floater Mode	Spar	TLP	Semi
Surge	> 100	> 100	> 100
Sway	> 100	> 100	> 100
Heave	$20 - 35$	< 5	$20 - 50$
Roll	$50 - 90$	< 5	$30 - 60$
Pitch	$50 - 90$	< 5	$30 - 60$
Yaw	> 100	> 100	$>$ 50-60

In this work, the WindBarge, a barge-type floater from Green Floating Marine Structures (GFMS), is studied and utilized, which is introduced in section 1.3. However, other barge-type FOWTs are first discussed in the following section.

1.2 Barge-type FOWTs

A research was conducted to find existing concepts for barge-type FOWTs and identify design patterns, if present, for this type of floater. Most of the FOWT concepts, however, are semi-submersibles, TLPs or spars, therefore, the available barge-type of floaters are limited. Over the next sections, the identified floaters are presented and commented on. This research is expected to provide some insight regarding the configuration of the inner structure.

BW Ideol Floatgen (2 MW)

The BW Ideol Floatgen (Figure 2) is a 2 MW barge-type FOWT that looks like a rectangular ring. It is made up of concrete, but steel can also be used. Moreover, it can be upgraded to a larger wind turbine by scaling the floater as well. The damping pool in the middle of the floater optimizes its stability and performance due to the sloshing of the water.

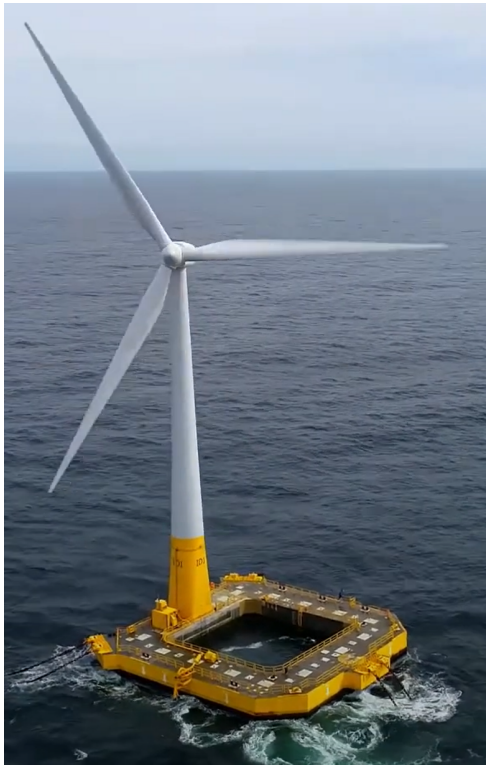

Figure 2: BW Ideol Floatgen, 2 MW [5].

In Figure 3, the outer structure of the floater is depicted. A large heave plate is present at the bottom of the floater that primarily reduces the heave (vertical) motion and can indirectly reduce the roll and pitch motion too. Also, some brackets are included that support the heave plate. The total number of mooring lines is six.

The inner structure of the floater is shown in Figure 4. Several vertical walls (bulkheads) divide the internal space in smaller compartments. Apart from strengthening the whole structure, they also act as a barrier in case there is a puncture (for example, due to an accident), so that only part of the floater will fill up with water. Near the tower region, there doesn't seem to be any extra support or bulkheads starting from the internal part of the tower. However, the tower transition piece is rectangular with larger dimensions than the tower at its base.

Figure 3: Outer structure of BW Ideol Floatgen, 2 MW [5].

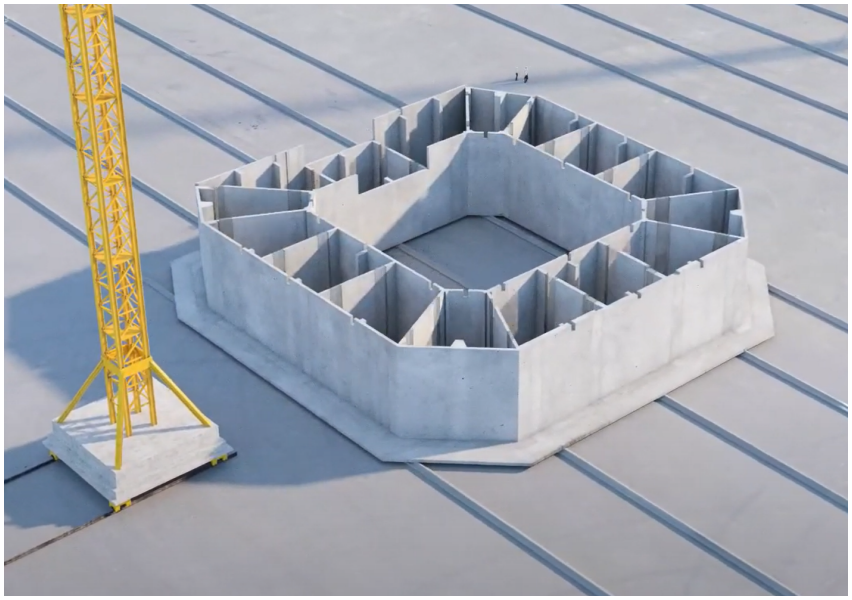

Figure 4: Inner structure of BW Ideol Floatgen, 2 MW [5].

Beridi TRIWIND floater

The TRIWIND from Beridi [6] is another type of barge-type floater with a symmetric triangular shape (Figure 5). It has a honeycomb inner structure with watertight spaces (Figure 6), it is made up of concrete, and it is built as a monolithic structure through a slip-forming technique.

The inner structure has vertical walls that strengthen the floater and uniformly distribute the loads from the tower towards the rest of the floater. The radial distribution of the walls, starting from the tower, speculate the importance of strengthening that area. As noted in [7], the internal configuration and general design lead to mainly compression stresses as the bending moment is compensated.

The tower has a conical interface with the floater at its base, significantly increasing its diameter. Moreover, a heave plate is present at the bottom of the floater.

Figure 5: Beridi TRIWIND floater [8].

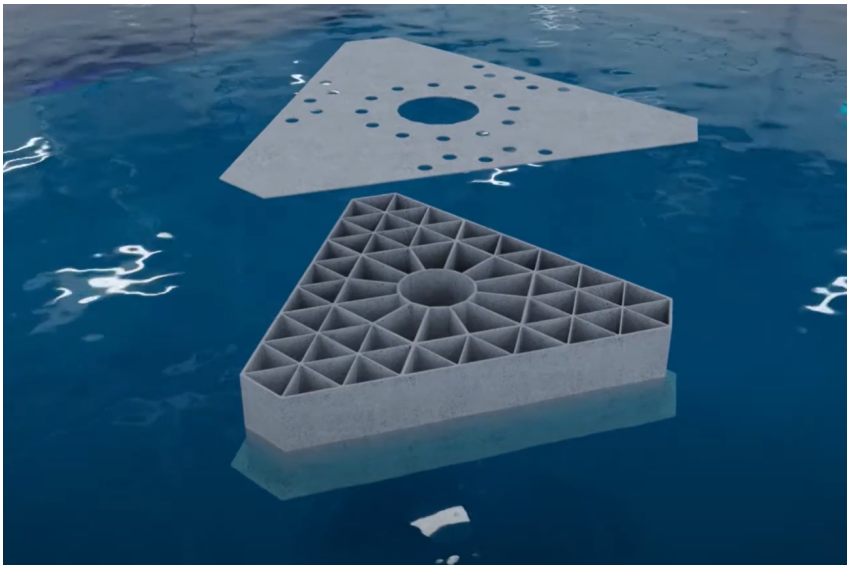

Figure 6: Inner structure of TRIWIND [8].

Beridi FLOWIN floater

FLOWIN (Figure 7) is a revised floater design [9] that comes from its predecessor TRIWIND floater, with improved hydrodynamic performance. It has a rectangular shape and it is symmetrical. The inner structure, though, remained almost the same, with vertical walls starting from the tower and a honeycomb-like pattern. Also, the heave plate is present.

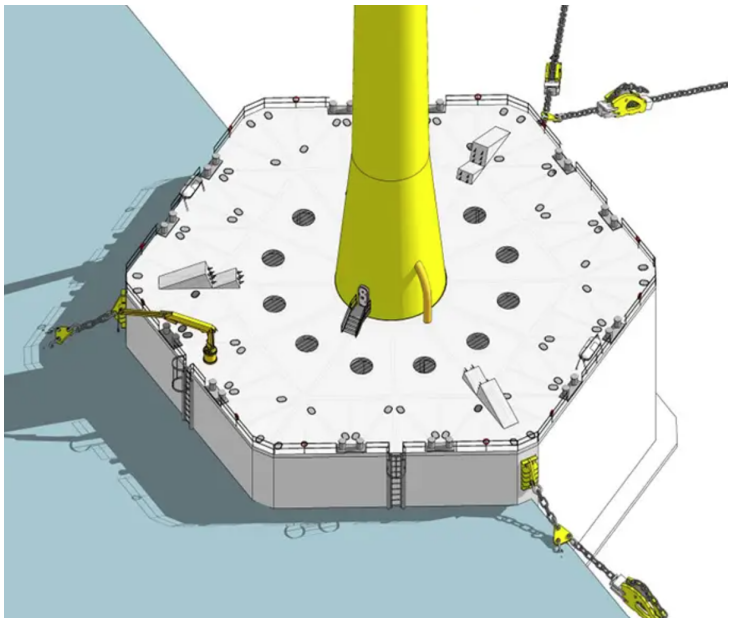

Figure 7: Beridi FLOWIN floater [9].

1.3 WindBarge concept

The WindBarge is a barge-type floating structure concept by GFMS (Green Floating Marine Structures) that integrates, as a first design iteration, a 15 MW upwind turbine on a barge-type structure, with vertical side walls, horizontal bottom, and one mooring line including internal redundance. The complexity of the mooring system is reduced, and the utilization of the weathervane principles reduces loads, which is crucial for shallow water mooring. The floating steel structure uses structural building blocks based on flat plates without any complex bending or welding. Thus, simplified fabrication techniques can be applied, as standardized yard fabrication is available. The steel usage in the floater is optimized against the mooring system and the motions are reduced due to mooring-dependent ballast distribution. GFMS has many competent partners that contribute to the project: VATTENFALL, FOSEN YARD, EDR MEDESO, CFD marine, NTNU, APL|NOV and Norconsult.

The structure is illustrated in the front and back view in Figure 8 and Figure 9 respectively.

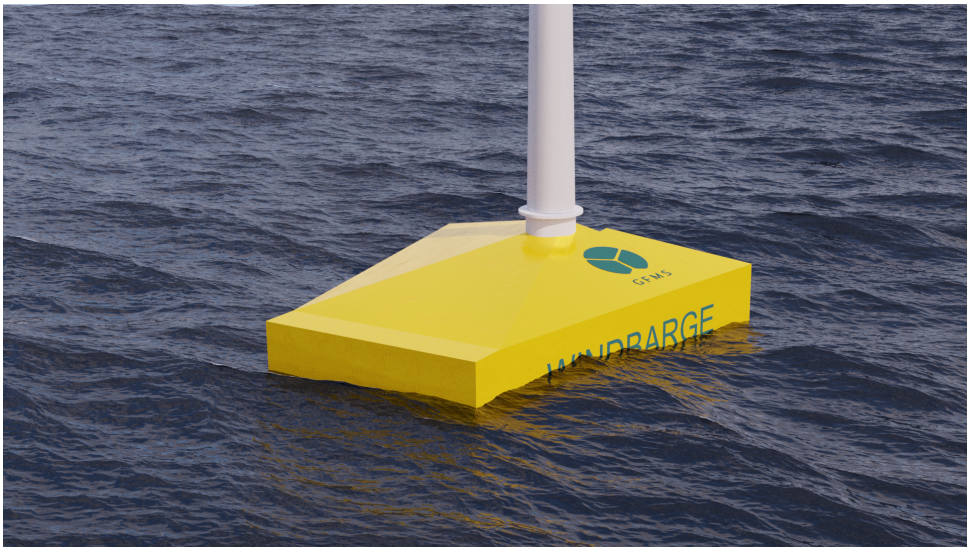

Figure 8: WindBarge front view.

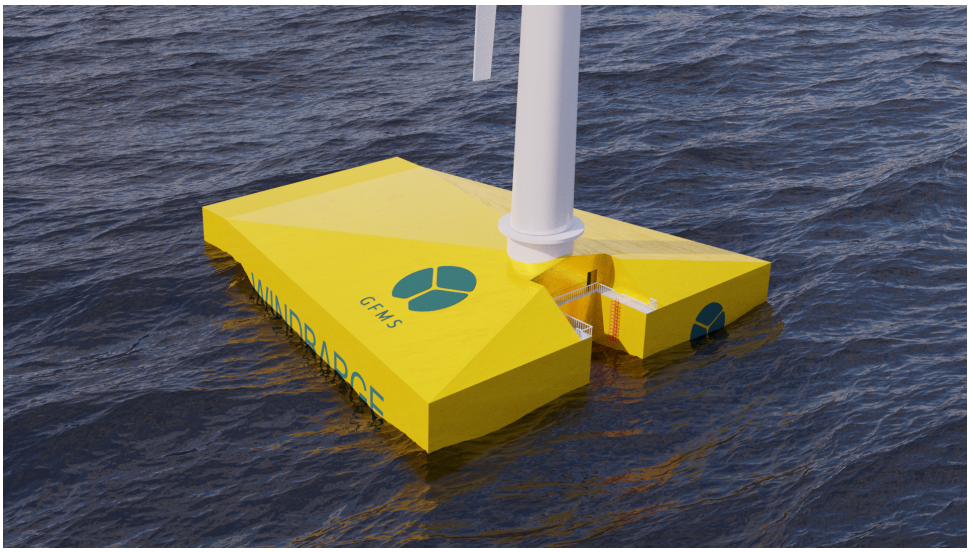

Figure 9: WindBarge back view.

The fundamental design choices, according to [10] and [11], that make WindBarge a competitive option for a floater, are the following:

- **Low draft**: The draft is less than 10 meters for easy quayside production in most shipyards and easy installation, maintenance, and decommissioning with tugboats.
- **Single Line Mooring (SLM)**: The single-line will reduce cost, minimize seabed impact, and allow for weathervaning of the structure, in addition to the yaw control, to maximize power production by avoiding the wake from upstream turbines. However, redundancy of the mooring line must be considered. The fairlead is located in the bow of the structure.
- **Fixed ballast**: The fixed ballast reduces cost by avoiding complex ballasting systems. The structure is divided inside into compartments for ballasting and to avoid the whole structure getting flooded in case of a puncture.
- **Thruster**: The thruster will provide pretension in the mooring system to avoid a slack mooring line when there is no loading in the structure.
- **Turbine position**: The turbine is located such that the aerodynamic attack point is after the horizontal center of gravity (COG) and towards the stern. This is necessary to avoid fish-tailing (lateral oscillation) of the mooring line [11].
- **Access**: There is a docking area in the stern of the structure that minimizes wave heights for easy access and docking of ships.
- **Manufacturing**: The WindBarge will utilize flat plates with low carbon steel and low CO2 emissions, making it easy to manufacture and environmentally friendly.

The floater is designed for intermediate water depths (40 to 80 meters). The locations and sea conditions for which it was studied are the following, according to [12]: Dogger Bank at 75 meters, Creyke Beck at 40 meters, and Southern North Sea II at 57 meters.

Additional details about the model that is used in this thesis are presented in section 3.2.

1.4 Problem description

The floating offshore wind turbines (FOWT) are complex dynamic systems exposed to both aerodynamic and hydrodynamic loads. In addition to them, the control schemes and the mooring lines have an impact on the global response and loading of the FOWT. Before manufacturing and deploying a floating wind turbine, several studies are needed to analyze its structural response and motions in order to verify that they are within safe limits. Therefore, an accurate representation of the environmental loads is

necessary when simulating a floating structure.

The operational lifetime of floating offshore wind turbines is around 20 to 30 years. The environmental conditions must consider site-specific data that account for a longer return period for extreme scenarios. Then, the stress levels of the FOWT are important in order to examine if they are below the yield strength of the material. Apart from extreme loads, cyclic loads below the yield strength cause fatigue and can lead to failure. An accurate estimation of the fatigue life is important to avoid unanticipated cracks, repair costs, and the need for regular inspections.

The complex geometry and dynamic loading in floating wind turbines can lead to multiaxial non-proportional stress conditions. The non-proportionality refers to a stress state where the normal and shear stress components are out of phase, and they can also have different frequencies. A proportional stress state is also important where the stress components are in phase. Considering only one stress component, normal to the weld line, and excluding the shear stresses may underestimate fatigue damage, especially when the level of non-proportionality is significant. On the other hand, the use of principal stresses can overestimate fatigue damage for non-proportional stress conditions when the direction of the principal stress changes considerably.

The main problem that is dealt within this thesis is to identify whether a multiaxial stress state appears on complex floating structures, and specifically, barge-type floaters such as the WindBarge. Therefore, a screening procedure is investigated, and different fatigue assessment methods are assessed. This study will highlight the necessity for using multiaxial fatigue assessment methods for FOWT and the potential miscalculations of the fatigue damage with not suitable methods. Moreover, a focus is given on understanding the cause of multiaxiality. The tower transition region is selected for the fatigue study because high stress levels are present there from the wind turbine, and the geometry changes significantly.

The configuration of the internal structure of FOWTs is of additional interest in this thesis, which has not been investigated in academic research before. The provided model for the WindBarge is used as a working model to study how the current configuration of this first design iteration can be related to external loading and the eigenfrequencies of the structure, providing insight for this type of structure, which can be used when making design choices. Operating and extreme load cases are examined in this thesis, but faulty conditions are not considered due to time limitations.

As the topic of the analysis of a FOWT is quite complicated, some focus is also set to studying the available standards regarding the modeling of the environment and the design load cases for ultimate and fatigue limit state, as well as the theory regarding hydrodynamic loads, aerodynamic loads, and control. In addition, the environmental parameters derived by the WindBarge project are studied and utilized.

1.5 Scope of thesis

As presented in the problem description, the two main research topics of this thesis are primarily fatigue with a focus on multiaxiality and secondarily the configuration of the internal structure. There is also an additional input for the aero-hydro-servo analysis theory, the environment, the design load cases, and the finite elements and stresses. Moreover, existing designs of the inner structure for barge-type floaters were already presented (section 1.2). Several topics are selected for the theoretical background (literature review) and specific tasks for the implementation, as described in the following paragraphs.

The focus of the theoretical background (literature review) is set to the following subjects:

- Hydro-aero-servo theory for FOWT.
- Wind and wave modeling and design load cases (DLCs) according to standards.
- Shell/beam elements and stresses.
- Uniaxial and multiaxial fatigue assessment and screening methods (standards, procedures).

Regarding the modeling and implementation, the following tasks are set for the thesis:

- Extend the structural (shell) model of the floater from the provided model to include the tower and study the tower transition region regarding the stress response.
- Define the relevant wind and wave environment for the location of the WindBarge to study the ultimate limit state (operational and/or parked wind turbine) and fatigue limit state (operational wind turbine) from the background material.
- Describe the internal stress distribution (from the tower to the floater's inner structure and outer shell) by selecting relevant elements along the bulkheads and plotting the stress time series to derive the conclusions through statistical and power spectral density analysis of the stress time series. Propose and implement at least one alternative inner structure configuration. The investigation shall be conducted according to the ultimate limit state environmental conditions.
- Examine if the maximum tower moment's timing corresponds to the floater's maximum stress amplitude. Also, quantify the difference in the stress amplitude when only the wind is considered (no waves).
- Perform structural screening in the tower interface (deck), display if the stresses are out of phase (non-proportionality), and identify multiaxial stress response fatigue governing locations.
- Perform uniaxial and multiaxial fatigue assessment in the tower transition region. Discuss whether the nominal uniaxial fatigue assessment overestimates or underestimates the fatigue damage.
- Suggest, based on the simulated conditions, whether the design is ultimate or fatigue limit state driven.

For the implementation, DNV's SESAM software suite is selected because it provides the capability for an integrated global and structural analysis for floating offshore wind turbines. The license was available from NTNU, as well as some knowledge about the software. This software suite was also used by the WindBarge project. An initial model of the WindBarge was provided as a working basis by the WindBarge project, but further modifications are proposed in the thesis.

Research questions

From the analysis in this thesis, an answer to the following research questions is aimed for:

1. Is multiaxiality and non-proportionality present at the tower transition region of barge-type floating wind turbines? What is the cause? Is fatigue damage overestimated or underestimated when utilizing not suitable methods for multiaxial non-proportional stress states?
2. What are the design considerations on the internal structure of a barge-type floating wind turbine?
3. Is the design of barge-type floating wind turbines ultimate or fatigue limit state driven?

Assumptions and simplifications

Several assumptions and simplifications are made to account for the time limitations of the thesis, as follows:

- Only one barge-type floater is examined, the WindBarge, and it is assumed that multiaxiality is also present at the deck in similar geometries. The WindBarge model corresponds to a first design iteration model. Changes in the model can lead to a different response.
- Limited load cases are examined, accounting for the most representative ones, as the computation time is high. It is assumed, though, that for fatigue, they provide a representative basis for an initial calculation. The current is disregarded, and only one location is examined.
- The internal structure is studied using ultimate limit state (ULS) load cases (operational and parked wind turbine) only. Faulty conditions are not considered.

Additional assumptions and simplifications regarding the simulation procedure and modeling are discussed in section 3.1.5.

1.6 Thesis structure

The thesis consists of six chapters, which are briefly introduced here:

- **Chapter 1: Introduction**. The floating wind turbines, barge-type floaters, and the WindBarge concept are introduced. The problems that are addressed in this thesis are discussed, and the specific research questions and tasks are presented, as well as the assumptions and simplifications of the work.
- **Chapter 2: Theoretical background (Literature review)**. This chapter focuses on the theory of fatigue, multiaxial fatigue, and screening that are more relevant to this study, with references from literature. Since this study refers to an integrated analysis of FOWT, important aspects of the theory regarding hydrodynamic loads, aerodynamic loads, and control systems are also included, with some additional in Appendix A. Also, the environment modeling and design load cases according to standards for FOWT are presented. Finally, the theory about the shell/beam elements and the stresses is briefly discussed.
- **Chapter 3: Methodology**. In this chapter, the simulation procedure for the integrated structural analysis and the fatigue analysis are described. Also, the WindBarge model is presented in addition to the proposed modifications. Finally, the meteocean data by the WindBarge project and the selected design load cases for this study are discussed.
- **Chapter 4: Results and Discussion**. The results from the study of the internal structure by using ultimate limit state (ULS) load cases and the nominal uniaxial and multiaxial fatigue and screening are presented and discussed.
- **Chapter 5: Conclusions and Future Work**. A summary of the conclusion of this study is presented in addition to recommendations for future work.

In addition to these chapters, the appendix includes chapters with additional theory, results, and studies, as summarized here:

- **Appendix A: Hydro-aero and dynamic time domain analysis of FOWT**. A more extended overview of the hydrodynamic and aerodynamic loads in addition to the dynamic time domain analysis procedure for FOWT is presented.
- **Appendix B: Methods for internal loads in offshore platforms and FOWTs**. Guidelines from standards for the structural analysis of marine structures are discussed. Also, different approaches and software for the structural analysis of FOWT from literature are presented.
- **Appendix C: Power spectral density of uniaxial stress**. The power spectral density for all design load cases are given regarding the nominal uniaxial stress.
- **Appendix D: Multiaxial screening**. Additional results from the multiaxial screening are given.
- **Appendix E: Supplementary studies**. Supplementary studies were carried out to identify the cause of the roll motions that increase fatigue and the effect of the yaw controller to them.

2 Theoretical background

In this chapter, the relevant background theory for this research work is provided. The topic of hydrodynamic and aerodynamic loads and control systems for FOWTs is briefly discussed in section 2.1, which constitutes the basis of the integrated analysis of FOWTs. Then, the modeling techniques of the wind and wave environment, in addition to the limit states and design load cases from standards, are presented in section 2.2. The theory about the shell and beam elements and the stresses in a structural model is provided in section 2.3, which is important in order to understand and analyze the stress response. Finally, the topics of fatigue, multiaxial fatigue, and screening are discussed in sections 2.4 and 2.5, regarding the theory and available methods, including references to literature for implementation in FOWTs.

2.1 Hydro-aero-servo theory

A summary of the modeling of the hydrodynamic and aerodynamic loads, in addition to the control techniques for FOWTs, is presented in the following sections. A more complete analysis of the hydrodynamic and aerodynamic loads can be found in Appendix A. Regarding the software references, SIMA, a simulation tool from SINTEF Ocean for floating structures and marine operations, is mentioned to describe the required input and is also used in this study. Moreover, WADAM and WAMIT are referred to for the frequency domain analysis.

2.1.1 Hydrodynamic loads

A floating structure is subject to hydrostatic and hydrodynamic loads. The Navier-Stokes equations are the governing equations for solving fluid motions and require Computational Fluid Dynamics (CFD), which is a computationally expensive procedure. By introducing simplifications, the potential flow theory is derived, which reduces the computation time. The fluid is considered inviscid, incompressible, and the flow is irrotational. The flow separation and vortices are not modeled. From this simplification, the Bernoulli equation (Equation 49) is derived, and the velocity potential ϕ is introduced with $\boldsymbol{u} = (u, v, w) = \nabla\phi$, where $\boldsymbol{u} = (u, v, w)$ is the velocity vector of the fluid and $\nabla = (\partial/\partial x, \partial/\partial y, \partial/\partial z)$ is the vector of partial derivatives. Then, the continuity of mass, which is also considered, is expressed as $\nabla\phi^2 = 0$.

The formulated problem is called a boundary value problem (BVP) and requires numerical tools. The wetted surface of the structure is discretized, and the developed codes are called panel codes. WADAM or WAMIT can be used to derive the hydrodynamic data. The resulting restoring forces, added mass, damping coefficients, and additional second-order elements and loads are used for the time domain analysis of the floater, as further discussed in Appendix A.

The first-order boundary value problem is linear, and therefore, the velocity potential can be expressed as a sum of velocity potentials: the incident wave velocity potential, the diffraction velocity potential, and the radiation velocity potentials for the six degrees of freedom (DOFs) of rigid bodies. These problems are solved separately. The diffraction refers to a fixed structure when there are incident waves, and the radiation refers to a moving structure in calm water. The wave excitation forces are derived from the incident wave and diffraction problem, and the restoring forces, added mass, and damping coefficients from the radiation problem. The required input for the model of the floater is presented in the following section.

Floater model

The floater is considered rigid (not flexible) and, therefore, it is modeled as a SIMO body in SIMA. According to SIMA documentation [13], the model requires specific input to calculate the global response. Specifically:

- Structure mass: The mass, moment of inertia, and Center of Gravity (COG) of the floating structure are calculated and imported, considering the ballast. The contribution from the tower and the turbine is not considered, as they are added separately in SIMA as flexible bodies and in order not to account for them twice [14].

- Linear and Quadratic Damping: The linear and quadratic damping coefficients are introduced to include viscous damping, which is not calculated from the diffraction theory programs (WAMIT or WADAM). They are imported as 6x6 matrices and can be calculated from CFD or towing tank tests. The contribution from the frequency-dependent added mass and damping from WAMIT or WADAM is removed in order not to account for it twice.

- Hydrostatic Stiffness: The hydrostatic coefficients are imported from WAMIT or WADAM, as a 6x6 matrix. The tower and the turbine are not considered, because they are added later in SIMA and in order not to account for them twice. The fictitious coupling terms between roll and yaw come from the imbalance of gravity and buoyancy in WAMIT and they can be removed [14].

- First Order Motion Transfer Function: The Response Amplitude Operators (RAOs) for the motions are imported from WAMIT or WADAM, providing the amplitude and phase for each degree of freedom (surge, sway, heave, roll, pitch, yaw) and each wave frequency.

- First Order Wave Force Transfer Function: The RAOs for the forces are imported from WAMIT or WADAM, providing the amplitude and phase for each degree of freedom ($F_{\mathrm{x}}, F_{\mathrm{y}}, F_{\mathrm{z}}, M_{\mathrm{x}}, M_{\mathrm{y}}, M_{\mathrm{z}}$) for each wave frequency.

- Quadratic Transfer Functions: These functions (QTFs) are calculated by diffraction theory programs (such as WAMIT and WADAM) and they provide difference-frequency (wave drift) and sum-frequency (ringing) forces.

- Second Order Wave Drift Forces: The wave drift forces ($F_{\mathrm{x}}, F_{\mathrm{y}}, M_{\mathrm{z}}$) are imported from WAMIT or WADAM as QTFs.

- Wave Drift Damping: The second-order damping coefficients are also considered for low-frequency motions and are calculated from the wave drift forces.

- Quadratic Wind Coefficients: The wind force coefficients (translational: C1, C2, C3 and rotational: C4, C5, C6) are given for each wind direction, which can be calculated from CFD, wind tunnel tests, or towing tank tests.

- Linear and Quadratic Current Coefficients: The current force coefficients (translational: C21, C22, C23 and rotational: C24, C25, C26) are given for each current direction, which can be calculated from CFD, wind tunnel tests, or towing tank tests.

- Retardation Function: Accounts for the influence of past motions on current forces and it is given as a time series for all dofs, whereas each dof has an effect on all other dofs.

- Frequency Dependent Added mass: The frequency-dependent added mass coefficients are calculated and imported from WAMIT or WADAM.

- Frequency Dependent Damping: The frequency-dependent damping coefficients are calculated and imported from WAMIT or WADAM.

- Added mass Zero Frequency: The added mass coefficients at low accelerations are imported from WAMIT or WADAM, as a 6x6 matrix. These coefficients are larger than the ones for infinite frequency because the water contributes to the system's inertia at slow motions.

- Added mass Infinite Frequency: The added mass coefficients at high accelerations are imported from WAMIT or WADAM, as a 6x6 matrix.

For the hydrodynamic data, the tower and the turbine are considered, accounting for the actual mass distribution [14]. The reader can refer to [13] for more information about the required input to the model.

2.1.2 Aerodynamic loads

The aerodynamic loads account for the forces from a dynamic wind inflow. The blade element momentum (BEM) method is used (see Appendix A), considering annular elements at the wind turbine to calculate the thrust, power, and torque. The algorithm is run for each strip iteratively and independently. The axial a and tangential a' induction factors, the flow angle ϕ, the angle of attack α, and the

normal C_{n} and tangential C_{t} force coefficients are calculated, as defined in Appendix A.

The BEM theory requires a few corrections. An infinite number of blades is considered with the BEM theory, and therefore, Prandtl's tip loss factor F is introduced to correct this. Also, for an induction factor higher than 0.4, the relation between the thrust coefficient C_{T} and axial induction factor a is inaccurate, and empirical equations are used to correct it. An iterative procedure is followed in combination with Prandtl's correction.

Additional corrections are implemented to account for the dynamic inflow because the BEM theory considers quasi-static conditions. These are the dynamic wake (time delay in the induced velocities due to the vorticity being convected downstream), the dynamic stall (changing lift and drag coefficients due to flow separation and the change of the angle of attack), the effect of tilt angle of the rotor and the yaw angle in the induction factor, and the tower shadow (velocity deficit upwind of the tower), as further discussed in Appendix A.

Wind turbine model

SIMA is used to simulate the wind turbine (blades, hub, nacelle, and tower) attached to the floater. The hub and nacelle are modeled as SIMO bodies and are considered rigid (not flexible). The blades and the tower are modeled as RIFLEX elements and are considered flexible. The model details are specified as follows:

- Blades: The blades are modeled with beam elements. Each blade is represented with a line associated with a line type which consists of several elements with different cross-sections. Cross-sections are defined with mass and stiffness properties and are assigned with an airfoil and a chord length. The airfoil characteristics (drag C_{d}, lift C_{l}, and moment C_{m} coefficients) are given for different Reynolds numbers. Apart from the blade line, an eccentricity line is defined that connects the blade line with the shaft line rigidly. The endpoints of the lines are called supernodes. At the connection joint, the supernode of the blade line is the slave node and the supernode of the eccentricity line is the master node. This combination is used for the individual pitch control of each blade.

- Shaft: The shaft is modeled with a line that is associated with a line type consisting of two segments. Between the segments, there is a Flex joint (el_torq) with a high axial stiffness where the generator torque is applied. The supernode at the shaft end towards the hub is free, whereas the supernode at the other end is slave to the supernode at the tower top (master node).

- Hub: The hub is modeled as a mass at the shaft end towards the wind turbine.

- Nacelle: The nacelle is modeled as a mass at the tower top.

- Tower: The tower is modeled with beam elements. It is represented with a line associated with a line type which consists of several elements with different cross-sections (diameters). The supernode at the tower top is free, whereas the supernode at the tower bottom is slave to a center of gravity of the platform $(X_{\mathrm{g}}, Y_{\mathrm{g}}, Z_{\mathrm{g}}) = (0, 0, 0)$. Then, this point is linked to the fairlead where the mooring line is connected.

- Mooring line: The mooring line is also modeled with beam elements.

The reader can refer to [13] for more information about the required input to the model.

2.1.3 Control systems

The control strategies are discussed according to [15] and [4]. The control levels on a wind turbine can be distinguished into supervisory control and operational control. The supervisory control is responsible for start-up, shut-down, standby, and faults. The operational control deals with objectives such as maximizing power production and minimizing structural loads, and is implemented by regulating blade pitch, generator torque, and nacelle yaw. This study focuses on operational control.

Control regions

There are four control regions:

- Region 1 is below cut-in speed and the wind turbine is not rotating.
- Region 2 is between cut-in speed and rated speed. The pitch angle is zero in this region, and the rotational speed and generator torque are adjusted to achieve optimal performance (maximum power production, therefore power coefficient C_p).
- Region 3 is between rated and cut-out speed. The pitch angle varies in this region, the blade pitch angle is controlled, and the rotor speed and generator power (or torque) are constant.
- Region 4 is above cut-out speed, the blades are pitched 90 deg and there is no power extraction.

Therefore, different control strategies are implemented in each region to satisfy the control objectives.

Generator torque control

The control strategy for maximum power is called Maximum Power Point Tracking (MPPT). The rotor speed is measured and compared with a reference rotor speed at each wind speed. Algorithms such as proportional-integral (PI), proportional-integral-derivative (PID), and sliding mode controllers can be used to adjust the rotor speed. Otherwise, the torque can be adjusted to obtain the optimal power coefficient C_p. A simple wind turbine model commonly used is:

$$J_\mathrm{R}\dot{\Omega} = (M_\mathrm{aero} - M_\mathrm{g}) \tag{1}$$

where J_R is the inertia of the drivetrain, Ω is the rotational speed of the shaft, M_aero is the aerodynamic torque, and M_G is the generator torque. Advanced control techniques such as H_∞ and sliding mode controller can also be used.

Collective pitch control (CPC)

A PI controller can be derived with suitable gains K_p and K_I for the proportional and integral terms of the error between the measured and the reference rotor speed ($\Delta\omega$), as shown in the following equation:

$$\beta = K_\mathrm{P}\Delta\omega + K_\mathrm{I}\int_0^t \Delta\omega d\tau \tag{2}$$

where β is the blade pitch angle. These gains are different for each pitch angle, which is called gain-scheduling, as they change. All the blades have the same pitch angle with the collective pitch controller (CPC).

Apart from PI controllers, other optimal controllers can be used to consider more than one objective. Such controllers are Linear Quadratic Regulators (LQR), Model Predictive Controllers (MPC), and H_2 and H_∞ controllers. Better performance can be achieved, but the controller complexity is increasing.

Individual pitch control (IPC)

The individual pitch control (IPC) allows for different pitch angles between the blades. This can decrease the wind turbine loads and provide restoring forces as the rotor is asymmetrically loaded. However, hydraulic actuators are required for each blade.

For single-point mooring (SPM) floating wind turbines, a significant yaw drift is present due to wind shear, shaft tilt, coning angle, and platform pitch that leads to an additional angle between the rotor disc and wind direction, turbulence, and aeroelastic response of the blades, as stated in [16]. In this case, an IPC scheme can be applied to align the rotor with the wind direction. The error between the wind direction and the rotor hub axis can be utilized as an input to the controller.

Yaw control

For the yaw misalignment, a yaw mechanism can be used instead of an IPC scheme. The yaw rate of the motor is applied when the misalignment exceeds a threshold at specific time intervals. According to [16], the smaller the time interval, the better the aligning, however, a very rapid actuation is not feasible. By saturating the minimum and maximum yaw angles, larger time intervals are accepted. Nevertheless, IPC achieves stability faster and is more reliable.

Negative damping

The negative damping phenomenon is related to the floater pitch motion and the blade pitch angle. The objectives for the rotor speed and the floater pitch are contradictory when adjusting the blade pitch angle. As the wind speed increases, the blade pitch angle is increased to maintain the rated power. Then, the thrust is reduced and the floater pitches upwind which leads to an increase in the effective wind speed, and this cycle repeats.

The floater radiation characteristics must be such that they minimize the negative damping. Additional measures that can be taken to limit the negative damping are slowing down the wind turbine controller dynamics, removing a frequency range from a signal with a notch filter, and considering the tower top acceleration in the controller when adjusting the blade pitch angle. In [17], the HYWIND spar FOWT was examined and they reduced the controller frequency. However, to limit the rotational speed variations, they applied a constant torque instead of a constant power generator control scheme.

2.2 Environment modeling and Design Load Cases

2.2.1 Wind

The wind is modeled with appropriate methods that are derived from environmental data observation. As noted in the offshore standard DNV-OS-J101 [18], the spectral density of the wind speed $S_{\mathrm{U}}(f)$ is usually represented by the Kaimal spectrum:

$$S_{\mathrm{U}}(f) = \sigma_{\mathrm{U}}^2 \frac{\frac{4L_{\mathrm{k}}}{U_{10}}}{\left(1 + 6\frac{fL_{\mathrm{k}}}{U_{10}}\right)^{5/3}} \tag{3}$$

where f is the frequency, σ_{U} is the standard deviation of the wind speed, U_{10} is the 10-min mean wind speed, and L_{k} is an integral scale parameter with

$$L_k = \begin{cases} 5.67z & \text{for } z < 60 \text{ m} \\ 340.2 \text{ m} & \text{for } z \geq 60 \text{ m} \end{cases} \tag{4}$$

where z is the height above seawater level.

The 10-min mean wind speed U_{10} is usually represented by a Weibull distribution and the standard deviation of it σ_{U} with a lognormal distribution. The ratio $\sigma_{\mathrm{U}}/U_{10}$ is defined as the turbulence intensity.

The power law for the wind speed profile at different heights is defined as

$$u(z) = U_{10}(H)(\frac{z}{H})^{\alpha} \tag{5}$$

where $u(z)$ is the wind speed at height z, H is the reference height and α is an exponent according to atmospheric conditions.

For the design load cases examined in this study (section 2.2.4), the following wind models [18] are relevant:

- Normal Turbulence Model (NTM) for turbulent wind,
- Extreme Turbulence Model (ETM) for turbulent wind (higher turbulence), and
- Extreme Wind Speed Model (EWM) for a steady or turbulent wind for extreme wind conditions.

The international standard IEC 61400-1 [19] is often referred to regarding the design requirements for wind turbines. It is not intended to be used for offshore wind turbines, however it may be considered with caution. The wind turbines are classified for different site conditions based on the wind speed (classes I, II, and III, starting from higher to lower wind speed) and turbulence according to the following categories:

- Class A for high turbulence,
- Class B for medium turbulence, and
- Class C for low turbulence.

The international standard IEC 61400-3-2 [20] is referred to for the design requirements of offshore floating wind turbines. As noted in [21], as well as in [20], the turbulence intensity offshore is lower than that onshore (see Figure 10).

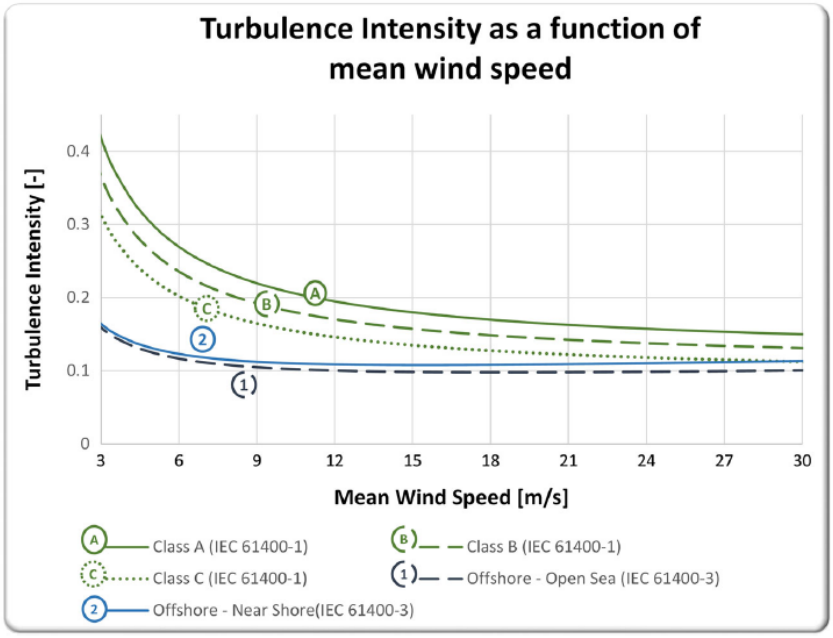

Figure 10: Turbulence intensity for onshore wind turbines (classes A, B, and C) and ofhsore wind turbines [21].

For more information regarding the environmental conditions and loads, the reader is also referred to the recommended practice DNVGL-RP-C205 [22]. In the standard DNVGL-ST-0437 [23] regarding loads and site conditions for wind turbines, the offshore normal and extreme turbulent models deviate from IEC 61400-1, introducing some equation for the standard deviation of the longitudinal wind velocity at hub height.

The TurbSim option is selected in SIMA to model the wind environment among other options. TurbSim is an open-source program from NREL that generates full-field turbulent wind files. It complies with IEC standards, producing a time series of wind data (.wnd) with normal or extreme turbulence, as mentioned in the documentation of SIMA [13]. For more information about this stochastic inflow turbulence code that provides coherent turbulence structures, the reader is referred to [24].

For the normal turbulence model (NTM), the following conditions were applied by the WindBarge project: a Kaimal wind spectral model with class C turbulence characteristics and a power law exponent α equal to 0.069, according to the IEC standard 61400-1 [19] (Ed. 3:2005) . As the turbulence intensity offshore is expected to be even less than that of class C onshore, this configuration shall be further evaluated regarding its effect on the structural response and power production and potentially revised in a future iteration. It is, however, deemed an acceptable and conservative initial setting.

2.2.2 Wave

The waves are modeled with the significant wave height H_s and the peak period T_p. The spectral density of the wave elevation $S_\zeta^+(\omega)$ is usually expressed by the Jonswap spectrum, which is noted in SIMA documentation [13] as follows:

$$S_\zeta^+(\omega) = \frac{\alpha g^2}{\omega^5} \exp\left(-\beta \left(\frac{\omega_\mathrm{p}}{\omega}\right)^4\right) \gamma \exp\left(-\left(\frac{\left(\frac{\omega}{\omega_\mathrm{p}} - 1\right)^2}{2\sigma^2}\right)\right) \tag{6}$$

where α is a spectral parameter, ω_p is the peak frequency, γ is a peakedness parameter, β is a form parameter (equal to 1.25), and σ is a spectral parameter (equal to 0.07 for $\omega < \omega_\mathrm{p}$ or 0.09 for $\omega > \omega_\mathrm{p}$). A Weibull distribution is commonly used for the significant wave height H_s.

For the design load cases examined in this study (section 2.2.4), the following sea state models according to the offshore standard DNV-OS-J101 [18] are relevant:

- Normal Sea State (NSS) with a conditional significant weight height H_s linked to the concurrent 10-minute mean wind speed,
- Severe Sea State (SSS) with extrapolated metocean data to account for a 50-year return period for the significant weight height H_s, and
- Extreme Sea State (ESS) with an unconditional significant wave height H_s derived from the distribution of the annual maximum significant weight height for a 50-year or 1-year return period.

The linear (airy) wave theory is utilized in SIMA. The wave height varies with a cosine function and it must be smaller than the wavelength and water depth. The irregular wave state is defined by the wave components, an output from SIMA containing the period, amplitude, heading, and phase of the waves.

The waves come from different directions in an actual irregular sea state, therefore, the directionality must be modeled. As noted in [25] for the computation of the wave loads under multidirectional sea states, the total spectrum $S(\omega, \theta)$ is defined as:

$$S(\omega, \theta) = S(\omega)D(\theta) \tag{7}$$

where $S(\omega)$ is the wave spectrum without considering directionality and $D(\theta)$ is a directional spectrum expressed as:

$$D(\theta) = C \left| \cos\left(\frac{\pi(\theta - \bar{\theta})}{2\theta_{\max}} \right) \right|^{2s} \tag{8}$$

where θ is the wave direction, $\bar{\theta}$ is the mean wave direction, $\theta_{\max}$ is the maximum deviation from the mean wave speed, s is the wave spreading parameter, and C is a normalizing constant. It is a requirement that:

$$\int_{-\theta_{\max}}^{\theta_{\max}} D(\theta)\, d\theta = 1 \tag{9}$$

There are different methods to calculate the wave elevation [25]: the double-sum, single-sum, and equal-energy methods, regarding how the energy is distributed in different directions. In this study, eleven directions from -180 to +180 degrees are considered with different spreading exponent (2s), depending on the wind speed. In Figure 11, an example of the wave spectrum is presented for a significant wave height $H_s = 4$ and a peak period $T_p = 10$ with different spreading exponent (2s) and a main direction at zero degrees. The larger the spreading exponent, the higher the energy at the main direction, which is reduced in the other directions.

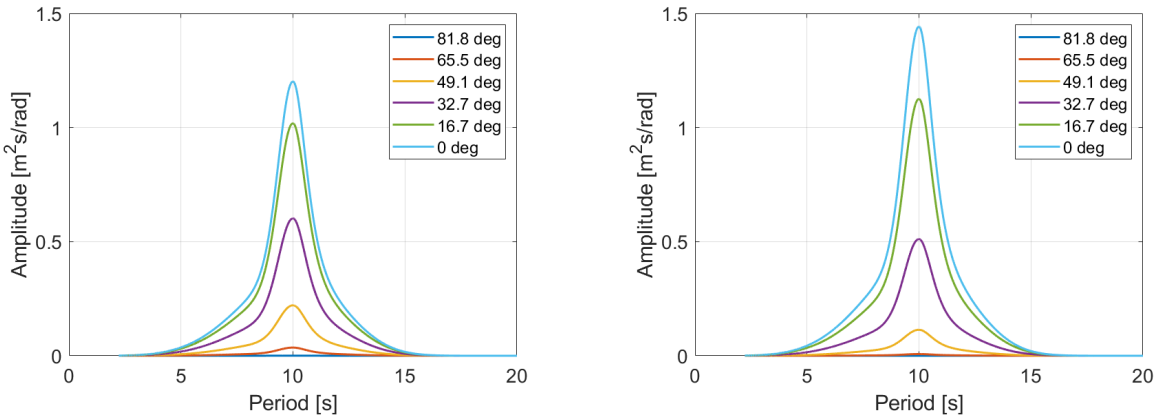

(a) 2s = 4. (b) 2s = 6.

Figure 11: Wave spectrum for different spreading exponents (2s).

As the wind speed increases, the waves become more unidirectional and can resemble long-crested waves. In this study, a spreading exponent equal to 4 is used for wind speeds below 22 m/s and equal to 6 for higher wind speeds.

2.2.3 Limit states

The offshore standard "Design of Offshore Wind Turbine Structures" (DNV-OS-J101) [18] is often referred to for guidelines regarding the structural design of offshore wind turbines. The limit states considered are listed below:

- Ultimate limit state (ULS) to account for maximum loads and the resistance of the structure,
- Fatigue limit state (FLS) for repeated loads that cause a cumulative damage,
- Accidental limit state (ALS) for accidental loads and their effect on the structures, and
- Serviceability limit state (SLS) to verify that the structure response is within acceptable limits under normal loads.

In this study the ULS and FLS are examined as more characteristic for the initial assessment of an offshore floating structure.

2.2.4 Design load cases (DLCs)

There are several design load cases (DLCs), including irregular cases, to be accounted for when designing a floating wind platform. As noted in the offshore standard DNV-OS-J101 [18], the following load cases are relevant:

1. Power production
2. Power production plus occurrence of fault
3. Start-up
4. Normal shutdown
5. Emergency shutdown
6. Parked (standing still or idling)
7. Parked and fault conditions

The LIFES50+ project [26], which is a European H2020-funded programme for floating wind turbines at water depths greater that 50 m, had the purpose to optimize four floater concepts for a 10 MW wind turbine and provide the criteria and design load case (DLCs) for the analyses. Apart from the IEC standard 61400-1[19], the LIFES50+ project was mainly based on the offshore standard "Design of Floating Wind Turbine Structures" (DNV-OS-J103) [27], which is now updated to the standard "Floating Wind Turbine Structures" (DNV-ST-0119) [28].

The number of load cases were reduced in the LIFES50+ project, accounting only for the most relevant regarding the design. Therefore, only selected cases were considered for power production with and without faults, parked condition and mooring line failure. In this study, only the power production DLC 1.6 and parked condition DLC 6.1 are considered for the ULS study and the power production DLC 1.2 for the FLS study, as summarized in Table 2.

Table 2: Load cases based on [18] and [26].

Design situation	Load case	Wind condition	Wave condition	Wind/wave directionality	Current	Limit state
Power production	1.6	NTM $v_{\text{in}} < U_{10,\text{hub}} < v_{\text{out}}$	SSS $H_{\text{s}} = H_{\text{s},50-\text{year}}$	Codirectional (one direction)	Wind current	ULS
Parked	6.1	EWM $U_{10,\text{hub}} = U_{10,50-\text{year}}$	ESS $H_{\text{s}} = H_{\text{s},50-\text{year}}$	Misaligned (many directions)	50-year current	ULS
Power production	1.2	NTM $v_{\text{in}} < U_{10,\text{hub}} < v_{\text{out}}$	NSS $H_{\text{s}}, T_{\text{p}}$ joint dist.	Codirectional (many directions)	-	FLS

In [29], a short-term fatigue analysis of a spar FOWT is studied. It is mentioned that for a fatigue analysis, a bin size of 2 m/s for the wind speed, 0.5 m for the wave height and 0.5 s for the wave period are recommended by the IEC 61400-3 [30]. Also, for a precise fatigue damage analysis and derivation of the probabilities, a joint distribution of the wind and wave must be considered [29] with:

$$f_{\mathrm{U_W},\mathrm{H_S},\mathrm{T_P}} = f_{\mathrm{U_W}} \cdot f_{\mathrm{H_S}|\mathrm{U_W}} \cdot f_{\mathrm{T_P}|\mathrm{U_W},\mathrm{H_S}} \tag{10}$$

where $f_{\mathrm{U_W},\mathrm{H_S},\mathrm{T_P}}$ is the joint probability density function (PDF) of the mean wind speed U_W, the significant wave height H_s and the peak period T_p, $f_{\mathrm{U_W}}$ is the PDF of the mean wind speed U_W, $f_{\mathrm{H_S}|\mathrm{U_W}}$ is the PDF of the significant wave height H_s for a given mean wind speed U_W and $f_{\mathrm{T_P}|\mathrm{U_W},\mathrm{H_S}}$ is the PDF of the peak period T_p for a given mean wind speed U_W and significant wave height H_s.

The $f_{\mathrm{U_W}}$ can be represented by a Weibull distribution, the $f_{\mathrm{H_S}|\mathrm{U_W}}$ by a Weibull distribution as well, and the $f_{\mathrm{T_P}|\mathrm{U_W},\mathrm{H_S}}$ by a lognormal distribution. With this approach, the misalignment between the wind and the waves is not considered.

The joint probability distribution is further analyzed and discussed in [31] where the wind/wave misalignment is included in the joint PDF. It is found that more than many sea states are required to include wind speeds above the rated wind speed, however, merging similar sea states can reduce the simulation time.

2.3 Shell/beam elements and stresses

The characteristics of the elements in the finite element model and the definition of the available stresses are deemed necessary for a comprehensive analysis of the results. As DNV's software packages are used, the following sections are mainly based on DNV's Xtract manual [32].

2.3.1 Shell and beam elements

For the plates, shell elements are used as noted in section Appendix B. In this study, second-order elements are selected for higher accuracy and reduced shear locking behavior, and mostly quadrilateral 8-node shell elements. Triangular 6-node shell elements are also used, but they are generally avoided because they can be less accurate and introduce additional stiffness. However, in complex geometrical areas they are necessary for the mesh. Similarly, second-order 3-node beam elements are used.

In Figure 12, the 8-node and 6-node shell elements are presented. They have 8 (2x2x2) and 6 (2x3x3) integration (Gauss) points respectively, so they represent a reduced integration setup with lower computation time and reduced shear locking effect.

The shell elements are subparametric; the nodal coordinate points are less than the points at which the displacement parameters are specified [33]. Therefore, the geometry is interpolated with one lower order model (first-order) than the displacements (second-order). The curves are approximated with straight lines.

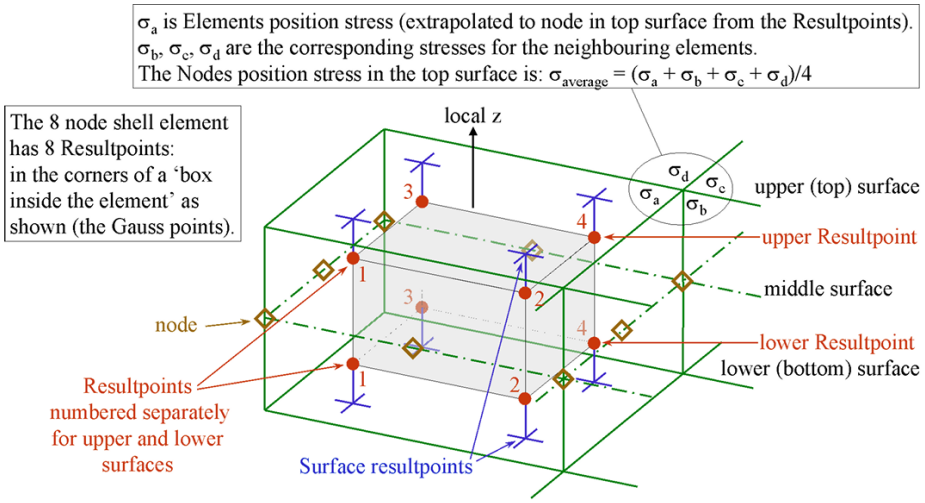

(a) 8-node quadrilateral shell element.

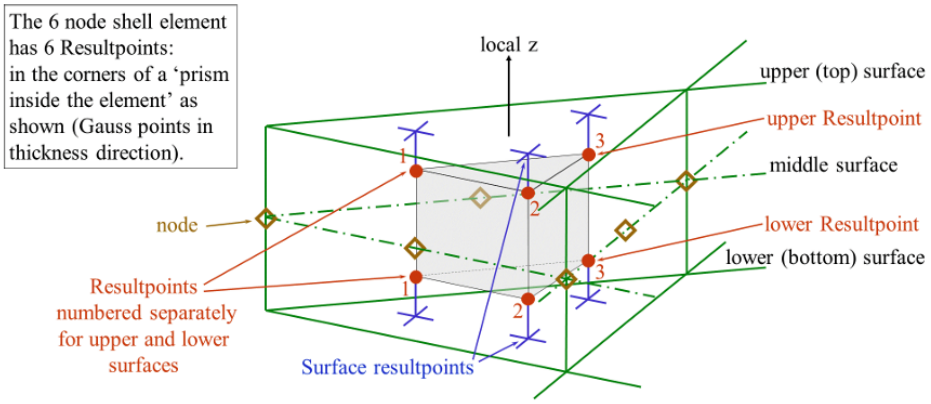

(b) 6-node triangular shell element.

Figure 12: Subparametric shell elements [32].

In Figure 13, the 3-node beam element is presented as well.

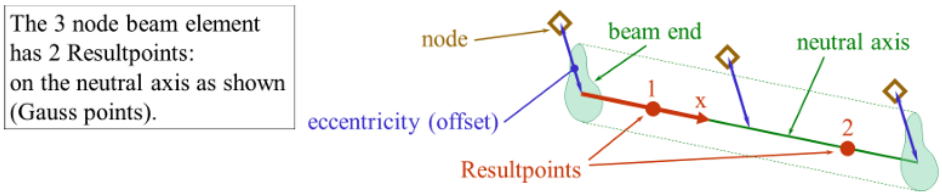

Figure 13: 3-node beam element [32].

2.3.2 Element stresses

The relevant stresses in this study are the following:

- σ_x: normal stress in the direction of the x-axis
- σ_y: normal stress in the direction of the y-axis
- σ_z: normal stress in the direction of the z-axis
- τ_{xy}: shear stress in the direction of the y-axis in a plane normal to the x-axis
- τ_{xz}: shear stress in the direction of the z-axis in a plane normal to the x-axis
- τ_{yz}: shear stress in the direction of the z-axis in a plane normal to the y-axis
- vonMises: vonMises stress
- P1: first principal stress
- P2: second principal stress

Apart from these general stresses, the decomposed membrane and bending part can be referred to. For example, σ_{Mx} and σ_{Bx} refer to the membrane and bending part of the normal stress σ_x, τ_{Mxy} and τ_{Bxy} refer to the membrane and twisting part of the shear stress τ_{xy}, and τ_{Bxz} and τ_{Byz} refer to the bending part of the shear stresses τ_{Bxz} and τ_{Byz} respectively. The τ_{Mxz} and τ_{Myz} are zero. These stresses can be illustrated in Figure 14 to Figure 16.

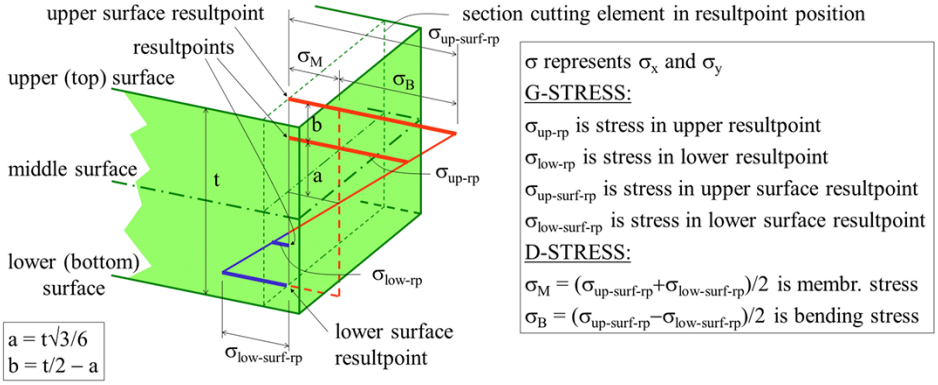

Figure 14: Normal stress for 8-node shell element [32].

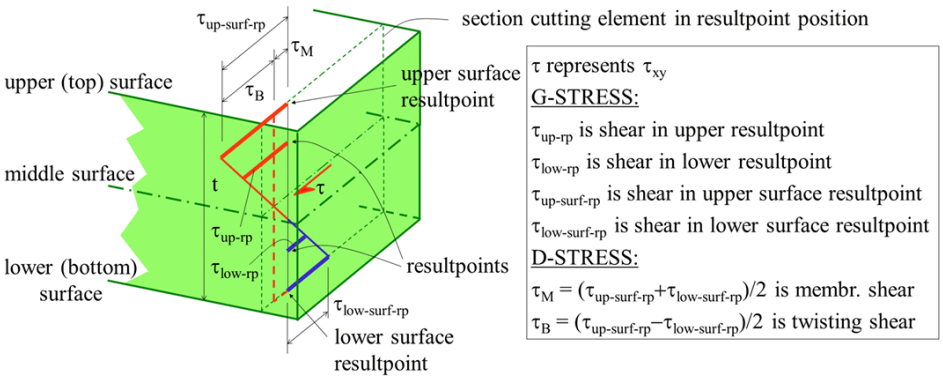

Figure 15: Membrane/twisting (in-plane) shear stress for 8-node shell element [32].

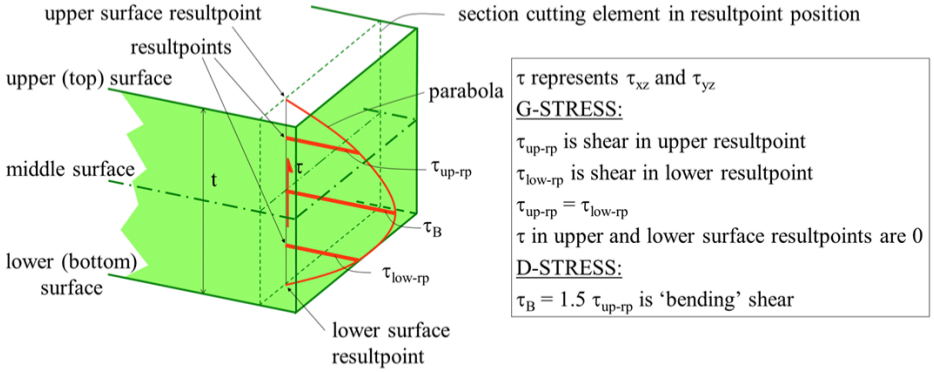

Figure 16: Bending (transverse) shear stress for 8-node shell element [32].

For thick shell elements, the von Mises (equivalent) stress σ_{vonMises} is defined as follows:

$$\sigma_{\text{vonMises}} = \sqrt{\sigma_{\text{x}}^2 + \sigma_{\text{y}}^2 - \sigma_{\text{x}}\sigma_{\text{y}} + 3(\tau_{\text{xy}}^2 + \tau_{\text{xz}}^2 + \tau_{\text{yz}}^2)} \tag{11}$$

whereas for a thin shell τ_{xz} and τ_{yz} are zero.

The first (P_1) and second (P_2) principal stresses correspond to the maximum and minimum normal stress of a point, respectively, in an orientation where the shear stress is zero.

2.3.3 Structural stress

Unlike the regular normal and shear stresses that are mesh-dependent, the mesh-size insensitive equilibrium-equivalent structural stresses can be used for fatigue calculations as defined in [34] and further utilized in [35] for a rectangular hollow section joint and in [36] where a path-dependent counting method is presented. The structural stress is less sensitive to the mesh size than the principal stress and von Mises [35].

As noted in [34], the procedure is as follows: the nodal displacement vector $\{\mathbf{u}\}_i^{\text{T}} = \{u_{\text{x}i}, u_{\text{y}i}, u_{\text{z}i}, \theta_{\text{x}i}, \theta_{\text{y}i}, \theta_{\text{z}i}\}$ is calculated in a FEA software, where $u_{\text{x}i}, u_{\text{y}i}, u_{\text{z}i}$ are the three translational displacements and $\theta_{\text{x}i}, \theta_{\text{y}i}, \theta_{\text{z}i}$ are the three rotational displacements. Then, the element nodal force vector $\{\mathbf{F}^{\text{e}}\}_i^{\text{T}} = \{F_{\text{x}i}, F_{\text{y}i}, F_{\text{z}i}, M_{\text{x}i}, M_{\text{y}i}, M_{\text{z}i}, \dots\}$ is obtained from the equation $\{\mathbf{F}^{\text{e}}\} = \{\mathbf{K}^{\text{e}}\}\{\mathbf{u}\}$, where $\mathbf{K}^{\text{e}}$ is the element stiffness matrix.

The resulting balanced element nodal forces $(F_1, F_2, ..., F_{\text{n}})$ and moments $(M_1, M_2, ..., M_{\text{n}})$ are given in a global coordinate system (x, y, z). Therefore, they are transformed to a local coordinate system (x', y', z') that is perpendicular and parallel to the area of interest (weld toe), as shown in Figure 17.

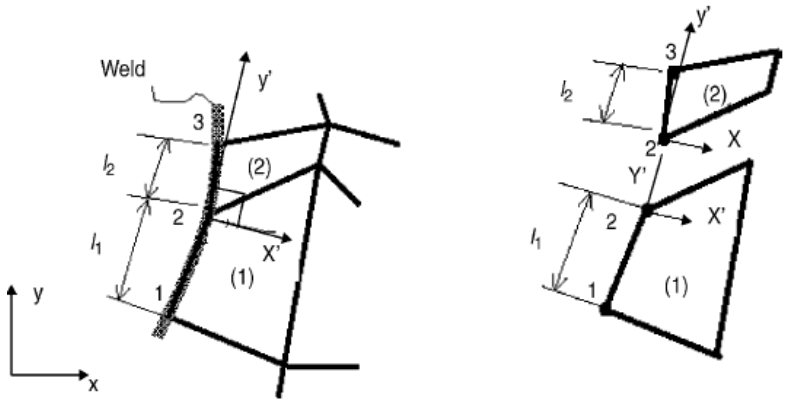

Figure 17: Global and local coordinate system [35].

The following system [35] is solved with the balanced element nodal forces $(F_1, F_2, ..., F_\mathrm{n})$ in order to calculate the line forces $(f_1, f_2, ..., f_\mathrm{n})$:

$$\begin{Bmatrix} F_1 \\ F_2 \\ F_3 \\ \vdots \\ F_\mathrm{n} \end{Bmatrix} = \begin{bmatrix} \frac{l_1}{3} & \frac{l_1}{6} & 0 & 0 & \cdots & 0 \\ \frac{l_1}{6} & \frac{(l_1+l_2)}{3} & \frac{l_2}{6} & 0 & \cdots & 0 \\ 0 & \frac{l_2}{6} & \frac{(l_2+l_3)}{3} & \frac{l_3}{6} & \cdots & 0 \\ 0 & 0 & \ddots & \ddots & \ddots & \frac{l_{n-1}}{6} \\ 0 & \cdots & 0 & 0 & \frac{l_{n-1}}{6} & \frac{l_{n-1}}{3} \end{bmatrix} \begin{Bmatrix} f_1 \\ f_2 \\ f_3 \\ \vdots \\ f_\mathrm{n} \end{Bmatrix} \tag{12}$$

where $l_1, l_2, ..., l_\mathrm{n}$ is the element length. In a like manner, the line moments $(m_1, m_2, ..., m_\mathrm{n})$ are computed.

For the crack plane and coordinate system presented in Figure 18, the following equations for the structural stress are defined:

$$\sigma_\mathrm{s} = \sigma_\mathrm{m} + \sigma_\mathrm{b} = \frac{f_{\mathrm{y}'}}{t} - \frac{6m_{\mathrm{x}'}}{t^2} \tag{13}$$

$$\tau_\mathrm{s} = \tau_\mathrm{m} + \tau_\mathrm{b} = \frac{f_{\mathrm{x}'}}{t} + \frac{6m_{\mathrm{y}'}}{t^2} \tag{14}$$

$$\tau_\mathrm{z} = \frac{f_{\mathrm{z}'}}{t} \tag{15}$$

where t is the thickness, σ_m and σ_b are the membrane and bending components of the normal structural stress σ_s, τ_m and τ_b are the membrane and bending components of the shear structural stress τ_s, $f_{\mathrm{x}'}, f_{\mathrm{y}'}$, and $f_{\mathrm{z}'}$ are the line forces in x', y', and z' direction respectively, and $m_{\mathrm{x}'}$ and $m_{\mathrm{y}'}$ are the line moments in x' and y' direction respectively. The transverse shear structural stress τ_z has only a membrane component, and it is usually negligible.

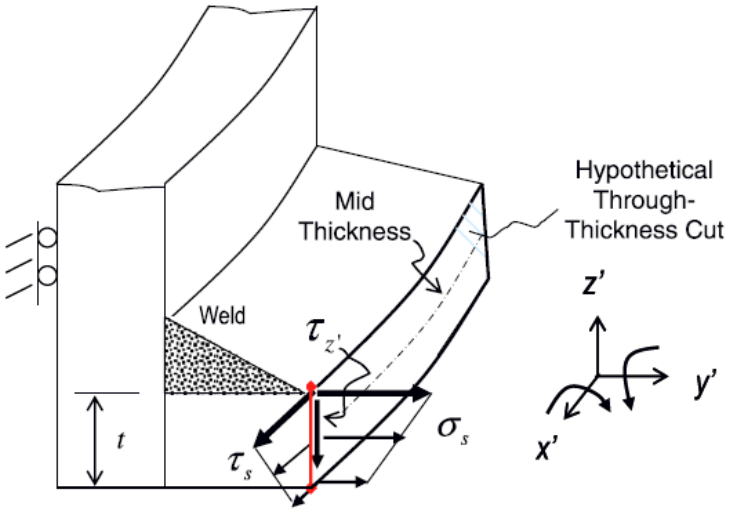

Figure 18: Structural stress definition in the crack plane [36].

The balanced nodal forces and moments are not an available output of SESTRA, as they are in ANSYS and Abaqus. Therefore, they are not utilized further in this study, however their definition was deemed necessary as the multiaxial fatigue calculation procedure is mostly based on structural stress in the literature. Nevertheless, the same procedure may be followed with the element stresses.

2.4 Fatigue

Under repeated loading below the material yield strength, fatigue damage may be significant, especially for complex systems with dynamic loading from the wind, waves, and mooring lines. Different fracture modes appear depending on the stress components. Typically, the rainflow algorithm is used for identifying and counting the stress cycles. Then, an S-N curve is selected as reference for the maximum number of cycles for each stress range before fatigue failure. To account for the local stresses at hot spot regions, a shell model can be utilized with the hot spot method according to DNVGL-RP-C203 [37]. Alternatively, using a nominal definition of the stress can provide an insight into the stress amplitude level, and it can be scaled with a stress concentration factor (SCF) to account for local geometry effects.

The theory of the aforementioned and other relevant to fatigue topics is presented in the following sections.

2.4.1 Fracture modes and hot spots

Based on the stress component and direction, the crack develops in three different modes, as presented in Figure 19. These modes are the following [38]:

- Mode I - opening mode: a normal tensile stress acts perpendicular to the crack plane
- Mode II - sliding mode: a shear stress acts parallel to the crack plane and perpendicular to the crack front
- Mode III - tearing mode: a shear stress acts parallel to the crack plane and parallel to the crack front

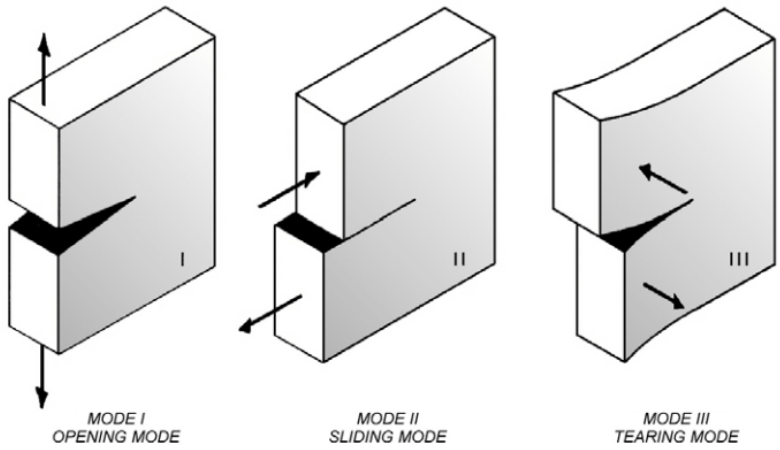

Figure 19: Modes of surface crack development [39].

Mode I is the dominant mode seen in most engineering cases. However, in-plane shear may be significant in some applications, and mode III becomes important due to the torsion; therefore, multiaxiality must be considered. Mode II stress components are generally negligible [36].

The location at which a fatigue crack may initiate is called a hot spot. For a plated structure, the following types can be classified as shown in Figure 20:

- Type A or B: weld toe at the weld end
- Type C: weld toe along the weld end

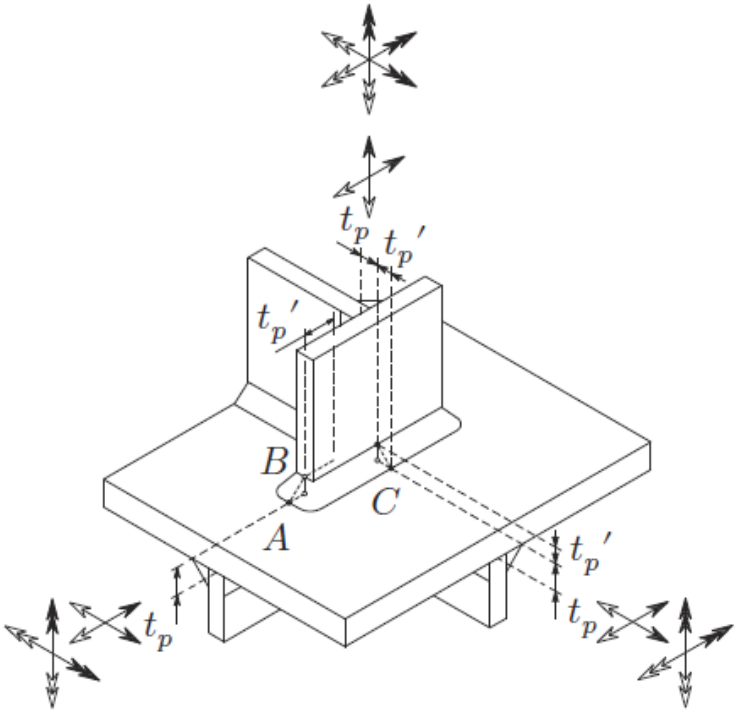

Figure 20: Hot spot types [40].

Observations have shown that the fatigue damage is proportional to the shear stress at material planes of easy gliding [41]. Also, the fatigue crack development is affected by the opening and closing of the crack caused by normal stress. Therefore, combining the normal and shear stress and examining different plane orientations is important when considering multiaxial conditions. These are various methods following this approach, which are called the critical plane methods [41]. Such a method is also used in the hot spot multidirectional fatigue method described in section 2.5.3.

2.4.2 Rainflow counting algorithm

The rainflow algorithm is frequently used for cycle counting when considering one stress component. The rainflow python package [42] is used in this study which is based on the ASTM E1049-85 rainflow cycle counting algorithm for fatigue analysis [43]. An example of the cycle counting procedure is shown in Figure 21.

The peaks, valleys, and cycles are identified and counted. The event A-B corresponds to a half cycle (b), as well as the event B-C (c), but with different ranges. The event E-F is taken as a full cycle, as it completes two half cycles within the event D-G (d). The event D-G acts as a half cycle (f). The event C-D and G-H correspond to two half cycles of about the same range (e,f). Similarly, the rest of the cycles are calculated in the stress signal.

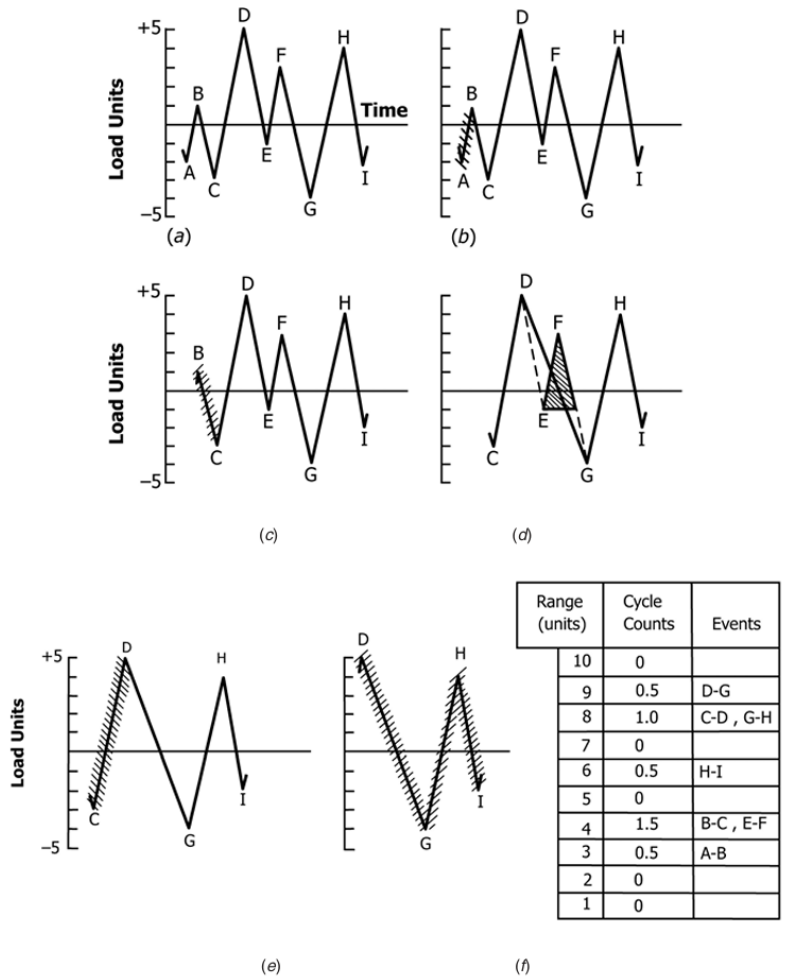

Range (units)	Cycle Counts	Events
10	0	
9	0.5	D-G
8	1.0	C-D , G-H
7	0	
6	0.5	H-I
5	0	
4	1.5	B-C , E-F
3	0.5	A-B
2	0	
1	0	

Figure 21: Rainflow counting example [43].

2.4.3 S-N curves

The S-N curve provides the maximum number of cycles for each stress range before fatigue failure with a 97.7 % probability of survival, according to the recommended practice DNVGL-RP-C203 [37], and they come from the mean minus 2 standard deviations curve based on experiments. They are bi-linear and depend on the stress range with a changing point of the slope and intercept at 10^7 cycles. The local stress concentration of the joint and the weld profile are already accounted for in the S-N curves.

The definition of the S-N curve, accounting for a plate thickness modification from a reference value, is as follows:

$$\log N = \log \bar{a} - m \log \left(\Delta\sigma \left(\frac{t}{t_{\text{ref}}} \right)^k \right) \tag{16}$$

where $\Delta\sigma$ is the stress range, N is the number of cycles to failure for the stress range $\Delta\sigma$, m is the negative inverse slope of the curve, $log\bar{a}$ is the intercept on the log N-axis of the curve, t_{ref} is the reference thickness which is equal to 25 mm for no tubular joints, t is the thickness where the crack develops, and k is the thickness exponent.

The different S-N curves in air are presented in Figure 22.

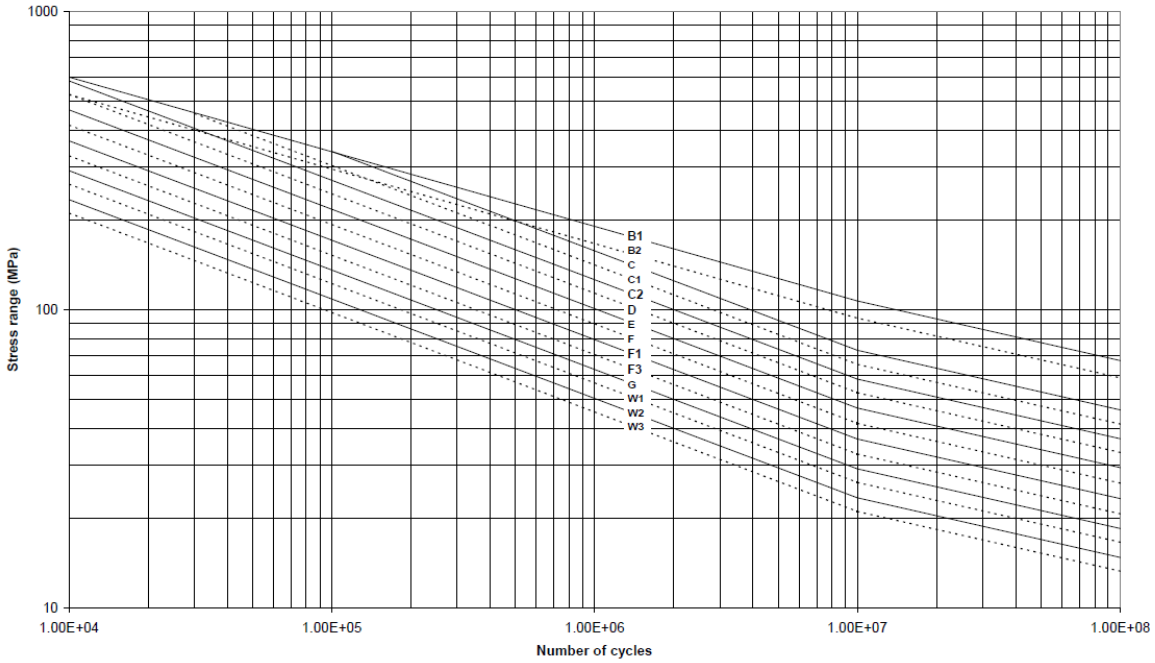

Figure 22: S-N curve in air [37].

A stress concentration factor (SCF) is defined as the ratio of the hot spot stress range over the nominal stress range according to the recommended practice DNVGL-RP-C203 [37]. Some initial misalignment due to fabrication tolerances is already included in the S-N curve. However, additional misalignment can be considered when calculating the stress concentration factor (SCF).

2.4.4 Mean stress correction

The S-N curves are based on stress ranges and refer to tensile conditions. According to DNVGL-RP-C203 [37], the stress ranges can be reduced when compressive conditions exist, only if post-weld heat treatment and low residual stresses are present.

A stress reduction factor f_m can then be applied to the stress ranges according to Figure 23. When the structure is in tension, f_m is equal to 1, when the mean stress is zero, f_m is equal to 0.9, and when it is only under compression, f_m is equal to 0.8.

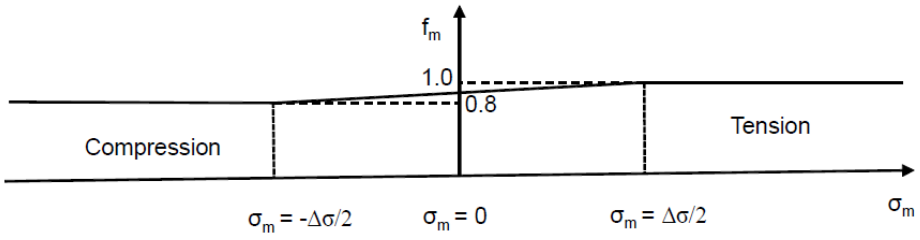

Figure 23: Stress reduction factor f_m for welded connections [37].

The stress reduction factor f_m is defined as follows:

$$f_\mathrm{m} = \frac{\sigma_\mathrm{t} + 0.8|\sigma_\mathrm{c}|}{\sigma_\mathrm{t} + |\sigma_\mathrm{c}|} \tag{17}$$

where σ_t is the maximum tension stress (positive) and σ_c is the maximum compression stress (negative).

Another mean stress correction that can be considered is the Goodman correction [44]. As noted in [29], the corrected stress σ^{RF} is defined as follows:

$$\sigma^{\mathrm{RF}} = \sigma^{\mathrm{R}} \cdot \left(\frac{\sigma^{\mathrm{ult}} - |\sigma^{\mathrm{MF}}|}{\sigma^{\mathrm{ult}} - |\sigma^{\mathrm{M}}|} \right)^{\varepsilon} \tag{18}$$

where σ^{RF} is the corrected stress range, σ^{R} is the stress range of each cycle with a corresponding mean stress σ^{M}, σ^{MF} is a fixed mean stress value of the time series, σ^{ult} is the ultimate stress before failure.

In this study, the stress correction from DNVGL-RP-C203 [37] is applied.

2.4.5 Hot spot stress method

With the hot spot method, a finite element model is used with a fine mesh at the examined detail, in combination with the S-N curve type D, according to DNVGL-RP-C203 [37]. The notch effect is included in that curve and the averaged stresses evaluated at 0.5t and 1.5t from the location of interest are utilized to calculate the hot spot stress with linear extrapolation, where t is the thickness of the plate, as shown in Figure 24. Therefore, 2nd-order (8-node) elements are recommended and the stresses at the middle of the element's side are read.

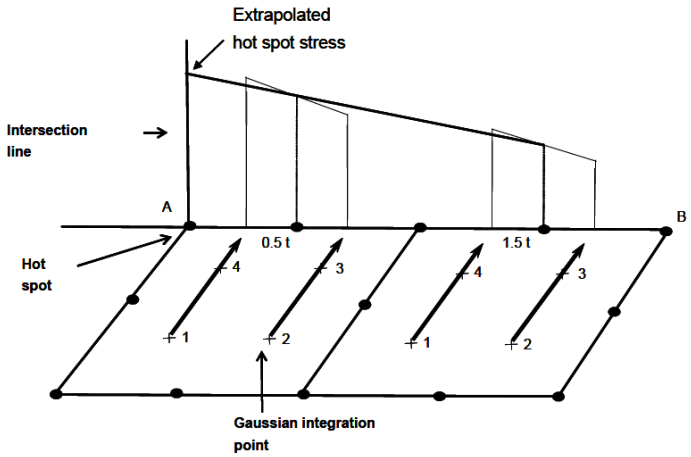

Figure 24: Hot spot stress from 8-node shell element [37].

The so-called effective hot spot stress range $\Delta\sigma_{\mathrm{Eff}}$ used with the hot spot S-N curve is defined as follows (method A):

$$\Delta\sigma_{\mathrm{Eff}} = \max\left\{ \sqrt{\Delta\sigma_{\perp}^2 + 0.81\Delta\tau_{\parallel}^2}, \quad \alpha|\Delta\sigma_1|, \quad \alpha|\Delta\sigma_2| \right\} \tag{19}$$

where $\Delta\sigma_{\perp}$ is the normal stress range perpendicular to the weld toe and $\Delta\tau_{\parallel}$ is the shear stress range parallel to the weld toe, as shown in Figure 25, α is a constant that depends on the detail, $\Delta\sigma_1$ is the first principal stress range, and $\Delta\sigma_2$ is the second principal stress range as follows:

$$\Delta\sigma_1 = \frac{\Delta\sigma_{\perp} + \Delta\sigma_{//}}{2} + \frac{1}{2}\sqrt{\left(\Delta\sigma_{\perp} - \Delta\sigma_{//}\right)^2 + 4\Delta\tau_{//}^2} \tag{20}$$

$$\Delta\sigma_2 = \frac{\Delta\sigma_{\perp} + \Delta\sigma_{//}}{2} - \frac{1}{2}\sqrt{\left(\Delta\sigma_{\perp} - \Delta\sigma_{//}\right)^2 + 4\Delta\tau_{//}^2} \tag{21}$$

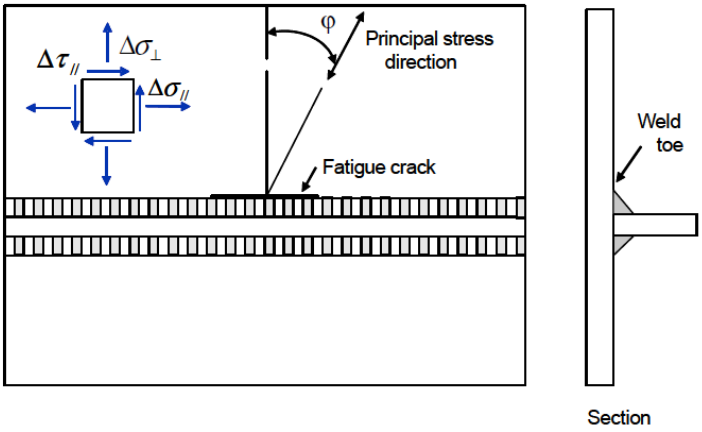

Figure 25: Principal stress direction [37].

Similar equation but with the effective stress range multiplied by 1.12 may be used alternatively if only the stresses at 0.5t are read (method B). The rainflow counting algorithm is then applied and the calculated accumulative fatigue damage must be compared with the different values from Equation 19. The direction of the stress is considered constant.

This method is utilized in this study with the hot spot plate and hot spot plate multidirectional fatigue presented in the section 2.5.

2.4.6 Nominal uniaxial fatigue

The most simplified approach for calculating fatigue in literature is based on nominal uniaxial fatigue. In the nominal uniaxial fatigue calculation, only one stress component is considered without the effect of structural details. This approach can be adopted for the towers of FOWT. Assuming there is no deformation at the cross-section of the tower, the nominal axial stress σ in polar coordinates is calculated as follows:

$$\sigma = \frac{N_z}{A} - \frac{M_y}{I_y} \cdot r\cos\theta + \frac{M_x}{I_x} \cdot r\sin\theta \tag{22}$$

where N_z is the axial force, A is the cross-sectional area, θ is the angle (see Figure 26), I_y and I_x are the sectional area moments over the y-axis and x-axis, respectively, and M_y and M_z are the bending moments over the y-axis and x-axis, respectively. The forces and moments are based on a beam model of the tower, as simulated in SIMA for the integrated FOWT. The local coordinate system with the polar coordinates for the examined model is referred to as shown in Figure 26.

The shear stress τ in polar coordinates for a thin-walled section is calculated as follows:

$$\tau = \frac{M_z}{J} r - 2\frac{F_x}{A}\sin\theta + 2\frac{F_y}{A}\cos\theta \tag{23}$$

where M_z is the torsion, J is the polar moment of inertia of the section, and F_x and F_y are the shear forces in the x-axis and y-axis respectively. The axial and shear stresses are defined in a like manner in [45] where a TLP FOWT is analyzed but for a different coordinate system.

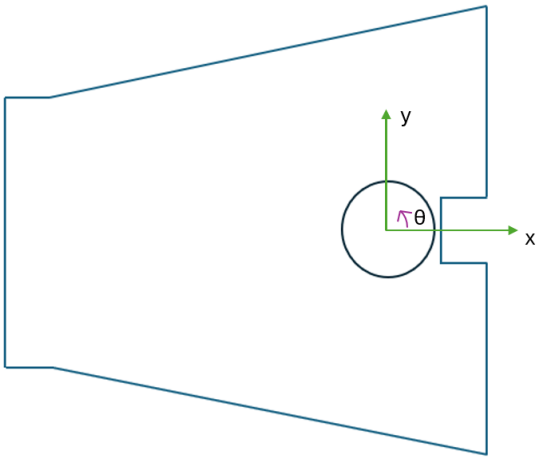

Figure 26: Local coordinate system for the uniaxial fatigue calculation.

Application for FOWTs

In the literature, the most common approach for calculating fatigue for FOWTs is based on the nominal uniaxial fatigue. In [46], the fatigue assessment of a semi-submersible 5 MW FOWT is performed. An S-N curve type D in air is selected from the recommended practice DNVGL-RP-C203 [37] for a girth weld detail at the tower base. In [47], the fatigue assessment and response of a flexible TLP 10 MW FOWT is carried out. The parameters of an S-N curve type D in air are selected for the tower, whereas the parameters of an S-N curve type D with cathodic protection are used for the platform. In [48], a 20 MW spar FOWT is studied. For the fatigue assessment of the tower, an S-N curve type D in air is also considered, whereas for the spar, an S-N curve type D with cathodic protection is used, based on the selected parameters. Finally, in [49], the tower design of the OO-STAR floater with a 10 MW wind turbine is studied. For the fatigue assessment, an S-N curve type F3 with cathodic protection is selected, focusing on the weld root of the girth weld, which has lower allowable cycles before failure than type D.

In [29, 46–48], no SCF is considered. In [49], an SCF is considered for the butt weld at the thickness transition of the girth weld, according to DNVGL-RP-C203 [37]. In this study, the SCF is taken equal to 1 as any additional misalignment due to fabrication tolerances is considered not relevant to this investigation.

The shear stress can be insignificant compared to the axial stress, as discussed in [46], where a semi-submersible FOWT is studied. This consideration was also applied in [29] for a spar FOWT, in [47] for a TLP FOWT, and in [48] for a spar FOWT. In this study, the fatigue damage is calculated based on the axial stress, but the shear stress is also calculated to verify that assumption.

In [46–48], no mean stress correction is used. In [29], the mean stress effect was considered with a Goodman correction [44].

2.4.7 Fatigue damage calculation

The stress time series (nominal axial, nominal shear, or effective hot spot stress) is analyzed using the rainflow counting algorithm to derive the stress ranges and the number of cycles. A stress concentration factor (SCF) is then multiplied in case of a nominal stress to account for the geometry effect or in general to account for additional fabrication misalignments. An appropriate S-N curve is also selected for the maximum number of cycles for each stress range before fatigue failure. Finally, assuming that the fatigue damage accumulates linearly, the Miner's rule is applied to calculate the design cumulative damage D by summing up the damage increments for each stress range cycle as follows:

$$D = DFF \frac{T_{\text{tot}}}{T_{\text{sim}}} \sum_{j=1} p_j \sum_{i=1}^{n} \frac{n_i}{N_i} \tag{24}$$

where n_i is the number of cycles from the rainflow algorithm for the i-th stress range cycle, N_i is the number of cycles to failure from the S-N curve for the i-th stress range cycle, p_i is the probability of occurrence of the j-th design load case, T_{tot} is the total time for the fatigue damage calculation, T_{sim} is the length of the simulation time in SIMA, and DFF is the design fatigue factor.

The design fatigue factor (DFF) is a partial safety factor. According to the offshore standard "Design of Offshore Wind Turbine Structures" (DNV-OS-J101) [18], in the atmospheric zone without inspections or with irregular inspections, the DFF is equal to 2.

The design requirement is that the design cumulative damage D must be less than or equal to 1.

2.5 Multiaxial fatigue and screening

When multiaxial stress conditions appear in a structure, a multiaxial fatigue damage calculation method is necessary, accounting for both the variable loading and the non-proportionality. The latter refers to a stress state where the normal and shear stress components are out of phase, with the same or different frequencies. A proportional stress state, though, is also important, where the stress components are in phase. In the nominal uniaxial fatigue calculation, only one stress component is considered. However, the interaction between the normal and shear stress may significantly impact the fatigue life. Geometry changes and external loading can lead to a multiaxial stress state. The presented hot spot method, which is based on effective stress, considers both normal and shear stress components, but it doesn't account for the non-proportionality.

Before calculating fatigue damage, it is necessary to identify first the critical locations in large structures. Therefore, a screening method may be used for that purpose, accounting for the multiaxiality. Traditional cycle counting methods, such as the rainflow algorithm, may not be as accurate because they consider only one stress component, so other methods need to be established.

The different approaches and theories regarding multiaxiality, screening, and cycle counting are discussed in the following sections. The focus is on the guidelines from DNVGL [37], but the guidelines from Eurocode 3 and the International Institute of Welding (IIW) about the multiaxial fatigue assessment are briefly presented according to [50]. Guidelines from ISO 19902 and BS 7608 may also be considered.

Application for offshore structures

The multiaxiality is investigated in very few studies in the literature for FOWTs. It is studied in [51] for the assessment of a turret in a Floating Production Storage and Offloading (FPSO) unit, in [52] for a TLP FOWT substructure, and in [53] for a column-pontoon connection in a semi-submersible FOWT. In [51], the path-dependent maximum range method (PDMR) is mainly used, accounting for the non-proportional multiaxial loading with the moment of load path (MLP) method (see section 2.5.4). The fatigue damage is also compared with the approach from DNV GL based on principal stresses. In [53], the path-dependent maximum range method (PDMR) is also proposed and described, but not implemented.

For screening, the same studies are referred to. In [53], a convex hull algorithm in Matlab is used to identify the exterior contour of the points in the 2-d stress space of the normal and shear stress components (see section 2.5.1). In [51], a minimum volume enclosed ellipse (MVEE) is used to find an ellipse that encloses all the points. The MVEE is also utilized in [52] and in this study (see section 2.5.1).

2.5.1 Multiaxial screening

2-dimensional stress space representation

The loading path in the structure may be visualized with a plot of the 2-dimensional stress space. In the x-axis, the normal to the weld line stress is plotted, and in the y-axis the in-plane shear stress parallel to the weld line is plotted, multiplied by $\sqrt{\beta}$. The parameter β is a material constant that is defined as a fatigue strength equivalency ratio [36]. It is used to correlate, on average, the fatigue damage induced by normal stress fatigue experiments with shear stress experiments.

A common range for the parameter β is from 2 to 4. In this study, it is taken equal to 3, as in [36]. It is worth mentioning that this value is the same as the von Mises yield criterion. The loading path in the 2-d stress space can be described with a minimum volume enclosed ellipse (MVEE), as explained in the following section.

Minimum volume enclosed ellipse (MVEE)

The minimum volume enclosed ellipse (MVEE) is, as the name suggests, an ellipse that encloses all the points in an n-dimensional space and has a minimum volume. The algorithm from [54] is used to

calculate the MVEE based on the Khachiyan Algorithm [55].

Considering a set $S = \{x_1, x_2, ..., x_m\} \epsilon \mathbb{R}^n$ with m points in a n-dimensional space and an ellipsoid $\mathcal{E} = \{x \in \mathbb{R}^{\mathrm{n}} \mid (x-c)^{\mathrm{T}} E(x-c) \leq 1\}$, where $c \epsilon \mathbb{R}^{\mathrm{n}}$ is the center of the ellipse $\mathcal{E}$ and E is an nxn positive definite symmetric matrix, the following optimization problem [54] is derived:

$$\begin{aligned} &\text{minimize}_{E,c} \quad \det(E^{-1}) \\ &\text{subject to} \quad (x_i - c)^{\mathrm{T}} E(x_i - c) \leq 1, \quad i = 1, \ldots, m, \quad E > 0 \end{aligned} \tag{25}$$

which is solved with a predefined tolerance.

The outputs of the algorithm are the center c^* of the ellipse $\mathcal{E}$ and the matrix E^*, where the asterisk * denotes the optimal solution for a given tolerance.

The radii and the orientation of the ellipse are calculated using the Singular Value Decomposition (SVD) with the SVD function in MATLAB for the matrix E^*.

Screening based on MVEE

Based on the MVEE, four factors are presented in [51] that form a screening tool to identify the fatigue critical locations when accounting for the multiaxiality. The factors referred to in this study are the level of non-proportionality G_{NP}, the maximum stress range $\Delta\sigma_{\mathrm{e}}$, and the multiaxial fatigue damage importance D_{imp}, which are described below.

The level of non-proportionality G_{NP} is defined as follows:

$$G_{\mathrm{NP}} = \frac{R_{\mathrm{minor}}}{R_{\mathrm{major}}}, \quad \{0 \leq G_{\mathrm{NP}} \leq 1\} \tag{26}$$

where R_{major} and R_{minor} are the radii of the ellipse's major and minor semiaxes, respectively. For $G_{\mathrm{NP}} \simeq 0$, the stresses are proportional (the principal stress direction doesn't change), whereas for $G_{\mathrm{NP}} \simeq 1$, the stresses are non-proportional.

The maximum stress range $\Delta\sigma_{\mathrm{e}}$ is defined as follows:

$$\Delta\sigma_{\mathrm{e}} = max\sqrt{(\sigma^{\mathrm{c}} - \sigma^{\mathrm{d}})^2 + \beta(\tau^{\mathrm{c}} - \tau^{\mathrm{d}})^2} \tag{27}$$

where c and d are two points in the 2-d stress space, σ is the normal stress, and τ is the shear stress. Two times the radius of the major axis of the ellipse may be considered directly.

The multiaxial fatigue damage importance D_{imp} is defined as follows:

$$D_{\mathrm{imp}} = [\Delta\sigma_{\mathrm{e}}(1 + G_{\mathrm{NP}})]^3 \tag{28}$$

combining the maximum stress range $\Delta\sigma_{\mathrm{e}}$ and the level of non-proportionality G_{NP}. It can stand as an indicator of a fatigue-sensitive location by comparing different locations in the structure. The power selection matches the S-N curve definition where $N \sim (\Delta\sigma)^{-m}$ with the slope often equal to 3.

2.5.2 Screening with DNV SESAM Core

SESAM Core is a new tool from DNV that facilitates fatigue calculation. According to SESAM Core's manual [56], proportional loading is assumed during screening, therefore the principal stress direction doesn't change. Even if there is change, it is considered that it doesn't affect the identification of critical areas.

The procedure resembles the hot spot method in the section 2.4.5. Hot spot patches are created in the areas of interest in the GeniE model, so that stresses can be read out at 0.5t and 1.5t. Then, the first principal stress σ_{p_1} and direction $\theta_{\sigma_{p_1}}$ are calculated. Finally, the rainflow counting algorithm using the 4-point method is applied to the time series for an initial fatigue calculation based on the first principal

stress σ_{p_1}. The upper and lower center result point and the element stress points may be used.

This method is not applied in this study.

2.5.3 Hot Spot Plate Multidirectional with DNV SESAM Core

The so-called "Hot Spot Plate Multidirectional" method is used in SESAM Core to calculate the fatigue damage when the direction of the principal stress changes, which is based on a newer version of the recommended practice DNVGL-RP-C203 [57]. A different approach is applied for proportional and non-proportional loading, and the implementation is based on critical planes. The fatigue crack is considered driven by the normal stress component $\sigma_\perp$.

For proportional loading, only one critical plane is accounted for, and the method is called "Hot Spot Plate". The principal stress angle $\theta_{\sigma_{p_1}}$ is constant and the effective hot spot stress $\Delta\sigma_{Eff}$ is calculated according to Equation 19. The hot spot S-N curve is used. If the change of the principal stress angle $\theta_{\sigma_{p_1}}$ is more than 10 % of its value, then more critical planes must be considered. This is based on the critical plane approach, where all directions at the weld surface must be examined.

When different critical planes are analyzed, the method is called "Hot Spot Plate Multidirectional". The procedure is as follows: the hot spot patches are created in the GeniE model, and the stress data $(\sigma_\mathrm{x}, \sigma_\mathrm{y}, \tau_\mathrm{xy})$ are read. The principal stress direction, the normal stress component $\sigma_\perp$, and the parallel shear stress component $\tau_\parallel$ are calculated for different directions. The different critical planes at angles θ'_cp are examined regarding fatigue damage with the rainflow algorithm. The normal stress component $\sigma_\perp$ is used for cycle counting and the effective hot spot stress $\Delta\sigma_\mathrm{Eff}$ for the S-N curve.

The stress $\sigma(\theta)$ at different critical plane directions with an angle θ are derived according to the following formula:

$$\sigma(\theta) = \sigma_\mathrm{x}\cos^2\theta + \sigma_\mathrm{y}\sin^2\theta + 2\tau_\mathrm{xy}\cos\theta\sin\theta \tag{29}$$

For non-proportional loading, the following formula is suggested [57] for the effective hot spot stress $\Delta\sigma_{Eff}$:

$$\Delta\sigma_\mathrm{Eff} = \gamma\sqrt{\Delta\sigma_\perp^2 + 0.81\Delta\tau_\parallel^2} \tag{30}$$

where γ is a factor that accounts for the non-proportionality. As summarized in [58], this factor can be taken from literature, and it depends on the material, the phase between the normal and shear stress, and the relation between the stresses.

For angle $-60 \leq \theta'_\mathrm{cp} \leq 60$, the fatigue damage is summed into $D_\perp$, whereas for angles $-90 \leq \theta'_\mathrm{cp} \leq -45$ and $45 \leq \theta'_{cp} \leq 90$ it is summed into $D_\parallel$, as noted in Equation 31 and Equation 32 respectively and presented in Figure 27 for the different critical plane sectors. For angles $-60 \leq \theta'_\mathrm{cp} \leq -45$ and $45 \leq \theta'_\mathrm{cp} \leq 60$, the damage is summed into both equations.

$$D_\perp = \sum D(\theta'_\mathrm{cp}) \quad \text{for} -60 \leq \theta'_\mathrm{cp} \leq 60 \tag{31}$$

$$D_\parallel = \sum_{T_s} D(\theta'_\mathrm{cp}) \quad \text{for} -90 \leq \theta'_\mathrm{cp} \leq -45 \quad \text{and} \quad 45 \leq \theta'_\mathrm{cp} \leq 90 \tag{32}$$

The final damage is the maximum of $D_\perp$ and $D_\parallel$. The assumed fatigue damage is unidirectional. The worst parallel and perpendicular damage is stored from all critical plane candidates.

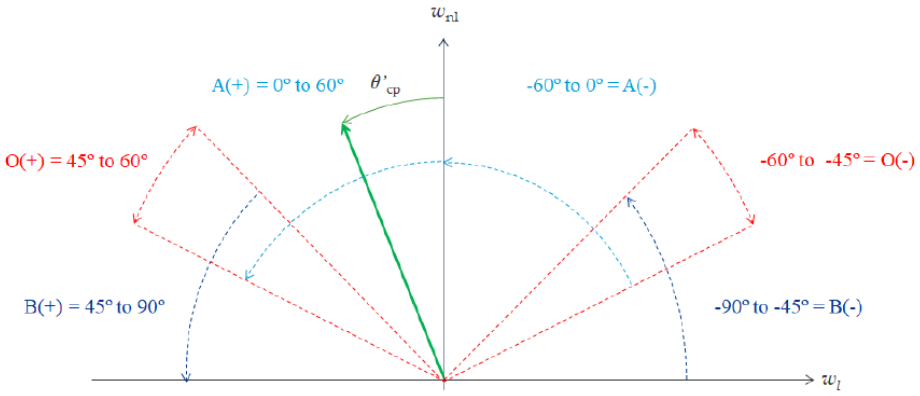

Figure 27: Critical plane sectors [56].

Different S-N curves are used in this implementation. For angle $-30 \leq \theta'_{\mathrm{cp}} \leq 30$, the S-N curve type D or T is used based on the detail (type D for plated structures and type T for tubular joints), whereas for angles $-90 \leq \theta'_{\mathrm{cp}} \leq -30$ and $30 \leq \theta'_{\mathrm{cp}} \leq 90$ the S-N curve type C2 is used.

For more information on this procedure, the reader is referred to SESAM Core's manual [56] and the newer version of the recommended practice DNVGL-RP-C203 [57]. This method is applied in this study with SESAM Core and SESAM Wind Manager.

2.5.4 Path Dependent Maximum Range Method (PDMR)

The path-dependent maximum range (PDMR) method was first presented in [36] for variable amplitude multiaxial loading conditions to identify stress ranges and count cycles for fatigue calculations. It is mainly based on the mesh-insensitive structural stress components ($\sigma_{\mathrm{s}}, \tau_{\mathrm{s}}$, and τ_{z}), and it gives the same results as the rainflow counting algorithm for uniaxial loading conditions. Moreover, the strains can be used instead of the stresses.

The stress components are considered in the $\sigma_{\mathrm{s}} - \sqrt{\beta}\tau_{\mathrm{s}}$ plane, as the transverse shear stress τ_z is often negligible, but the 3-d space can also be used. The algorithm searches for the maximum distances in the plane within the entire stress time series, considering a monotonic increase. When there are turning points in the path, where the distance is decreased, the distance from a reference point is the local maximum. When a point in the path has the same distance from the reference point, it is called a projected turning point, and the path between the turning point and the projected turning point is called a virtual path. The algorithm is applied for all remaining load paths (real and virtual) to identify the path-independent reference effective stress ranges (distances), the path-dependent effective stress ranges (path lengths), and the number of cycles. The path length for the ith reference stress range can be calculated for all its segments as follows:

$$\Delta S_{\mathrm{e}}^{(i)} = \int \sqrt{(d\sigma)^2 + \beta(d\tau)^2} \tag{33}$$

In [59], a modification is presented for non-proportional loading. As shown in Figure 28, the path of a non-proportional load follows a curved line ($\widetilde{AB}$), whereas the path of a proportional load is a line (AB).

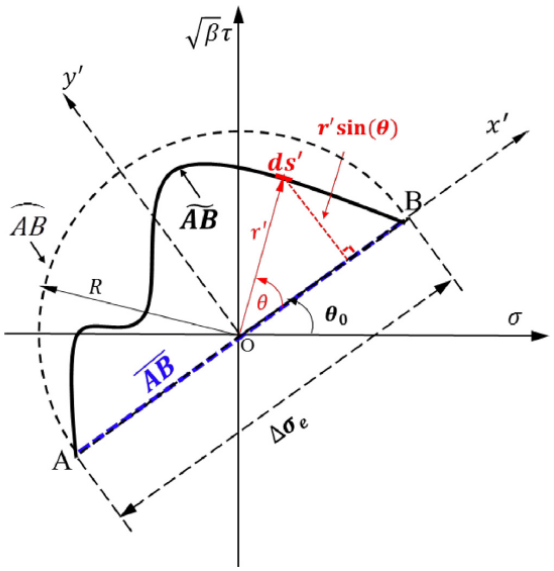

Figure 28: Non-proportional path $\widetilde{AB}$ and proportional path AB [59].

The fatigue damage D can be considered as the sum of the proportional damage D_{P} and the non-proportional deviated damage D_{NP}. This deviation can be calculated with the following integral:

$$D_{\mathrm{NP}} = \int_{\widetilde{AB}} r' \cdot |\sin(\theta)| ds' \tag{34}$$

which makes it the moment of load path (MLP) model.

Then, a dimensionless damage g_{NP} due to the non-proportionality can be introduced as follows:

$$g_{\mathrm{NP}} = \frac{D_{\mathrm{NP}}}{D_{\mathrm{Max}}} = \frac{\int_{\widetilde{AB}} r' |\sin(\theta)| ds'}{2R^2} \tag{35}$$

Finally, the effective stress range $\Delta\sigma_{\mathrm{e}}$ is corrected as follows:

$$\Delta\sigma_{\mathrm{NP}} = \Delta\sigma_{\mathrm{e}} \left(1 + \alpha \cdot g_{\mathrm{NP}}\right) \tag{36}$$

where α is a material-dependent non-proportionality sensitivity parameter.

This method was not developed in this study.

2.5.5 Variable amplitude fatigue based on Eurocode 3 and IIW

According to Eurocode 3 and the International Institute of Welding (IIW), there are two different approaches to assess multiaxial fatigue with variable loading (VA) [50]. The first is based on equivalent stress ranges using an interaction equation, and the second is based on a linear damage accumulation Palmgren-Miner (P-M) rule.

For the equivalent stress ranges, the following equation is used for IIW:

$$\Delta\sigma_{\mathrm{eq,IIW}} = \sqrt[m_1]{\frac{1}{D_{\mathrm{spec}}} \cdot \frac{\sum\left(n_i \cdot \Delta\sigma_{i,\mathrm{S,d}}^{m_1}\right) + \Delta\sigma_{\mathrm{L,d}}^{(m_1-m_2)} \cdot \sum\left(n_j \cdot \Delta\sigma_{j,\mathrm{S,d}}^{m_2}\right)}{\sum n_i + \sum n_j}} \tag{37}$$

where $\Delta\sigma_{i,\mathrm{S,d}}$, $\Delta\sigma_{j,\mathrm{S,d}}$, and $\Delta\sigma_{\mathrm{L,d}}$ are the stress ranges from the rainflow counting method above, below, and at the knee point of the S-N curve, and n_i, n_j are the number of cycles.

For the Eurocode 3 (EC3), the equation is:

$$\Delta\sigma_{\mathrm{eq,EC3}} = \lambda_i \times \Delta\sigma_{\mathrm{LM}} \tag{38}$$

where λ_i is a factor that depends on the load and the structure, and $\Delta\sigma_{\mathrm{LM}}$ is the stress range from the rainflow counting method based on the load model.

Then, the following interaction equations are used:

$$\left(\frac{\Delta\sigma_{\mathrm{eq,EC3}}}{\Delta\sigma_{\mathrm{R}}/SF}\right)^3 + \left(\frac{\Delta\tau_{\mathrm{eq,EC3}}}{\Delta\tau_{\mathrm{R}}/SF}\right)^5 \leq D_{\mathrm{EC3}} \tag{39}$$

$$\left(\frac{\Delta\sigma_{\mathrm{eq,IIW}}}{\Delta\sigma_{\mathrm{R}}/SF}\right)^2 + \left(\frac{\Delta\tau_{\mathrm{eq,IIW}}}{\Delta\tau_{\mathrm{R}}/SF}\right)^2 \leq CV \tag{40}$$

where $\Delta\sigma_{\mathrm{R}}$ and $\Delta\tau_{\mathrm{R}}$ correspond to the normal and shear stress fatigue strength respectively for a given number of cycles, SF is a safety factor, D_{EC3} is the damage sum for EC3 equal to 1, and CV is a comparison value for IIW that varies (1 for proportional and 0.5 for non-proportional according to [58]). Equation 40 is based on the Gouph-Pollard interaction equation; it is an ellipse, and for a stress state inside it, the fatigue life is supposed to be infinite as mentioned in [41].

As noted in [58], Equation 40 can be rearranged into an equivalent stress range so that it can be used with the normal stress S-N curves as follows:

$$\Delta\sigma_{\mathrm{IIW}} = \frac{1}{\sqrt{CV}}\sqrt{\Delta\sigma_{\mathrm{x}}^2 + k\cdot\Delta\tau_{\mathrm{xy}}^2} \tag{41}$$

where $k = \frac{\Delta\sigma_{\mathrm{T}}^2}{\Delta\tau_{\mathrm{R}}^2}$, which depends on the fatigue strengths and the number of cycles. This equation resembles the one used with DNV GL ([37],[57]).

For the approach based on the P-M rule, the total damage is calculated as follows:

$$D_{\mathrm{tot}} = D_\sigma + D_\tau \leq D_{\mathrm{real}} \tag{42}$$

by calculating the damage D_σ and D_τ for the direct and shear stresses respectively, using the rainflow counting method and a reference S-N curve.

Notably, these approaches do not use the principal stresses suggested by DNV GL [37]. Also, they examine the contribution from the normal and shear stresses separately when using the rainflow counting method and then add them together to compare with reference values. In comparison, the effective stress is used with the rainflow counting method in [37]. These methods were not used in this study. For a comparative study of the multiaxial fatigue methods and other approaches, the reader can refer to [60] and [41].

3 Methodology

3.1 Simulation procedure

Different approaches and software can be used for the analysis of floating wind turbines, as noted in Appendix B, where guidelines for the structural analysis are also referred to from standards. The coupled time-domain analysis procedure used in this study is based on [61–63] by utilizing DNV's SESAM software suite, including HydroD (WADAM, WASIM), GeniE, HydroMesh, SESTRA, Xtract, SESAM Manager, SESAM Wind Manager, and SIMA.

SIMA is a tool for the simulation of multi-body systems, including mooring lines, and combining wind, wave, and current for floating structures. GeniE is a tool for designing structures and FEM modeling, and HydroD is used for hydrodynamic analysis using WADAM or WASIM.

WADAM is a frequency-domain tool based on the 3D radiation-diffraction theory and the Morison theory. Panel models are employed for the structure, and beam models for the linearized Morison equation, which are created in GeniE. HydroD is then used as the modeling environment. The hydrodynamic coefficients, wave forces, and transfer functions are used as input in SIMA for the integrated analysis. In this study, this step is omitted, as it's already been implemented with WAMIT (and WADAM) in the provided model.

WASIM is a time-domain tool used to calculate global motions and local pressure loads in floating structures. It is based on the 3D radiation/diffraction theory and utilizes a Rankine panel method. Panel models are utilized not only for the hull but also for the free surface. WASIM is also executed from HydroD and is used in this study. Frequency-domain results may be obtained through Fourier transformations. A significant advantage is that non-linear interactions are considered.

The main difference between the Rankine panel method in WASIM and the Green's function based panel method in WADAM is that the integral equation is solved both at the hull and the free surface in WASIM, whereas only the free surface boundary condition is satisfied in WADAM. Therefore, a mesh is needed for both the hull and the free surface in WASIM. In WADAM, when the second order sum and difference frequencies are considered, then the free surface mesh is necessary too.

SESTRA is a tool for structural analysis, and Xtract is used for visualization of the finite element results. HydroMesh is a tool to create a free surface mesh. Finally, SESAM Manager is used to manage the workflow and SESAM Wind Manager is used for fatigue and ultimate strength analysis in the time domain.

The floater motions are prescribed from SIMA, where the integrated system of the floating wind turbine is simulated, to the shell model of the floater in HydroD. It is not possible to model the wind turbine and wind conditions in HydroD. The loads from the wind turbine and the mooring line are to be taken from SIMA for the integrated structural analysis.

3.1.1 Models

Based on the DNV's workflow and SESAM software suite, different models are needed to run the structural analysis, which are explained in the HydroD documentation [64], as follows:

- Panel model: The panel (FEM) model is used to calculate the 3D wave potential. All outer surfaces of the floating structures are modeled with panels, even above the water surface, but only the wet surfaces are considered automatically. In a structure where both sides are in contact with the water, the dipole elements can be used. The mesh can be coarser than the structural model to save computational time. In WASIM, the panel model is defined with a section model (.pln file) that consists of patches based on a set of curves. It is created using GeniE and HydroD.
- Morison model: The Morison (FEM) model is used to calculate the drag damping, added mass, and wave forces. However, Morison's theory is best suited for slender structures and not for a barge. For the coupled analysis, though, the Morison model is necessary as it is used to transfer the loads to the structural model.

- Compartment model: The compartments are calculated from enclosed areas and can be used as ballasts.
- Mass model: The mass model is used to account for the mass. A mass distribution must be defined to calculate sectional loads and more accurate motions, for example, from the structural model. Otherwise, a mass matrix can be defined.
- Structural model: The hydrostatic and hydrodynamic pressures are mapped to the structural (FEM) model from the panel model. The compartments are also modeled to account for the hydrostatic and hydrodynamic pressures.
- Free surface model: In order to account for the second-order sum and difference frequencies in the frequency domain in WADAM or the fluid-structure interaction in the time domain for the integral equation in the Rankine panel method in WASIM, a free surface (FEM) model is needed which can be created with HydroMesh or in GeniE. The free surface shall be a circle with a radius of at least the water depth for shallow water and the longest wavelength for deep water.

The floater and wind turbine model in SIMA require some input, as defined in section 2.1. This input has already been configured by the WindBarge project and no reiteration is performed.

3.1.2 Frequency and time domain analysis

The procedure using DNV's SESAM software suite is illustrated in Figure 30 for the time domain analysis, when taking into account the coupling between the floater and wind turbine with SIMA, and in Figure 29 for the frequency domain analysis, when only the floater is considered. The time domain analysis procedure is mainly used in this study, and the frequency domain analysis for the response reconstruction method for the unit-wave response (section 3.1.3).

The panel, Morison, structural, and compartment models are created in GeniE in both procedures and are input in HydroD. The free surface mesh is created with HydroMesh, but it can also be created in GeniE. The frequency domain (WADAM) analysis is then run through HydroD and the RAOs, added mass, damping, and restoring matrices are calculated, which are input in SIMA for the floater. This step is omitted in this study as the provided SIMA model was already defined. In the time domain (WASIM) analysis, which is also run through HydroD, the wave components, the floater's motions, velocities, and accelerations, and the mooring and tower loads are taken from SIMA to account for the integrated system. In both procedures, the structural analysis is carried out in SESTRA through HydroD and the resulting stress response is illustrated using Xtract.

For the WASIM analysis, the same model is used for the Morison and structural model in order to have the same node and element numbers. Beams are required to exist at the points that the loads from SIMA are acting. Then, the loads are transferred in the same elements in the structural model.

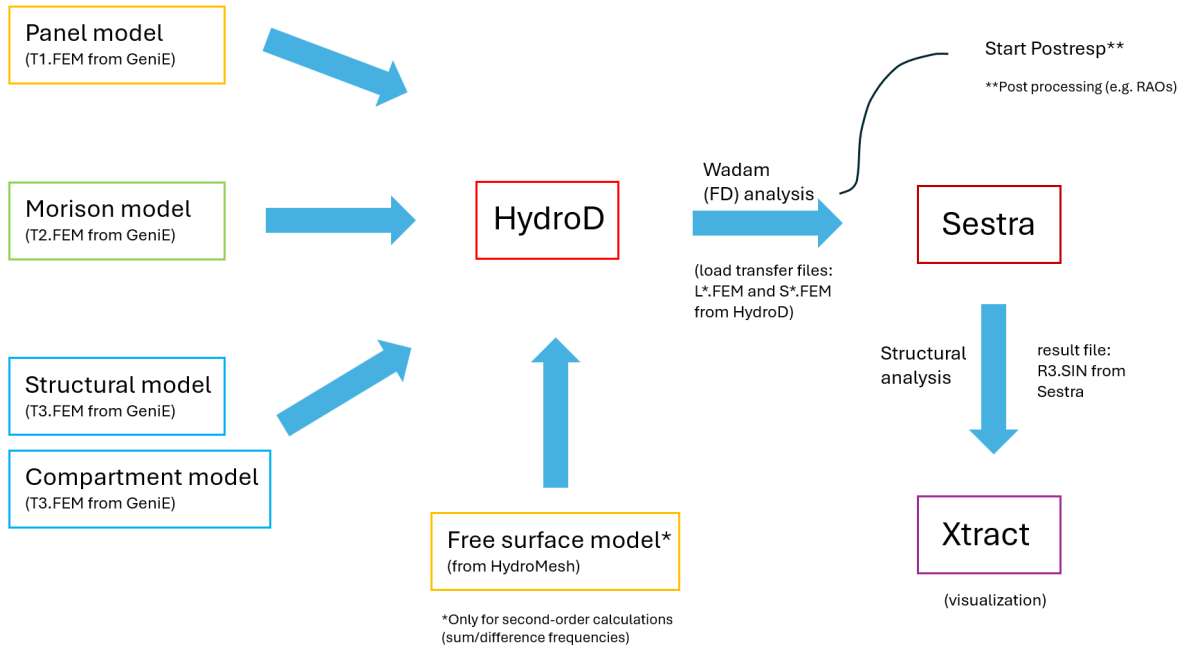

Figure 29: Frequency domain (FD) analysis procedure.

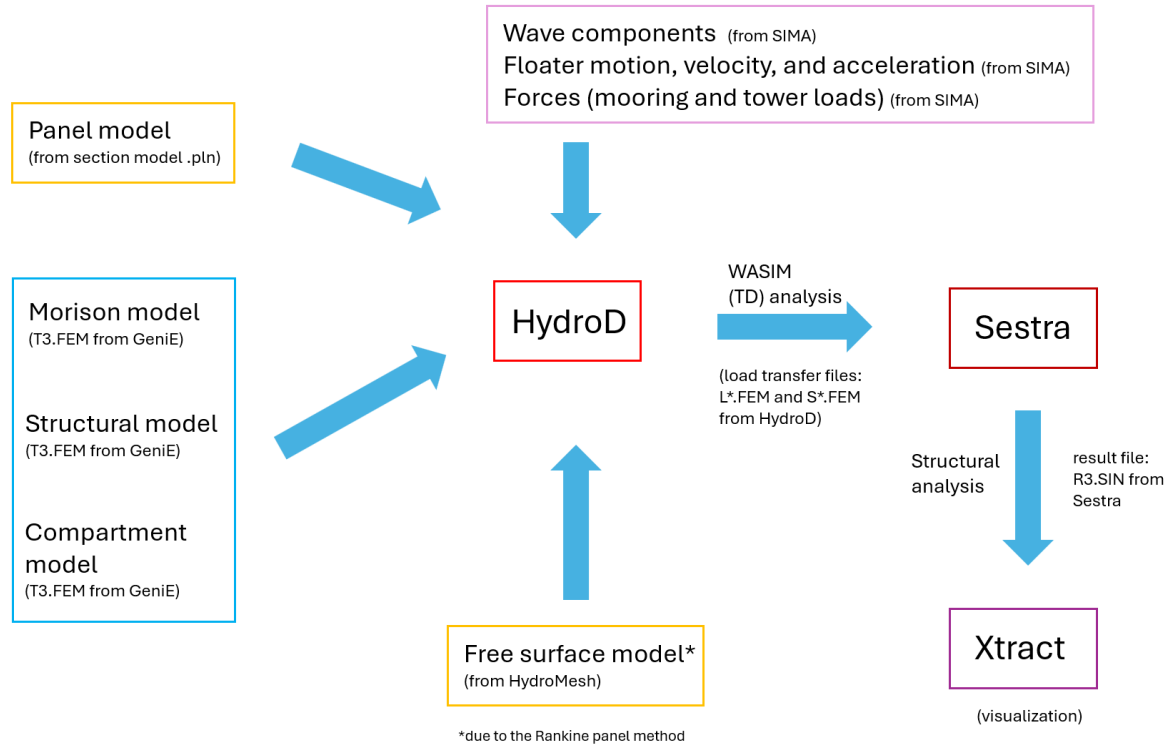

Figure 30: Time domain (TD) coupled analysis procedure.

3.1.3 Response Reconstruction method in SESAM Wind Manager

There are different approaches for the coupled analysis of FOWT. The methodology described in Figure 30 is based on direct load generation, where all loads are constructed in the time domain. This methodology is used to derive the stress time series in the ULS study and for fatigue screening in the FLS study. It is noted, though, that for a 30-minute simulation, the total computation time exceeded 24 hours for a model of about 50.000 elements or more. Also, the total size of the load and result files was around 100 GB for only one design load case (DLC). Therefore, this approach is not suited for large simulations, as other issues also arise (see section 3.1.4).

The response reconstruction method presented in [65] is 20x faster and also reduces the storage requirements from TBs to GBs. The workflow includes a precomputation of the following:

- Unit-nodal response: the nodes where the mooring and tower loads act are selected and the response to a unit load is calculated.
- Unit-motion response: the structural response for the 6 rigid body motions of the floater in still water is calculated.
- Unit-wave response: the structural response due to a unit incoming wave is calculated for a fixed floater.

Then, the responses are added linearly to calculate actual structural response based on the magnitude of the loads, the motions, and the incoming wave height. As shown in [65] for verification, the z-displacement of a node is identical with both methods. In this study, after calculating the response result files, the DLCs were run in just a few minutes. Therefore, this method is used for the multidirectional fatigue damage calculation.

This workflow is implemented in SESAM Wind Manager according to the tutorial in [66]. For the unit responses, SESAM Core is run. SESTRA is run in the background for all the structural responses, in addition to Wadam for the unit-motion and unit-wave response. Therefore, a Wadam file is generated from a frequency domain analysis in HydroD for this calculation. For more information on the procedure, the reader is referred to [65] and [66].

In addition, a FEM file of the floater is necessary which is produced in GeniE. The hot spots and screening locations are selected according to the tutorial in [66], and they are extracted in a .json file, which is used in SESAM Wind Manager. According to the SESAM Core manual in [56], the mesh size must be txt, where t is the thickness of the structure at the examined location.

3.1.4 SESAM Manager for SESTRA

SESAM Manager [67] is a software that manages the workflows between the different packages (GeniE, HydroD, Sestra, etc.). In this study, it was used for running SESTRA after the WASIM analysis in HydroD that produces the load transfer files. SESTRA can also be run through HydroD, however, the size of the files required some modifications in the settings of the analysis that could only be done outside HydroD.

Specifically, the device specifications did not allow to run the analysis due to insufficient memory (only 16 GB RAM). The sestra.inp file that is used from SESTRA needs to be modified and then used in SESAM Manager.

According to SESTRA's manual [68], the SOLV command must be added to control the memory usage. The low-memory mode was enabled, the number of load cases examined per iteration was reduced, the out-of-core matrix factorization was enabled to reduce the physical RAM usage and utilize the HDD, and an upper limit for the physical memory was set. These modifications allowed to run this computationally expensive simulation.

Further modifications can be done to reduce the size of the output files. Specifically, the results from only a subset of the model can be saved using the ERST command and the result data types can be modified. In this study, the inertia and external loads were excluded, which partially reduced the output file size.

3.1.5 Assumptions and simplifications

The simulation procedure that is followed in this work requires some simplifications and assumptions, which are discussed as following:

- In the integrated global analysis in SIMA, the floater is a rigid body, and the tower is modeled with beam elements. Considering the floater as non-flexible may introduce some error, as a deformed shape of the structure can alter the hydrodynamic data and lead to a different global response. Nevertheless, this potential error is considered not relevant for this study and needs to be further investigated on floating offshore wind turbines. Also, the use of beams for the tower leads to some loss of information from the actual design and local stresses. This is, however, a simplification and limitation of the software packages used, as well as others. Nevertheless, the floater flexibility is examined with a structural shell after running the global analysis by considering all loads.
- The balanced nodal forces and moments are not an available output of SESTRA to calculate the mesh-insensitive structural stress. Hence, the shell elements' stresses are used instead. Therefore, the stress level is more dependent on the mesh size.
- The increased computation time and storage requirements for the overall integrated structural analysis do not allow for a fine mesh with the direct load generation procedure. Therefore, a coarser mesh is used for fatigue screening at the tower base that also facilitates postprocessing. The response reconstruction methods based on linear superposition of responses allowed a finer mesh; however, only the fatigue damage is calculated, and information about the stress time series is not available for additional postprocessing. Moreover, the factor γ that accounts for the non-proportionality in the hot spot plate multidirectional fatigue cannot be adjusted.
- The additional damping due to the keel was not considered in this study with the response reconstruction method when running WADAM due to the increased complexity to include the keel and the fact that it would not be as accurate as with CFD. However, the unit-load response at the tower base is assumed to dominate in comparison to the unit-motion and unit-wave responses. Moreover, the actual motions are prescribed from SIMA, which are calculated with already calibrated damping matrices from CFD.
- The inclusion of part of the tower in the structural shell model (see section 3.2) without updating the SIMA model (mass and inertia) may lead to inaccuracies regarding the motions of the floater due to this extra part. However, the effect of the motions on the stress response of the tower transition region is studied in this work. Also, the addition of the bulkheads can change the global response of the FOWT, but its effect is considered insignificant for the purpose of this study.

3.2 WindBarge model

3.2.1 Structural model

The WindBarge is designed in GeniE, an analysis tool for structural design, and is depicted in Figure 31. It consists of shells and beams that strengthen the hull. Internally, longitudinal and lateral bulkheads create different compartments and distribute the load from the tower to the rest of the hull, as shown in Figure 31c.

The mooring and tower loads are taken from SIMA at the corresponding interface points, as shown in Figure 31a. Rigid links are used to connect the interface points with the structure. Since the tower is not designed as a shell model, the corresponding loads at the tower base are referred. The fairlead is located at the bow of the barge.

For the structural analysis, the hull must have some boundary conditions even though it is floating to restrict rigid body motions. This is a necessary condition for the solver. The location of the boundary conditions was selected as shown in Figure 31b. The noted translational degrees of freedom are fixed and all the rotational degrees of freedom are free. Some initial high reaction forces are expected at the start of the analysis, which are then reduced to approximately zero, as noted in the technical report [63], where the coupled dynamic analysis is examined. The structure accelerations and the hydrodynamic forces are balanced in the analysis. The model in GeniE was provided by the WindBarge project, but the analysis procedure was re-established according to Figure 30.

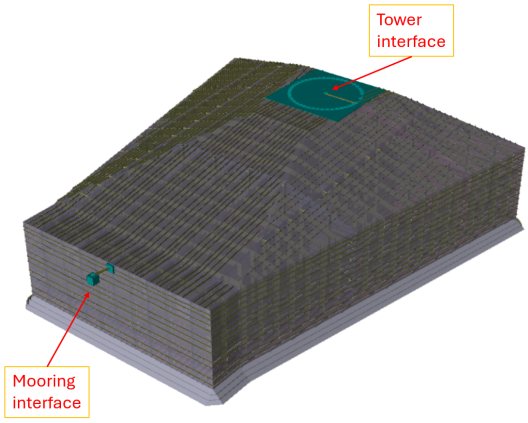

(a) Upper side.

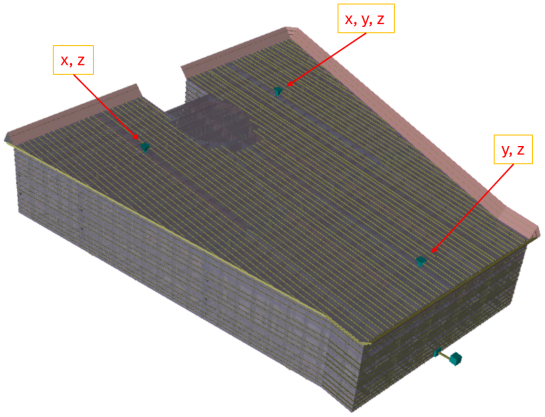

(b) Lower side.

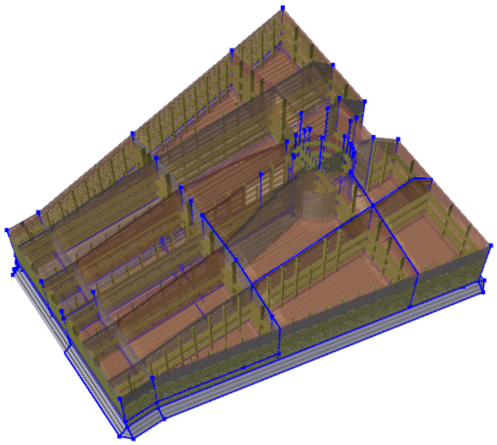

(c) Inner structure.

Figure 31: Windbarge design (images from [69]).

Since the purpose of this study is to study the tower transition region, the shell model was extended to include part of the tower, as shown in Figure 32. The included height of the tower is 11.52 m. Subsequently, the forces and moments have to be extracted at this height from SIMA, which required a manual modification.

The assumptions for this consideration are that this part of the tower is not deforming and that the change in the floater's motions, velocities, and accelerations is negligible. An example time series of the difference in the forces and moments is shown in Figure 53. Also, completely excluding the motions of the floater (section 4.1.5) showed that it has a small or insignificant impact on the floater stresses, therefore, the change due to the added part of the tower is considered not important.

The chosen height of the tower was a compromise between accurately representing the external forces and moments and being far from the intersection of the tower with the floater so that the stresses can properly develop. Including a larger part of the tower led to inaccuracies due to the shadow and inertia effect of the tower.

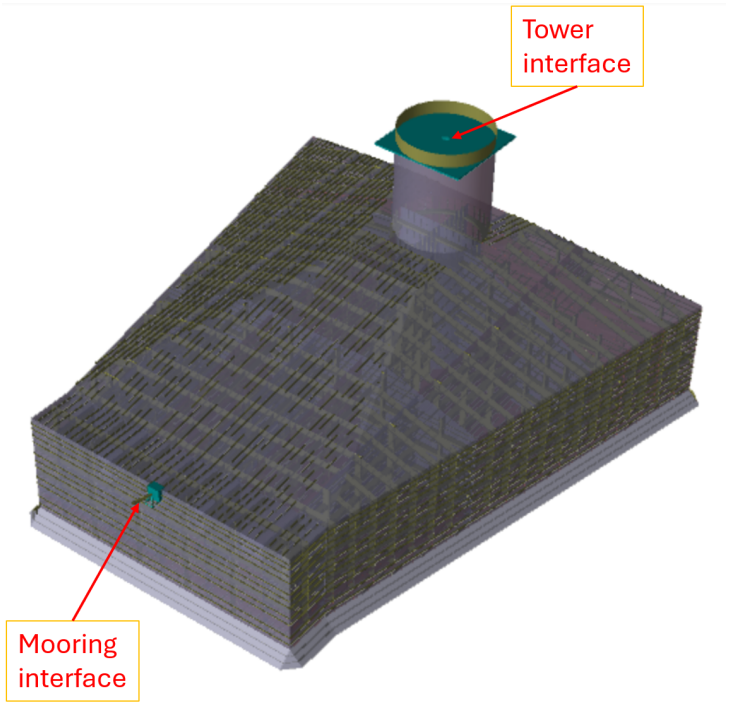

Figure 32: WindBarge model including part of the tower.

The results from the initial ULS and FLS study (see chapter 4), the multiaxiality screening, and the internal structure of other barge-type FOWTs with an axial arrangement of the internal bulkheads were considered when brainstorming a modification of the internal structure. According to the coordinate system in Figure 26, a higher fatigue damage is seen at $\theta = 90$ deg and $\theta = 270$ deg. Also, the bulkhead at $\theta = 270$ deg experiences a higher stress magnitude than at $\theta = 90$ deg, and a significant multiaxial stress state is also found around $\theta \approx 90$ deg and $\theta \approx 270$ deg according to the 2-d stress space representation, among other more critical locations.

The proposed modification of the internal structure of the WindBarge is shown in Figure 33, where four new bulkheads are added axially from the tower. Two of them are at about $\theta = 90$ deg and two of them at $\theta = 270$ deg, before and after these angles each. At the bow side of the floater, the internal thickness is further reduced as well as the stiffener spacing. The ballast compartments are not modified.

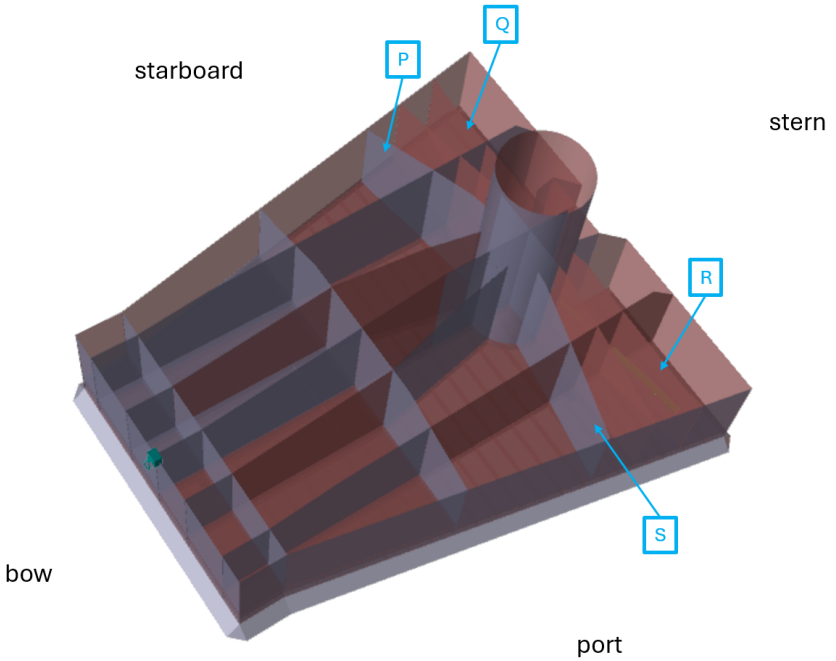

Figure 33: WindBarge model with a modification of the internal structure.

The alternative design is studied regarding its multiaxial response at the upper deck and the stress levels of the internal structure. A reduction in the thickness of the vertical walls and the stiffener spacing away from the tower was also implemented to counteract the additional weight of the new bulkheads. However, the mass and inertia were not modified in SIMA, as this was not considered important for the nature of this study.

For the structural model, the element length is now set to 0.6-0.8 m internally and 1.6 m externally. The whole structure is selected for the structural model.

3.2.2 Compartments

The internal compartments are created in GeniE based on all the enclosed spaces in the model, as depicted in Figure 34a. Only the lowest compartments were selected as ballast tanks. They are filled with material of density 3600 kg/m^3 in HydroD, where the balancing and filling fraction selection is done. The filling of the ballast tanks is shown in Figure 34b, where it is noted that some tanks are empty (gray), some are full (green), and some are partially full (e.g. the two tanks between the empty tanks and the tower location). A ballast of 1700 kg/m^3 is considered to reduce cost in the next design iteration phase of the WindBarge.

The selection/filling of the ballast tanks was already carried out by the WindBarge project, and the same configuration is kept in this work. It is noted though, that the density of the structure was adjusted (increased) so that, in combination with the ballast tanks, the total mass/inertia matrix of the floater matches the one defined in SIMA from an initial estimation of the steel structure weight and ballast tank configuration [63]. Since the WindBarge is a pre-FEED conceptual project, it is accepted; however, in the next design iteration, the real density of the structure with additional details shall be considered, and if a readjustment of the ballast tanks doesn't lead to the initial total mass and inertia estimation, the model in SIMA must be updated. The update can change the equilibrium position (draft, trim, and heel angle).

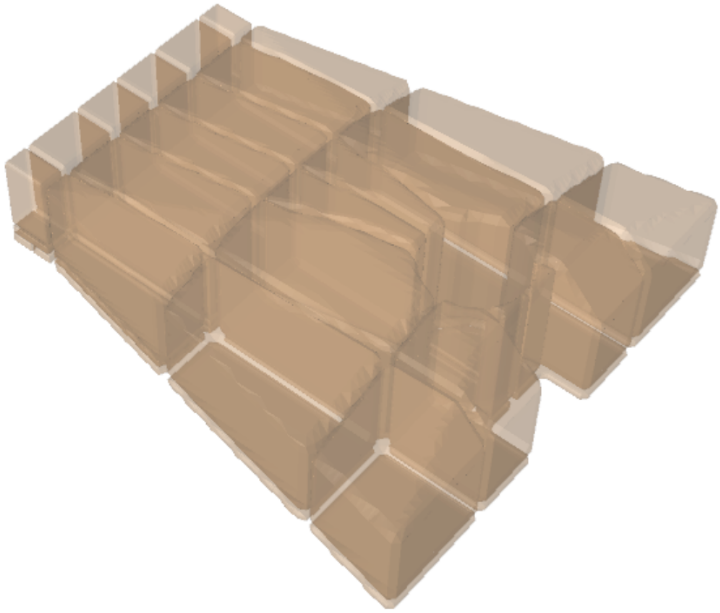

(a) Available compartments (GeniE).

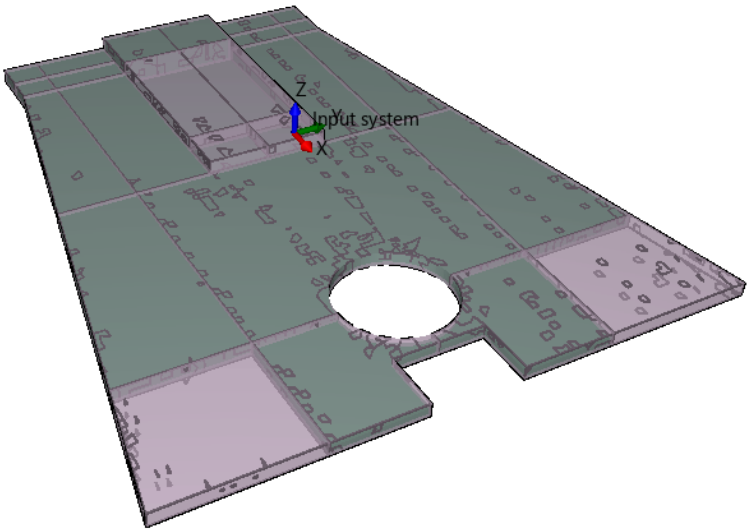

(b) Selected ballast tanks (HydroD).

Figure 34: Internal compartments (images from [69]).

3.2.3 Free surface mesh

The free surface mesh (Figure 35) is designed interactively with HydroMesh which is run through HydroD. The radius of the free surface is selected as five times the floater length to account for the wavelength of the examined sea conditions.

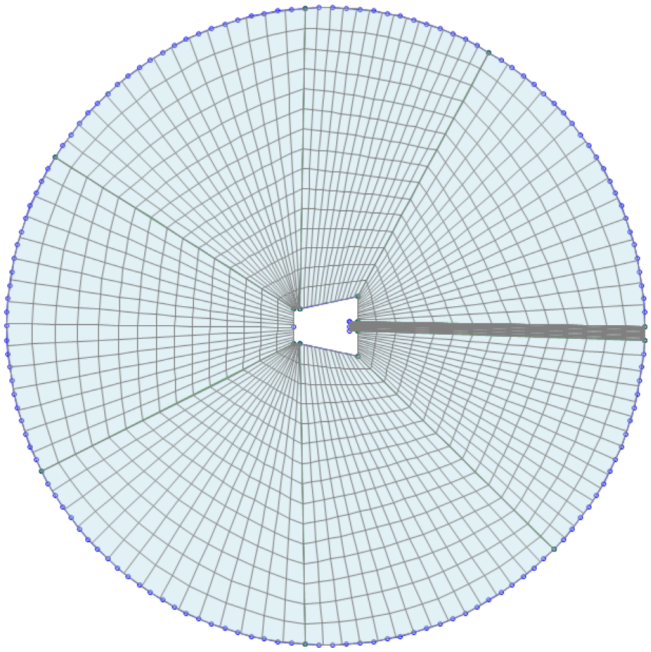

Figure 35: Free surface mesh (image from [69]).

3.2.4 SIMA model

The integrated model in SIMA is depicted in Figure 36. The floater, the tower, the nacelle, the hub, the blades, and the mooring line can be identified. The details of the SIMO bodies (floater, hub, and nacelle) and RIFLEX elements (blades and tower) are noted in section 2.1.

The hydrodynamic and aerodynamic data have already been configured in SIMA by the WindBarge project, therefore no reiteration is carried out in this study on that part. SIMA is used in this study to simulate the selected design load cases.

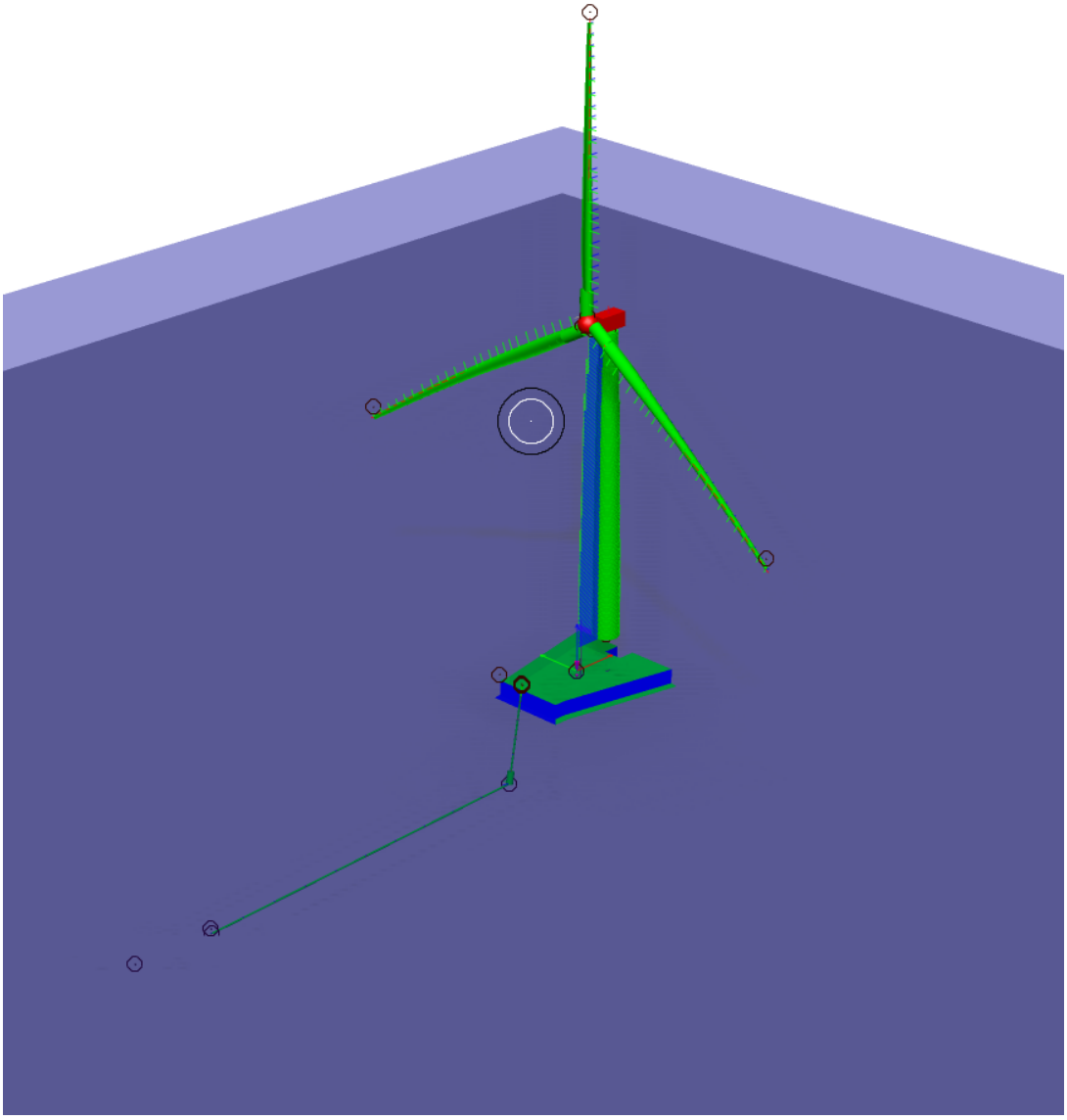

Figure 36: SIMA model.

The wall thickness and the tower height of the 15 MW NREL wind turbine [70] used in the WindBarge are slightly modified in the WindBarge concept [12].

The mooring line has a total length of 190 meters and is constructed with nylon. It includes a clump weight at 35 meters from the fairlead that pretensions the system and gives the final shape of the mooring line. The thruster is not included in the model for additional pre-tensioning when there is no loading in the structure to avoid a slack mooring line.

Regarding the reference system, the positive Z is upwards and the positive X is towards the stern. The origin is 27 m from the stern and Z=0 corresponds to an initial draft of 6 m. Therefore, the initial freeboard is 5 m, accounting for the total height of 11 of the floater towards the bow.

3.2.5 Wind turbine controllers of the WindBarge

Blade pitch controller

The WindBarge utilizes a modification of the 15 MW NREL wind turbine [70] pitch controller that was implemented for the UMaine VolturnUS-S Semisubmersible Reference Platform [71] to consider the dynamics of the floater, and is available on Github [72]. It is based on the NREL Reference OpenSource Controller (ROSCO), which is also available on Github [73]. The blade pitch controller is a collective pitch controller (CPC), meaning that the same blade pitch angle is applied to all the blades.

To avoid 3P excitation of the blades with the tower, a minimum rotational speed of 5 rpm is imposed. The cut-in speed is at 3 m/s, the rated wind speed is at 10.59 m/s, and the cut-out speed is at 25 m/s. The rated rotational speed is at 7.55 rpm.

Below 6.98 m/s wind speed, a PI controller is used to adjust the generator torque, maintaining minimum rotational speed and optimal C_p. An Extended Kalman-filter estimator is used in ROSCO for the wind speed to obtain blade pitch angles. Between 6.98 m.s and 10.59 m/s, a PI controller is used to adjust the rotor speed, maintaining the optimal tip speed ratio (TSR). Finally, between 10.59 m/s and 25 m/s, a PI controller adjusts the blade pitch angle to maintain the rated operational speed and a constant generator torque.

The main modifications of the controller are two [12]. First, a minimum blade pitch angle is applied at low wind speed (between 3 m/s and 7 m/s), which increases the generated power. Second, a peak shaving, or else called thrust clipping, is imposed by saturating the minimum pitch angle to limit the thrust force near rated wind speed. The blade pitch angle increases before the rated wind speed, at 9.5 m/s, as presented in Figure 37 (pitch saturation, PS). Therefore, the thrust force is limited, as shown in Figure 38, with a reduction of about 15 %.

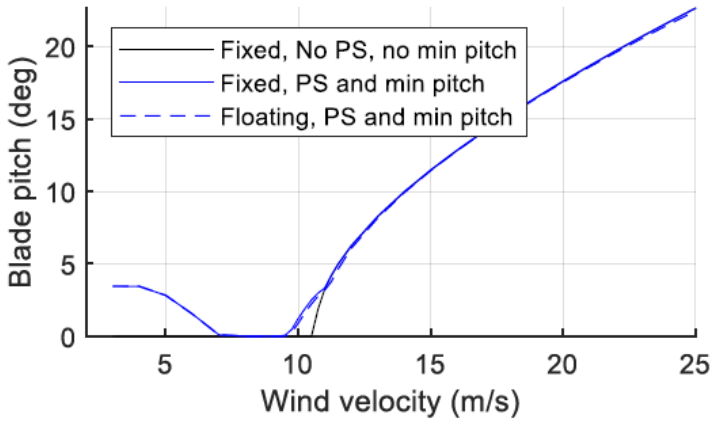

Figure 37: Blade pitch for different wind speeds [12].

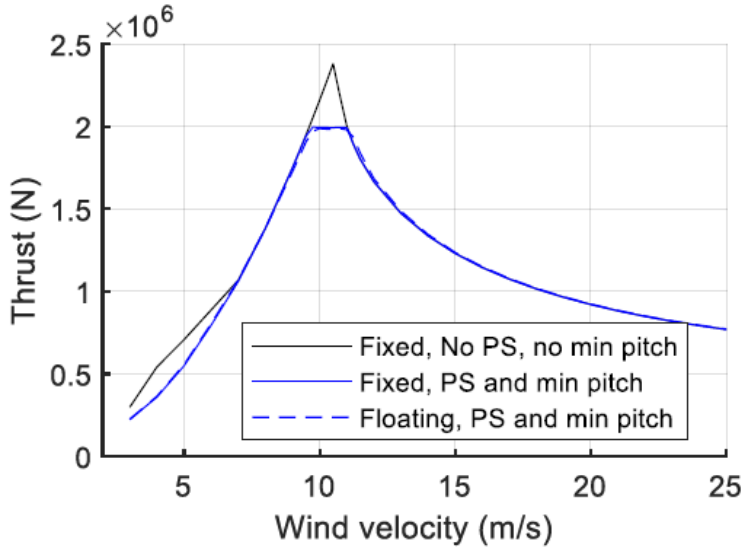

Figure 38: Thrust for different wind speeds [12].

Yaw controller

A significant yaw drift appears due to the yaw-drift issue of single-point mooring (SPM) floating wind turbines (see section 2.1.3), even for a zero-degree angle between the wind direction and the rotor hub axis. The WindBarge is moved laterally and doesn't align completely with the wind direction, which reduces the efficiency of the wind turbine and, therefore, the power production.

SIMA has an internal yaw controller based on [74], which was implemented in a preliminary study of the WindBarge in [69] by the author of the current study. The yaw controller is also used in this study. The yaw-drift issue of single-point mooring (SPM) floating wind turbines is solved and the power production is increased.

Wind measurements from a downwind wind vane are used to calculate the nacelle yaw misalignment. The controller applies a fixed yaw rate when an integrated error threshold is surpassed. A fast and a slow low-pass filter are utilized to establish when the yaw motors function.

3.3 Internal structure

The internal structure consists of several upright partitions, which are called bulkheads. They are named according to Figure 39 to recognize them. The bow, stern, port, and starboard sides of the floater are presented in the same figure.

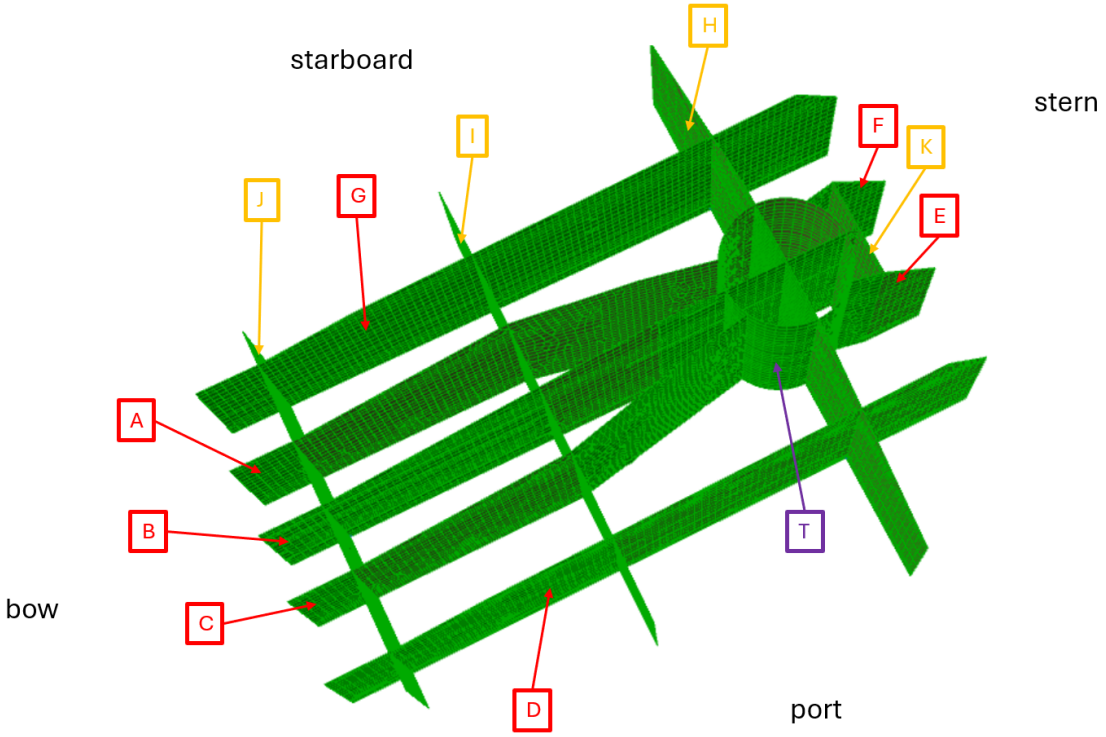

Figure 39: Internal structure naming and sides.

Several elements are selected at each bulkhead to study the stresses. The naming of the elements for the bulkheads A, C, and H is presented in Figure 40. Only a few elements, though, are compared in this study, as more representative of the stress levels at each location.

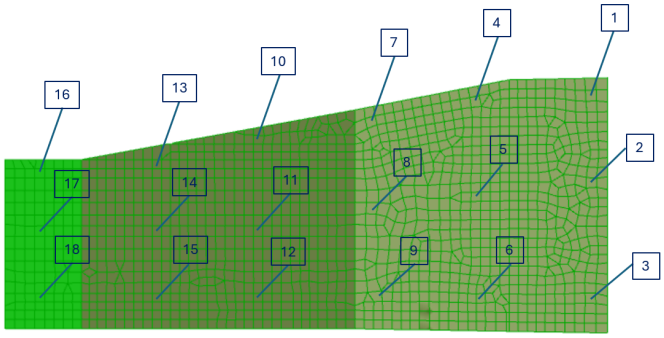

(a) Bulkhead A.

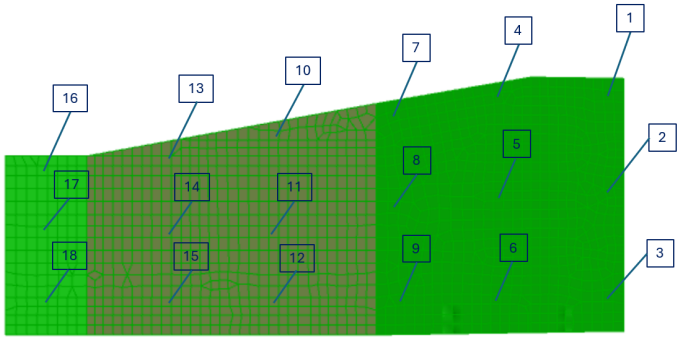

(b) Bulkhead C.

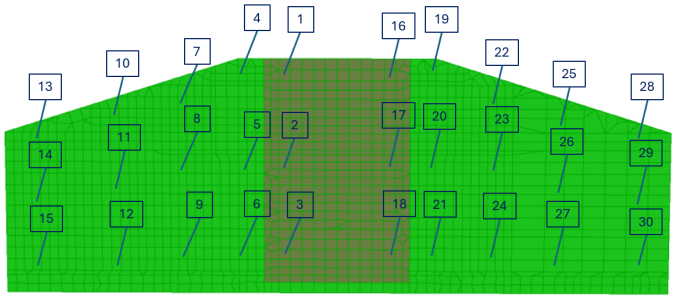

(c) Bulkhead H (as viewed from the bow).

Figure 40: Shell elements naming in bulkheads A, C, and H.

The added bulkheads are presented and named in Figure 41, and the selected elements in Figure 42. Additionally, as the mesh was different between the initial and the modified design, selected elements from bulkheads A and H in the new design are presented in Figure 43 at approximately the same position as the elements from the initial design with which they are compared.

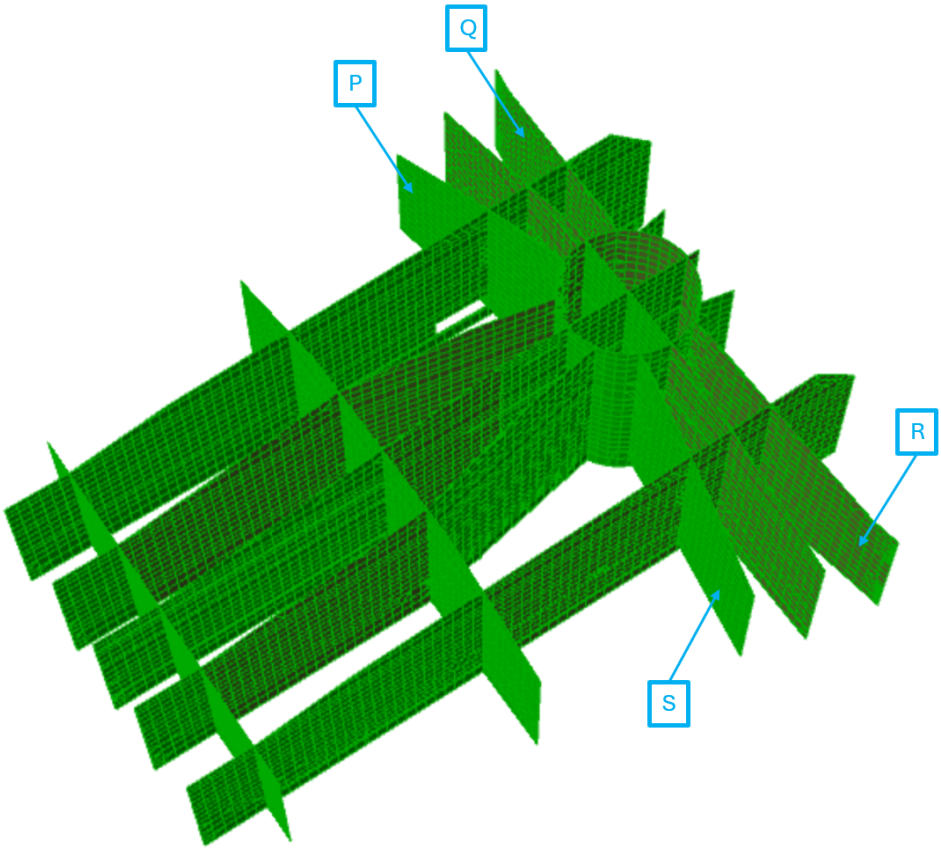

Figure 41: Naming of the bulkheads in the modified internal.

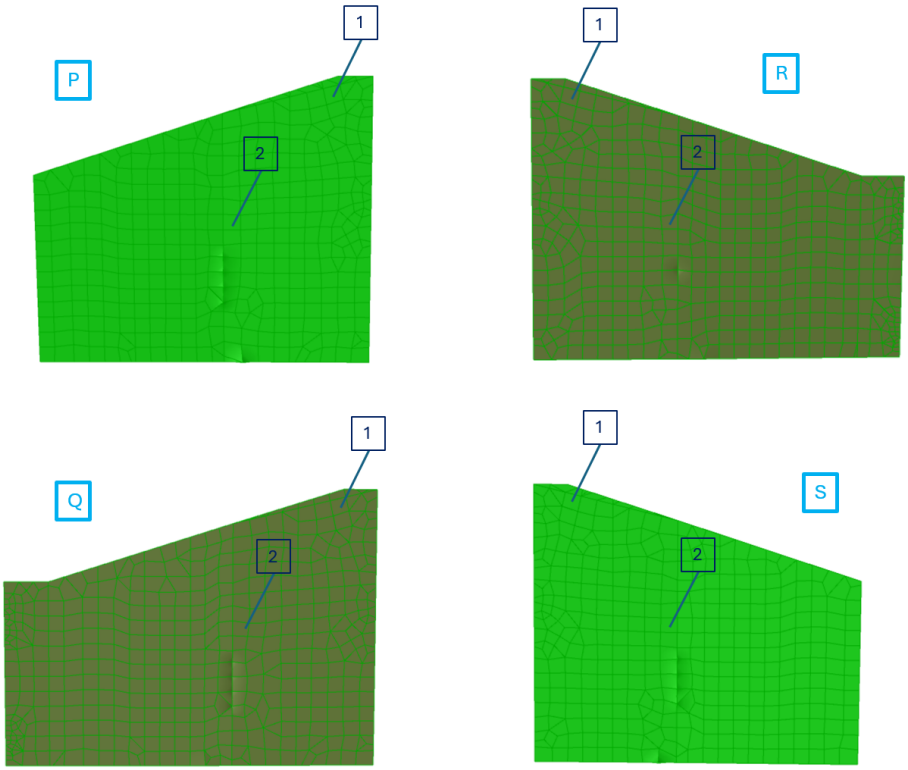

Figure 42: Shell elements naming in bulkheads P, Q, R, and S.

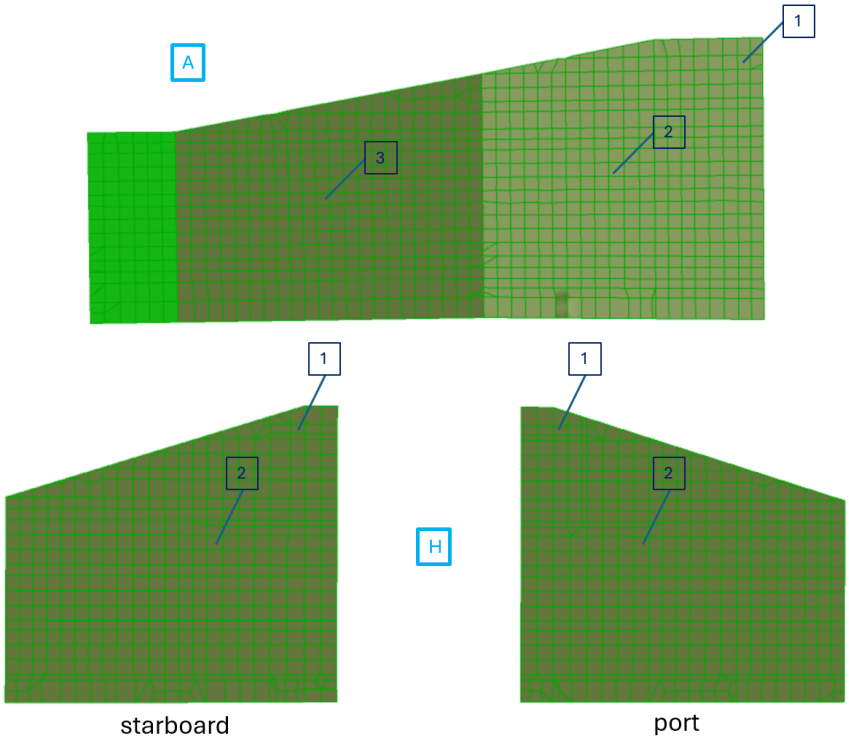

Figure 43: Shell elements naming in bulkheads A and H in the new design.

3.3.1 Local coordinate system of shell elements

The local coordinate system in the shell elements is calculated as referred to in Xtract's manual [32] in the following manner: The local x-axis of the elements results from the projection of the global X axis to the shell surface. Then, the local y-axis is derived from a right hand rotation whereas the local z-axis is perpendicular to the surface. In Figure 44, the x-axis and y-axis of the elements are presented for the internal structure and outer structure in the areas of interest (zoom is required).

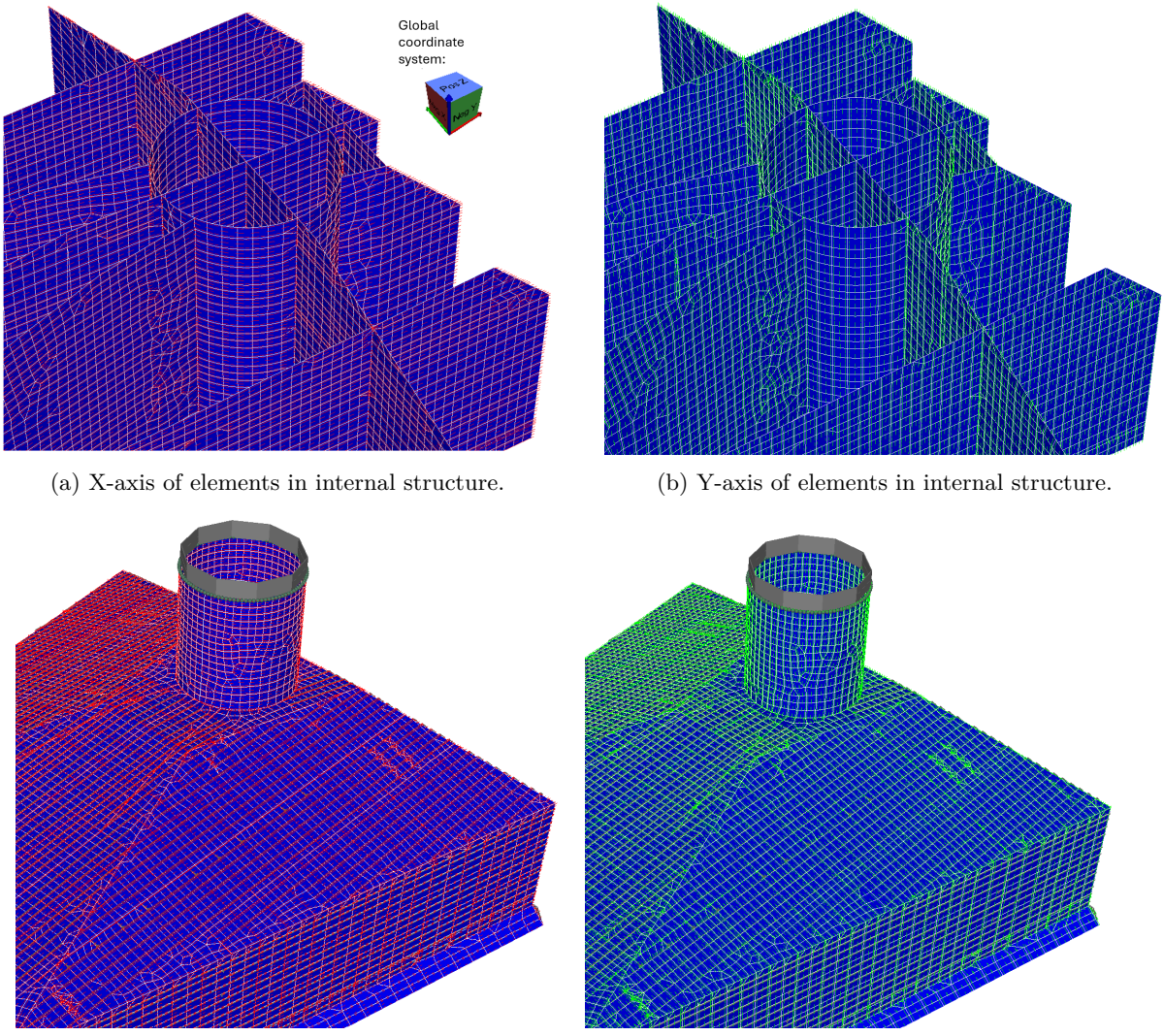

(a) X-axis of elements in internal structure.

(b) Y-axis of elements in internal structure.

(c) X-axis of elements in outer structure.

(d) Y-axis of elements in outer structure.

Figure 44: X-axis and y-axis of elements.

The element x-axis in the longitudinal bulkheads of the internal structure and in the upper deck is approximately towards the +X (red arrow) of the global axis (apart from the tower) and the element x-axis in the lateral bulkheads of the internal structure is approximately towards the +Y (green arrow) of the global axis.

The element y-axis is a bit more complicated. According to the bulkheads naming in Figure 40, the element y-axis in the internal structure is towards the +Z (blue arrow) of the global axis for bulkheads G, H, K, F, B and C (towards the tower) and for all the bulkheads towards the bow. For the rest bulkheads, the element y-axis is towards the -Z of the global axis. The element y-axis at the port side of the tower is towards the +Z (blue arrow) of the global axis and the at the starboard side towards the -Z of the global axis.

The element y-axis in the upper deck is approximately towards the +Y (green arrow) of the global

axis.

3.3.2 Stress transformation

As the structural stress, commonly used in multiaxial fatigue calculations, is not an available output from SESTRA, the elements stresses are used instead in this study. This approach may introduce some discrepancies, especially if the mesh is coarse, but it is deemed as acceptable for screening and identifying whether a multiaxial stress state appears.

Since the local coordinate system (x, y, z) of the shell elements is defined as explained in section 3.3.1, it has to be transformed to a new coordinate system (x', y', z') so that x' is normal to the weld line at the tower base. The rotation angle θ is different for every location (and consequently shell element) around the tower base, as shown in Figure 45. The stress state in the new coordinate system is calculated according to the following equations:

$$\sigma'_{\mathrm{x}} = \sigma_{\mathrm{x}} \cos^2\theta + \sigma_{\mathrm{y}} \sin^2\theta + 2\tau_{\mathrm{xy}} \sin\theta \cos\theta \tag{43}$$

$$\sigma'_{\mathrm{y}} = \sigma_{\mathrm{x}} \sin^2\theta + \sigma_{\mathrm{y}} \cos^2\theta - 2\tau_{\mathrm{xy}} \sin\theta \cos\theta \tag{44}$$

$$\tau'_{\mathrm{xy}} = (\sigma_{\mathrm{y}} - \sigma_{\mathrm{x}}) \sin\theta \cos\theta + \tau_{\mathrm{xy}}(\cos^2\theta - \sin^2\theta) \tag{45}$$

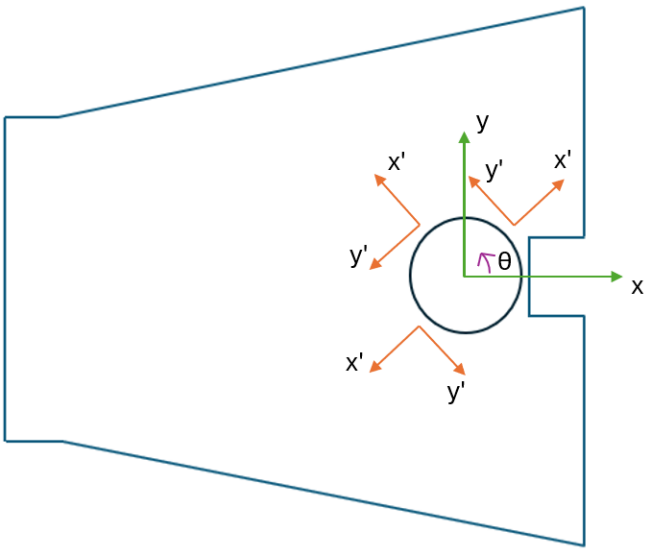

Figure 45: Transformed coordinate system for different locations around the tower base.

3.4 Meteocean data

The environmental conditions are different in every location and must be studied to simulate a floating wind turbine. Also, various design load cases must be considered according to standards. The design basis summary [12] and the meteocean design basis [75] by the WindBarge project, among other reports and standards, were studied and referred regarding approaches and environmental parameters.

The location examined in this study is Creyke Beck (55.35N, 01.69 E) in the North Sea (see Figure 46) with 40 meters of water depth. A new design must account for location-specific environmental loads, therefore, measurements from the area for the wind and wave state are necessary.

Figure 46: Creyke Beck location from Google Maps.

According to the meteocean design basis [75] and the design basis summary [12] for the WindBarge, data from the NORA3 hindcast database have been utilized to define the wind and wave environment. The database has information over a period of 28 years (1993-2021). The wave data are hourly and they are averaged based on the significant wave height to get a 3-hour sea state.

The wind data are also provided for different heights and they are adjusted for the hub height at 142 meters with the power law equation. Finally, the current data are derived from the Copernicus Global Ocean Physics Analysis and Forecast dataset. The scatter table for the joint distribution of the significant wave height H_s and the wave period T_p is given in Figure 47 from [75].

For a given return period, the contour of the environmental parameters (H_s, T_p) can be found based on the Inverse First-Order Reliability Method (IFORM), according to [76]. At first, the environment variables are transformed to standard normal variables. A hypersphere in standard normal space with radius β (reliability index) specifies the exceedance probability p_F. The higher the reliability index, the higher the return period as well. Finally, the variables are transformed back to the physical space that produces the environmental contours.

The available meteocean data are usually limited for a location of interest. However, it is necessary to know the wind and sea state with a high return period (e.g. 50 years) to account for the loads when designing a new offshore structure. The need for this information is also incorporated in standards. Therefore, IFORM or ISORM (inverse second-order reliability method) may be used.

FREQUENCY TABLE of Hm0 vs. Tp					Hs	data at	55.35 / 1.69		01 jan 1993		30 Nov 2021											
	Tp																				Marg.	Cum.
Hm0	<2	2-3	3-4	4-5	5-6	6-7	7-8	8-9	9-10	10-11	11-12	12-13	13-14	14-15	15-16	16-17	17-18	18-19	19-20	>20	Sum	distr.	distr.
0.50	9	863	3784	3790	1748	1339	784	1149	677	324	146	102	66	79		16	4		2	3	14876	0.059	0.059
1.00		63	5705	14779	12357	7398	3443	3295	3046	2384	1087	595	287	147		55	29		5		54675	0.216	0.274
1.50			145	7030	20286	11771	4860	4405	3656	3991	2442	1280	364	149		57	20		1		60457	0.239	0.513
2.00				200	11054	18368	3950	3685	2706	2412	2398	1532	524	214		63	24		1		47131	0.186	0.699
2.50					1098	15485	4640	2868	2043	1479	1178	1052	527	165		53	17		10	2	30617	0.121	0.820
3.00					34	6041	5544	2470	1736	1217	743	632	407	174		57	19		3		19077	0.075	0.895
3.50					1	796	4151	2694	1358	925	411	437	216	141		46	5				11181	0.044	0.939
4.00						29	924	2541	1272	907	442	226	130	76		32	5				6584	0.026	0.965
4.50						2	75	1081	1328	722	448	196	73	46		10	3				3984	0.016	0.981
5.00							1	197	866	483	372	126	87	24		13	7				2176	0.009	0.989
5.50								17	382	351	242	144	40	26		17	2				1221	0.005	0.994
6.00									71	212	164	145	45	32		21					690	0.003	0.997
6.50									1	110	90	82	34	10		17	1				345	0.001	0.998
7.00									1	26	74	39	36	9		2					187	0.001	0.999
7.50										6	49	17	26	11		1					110	0.000	0.999
8.00											14	13	20	11							58	0.000	1.000
8.50											7	13	20	13							53	0.000	1.000
9.00												6	10	8		1					25	0.000	1.000
9.50													1	3		4					8	0.000	1.000
																					253455		
Sum	9	926	9634	25799	46578	61229	28372	24402	19143	15549	10307	6637	2913	1338	0	465	136	0	22	5	253464		
Marg. distr.	0.000	0.004	0.038	0.102	0.184	0.242	0.112	0.096	0.076	0.061	0.041	0.026	0.011	0.005	0.000	0.002	0.001	0.000	0.000	0.000			
Cum. distr.	0.000	0.004	0.042	0.143	0.327	0.569	0.681	0.777	0.853	0.914	0.955	0.981	0.992	0.998	0.998	0.999	1.000	1.000	1.000	1.000			

Figure 47: Scatter table for the joint distribution of the significant wave height and wave period for Creyke Beck [75].

In Figure 48, the contour plots of the environmental parameters H_s and T_p are presented for a 1-year and a 50-year return period. In Figure 49, the contour plot for different wind speeds is illustrated for a 50-year return period. The different wave directions are not distinguished.

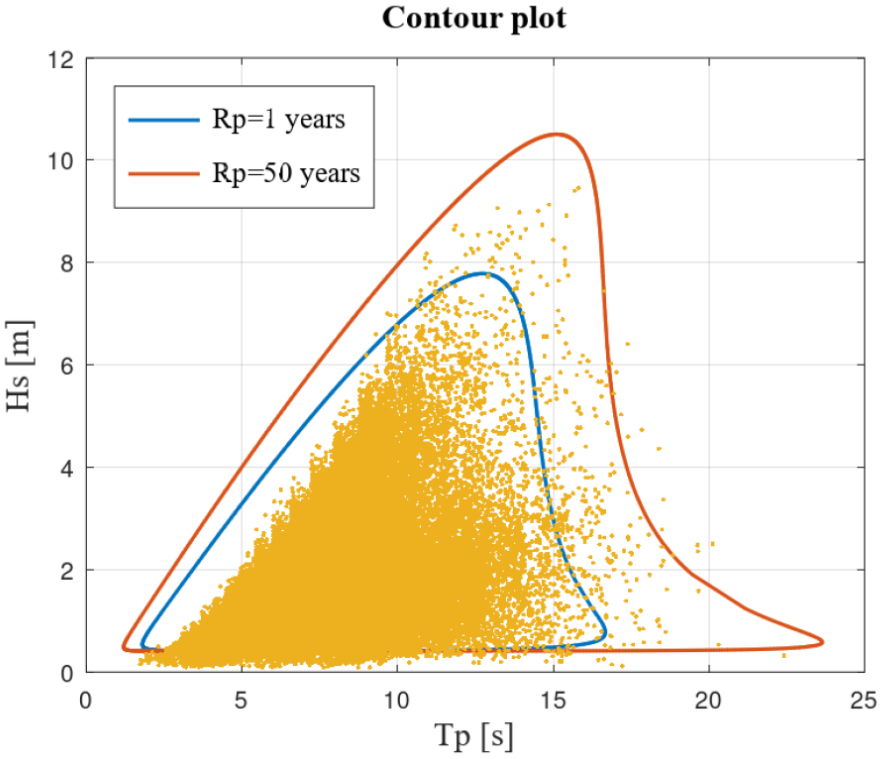

Figure 48: Contour plot of the environmental parameters H_s and T_p for Creyke Beck [75].

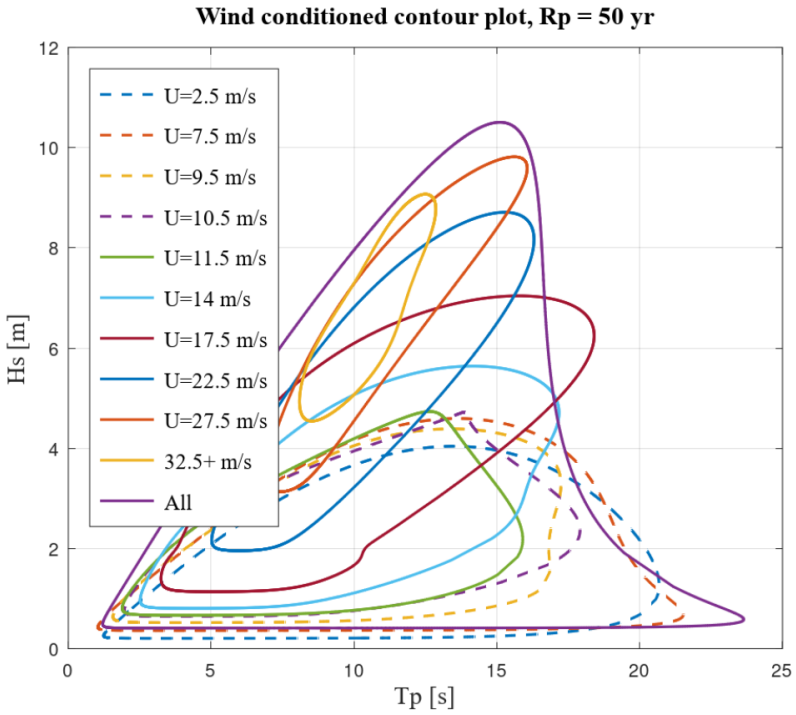

Figure 49: Wind conditioned contour plot of the environmental parameters H_s and T_p with a return period of 50 years for Creyke Beck [75].

The misalignment between the mean wind and the wave directions falls mainly within the area from -30 to +30 degrees for all wind speeds, except for wind speed 0-5 m/s where the distribution is uniform. An example distribution is shown for wind speeds 10-11 m/s in Figure 50.

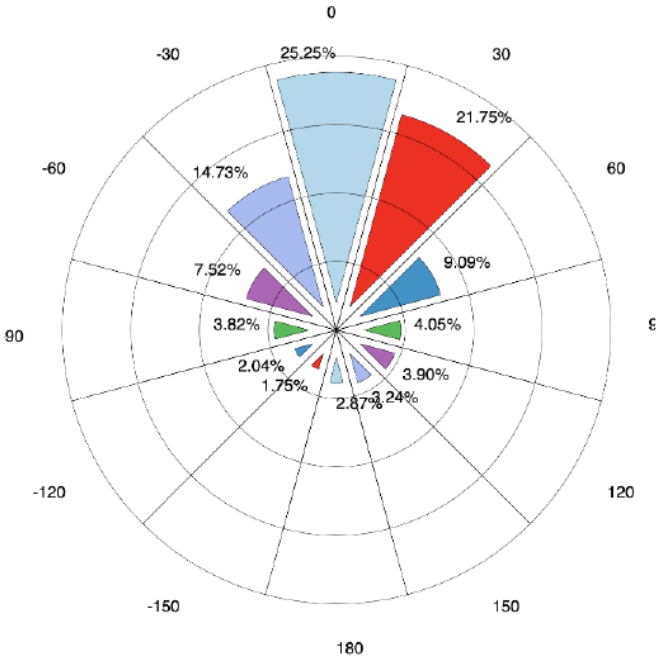

Figure 50: Misalignment distribution for wind speeds 10-11 m/s for Creyke Beck [75].

The current and tidal profile is omitted in this study. A constant current velocity value is only expected to slightly affect the structural response, as seen from a limited number of simulations.

3.5 Design load cases (DLCs)

The selected conditions for the ULS study are considered as representative to describe the internal stress distribution from the tower to the floater's inner structure and outer shell. Also, the fatigue study is implemented for power production only, without faults. Before the FOWT is qualified for deployment, a complete assessment should be carried out with the rest of the simulation cases.

For the DLC 1.6 (see section 2.2.4), only specific wind speeds and sea states are selected in this study, based on engineering judgement, from the many cases examined by the WindBarge project. At the rated wind speed, the thrust is maximum, as shown in Figure 38, which increases the loads from the wind turbine to the floater. Therefore, this wind speed at 10.5 m/s is of interest. From the wind conditioned contour plot for the 50-year return period (see Figure 49), the sea state with the largest significant wave height H_s is selected that introduces more energy in the system.

As the wind speed increases, the significant wave height increases as well. Therefore, a higher wind speed at 24.5 m/s is also selected as a study case with a higher significant wave height H_s and peak period T_p. Two different wind directions are considered for both wind speeds at 0 and 30 or 20 degrees, which are the most representative for the specific location. As the wind speed increases, the waves become more unidirectional, so the wind misalignment is considered smaller. The simulation parameters are summarized in Table 3.

Table 3: Simulation table for DLC 1.6 (ULS) based on [77].

ULS DLC [-]	**Wind speed** [-] [m/s]	**Peak period** T_p [s]	**Significant wave height** H_s [m]	**Spreading exponent (2s)**	**Wind/wave misalignment** [deg]
A	10.5	13.46	4.95	4	0
B	10.5	13.46	4.95	4	30
C	24.5	15.97	6.18	6	0
D	24.5	15.97	6.18	6	20

For the DLC 6.1 (see section 2.2.4), where the wind turbine is parked, a wind speed above the cut-out speed is used at 27.5 m/s. Again, the sea state with the largest significant wave height H_s is selected from the wind conditioned contour plot for the 50-year return period (see Figure 49) with different wind directions. The wind turbine doesn't rotate, and the blades are feathered to reduce the loads, therefore, this is a no-power production situation. The simulation parameters are summarized in Table 4.

Due to the significantly increased wave height, it is expected that the parked condition will cause large floater motions, which will subsequently increase the loads at the tower base. The cause for that can be attributed to an oscillating tower, together with the rotor nacelle assembly. Therefore, it is important to study the structural effect in such conditions.

Table 4: Simulation table for DLC 6.1 (ULS) based on [77].

ULS DLC [-]	**Wind speed** [m/s]	**Peak period** T_p [s]	**Significant wave height** H_s [m]	**Spreading exponent (2s)**	**Wind/wave misalignment** [deg]
E	27.5	16.73	9.57	6	0
F	27.5	16.73	9.57	6	20

For the fatigue limit state (FLS) study, the scatter data have been aggregated by the WindBarge project in areas as shown in Figure 51 with the different colors to limit the number of simulation cases [78]. A weighted average has been used in each area to derive a representative value for the significant wave height H_s and peak period T_p based on the number of occurrences. Then, the wind speed time series was compared with the range of (H_s, T_p) in each area to derive the number of occurrences for each wind speed bin.

The wind speed bins used are the following in m/s: 0-5, 5-7, 7-9, 9-10, 10-11, 11-12, 12-13, 13-14, 14-15, 15-16, 16-17, 17-20, 20-25, 25-30, and 30-40. Similarly, a weighted average was used to derive a representative value for the wind speed in each area. Finally, the direction of the wind was accounted for, with directions from -15 to +15 degrees considered as 0 degrees and from -15 to -45 and +15 to +45 as -30 and +30 degrees accordingly. The rest of the directions have a lower probability and were excluded.

		Tp	[s]																		
[m]	Hm0	<2	2-3	3-4	4-5	5-6	6-7	7-8	8-9	9-10	10-11	11-12	12-13	13-14	14-15	15-16	16-17	17-18	18-19	19-20	>20
<	0.50	9	863	3784	3790	1748	1339	784	1149	677	324	146	102	66	79		16	4		2	3
	1.00		63	5705	14779	12357	7398	3443	3295	3046	2384	1087	595	287	147		55	29		5	
	1.50			145	7030	20286	11771	4860	4405	3656	3991	2442	1280	364	149		57	20		1	
	2.00				200	11054	18368	3950	3685	2706	2412	2398	1532	524	214		63	24		1	
	2.50					1098	15485	4640	2868	2043	1479	1178	1052	527	165		53	17		10	2
	3.00					34	6041	5544	2470	1736	1217	743	632	407	174		57	19		3	
	3.50					1	796	4151	2694	1358	925	411	437	216	141		46	5			
	4.00						29	924	2541	1272	907	442	226	130	76		32	5			
	4.50						2	75	1081	1328	722	448	196	73	46		10	3			
	5.00							1	197	866	483	372	126	87	24		13	7			
	5.50								17	382	351	242	144	40	26		17	2			
	6.00									71	212	164	145	45	32		21				
	6.50									1	110	90	82	34	10		17	1			
	7.00									1	26	74	39	36	9		2				
	7.50										6	49	17	26	11		1				
	8.00											14	13	20	11						
	8.50											7	13	20	13						
	9.00												6	10	8		1				
	9.50													1	3		4				

Figure 51: Scatter table with aggregated areas [78].

The resulting simulation data for the fatigue limit state (FLS) study by the WindBarge project are summarized in Table 5. The probability of occurrence for each case was derived based on the number of occurrences in the corresponding area over the total number of occurrences. The direction of the wind speed was also considered with the two bins at 0 and 30 degrees. As the rest of the misalignment cases were not examined (over +/- 45 degrees), the probabilities were scaled for each wind speed so that they sum up to 1 for all simulation cases.

Table 5: Simulation table for DLC 1.2 (FLS) without wind/wave misalignment based on [78].

FLS DLC [-]	**Wind speed [m/s]**	**Peak period T_p [s]**	**Significant wave height H_s [m]**	**Spreading exponent (2s)**	**Probability with no misalignment**	**Probability with 30 deg misalignment**
A	7.0	13.10	1.30	4	0.008	0.014
B	7.6	8.00	1.30	4	0.117	0.238
C	9.1	4.90	1.00	4	0.143	0.182
D	10.5	13.30	2.70	4	0.008	0.009
E	15.3	7.90	2.70	4	0.128	0.118
F	18.9	13.30	5.50	4	0.002	0.003
G	21.9	10.00	4.70	4	0.016	0.013

As the wind speed increases, it is expected that the significant wave height H_s and peak period T_p will increase as well. However, by analyzing the resulting simulation cases in Table 5, it is seen that this is not always the case, which can be attributed to the presence of swell waves.

Additionally, for the most probable situations, the resulting significant wave height H_s is between 1 and 3 m and the peak period T_p is between 4 and 8 s. As shown in Figure 52, where a conditional formatting is applied in the scatter table based on the number of occurrences, these simulation parameters are indeed within the area with the highest number of occurrences (red color).

		Tp	[s]																		
[m]	Hm0	<2	2-3	3-4	4-5	5-6	6-7	7-8	8-9	9-10	10-11	11-12	12-13	13-14	14-15	15-16	16-17	17-18	18-19	19-20	>20
<	0.50	9	863	3784	3790	1748	1339	784	1149	677	324	146	102	66	79		16	4		2	3
	1.00		63	5705	14779	12357	7398	3443	3295	3046	2384	1087	595	287	147		55	29		5	
	1.50			145	7030	20286	11771	4860	4405	3656	3991	2442	1280	364	149		57	20		1	
	2.00				200	11054	18368	3950	3685	2706	2412	2398	1532	524	214		63	24		1	
	2.50					1098	15485	4640	2868	2043	1479	1178	1052	527	165		53	17		10	2
	3.00					34	6041	5544	2470	1736	1217	743	632	407	174		57	19		3	
	3.50					1	796	4151	2694	1358	925	411	437	216	141		46	5			
	4.00						29	924	2541	1272	907	442	226	130	76		32	5			
	4.50						2	75	1081	1328	722	448	196	73	46		10	3			
	5.00							1	197	866	483	372	126	87	24		13	7			
	5.50								17	382	351	242	144	40	26		17	2			
	6.00									71	212	164	145	45	32		21				
	6.50									1	110	90	82	34	10		17	1			
	7.00									1	26	74	39	36	9		2				
	7.50										6	49	17	26	11		1				
	8.00											14	13	20	11						
	8.50											7	13	20	13						
	9.00												6	10	8		1				
	9.50													1	3		4				

Figure 52: Scatter table with conditional formatting based on the number of occurrences.

It is noted, though, that the aggregated areas are significantly large and important information can be lost regarding the real environment. Smaller areas of H_s, T_p and more wind speeds cases for each area are suggested, which will alter the probabilities, and might significantly differentiate the fatigue life calculations. Moreover, a distinction between wind and swell waves by comparing the wind and wave direction in the data can provide more information about the sea state.

Nevertheless, the provided simulation cases are utilized, as the limited time of the thesis and the increased simulation cost would not allow for such an extended analysis. It is expected, though, to provide a representative basis for an initial fatigue life calculation.

3.6 Fatigue analysis

Nominal uniaxial fatigue

In this study, the nominal uniaxial fatigue presented in section 2.4.6 is applied for the tower at its base. The forces and moments from the beam model in SIMA are used to calculate the axial (and shear) stress, and then the rainflow algorithm is utilized to identify stress ranges and count the cycles.

An S-N curve type D in air is considered, assuming a girth weld close to the tower base. The parameters of the selected S-N curve type D in air are summarized in Table 6. The actual connection of the tower with the upper shell of the barge is different. However, a structural detail that accounts for this type of connection was not found explicitly in the recommended practice DNVGL-RP-C203 [37] to select a more appropriate S-N curve, but this selection is considered conservative and it also aligns with the S-N curve type when using the hot spot stress method (section 2.4.5).

Table 6: Selected S-N curve based on [37].

S-N curve	m_1*	$log\bar{a}_1$*	m_2**	$log\bar{a}_2$**	Fatigue limit [MPa]	k
D	3	12.164	5	15.606	52.63	0.2

* $N \leq 10^7$ cycles, ** $N > 10^7$ cycles

A girth weld consideration, slightly over the tower-barge connection, is also of interest. A uniaxial fatigue assessment based on this type of connection can be a significant input on fatigue damage. The actual connection of the tower with the barge shall also be investigated, as will follow, with the hot spot plate and hot spot plate multidirectional fatigue damage approaches using the structural model.

Multiaxial fatigue and screening

The screening method based on the MVEE (see section 2.5.1) is applied for the deck at the tower transition region, which is a location with high stresses. Then, the hot spot plate multidirectional fatigue method (see section 2.5.3) is applied both at the deck and the tower, and it is compared with the hot spot plate method, by using the response reconstruction method. Moreover, the fatigue damage is compared with the nominal uniaxial fatigue approach for the tower.

4 Results and Discussion

4.1 Ultimate Limit State (ULS) study for the internal structure

The purpose of the ULS study, after selecting the most relevant DLCs, is to:

- describe the internal stress distribution (from the tower to the floater's inner structure and outer shell), and
- identify critical areas and maximum stress levels.

The ULS DLCs from A to F are simulated for 2100 s (from t=200 s to t=2300 s) in HydroD/WASIM for the structural analysis, from a total simulation time of t=2400 s in SIMA. The resulting stress field, the statistical analysis of the time series, and the power spectral density are presented in the following sections, as well as a comparison with the new design.

4.1.1 Forces and moments

Before studying the stress field in the internal structure, it is important to examine the external load levels to identify patterns that can be associated with the stress response of the floater. An example time series of the forces and moments is presented in Figure 53 for the ULS DLC A at the tower base and 11.52 m above it for comparison. The latter time series is utilized for the updated structural model that includes a part of the tower.

As expected, the force F_z is smaller at 11.52 m above the tower base, as the tower's weight is excluded from the external force, but is included as self-weight in the structural shell model. The forces and moments at the two locations are approximately the same, with some small variations that account for the shadow effect and inertial forces. Nevertheless, as the distance from the tower base is small compared to the total length of the tower, their contribution is considered insignificant in this study. Also, the rigid link that is used to transfer the loads from a beam model to the shell part of the tower is a source of some small discrepancy.

The torsion M_z has a much smaller magnitude than the bending moments M_x and M_y. The bending moments have a positive mean value, which leads to the stress field seen in the following section, and the torsion has a mean value closer to zero. In line with the resulting bending moments, the force F_y has a negative mean value, and the force F_x has a positive mean value. The lateral force F_y is a result of the rotating wind turbine, and it is smaller in magnitude than the longitudinal force F_x, but it is still a significant force.

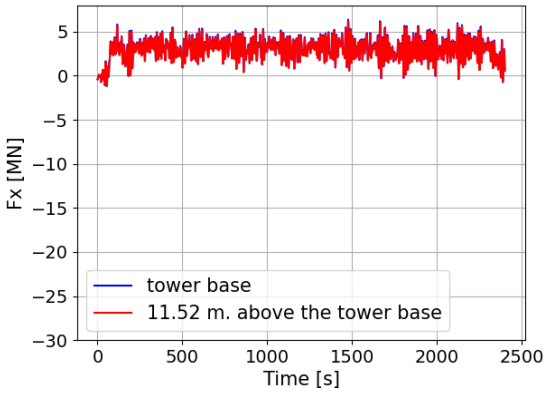

(a) Force F_{x}.

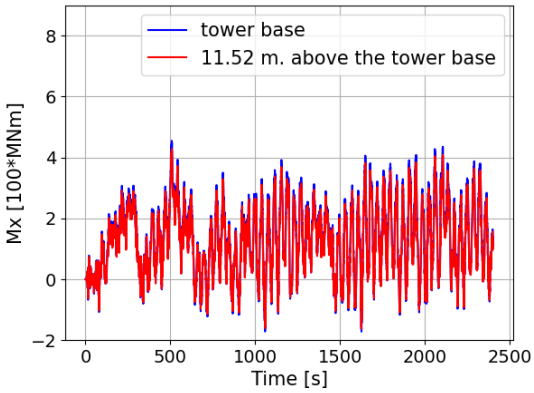

(b) Moment M_{x}.

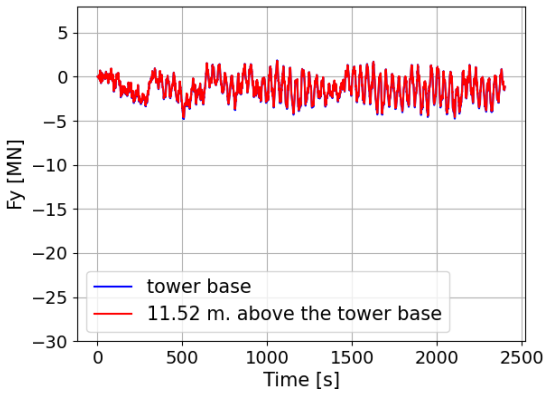

(c) Force F_{y}.

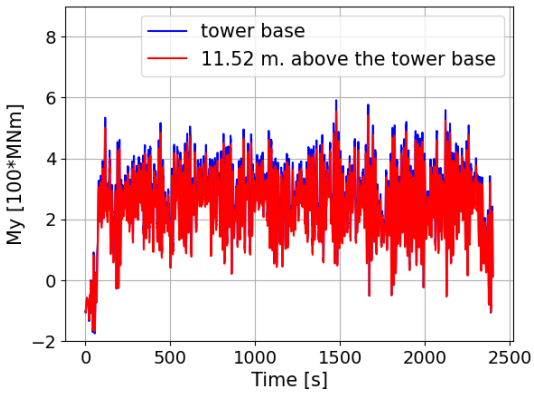

(d) Moment M_{y}.

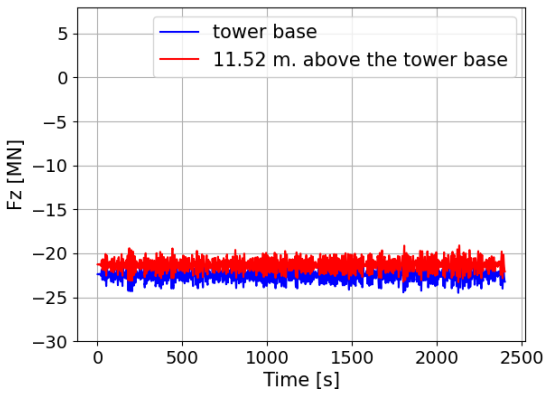

(e) Force F_{z}.

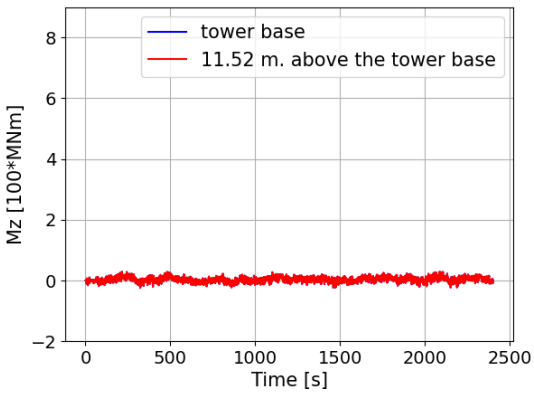

(f) Moment M_{z}.

Figure 53: Time series of forces and moments for ULS DLC A (U_{w}=10.5 m/s, no wind/wave misalignment) with a total duration of t = 2400 s.

4.1.2 Stress field

The stress field for the ULS DLC A is presented in the following figures at the timing of maximum moment M_x (from Figure 54 to Figure 56) and M_y (from Figure 57 to Figure 59) in an attempt to describe the load path in the barge. The elements' coordinate system explained in Figure 44 is utilized.

For the timing of maximum moment M_x, the following conclusions are derived:

- The stress σ_x is negative at both bulkhead H and I, whereas towards the bottom of bulkhead H at the port side, it becomes positive, as well as at the top of bulkhead H at the starboard side. Therefore, the stress σ_x follows the direction of the negative force F_y for the most part and moment M_x. At the longitudinal bulkheads, it is positive at the upper part and negative at the lower part, therefore, it is bends, following the moment M_y. At the deck, it is positive at the bow side of the tower and negative at the stern side.
- At the starboard side of bulkhead H, the stress σ_y is positive, whereas at the port side of it, it's negative. This indicates that the stress σ_y follows the direction of the positive moment M_x. The opposite behavior is observed in bulkhead I, as it is twisted (positive y-axis in this bulkhead is downwards). At the tower, the direction of the stress σ_y is downwards with a larger magnitude towards the deck than towards the bottom. At the deck, the stress σ_y is mainly positive at the starboard side and negative at the port side. The largest stress magnitudes are around the tower base and where the bulkheads are.
- The shear stress τ_{xy} magnitude is larger at the port side than the starboard side of bulkhead H, and it's negative. However, at the bottom of the bulkhead near the tower at the starboard side, it becomes positive. At bulkhead I, the shear stress τ_{xy} is positive. At the deck, it is negative but becomes positive at the port-stern side of the deck.
- The von Mises stress is larger at the port side of bulkhead H than the starboard side as a result of the larger stress components. The port side of bulkhead H experiences the largest von Mises stress in the whole internal structure. The magnitude of the von Mises stress in the bulkheads towards the towards the bow is smaller than towards the stern, which indicate that a thickness reduction or stiffener spacing increase can be considered to have relatively equal stresses all over the structure. At the deck, the largest stress magnitudes are around the tower base.

For the timing of maximum moment M_y, the following conclusions are derived:

- The stress σ_x is negative at both bulkhead H and I, whereas towards the bottom of bulkheads it becomes positive. Therefore, the stress σ_x follows the direction of the negative force F_y for the most part again. At the longitudinal bulkheads, it is positive at the upper part and negative at the lower part, therefore, it bends as well, following the moment M_y, with higher stresses due to the increased moment. At the bulkhead B in the connection with the tower, the stress σ_x has a maximum due to the positive moment M_y. At the deck, it is positive at the bow side of the tower and negative at the stern side. The largest stress magnitudes are around the tower base at around 45, 135, 215, and 305 degrees.
- At the bulkhead H, the stress σ_y is negative (downwards), whereas at the bulkhead I that it's again negative, the direction is upwards (according to the elements' coordinate system in Figure 44). This indicates that the stress σ_y follows the direction of the positive moment M_y. Some high stresses are observed towards the boundary conditions, which indicates that they are not always very close to zero. At the tower, the direction of the stress σ_y is positive towards the bow and negative towards the stern. At the deck, the stress σ_y is mainly negative.
- The shear stress τ_{xy} magnitude is significant at the bulkhead H and has a different sign at the port and starboard side. Similar is the case in the bulkhead I, but with a lower magnitude. At the deck, it is mainly negative at the starboard side and positive at the port side.
- At this timing, the von Mises stress has a similar magnitude both at the port and the starboard side of bulkhead H. The magnitude of the von Mises stress in the bulkheads towards the towards the bow is smaller than towards the stern, which indicates that a thickness reduction or stiffener spacing increase can be considered here as well to have relatively equal stresses all over the structure. At the deck, the largest stress magnitudes are around the tower base.

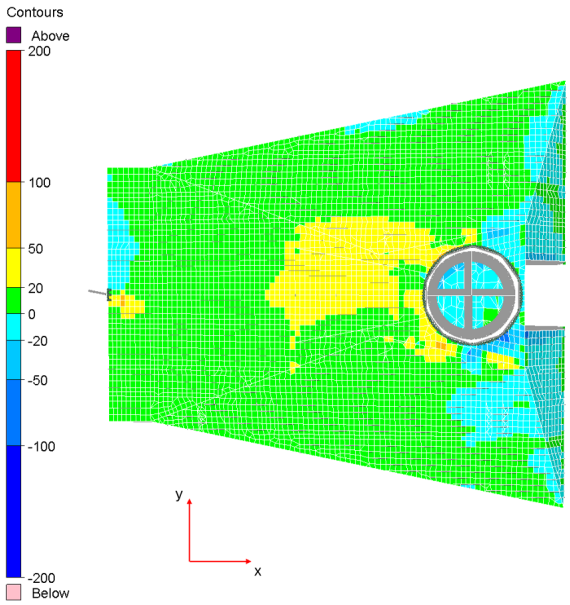

(a) Stress σ_x [MPa].

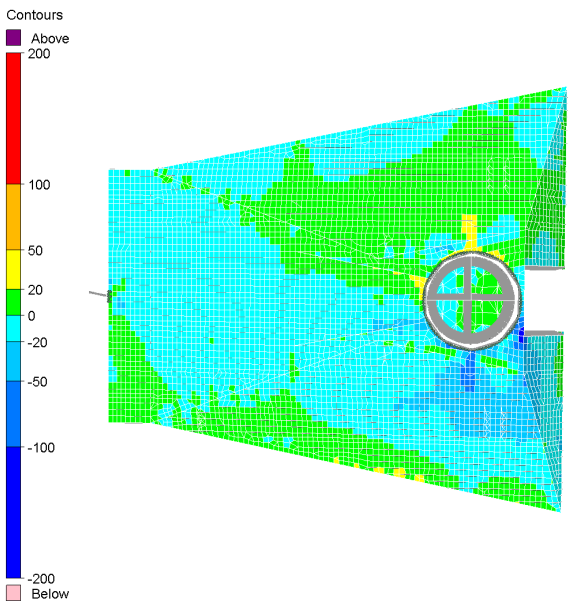

(b) Stress σ_y [MPa].

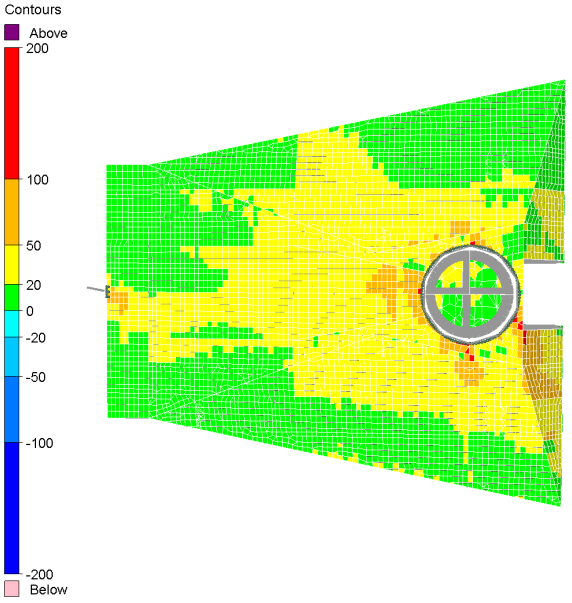

(c) Stress $\sigma_{vonMises}$ [MPa].

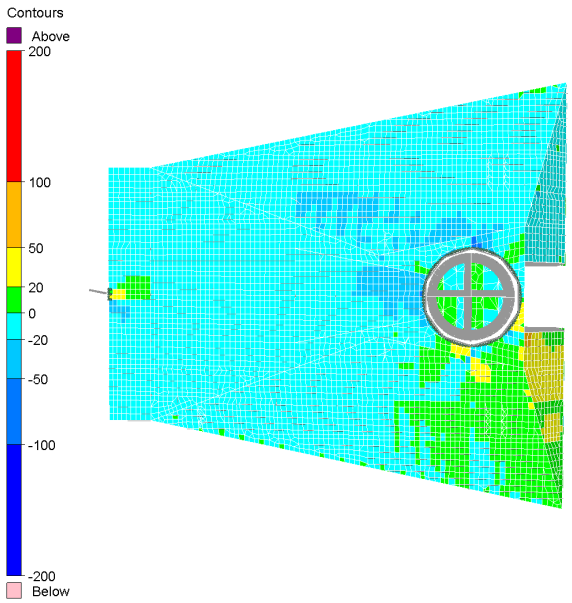

(d) Stress τ_{xy} [MPa].

Figure 54: Stress field for ULS DLC A (U_w=10.5 m/s, no wind/wave misalignment) at the timing of maximum moment M_x (t = 508 s).

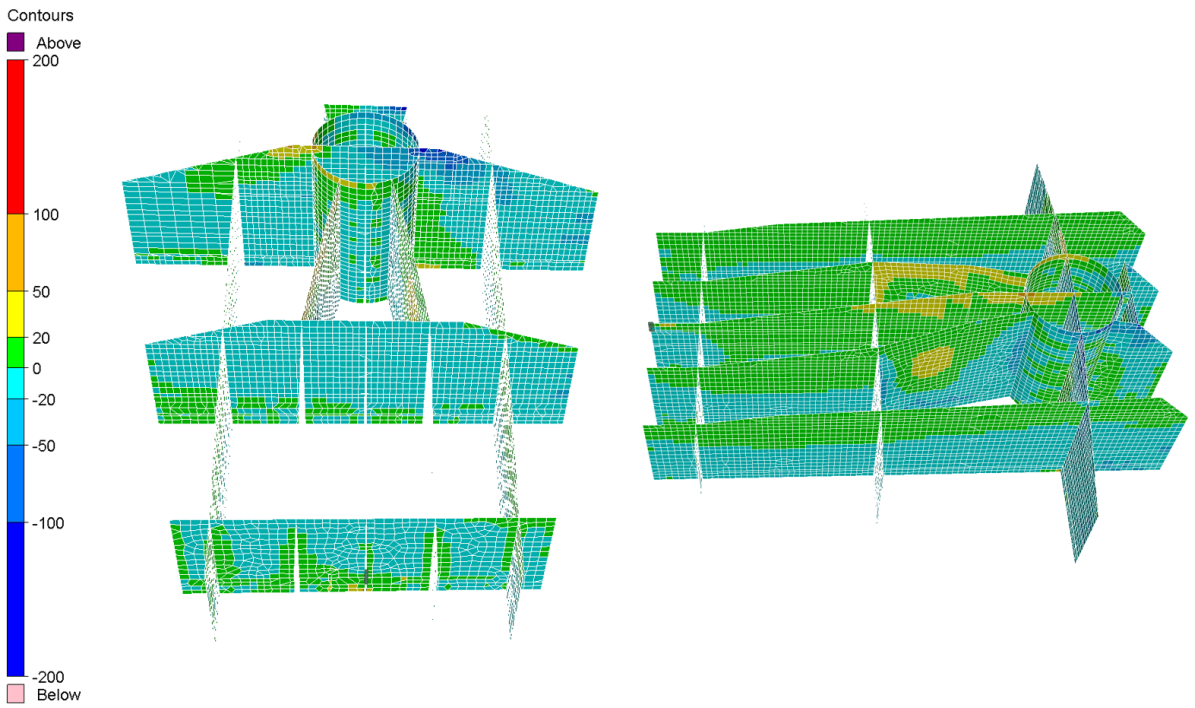

(a) Stress σ_x [MPa].

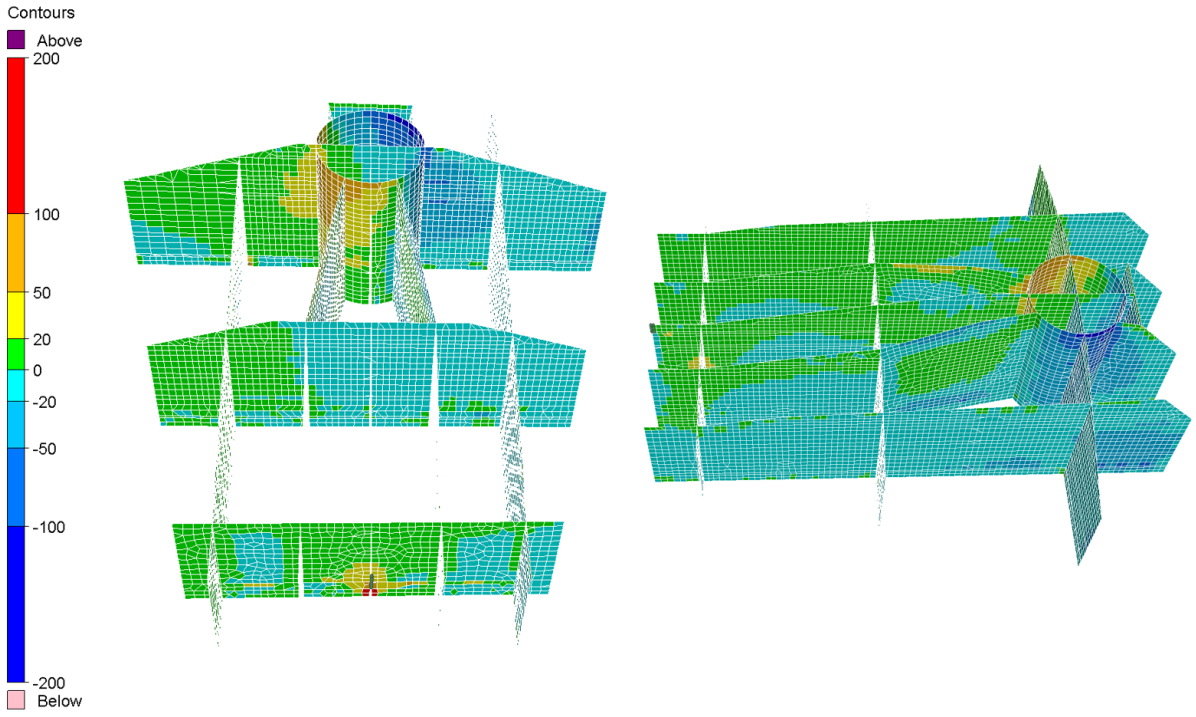

(b) Stress σ_y [MPa].

Figure 55: Stress field (σ_x, σ_y) of the internal structure for ULS DLC A (U_w=10.5 m/s, no wind/wave misalignment) at the timing of maximum moment M_x (t = 508 s).

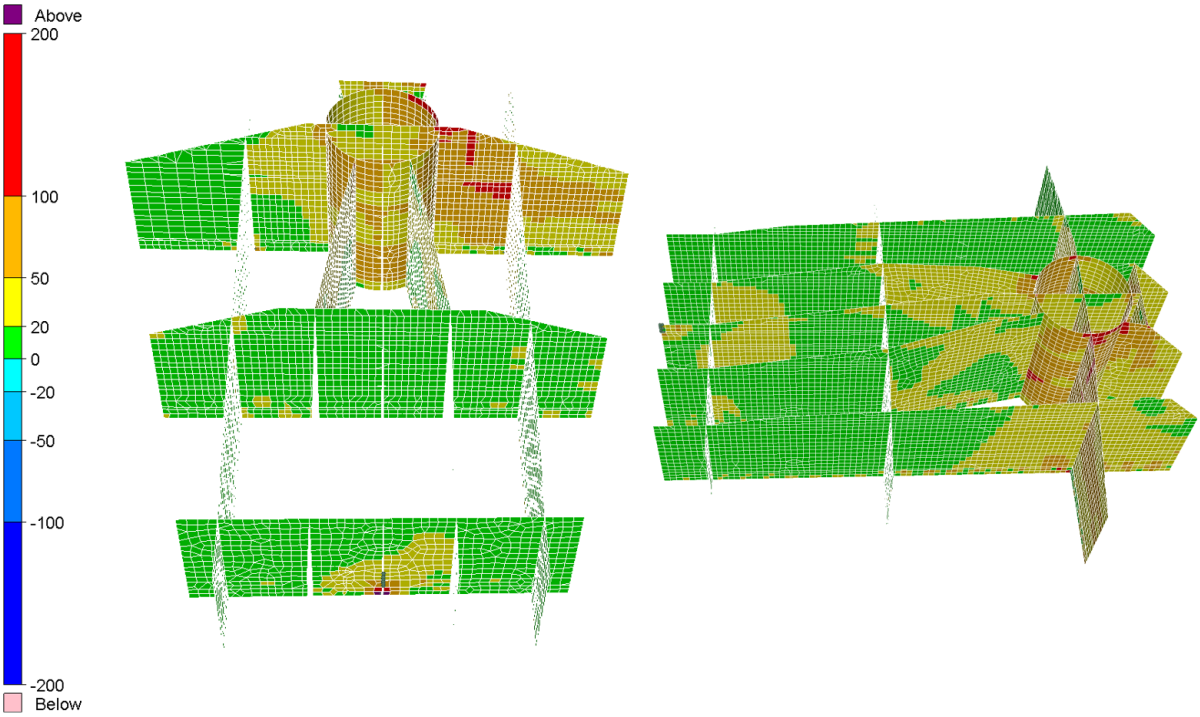

(a) Stress σ_{vonMises} [MPa].

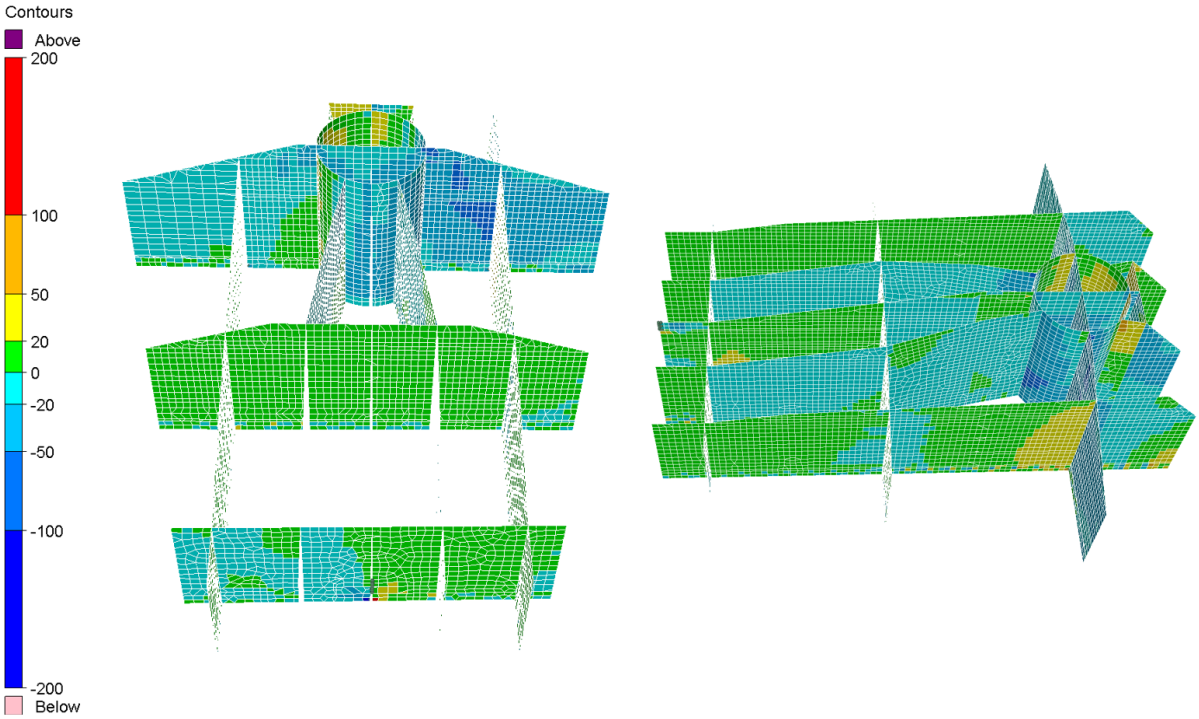

(b) Stress τ_{xy} [MPa].

Figure 56: Stress field ($\sigma_{\text{vonMises}}, \tau_{\text{xy}}$) of the internal structure for ULS DLC A (U_{w}=10.5 m/s, no wind/wave misalignment) at the timing of maximum moment M_{x} (t = 508 s).

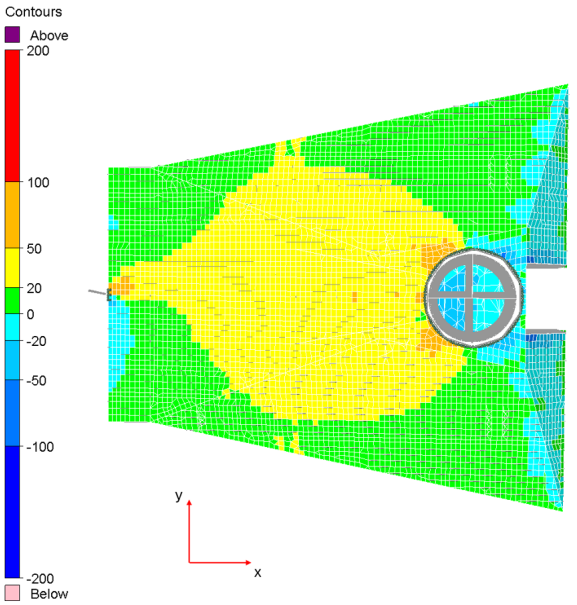

(a) Stress σ_x [MPa].

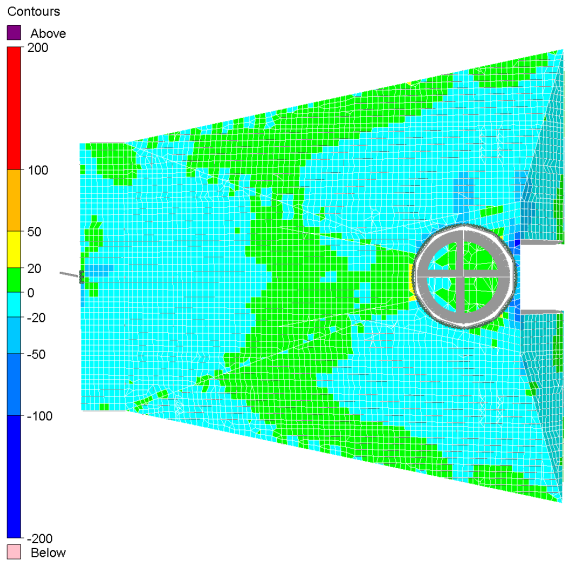

(b) Stress σ_y [MPa].

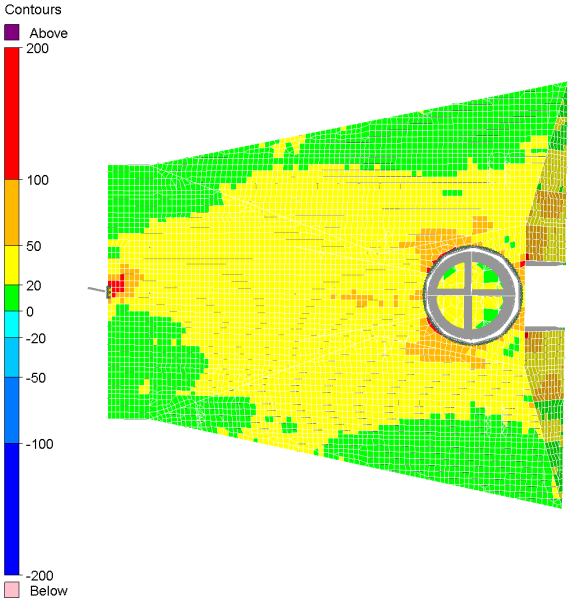

(c) Stress $\sigma_{vonMises}$ [MPa].

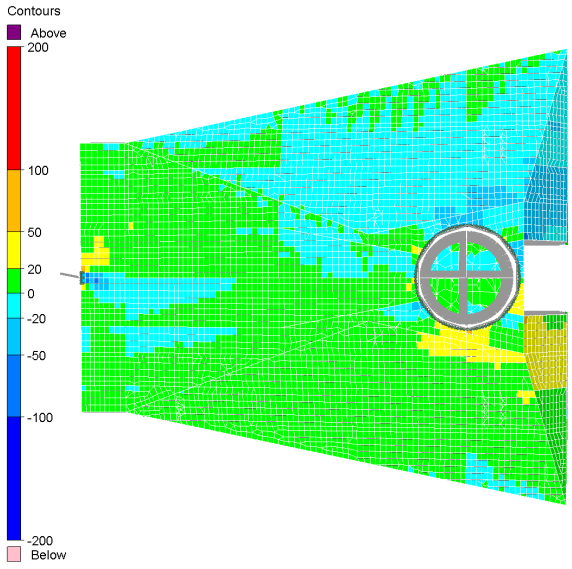

(d) Stress τ_{xy} [MPa].

Figure 57: Stress field for ULS DLC A (U_w=10.5 m/s, no wind/wave misalignment) at the timing of maximum moment M_y (t = 1477 s).

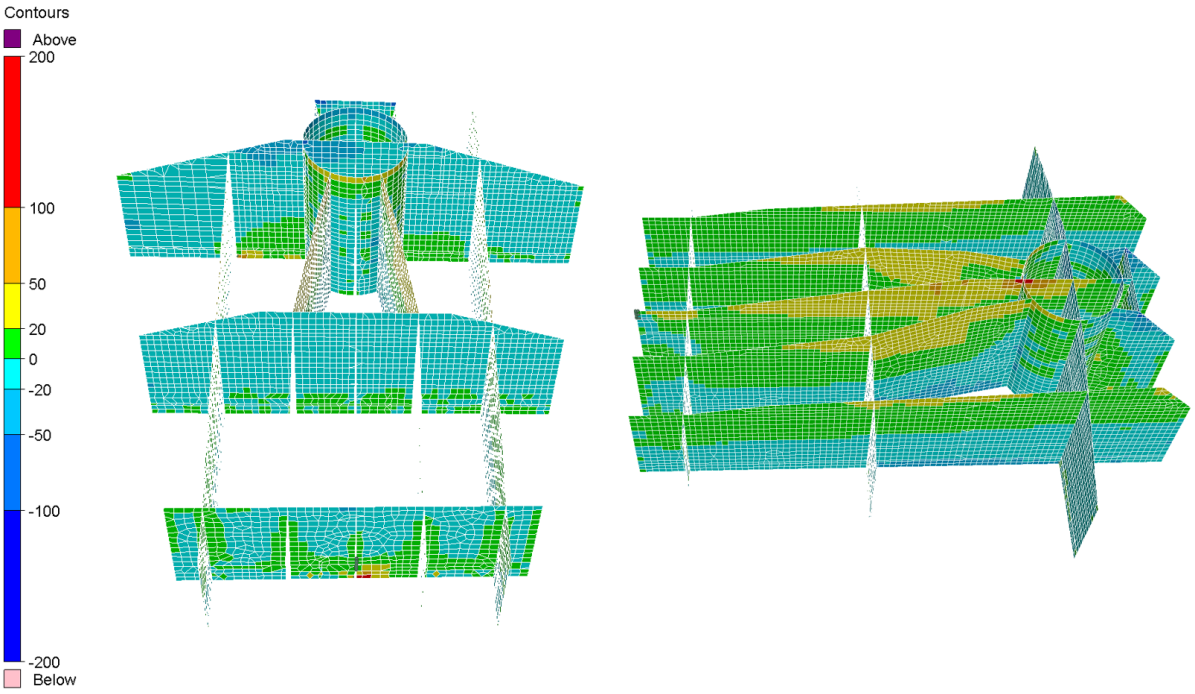

(a) Stress σ_x [MPa].

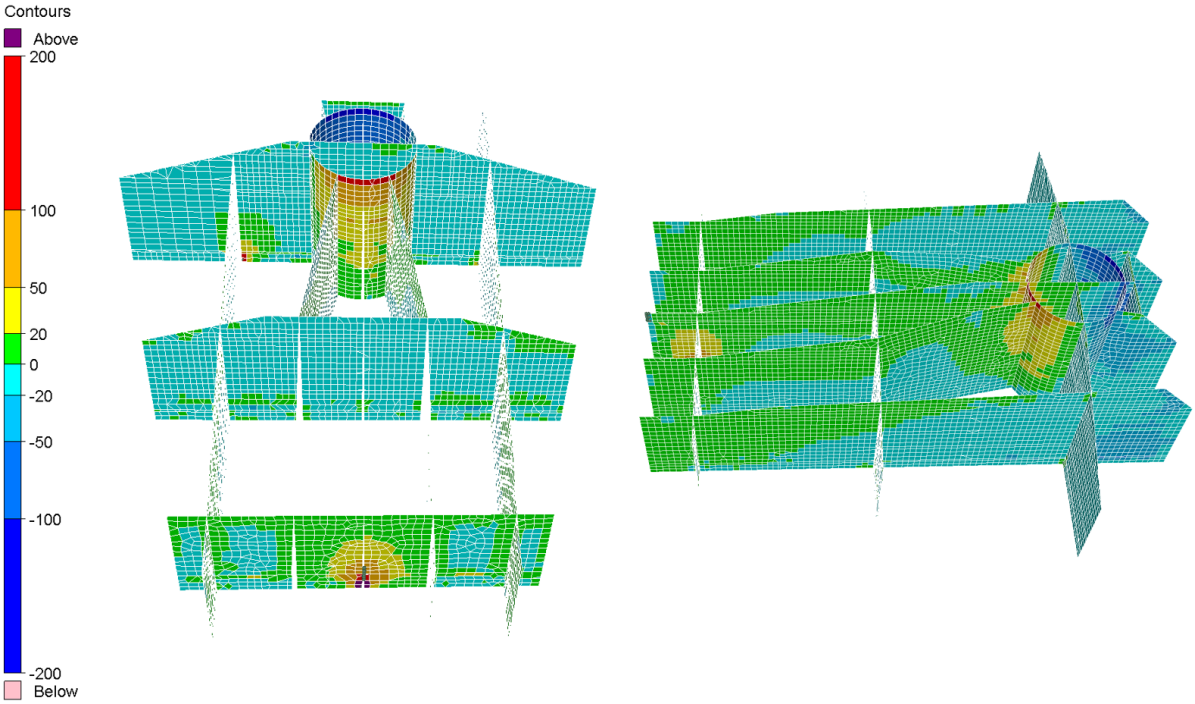

(b) Stress σ_y [MPa].

Figure 58: Stress field (σ_x, σ_y) of the internal structure for ULS DLC A (U_w=10.5 m/s, no wind/wave misalignment) at the timing of maximum moment M_y (t = 1477 s).

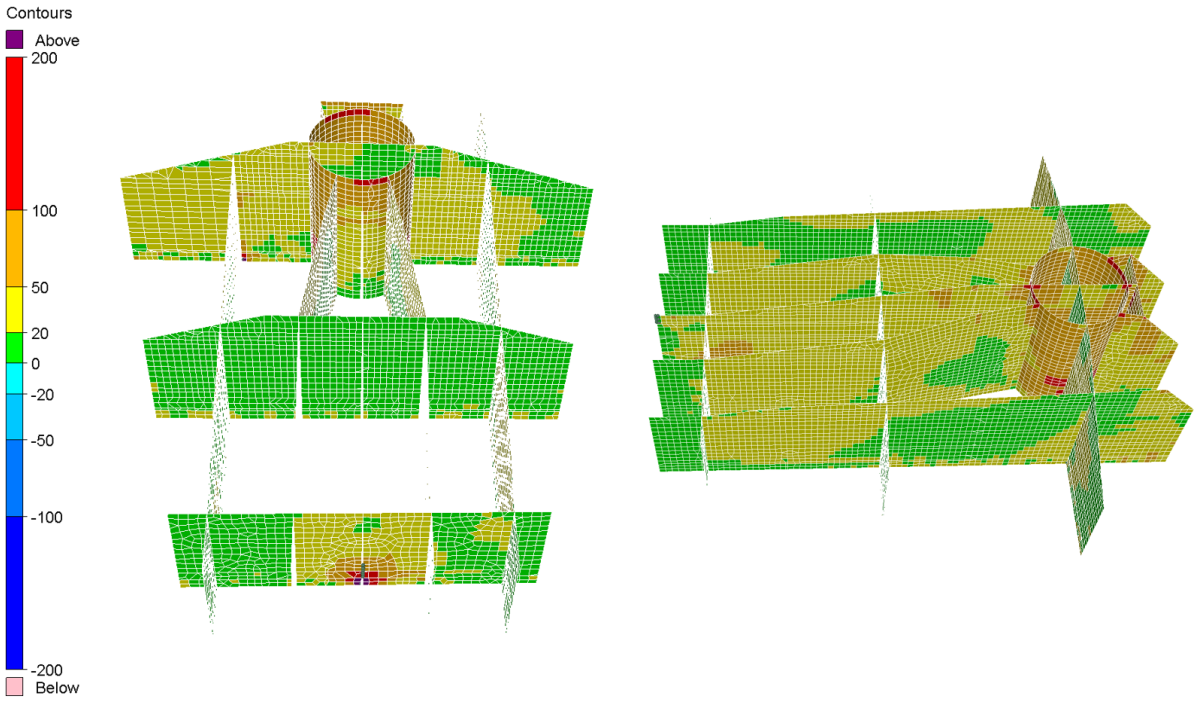

(a) Stress σ_{vonMises} [MPa].

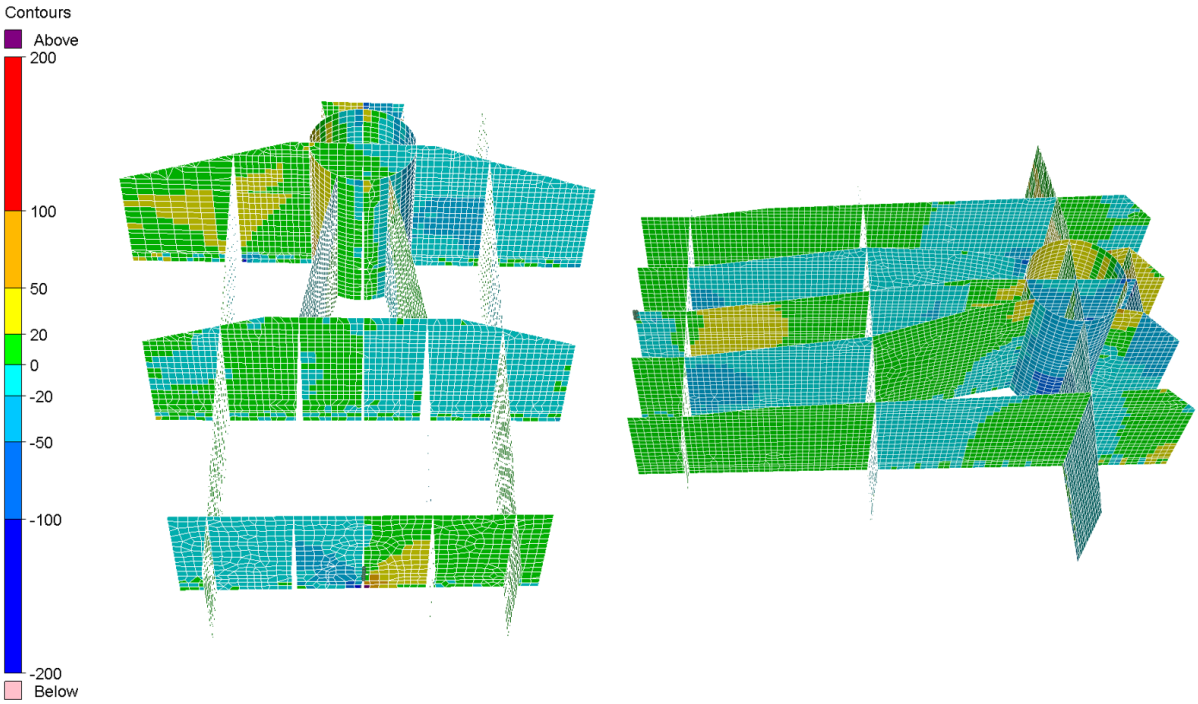

(b) Stress τ_{xy} [MPa].

Figure 59: Stress field ($\sigma_{\text{vonMises}}, \tau_{\text{xy}}$) of the internal structure for ULS DLC A (U_{w}=10.5 m/s, no wind/wave misalignment) at the timing of maximum moment M_{y} (t = 1477 s).

4.1.3 Statistical analysis of stress time series

Selected elements among bulkheads A, C, and H are compared regarding their normalized mean von Mises stress and standard deviation in Figure 60 and Figure 61. The maximum von Mises stress of element A1 in ULS DLC E is used to normalize the stresses in all time series. In general, the maximum von Mises stress is below the yield strength, assuming the steel S355.

By comparing the ULS DLCs A, B, and C, it is seen that in all cases the highest stresses are in the port side of bulkhead H (elements H4 and H8) rather than the starboard side, and that they are even higher than the longitudinal bulkhead A. This is strongly related to the positive moment Mx and negative force Fy resulting from the rotating wind turbine. At the rated wind speed (ULS DLC A and B), the stress levels are slightly higher than at the wind speed of $U_w = 24.5$ m/s (ULS DLC C). The difference between considering the wind/wave misalignment (ULS DLC B) and not (ULS DLC A) is minimal regarding the ultimate limit state study. The ULS DLC D is excluded in the graphs as similar results with ULS DLC C are expected.

By comparing the ULS DLC A, in which the wind turbine is operating, with the ULS DLCs E and F, where the wind turbine is stopped and the blades are feathered due to an extreme wind speed, the stress level and the standard deviation of the port side of bulkhead H is significantly reduced. On the other hand, they are increased on the starboard side of bulkhead H. The smaller stress level can be attributed to the non-rotating wind turbine, and therefore, a smaller magnitude of the moment Mx. The mean stresses in bulkhead A and C are in general increased and the standard deviation is also higher, due to the pitch motion of the floater in this extreme case.

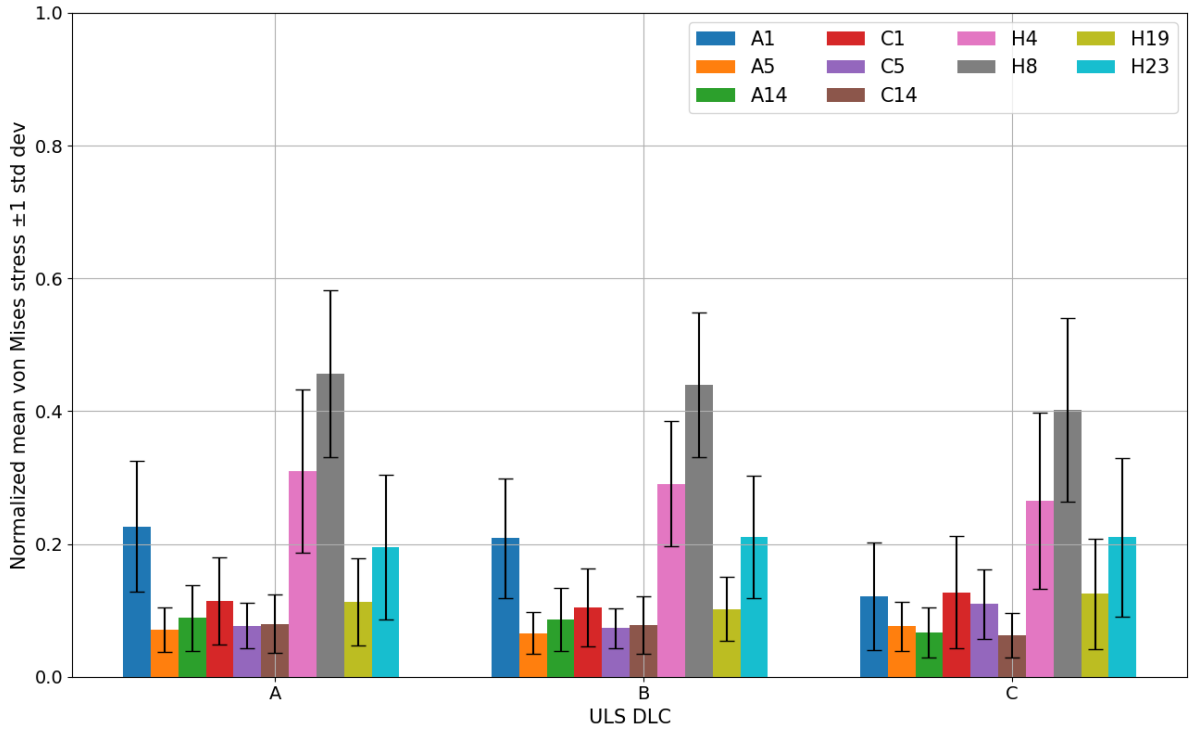

Figure 60: Mean normalized von Mises stress and standard deviation for selected shell elements at the bulkheads of the internal structure for ULS DLC A, B, and C.

The normalized von Mises time series for ULS DLC A is presented for two shell elements (A1 and C1) in Figure 62. For the shell element A1, it is observed that the maximum stress is not at the timing of the maximum bending moments M_x and M_y, at t=508 s and t=1477 s respectively, as it is for the shell element C1, where the maximum stress is at t=1477 s. Therefore, it is concluded that it is necessary to run the structural analysis for the whole time series rather than only at the timing of the maximum bending moments, as the combination of all the external loads may lead to an increased stress magnitude at another timing and for some location in the structure.

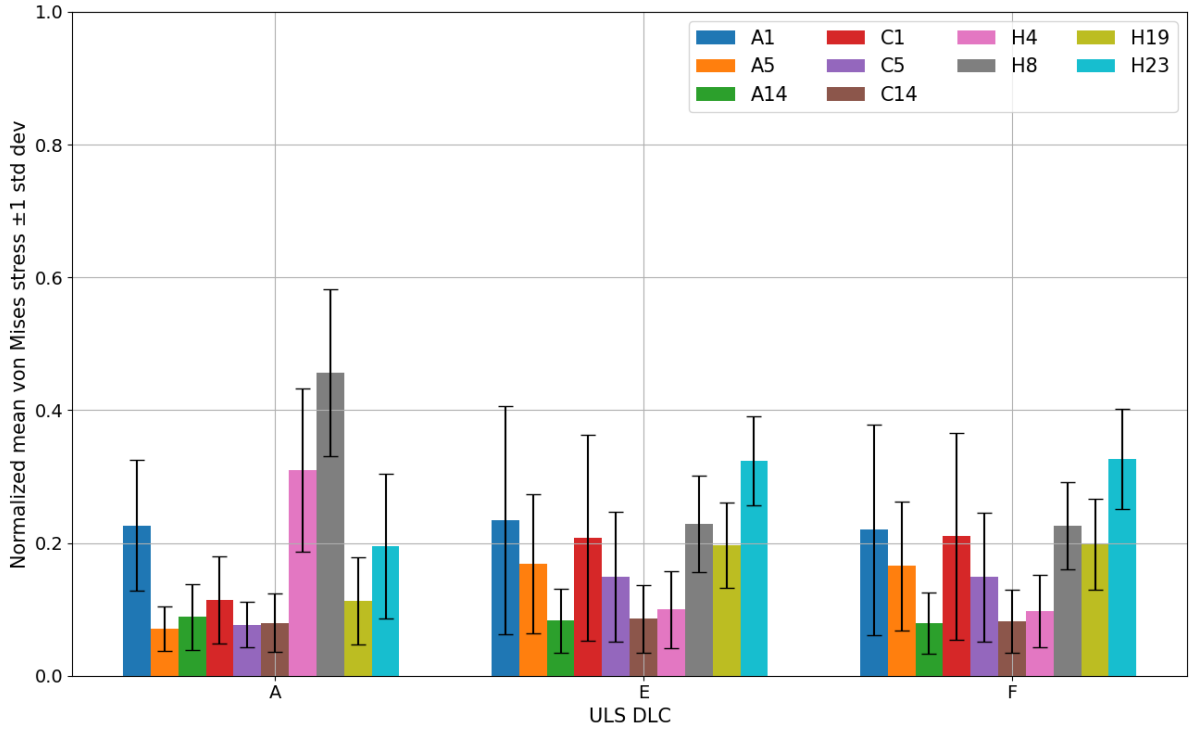

Figure 61: Mean normalized von Mises stress and standard deviation for selected shell elements at the bulkheads of the internal structure for ULS DLC A, E, and F.

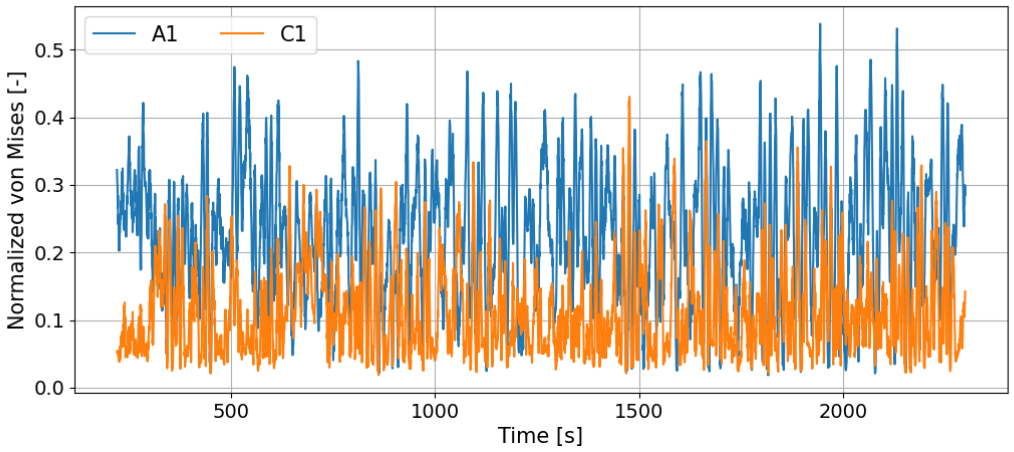

Figure 62: Mean normalized von Mises stress for shell elements A1 and C1 and for ULS DLC A.

The effect of the addition of bulkheads in the lateral direction of the floater is studied in Figure 63 and Figure 64 for ULS DLC A. The stress levels in bulkhead A remain the same, but in bulkhead H, they are decreased on both sides, as well as the standard deviation.

By comparing the stress levels among the added bulkheads, it is seen that the highest levels are experienced by bulkhead R on the port side of the floater. However, they are smaller than the initial configuration with only bulkhead H. Moreover, the standard deviation is smaller in the new design.

In conclusion, in an operating wind turbine, the port side is more loaded than the starboard and bow side of the floater. In extreme cases, when the wind turbine is stopped, the starboard side is loaded more. The closer to the tower, the higher the stress levels, but the further away (e.g., towards the bow), the stress levels are reduced. By adding more bulkheads, it is concluded that the ones towards the port

and stern side of the floater are more loaded, which is related to the positive mean moments M_x and M_y and the negative and positive forces F_y and F_x, respectively.

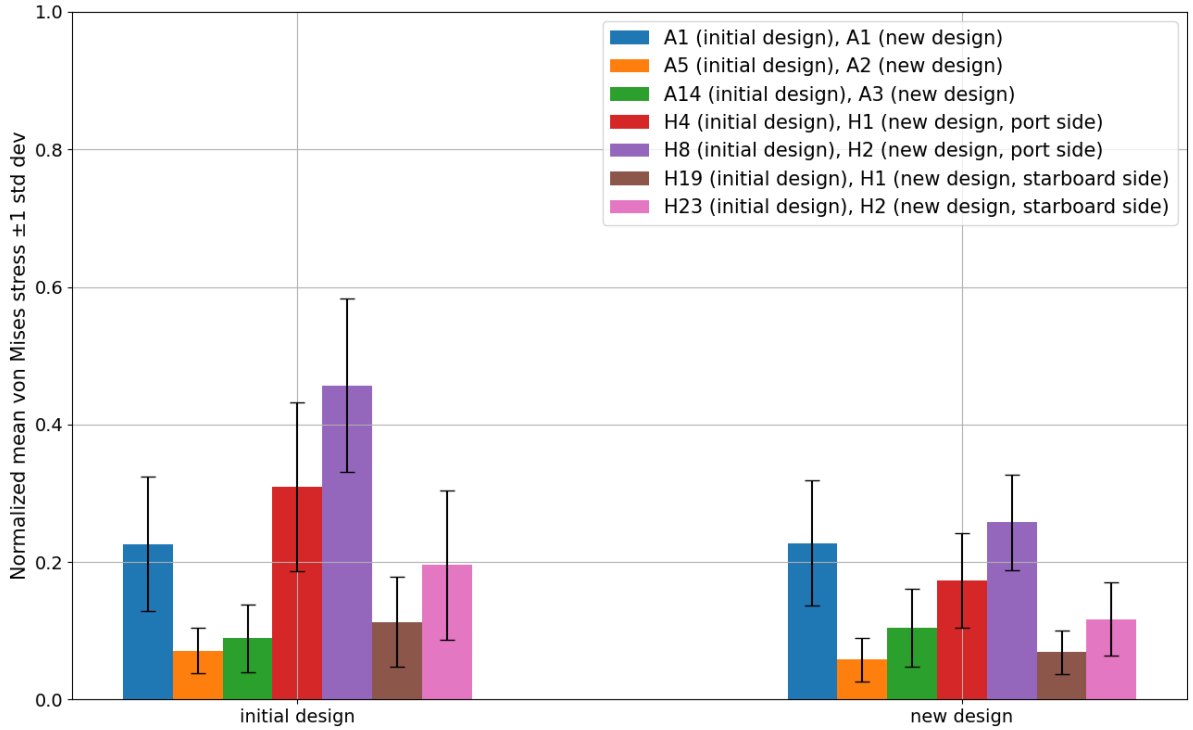

Figure 63: Mean normalized von Mises stress and standard deviation for selected shell elements at bulkheads A and H for ULS DLC A in the initial and the new design.

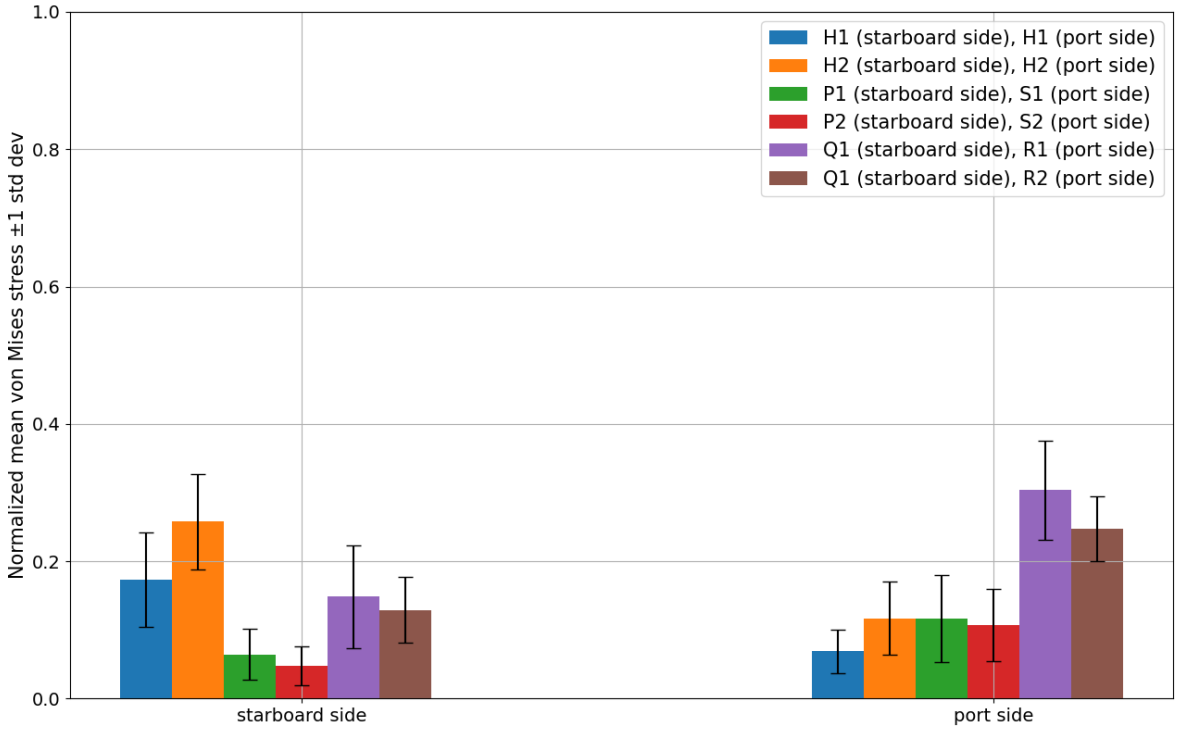

Figure 64: Mean normalized von Mises stress and standard deviation for selected shell elements at bulkheads H, P, Q, R, and S for ULS DLC A at the starboard and port side of the new design.

4.1.4 Power spectral density of stress time series

Apart from the statistical analysis of the stress time series, it is also important to identify dominating frequencies in the response. Welch's method is used from the scipy library in Python to calculate the power spectral density (PSD) of the signal by dividing it into overlapping segments, then computing the periodogram and averaging [79].

In the following figures, the power spectral density of the signal is presented for selected elements and ULS DLCs. The pitch and roll eigenfrequency of the floater, the tower bending eigenfrequency in y- and x-axis, the 1P, 3P, and 6P regions, and the wave peak frequency of the simulated wave environment are also presented to identify any correlations.

In Figure 65 and Figure 66, the PSD of different elements across bulkhead A and C is presented for ULS DLC A. The dominating frequencies are the roll eigenfrequency and the wave peak frequency. The presence of the roll eigenfrequency shows that there is some roll motion and that even though bulkheads A and C are not in a lateral direction inside the floater, the fluctuating stress of this period is still depicted in them. Moreover, the closer to the tower, the larger the power spectral density, meaning that more energy is present closer to the tower in all frequencies. The wave frequency is also appearing, as the main direction of the waves matches the longitudinal direction of the examined bulkheads. The pitch eigenfrequency is not appearing, as it is not excited significantly.

In Figure 67 and Figure 68, the PSD of different elements across bulkhead H is presented for ULS DLC A. The roll eigenfrequency is more dominant than in bulkheads A and C, as bulkhead H is in the lateral direction. The wave peak frequency is still present, but it has a lower energy than in the previously examined bulkheads. There is also a peak between the two tower bending eigenfrequencies, but their frequency is high compared to the other important frequencies.

In Figure 69 and Figure 70, the rest of the ULS DLCs are studied for elements A1 and H4. The roll eigenfrequency becomes less dominant in ULS DLC B compared to ULS DLC A as there is a wind/wave misalignment, but the difference is small. For the higher wind speed at ULS DLC C, the pattern seems to be very similar. For ULS DLC E and F, the pitch eigenfrequency is more dominant due to the extreme wind speed. In element H4, a peak is also seen at a frequency lower than the roll eigenfrequency, which may be related to a surge eigenfrequency that is generally difficult to calculate due to its dependency on the pretension.

In conclusion, it is seen that the emerging frequencies are related to the eigenfrequencies of the floater and the wave environment. The roll eigenfrequency is more dominant in operating conditions, where the pitch eigenfrequency is more apparent in an extreme load case where the wind turbine is stopped. The outcomes are mainly related to the specific concept examined and with the current controllers implemented, but similar results are expected to other concepts as well, with less or more dominating frequency components.

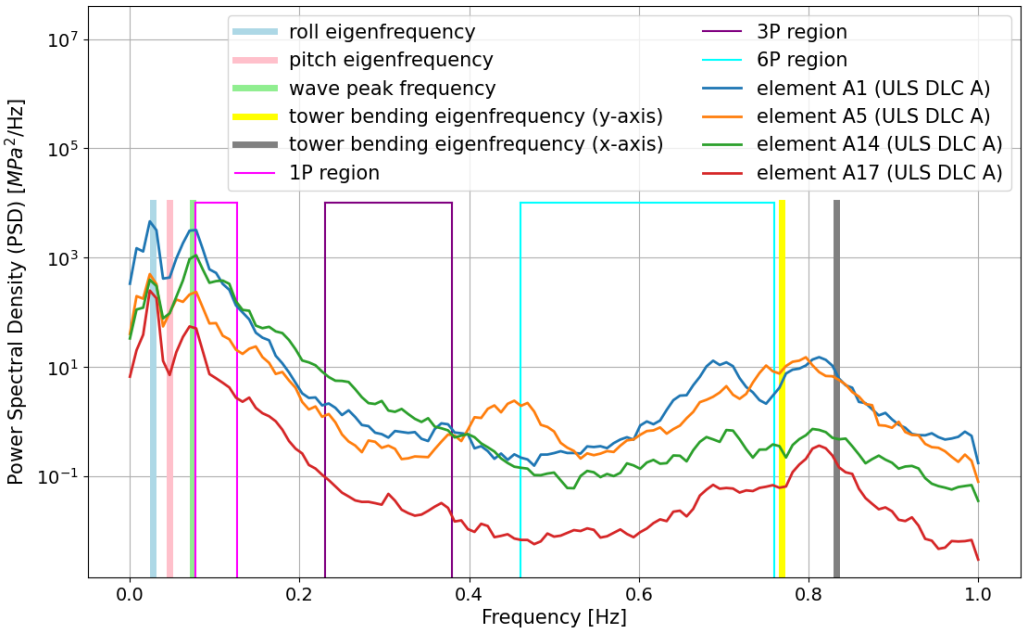

Figure 65: Power spectral density (PSD) of element von Mises stress in bulkhead A for ULS DLC A in combination with the eigenfrequency of pitch and roll, the wave peak frequency, the tower bending eigenfrequency over the y-axis and x-axis, and the 1P, 3P, and 6P regions.

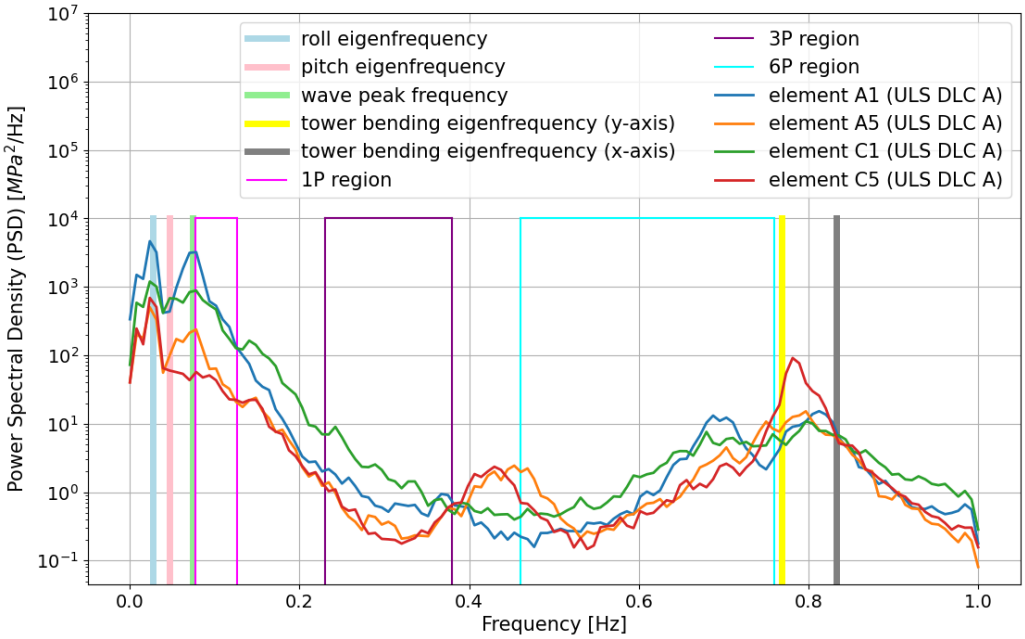

Figure 66: Power spectral density (PSD) of element von Mises stress in bulkheads A and C for ULS DLC A in combination with the eigenfrequency of pitch and roll, the wave peak frequency, the tower bending eigenfrequency over the y-axis and x-axis, and the 1P, 3P, and 6P regions.

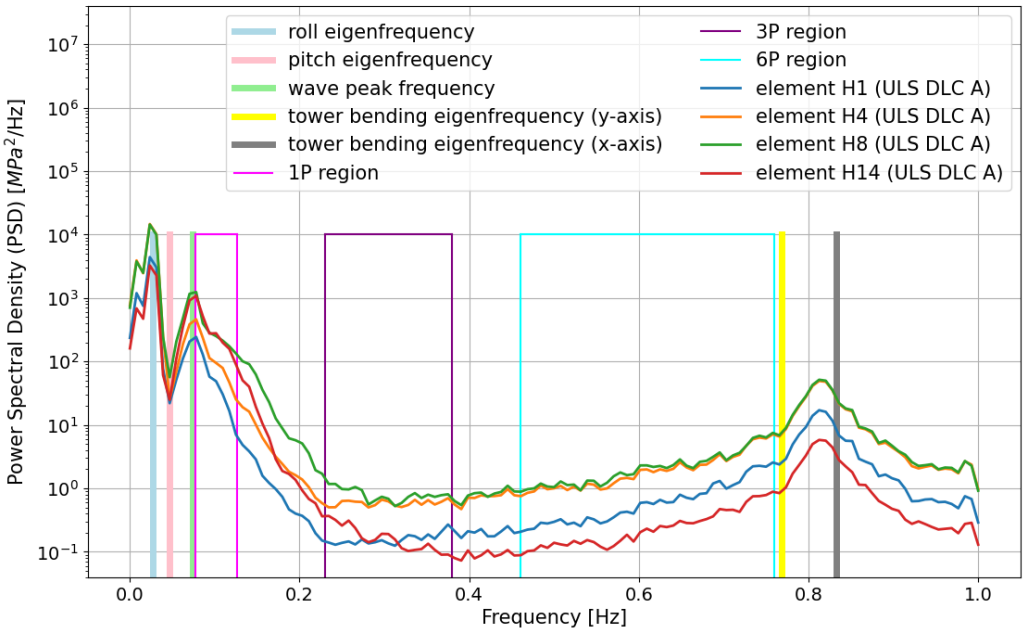

Figure 67: Power spectral density (PSD) of element von Mises stress in bulkhead H at the port side for ULS DLC A in combination with the eigenfrequency of pitch and roll, the wave peak frequency, the tower bending eigenfrequency over the y-axis and x-axis, and the 1P, 3P, and 6P regions.

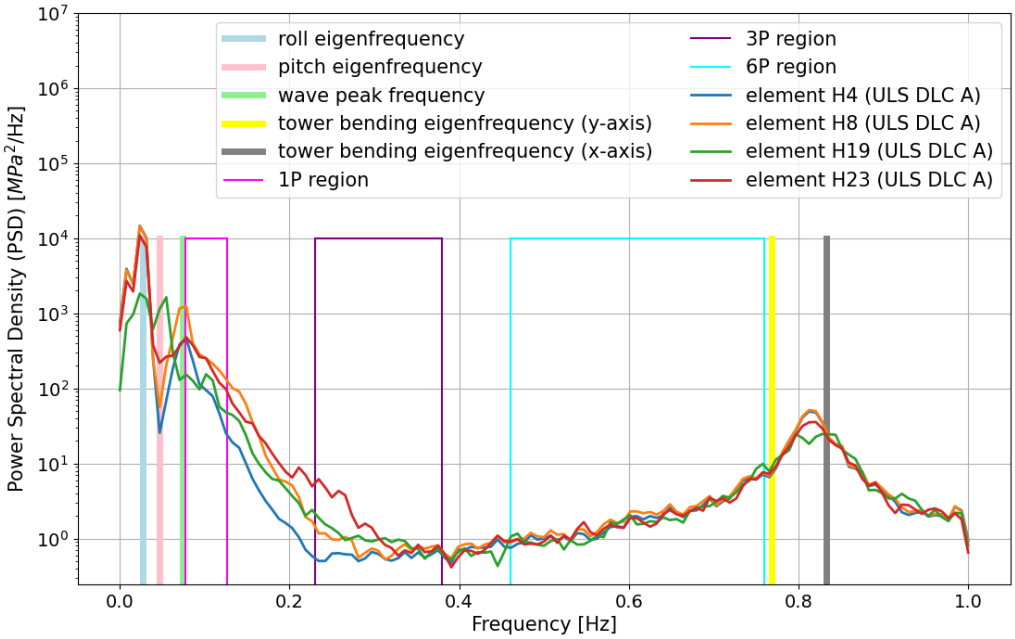

Figure 68: Power spectral density (PSD) of element von Mises stress in bulkhead H for ULS DLC A in combination with the eigenfrequency of pitch and roll, the wave peak frequency, the tower bending eigenfrequency over the y-axis and x-axis, and the 1P, 3P, and 6P regions.

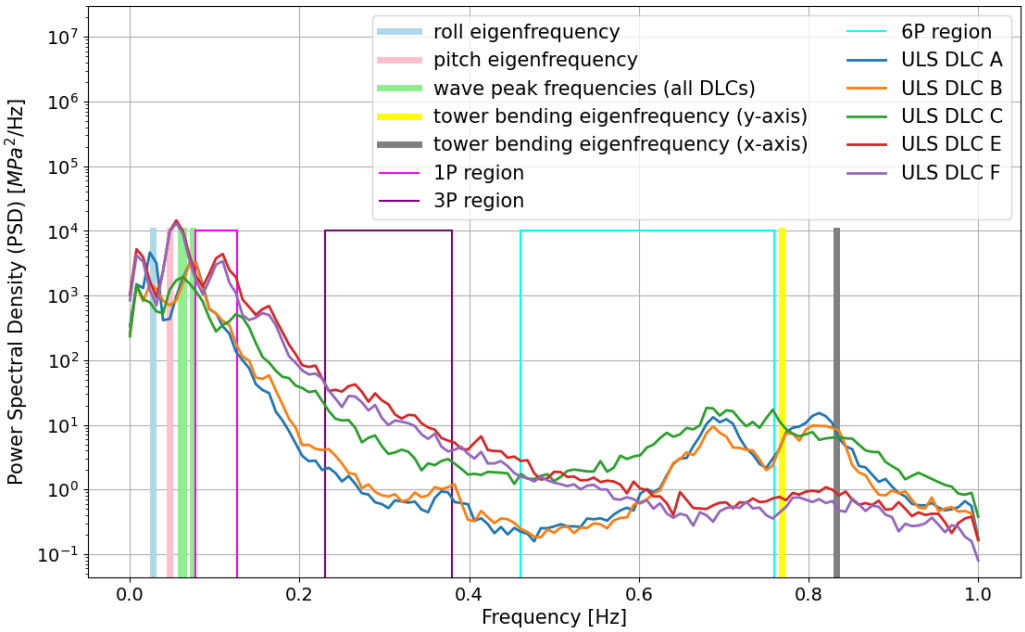

Figure 69: Power spectral density (PSD) of von Mises stress for element A1 and for different ULS DLCs in combination with the eigenfrequency of pitch and roll, the wave peak frequency, the tower bending eigenfrequency over the y-axis and x-axis, and the 1P, 3P, and 6P regions.

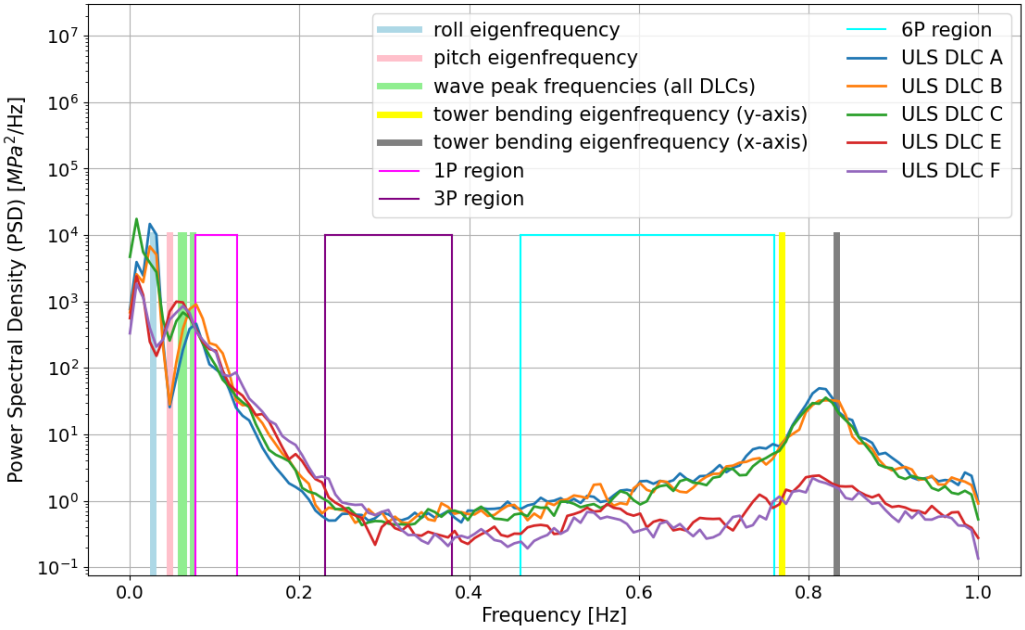

Figure 70: Power spectral density (PSD) of von Mises stress for element H4 and for different ULS DLCs in combination with the eigenfrequency of pitch and roll, the wave peak frequency, the tower bending eigenfrequency over the y-axis and x-axis, and the 1P, 3P, and 6P regions.

4.1.5 Contribution of waves and motions

The incoming waves and the wind with the rotating wind turbine induce the motions of the floater. These motions generate an additional pressure due to the radiation. A study was carried out to investigate the effect of the incoming waves and motions on the stress response of the barge.

In Figure 71, the pressure on the WindBarge is displayed, with and without the pressure part induced by the floater motions and incoming waves. The red color indicates a higher pressure magnitude, and the blue color indicates zero pressure. In all simulations, the wind and mooring forces are included.

In Figure 71a (Wind/mooring + motions + waves), the WindBarge is floating, the free surface changes due to the incoming waves, and the motions of the floater are included. In Figure 71b (Wind/mooring + motions), the incoming waves are not modeled, therefore, the free surface is still, but the radiation due to the motions is calculated. In Figure 71c (Wind/mooring), the incoming waves and the motions are not included, therefore, only the hydrostatic pressure is present.

In the following figures, from Figure 72 to Figure 80, some example time series are presented for selected elements and ULS DLCs. The following conclusions are derived:

- The forces and moments from the wind turbine are the main contributors to the internal stresses of the barge and shape the resulting stress response, whereas the contribution from the motions and the incoming waves is minimal. Nevertheless, the waves are important in the analysis in SIMA for the global response of the barge, affecting both the motions and the loads from the wind turbine indirectly.
- At the barge, near the tower base and all around its circumference (elements A1 and H4), there is a good agreement on the stress response even when the motions and incoming waves are not considered. Therefore, it is concluded that when a study focuses near the tower base, where higher stresses are seen, a simple structural analysis outside the sea environment and for a constrained barge at the bottom of the structure can be used. On the other hand, for a spar-type of floater, it is expected to be more critical to model the sea environment due to the direct contact of the tower with the water that induces the pressures.
- Further away from the tower base (elements A9 and A14), the effect of the waves and the motions are small; however, the further away from the tower (element A14), some more noticeable changes are seen. Therefore, there is a need for a complete analysis.
- For elements closer to the boundary conditions (element H5), a higher discrepancy is noted. When the motions of the barge are not accounted for, meaning that the floater is clamped, the constraining forces are increased and induce higher stresses around that location. This highlights the limitations of this modeling approach, at least when the floater motions are significant. Springs may be used alternatively at the boundary conditions to decrease their effect, even during the simulations with an oscillating body. For the ULS DLC E in Figure 80, a larger discrepancy is noted when modeling the motions without considering the waves.

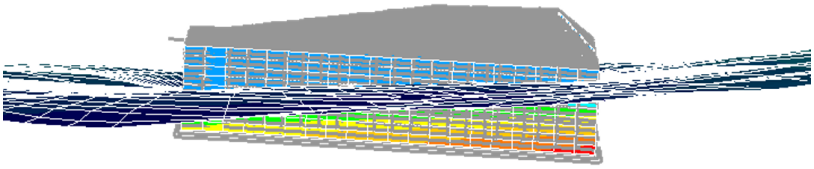

(a) Total dynamic pressure (with incoming waves and motions).

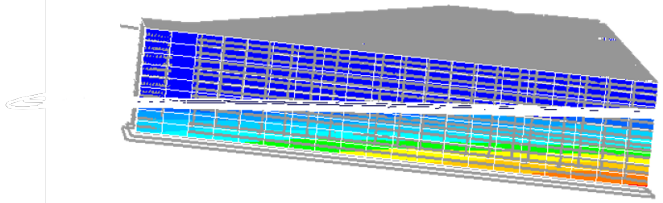

(b) Dynamic pressure without incoming waves.

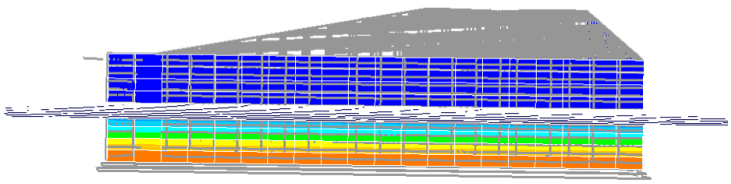

(c) Hydrostatic pressure only (no incoming waves or floater motions).

Figure 71: An example time series from the simulations with and without pressure induced by floater motions and incoming waves.

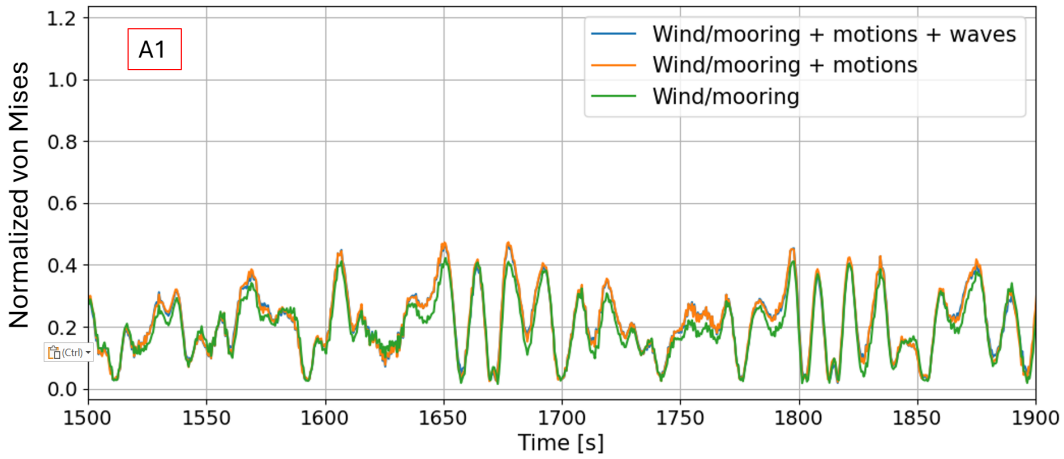

Figure 72: An example time series from ULS DLC A for element A1 with and without pressure induced by floater motions and incoming waves.

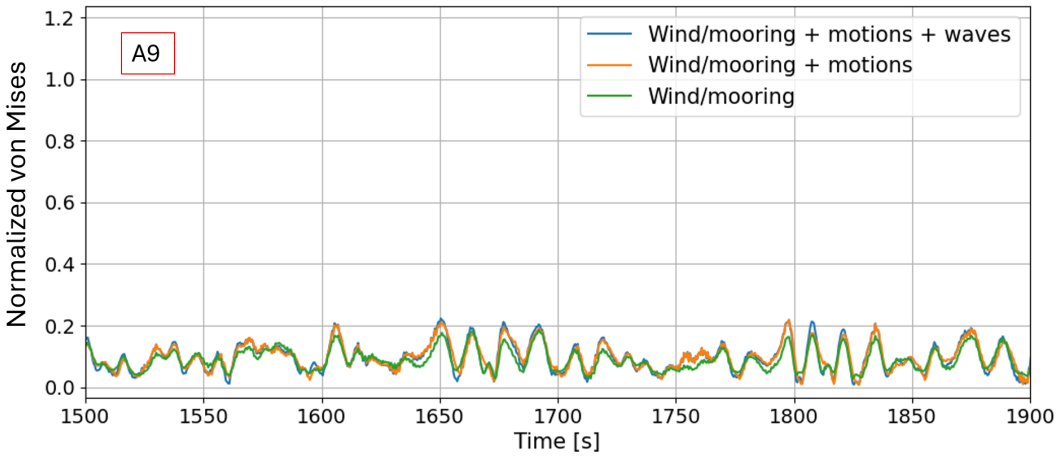

Figure 73: An example time series from ULS DLC A for element A9 with and without pressure induced by floater motions and incoming waves.

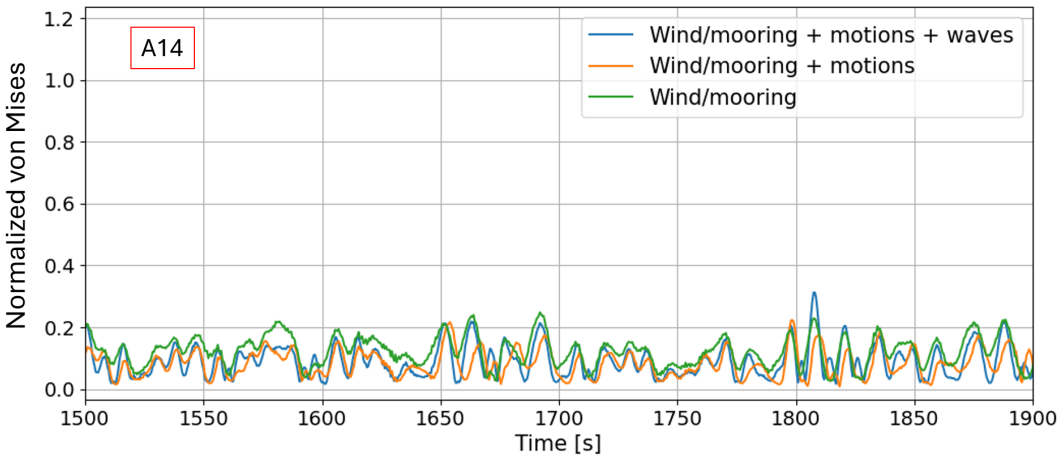

Figure 74: An example time series from ULS DLC A for element A14 with and without pressure induced by floater motions and incoming waves.

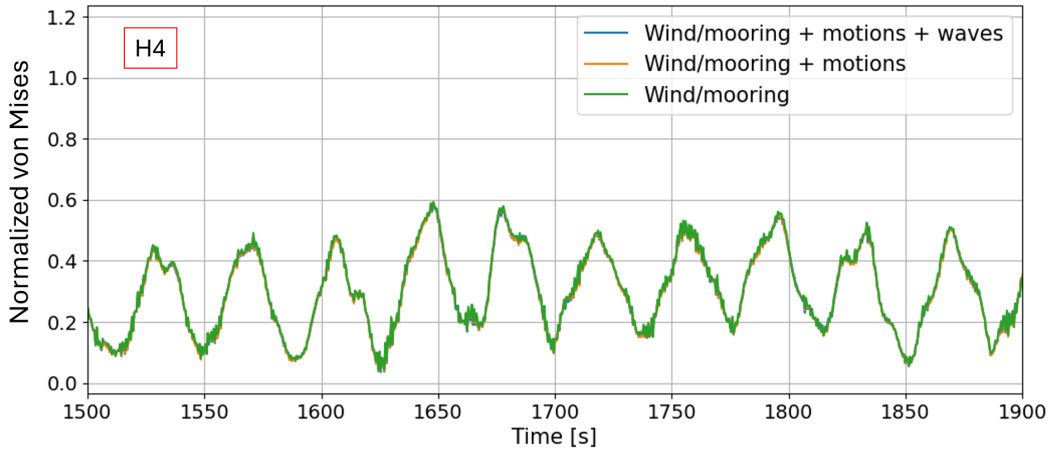

Figure 75: An example time series from ULS DLC A for element H4 with and without pressure induced by floater motions and incoming waves.

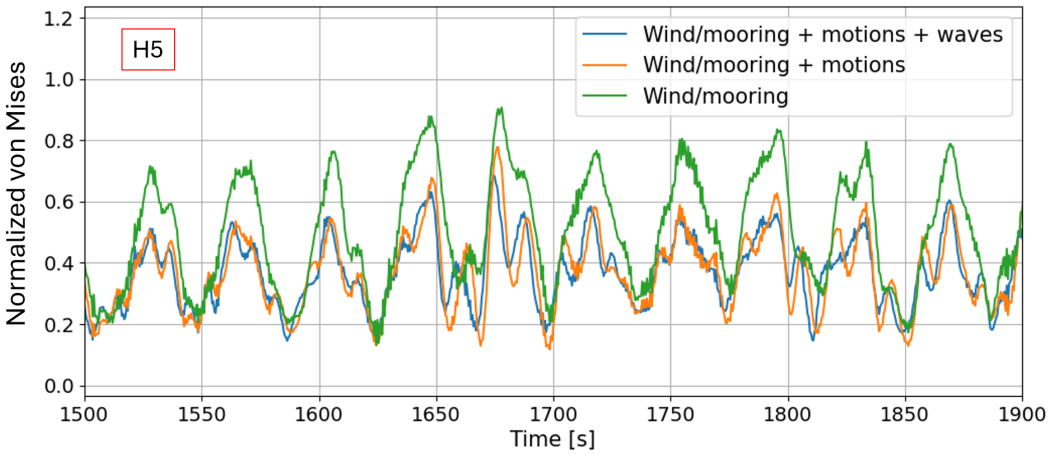

Figure 76: An example time series from ULS DLC A for element H5 with and without pressure induced by floater motions and incoming waves.

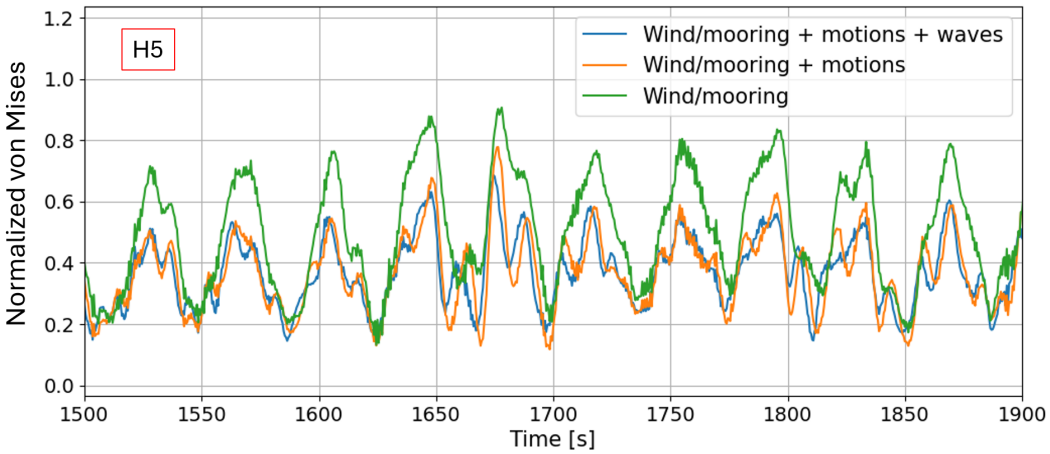

Figure 77: An example time series from ULS DLC A for element H5 with and without pressure induced by floater motions and incoming waves.

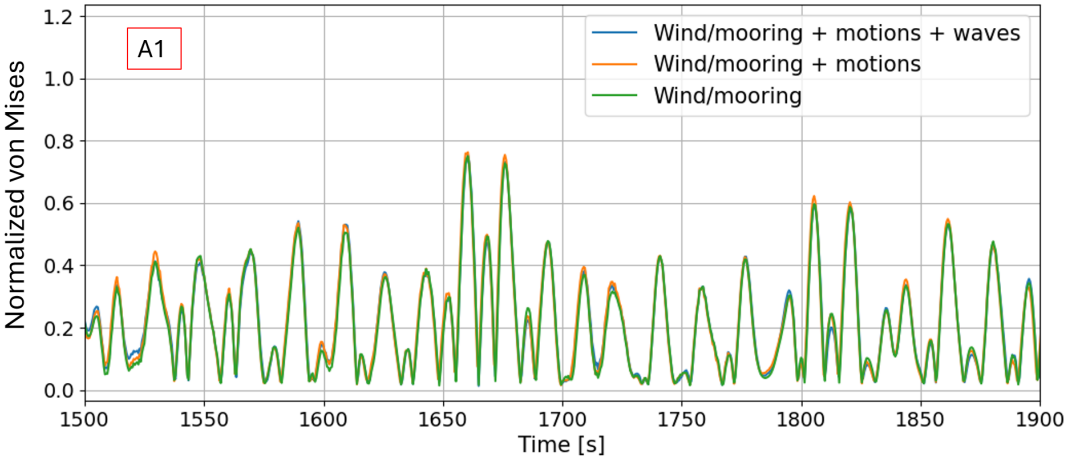

Figure 78: An example time series from ULS DLC E for element A1 with and without pressure induced by floater motions and incoming waves.

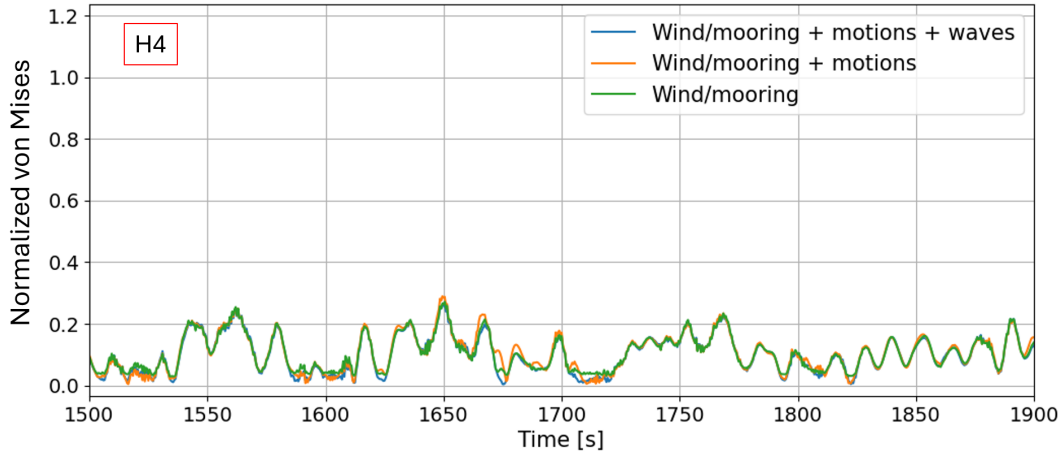

Figure 79: An example time series from ULS DLC E for element H4 with and without pressure induced by floater motions and incoming waves.

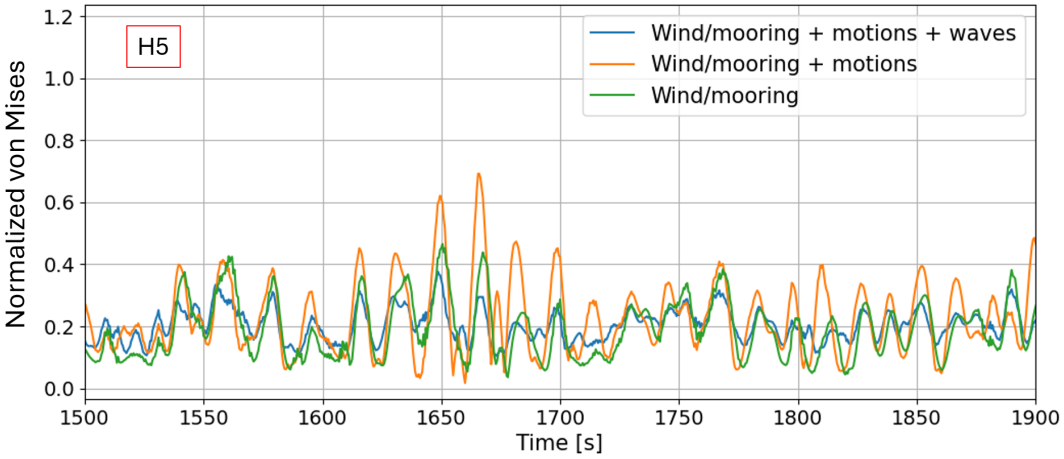

Figure 80: An example time series from ULS DLC E for element H5 with and without pressure induced by floater motions and incoming waves.

4.2 Fatigue Limit State (FLS) study for the tower transition region

4.2.1 Normalized nominal uniaxial fatigue damage

The fatigue damage is calculated based on the uniaxial stress for the seven FLS DLCs around the tower base, with and without the mean stress correction and the wind/wave misalignment. It is normalized with the maximum fatigue damage at $\theta = 90$ degrees and presented in Figure 81.

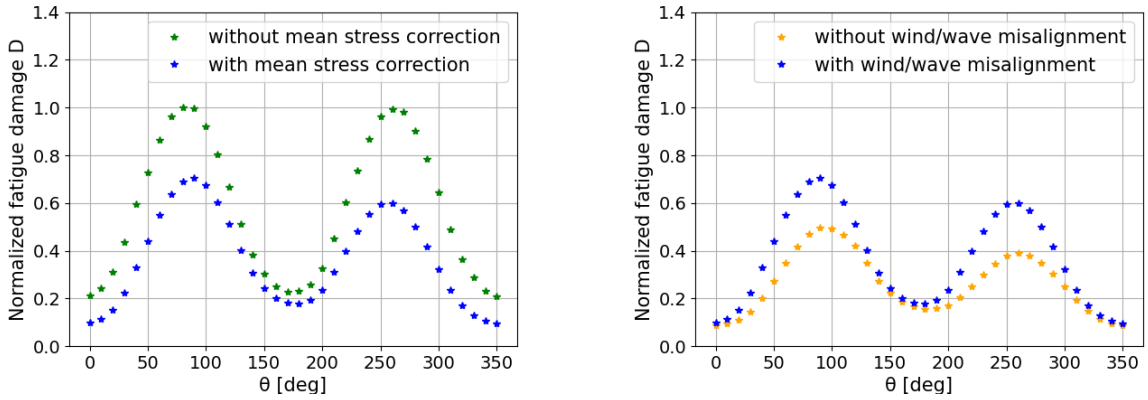

(a) Comparison with mean stress correction.

(b) Comparison with wind/wave misalignment.

Figure 81: Normalized fatigue damage D with and without mean stress correction, and with and without wind/wave misalignment consideration (including mean stress correction).

The fatigue damage varies significantly along the periphery of the tower base. The most critical locations are at $\theta = 90$ deg and $\theta = 270$ deg, which can be attributed to the roll motions (see section 4.2.2). Even though they are not large, they lead to higher fatigue damage at these locations. However, this difference can be reduced with an increased roll linear and quadratic damping, and yaw linear damping, as shown in Figure 82a. The roll and yaw damping can be increased with larger bilge keels and the inclusion of fins. Regarding fatigue life, the thickness of the tower should be increased by more than 20% for a service life of more than 20 years (Figure 82b), which is not required by the yield strength of the material; therefore, the overall design is fatigue-driven. However, this can be avoided with additional damping, advanced control, or a stiffer floater, as further discussed in Appendix E.

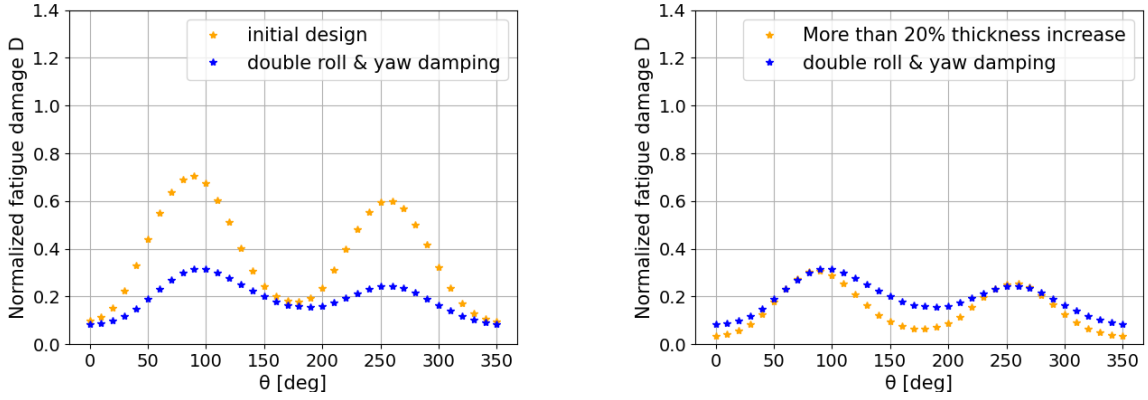

(a) Increased damping.

(b) Increased tower thickness.

Figure 82: Comparison of the normalized fatigue damage D with the initial damping and with double the roll linear, roll quadratic, and yaw linear damping, with wind/wave misalignment consideration and including mean stress correction.

Moreover, the mean stress correction factor seems to reduce the fatigue damage estimation, especially at the critical locations. Therefore, it is important to consider it even though it is often neglected in relevant studies. This reduction is because, most of the time, the tower is at compressive conditions. Interestingly, the fatigue damage at $\theta = 270$ deg is lower than at $\theta = 90$ deg, which can be attributed to the positive mean bending moment M_x and negative mean force F_y that lead to more compressive conditions at this side.

The normalized fatigue damage D for the different FLS DLCs, with and without their probability, is presented in Figure 83 for $\theta = 90$ deg and in Figure 84 for $\theta = 0$ deg. Apparently, the wind/wave misalignment induces a higher fatigue damage at $\theta = 90$ deg when the probability is also considered. This indicates the necessity to also account for the wind/wave misalignment when calculating the fatigue damage, even though the ULS study did not show a significant difference in the magnitude of the stress in the floater.

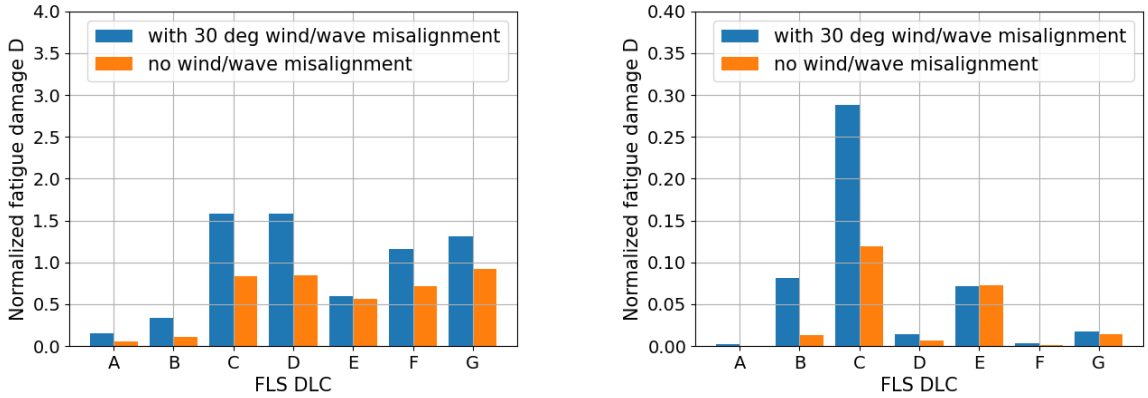

(a) Without the probability of each FLS DLC. (b) With the probability of each FLS DLC.

Figure 83: Normalized fatigue damage D at $\theta = 90$ deg for each FLS DLC.

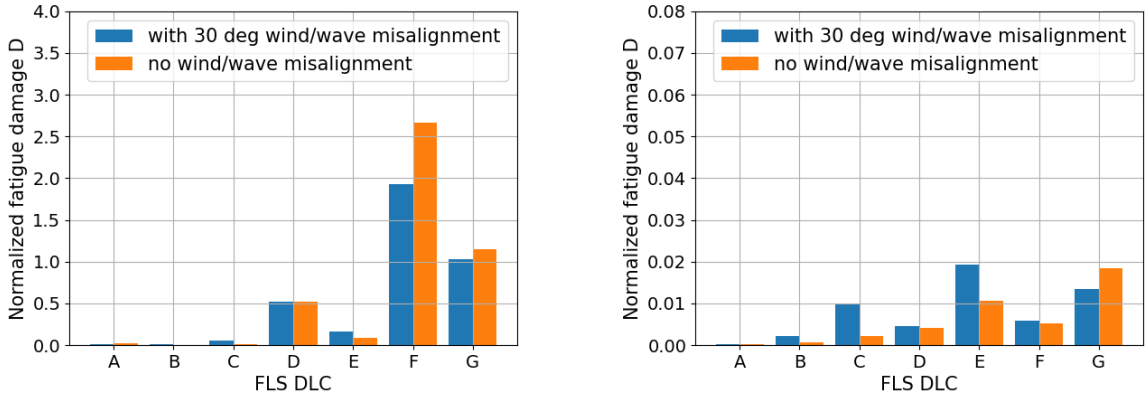

(a) Without the probability of each FLS DLC. (b) With the probability of each FLS DLC.

Figure 84: Fatigue damage D at $\theta = 0$ deg for each FLS DLC.

4.2.2 Uniaxial and shear stress

An example time series of the normalized uniaxial stress is shown in Figure 85 for FLS DLC D. The maximum von Mises stress of element A1 in ULS DLC E is used to normalize the uniaxial stress. The appearing period of the signal matches the roll eigenfrequency.

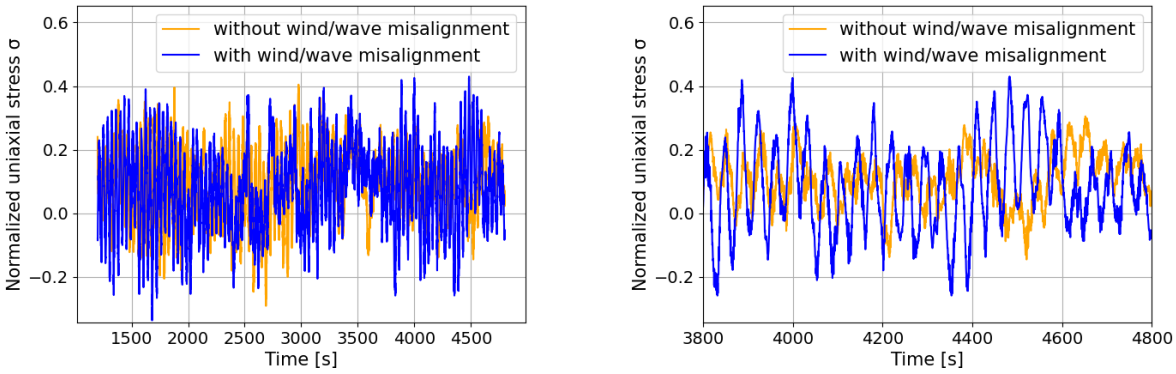

(a) 1-h time series.

(b) Time series from t = 3800 s to 4800 s.

Figure 85: Normalized uniaxial stress time series for mean wind speed $U_w = 10.5$ m/s at $\theta = 90$ degrees (FLS DLC D) with and without wind/wave misalignment consideration.

The power spectral density (PSD) of the calculated stress time series is presented in Figure 86 and Figure 87 for $\theta = 0$ and 90 degrees, respectively. At $\theta = 0$ degrees, the dominating frequency of the signal is the wave peak frequency. The pitch eigenfrequency is not excited significantly. On the other hand, at $\theta = 90$ degrees, the dominating frequency is the roll eigenfrequency. Therefore, steps may be taken to reduce the roll motions, as previously suggested. The spectral density (PSD) for the rest of the FLS DLCs is presented in Appendix C and the same conclusions are derived.

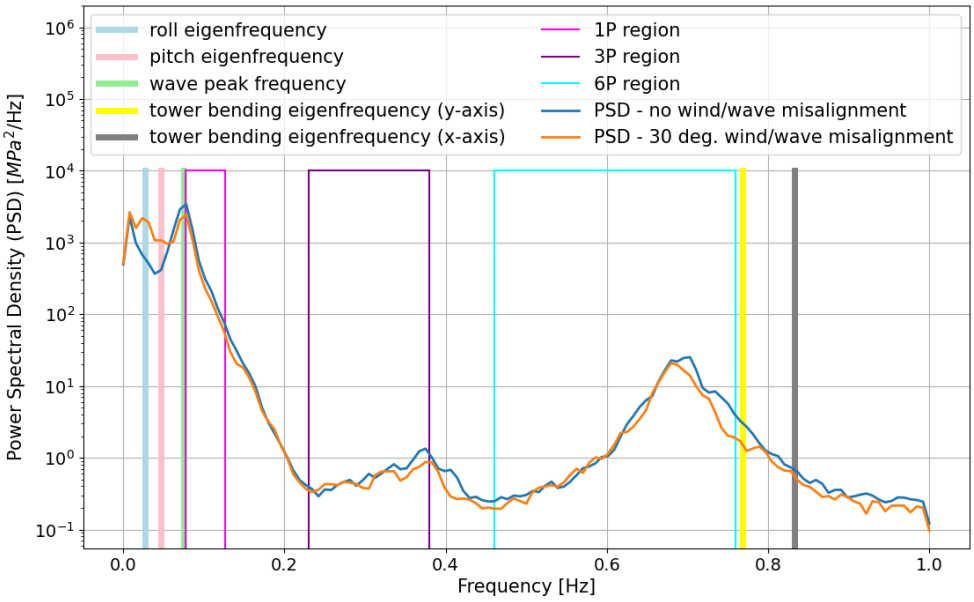

Figure 86: Power spectral density (PSD) of axial stress at the tower base with polar coordinate $\theta = 0$ degrees for mean wind speed $U_w = 10.5$ m/s (FLS DLC D) in combination with the eigenfrequency of pitch and roll, the wave peak frequency, the tower bending eigenfrequency over the y-axis and x-axis, and the 1P, 3P, and 6P regions.

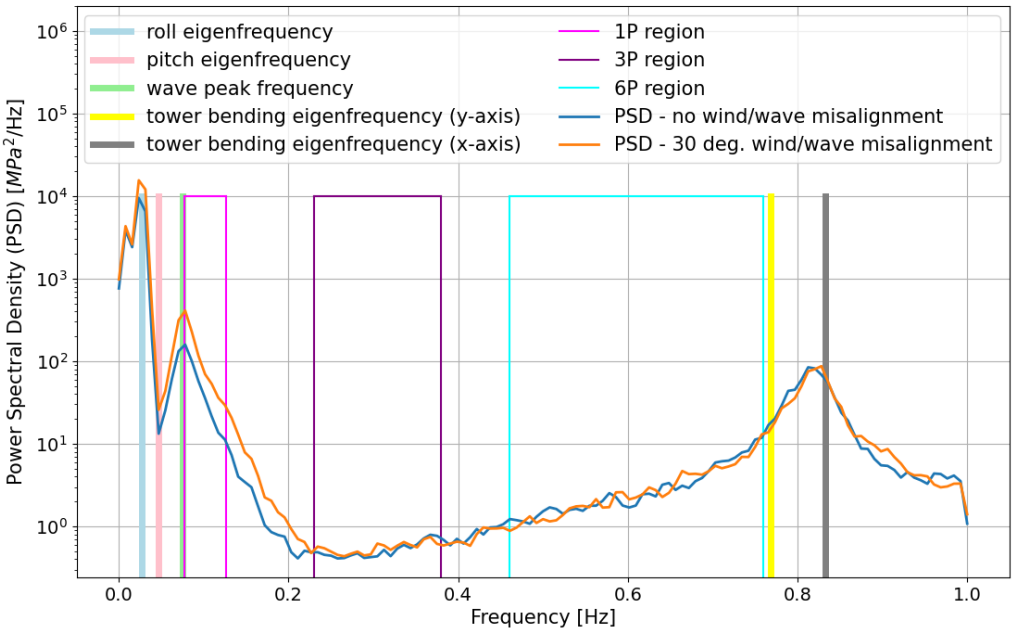

Figure 87: Power spectral density (PSD) of axial stress at the tower base with polar coordinate $\theta = 90$ degrees for mean wind speed $U_w = 10.5$ m/s (FLS DLC D) in combination with the eigenfrequency of pitch and roll, the wave peak frequency, the tower bending eigenfrequency over the y-axis and x-axis, and the 1P, 3P, and 6P regions.

The normalized shear stress at the tower base is presented for FLS DLC D in Figure 88. Comparing it to the normalized uniaxial stress, it is seen that the shear stress is one order of magnitude smaller, therefore, the fatigue damage due to this stress in negligible. Nevertheless, its effect on the multiaxial response of the floater is studied when the relevant forces and moments are excluded (torsion M_z and shear forces F_x and F_y).

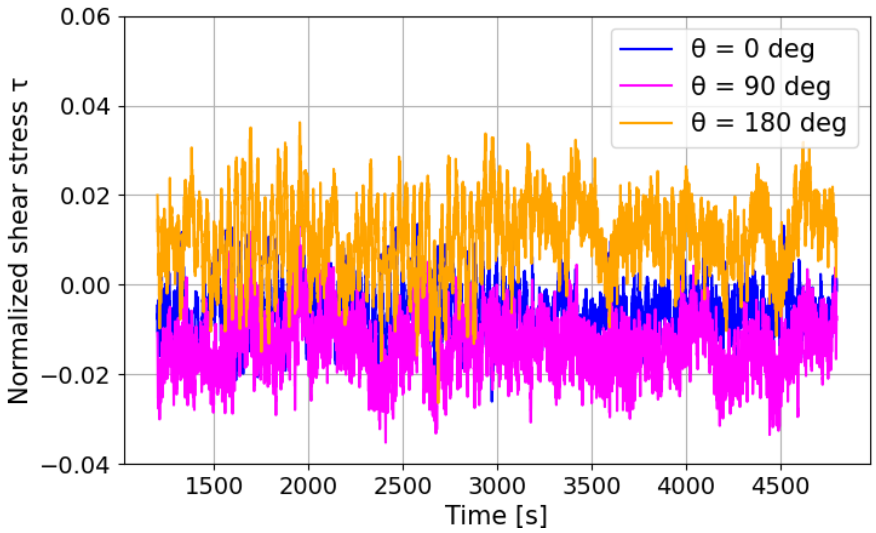

Figure 88: Normalized shear stress time series for mean wind speed $U_w = 10.5$ m/s at $\theta = 0$, 90, and 180 deg (FLS DLC D) without wind/wave misalignment consideration.

4.2.3 Multiaxial screening

The 2-dimensional stress space representation for the shell elements around the tower base at the deck is shown in the following figures (from Figure 89 to Figure 91). It is observed that the shear stress is significant in many locations and that multiaxial conditions exist. In general, a higher level of non-proportionality is observed from $\theta = 50$ to 300 degrees. The stresses are normalized based on the maximum stress value in all elements.

The level of non-proportionality G_{NP} over the normalized fatigue damage importance D_{imp} for all angles around the tower is presented in Figure 92.

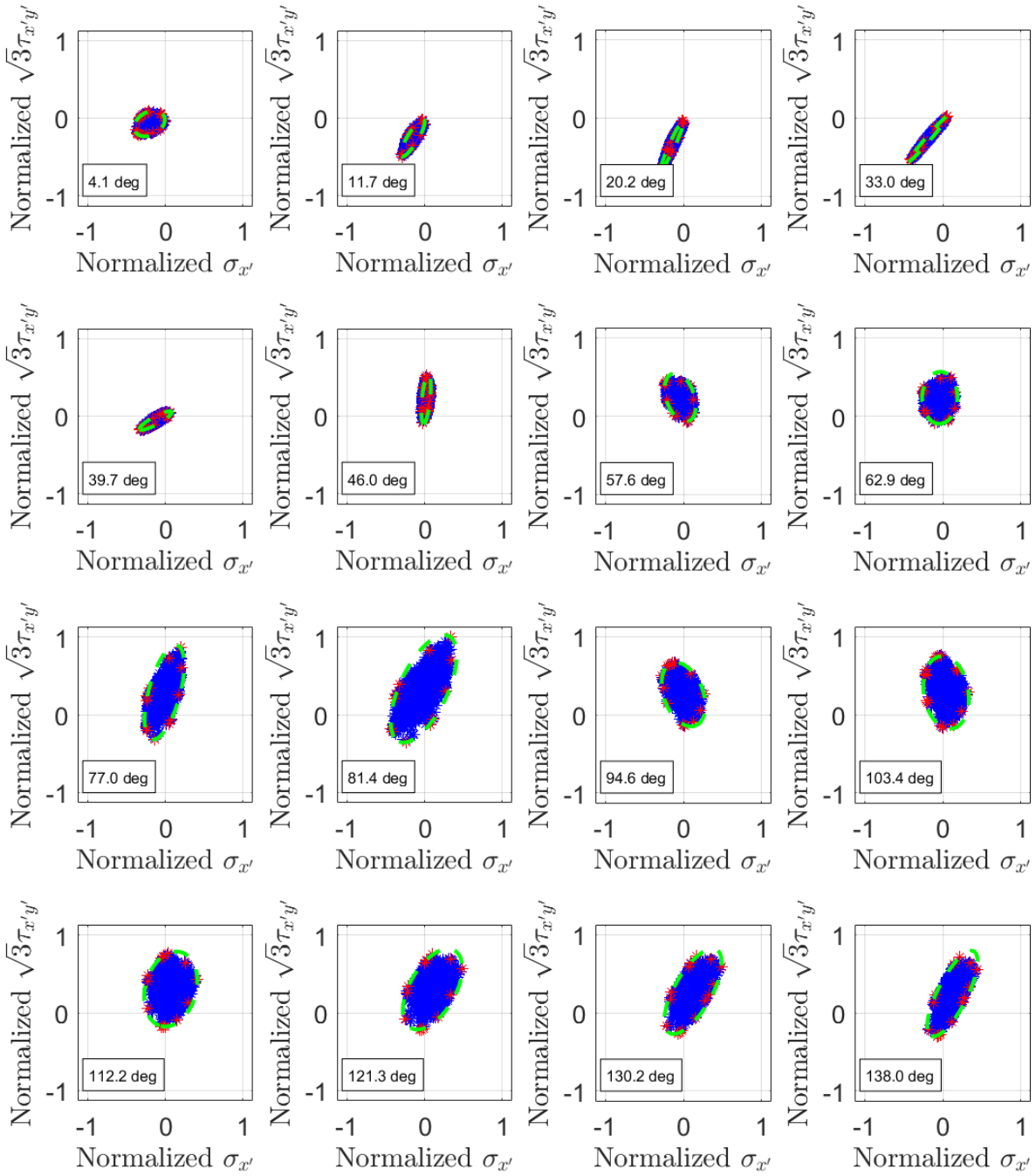

Figure 89: 2-dimensional stress space representation for the shell elements around the tower base from approximately 0 to 140 degrees for FLS DLC D with no wind/wave misalignment.

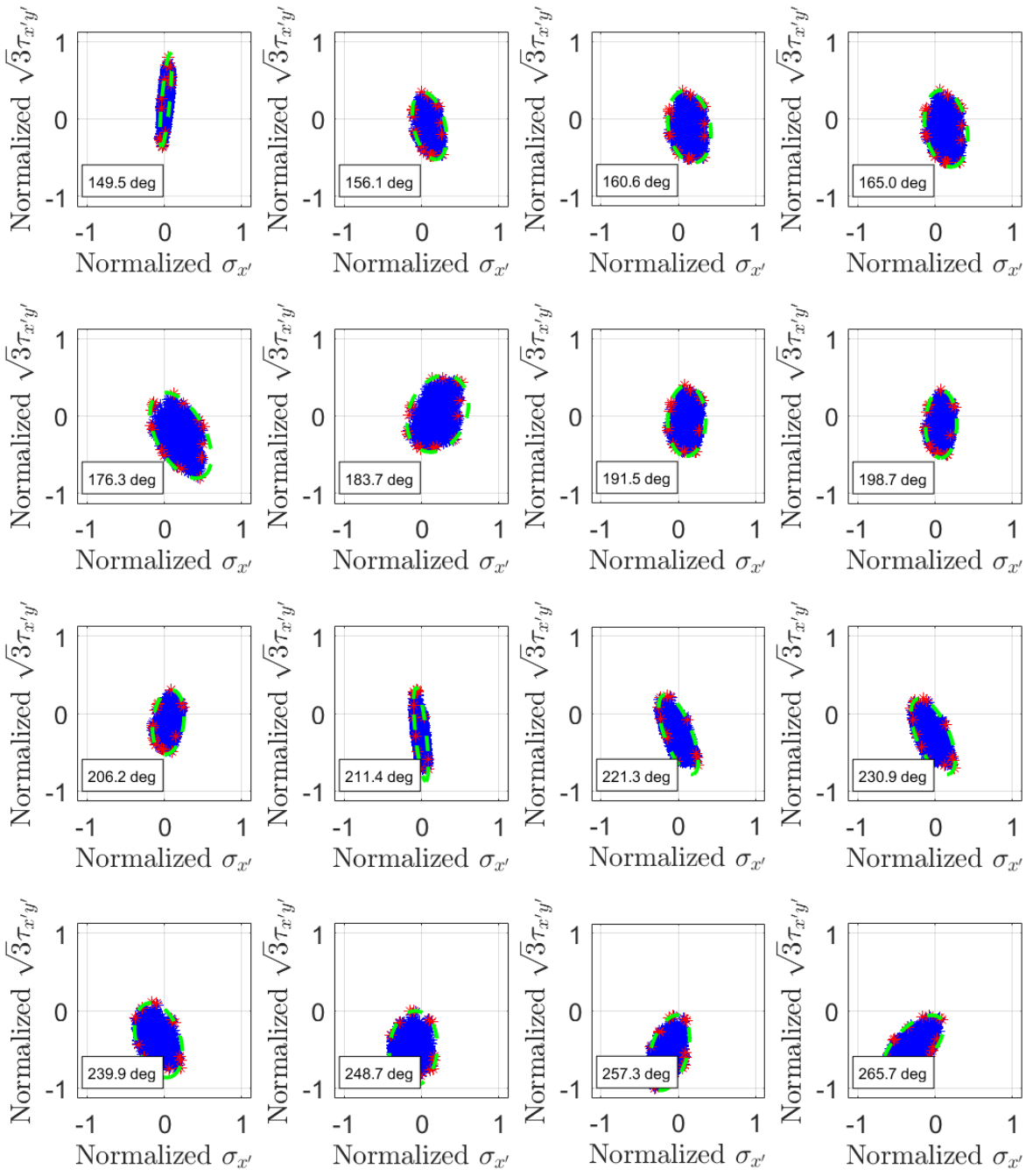

Figure 90: 2-dimensional stress space representation for the shell elements around the tower base from approximately 140 to 270 degrees for FLS DLC D with no wind/wave misalignment.

The most critical locations with a higher level of non-proportionality and fatigue damage importance are at around $\theta = 270, 180, 90, 120$ and 300 degrees. At $\theta = 81.4$ degrees, a triangular element is referred to, therefore, the high fatigue damage importance due to a high maximum stress range may be overestimated due to some artificial stiffness that often accompanies triangular elements. At $\theta = 180$ degrees, the bulkhead B is present inside the barge, but at $\theta = 150$ degrees, where bulkhead A is present, the level of non-proportionality and the fatigue damage importance are smaller. However, in other locations, such as around $\theta = 300$ degrees, the level of non-proportionality is also important, but no bulkheads are present. It is concluded that a combination of the external loading conditions and the design of the structure affects the level of non-proportionality and maximum stress range.

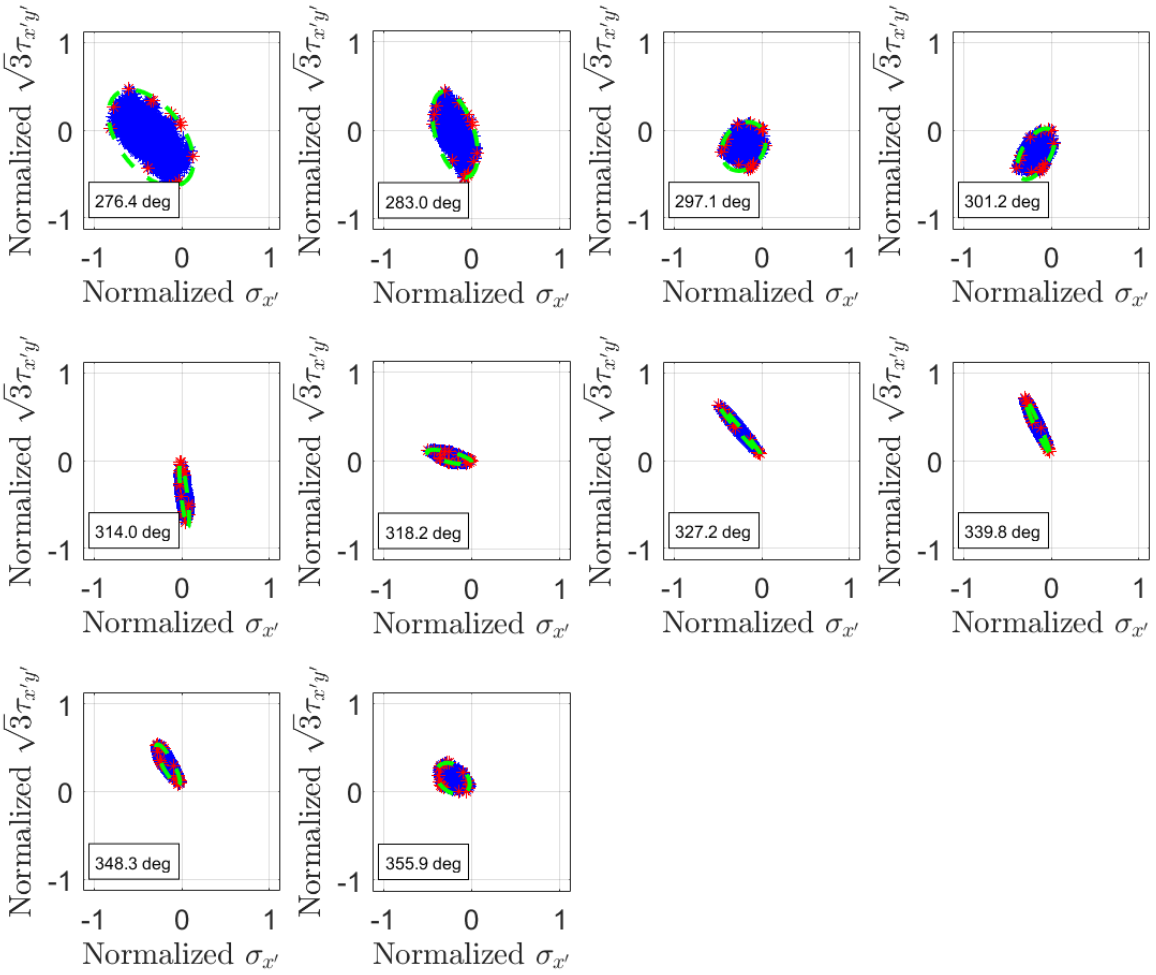

Figure 91: 2-dimensional stress space representation for the shell elements around the tower base from approximately 270 to 360 degrees for FLS DLC D with no wind/wave misalignment.

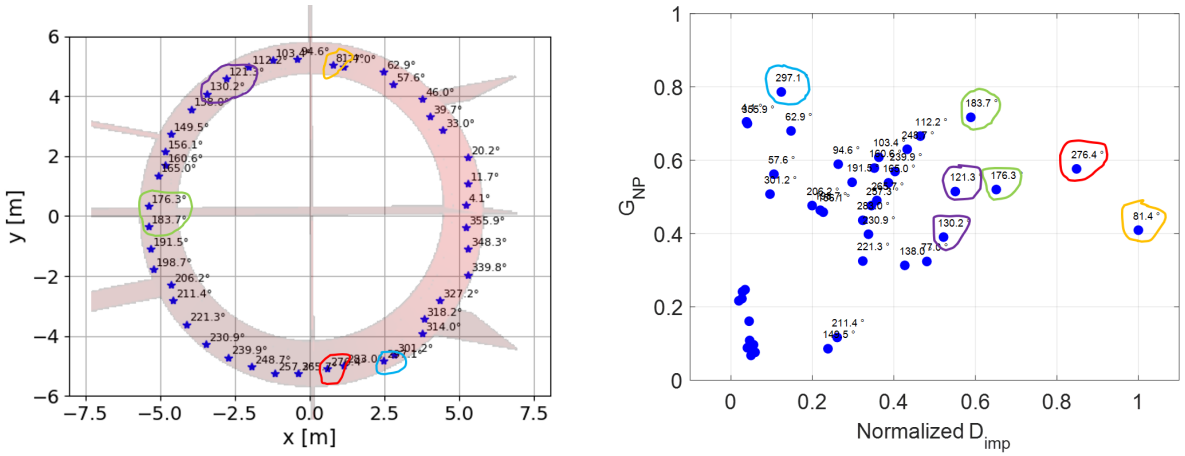

(a) Angle of shell elements around the tower base.

(b) G_{NP} vs. normalized D_{imp}.

Figure 92: Identification of high fatigue damage importance and non-proportionality around the tower base.

4.2.4 Multiaxial screening without shear

The 2-dimensional stress space representation for the shell elements around the tower base at the deck, with and without the shear contributing loads (torsion M_z and shear forces F_x and F_y), is shown in Figure 93 (from about 140 to 270 degrees), with the rest in Appendix D. The level of non-proportionality G_{NP} over the normalized fatigue damage importance D_{imp} for all angles around the tower is compared, with and without the shear contributing loads, in Figure 94.

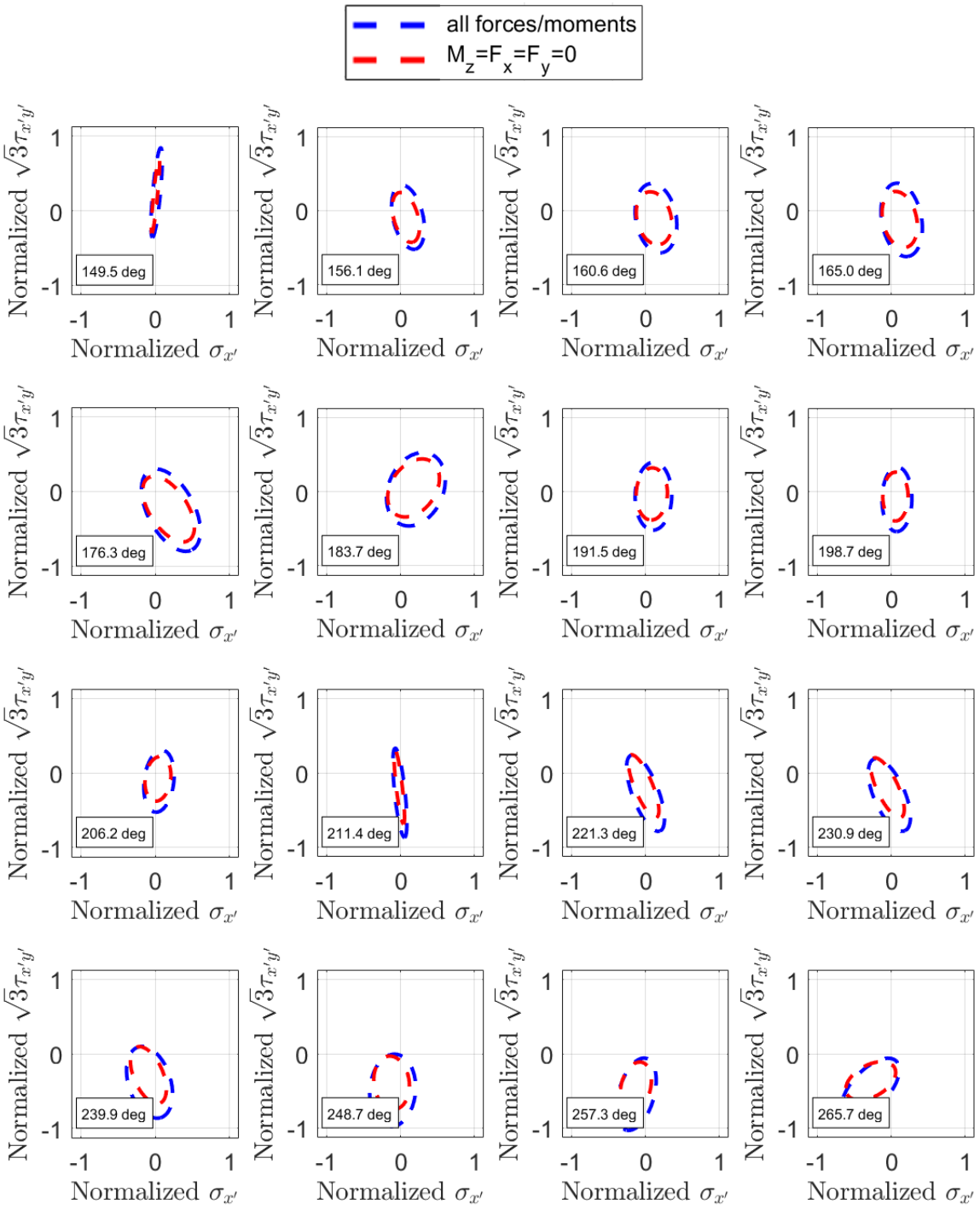

Figure 93: Comparison of the 2-dimensional stress space representation for the shell elements around the tower base from approximately 140 to 270 degrees with and without shear contributing forces and moments for FLS DLC D with no wind/wave misalignment.

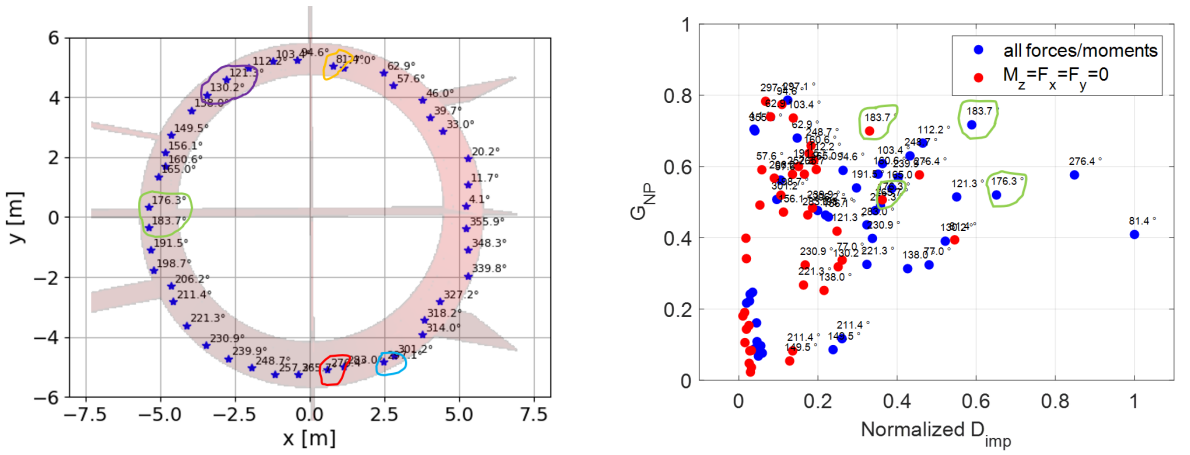

(a) Angle of shell elements around the tower base.

(b) G_{NP} vs. normalized D_{imp}.

Figure 94: Identification of high fatigue damage importance and non-proportionality around the tower base with and without shear contributing forces and moments.

It is seen that the maximum stress range is decreased in all locations. The level of non-proportionality is almost the same in most locations or slightly smaller, such as at $\theta = 183.7$ and 176.3 degrees. Therefore, the conclusion is that the external loading can affect the level of non-proportionality, but it is not the main cause of non-proportionality. The geometrical changes are a significant contributor.

4.2.5 Multiaxial screening of new design

The 2-dimensional stress space representation for the shell elements around the tower base at the deck, with the initial and the modified internal structure with the extra bulkheads, is shown in the following figures, with the rest in Appendix D. The level of non-proportionality G_{NP} over the normalized fatigue damage importance D_{imp} for all angles around the tower is compared in Figure 97.

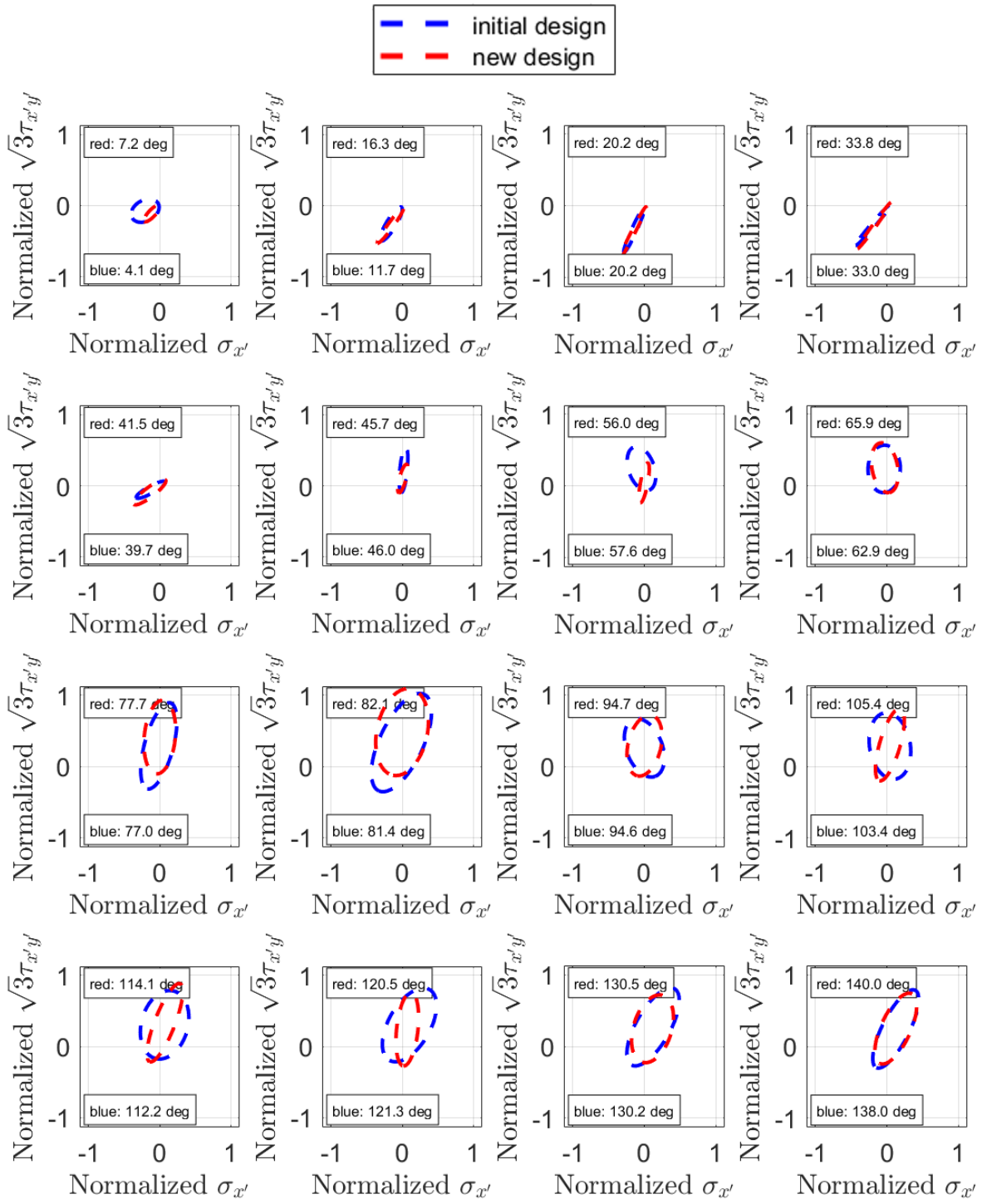

Figure 95: Comparison of the 2-dimensional stress space representation for the shell elements around the tower base from approximately 0 to 140 degrees in the initial and modified internal structure for FLS DLC D with no wind/wave misalignment.

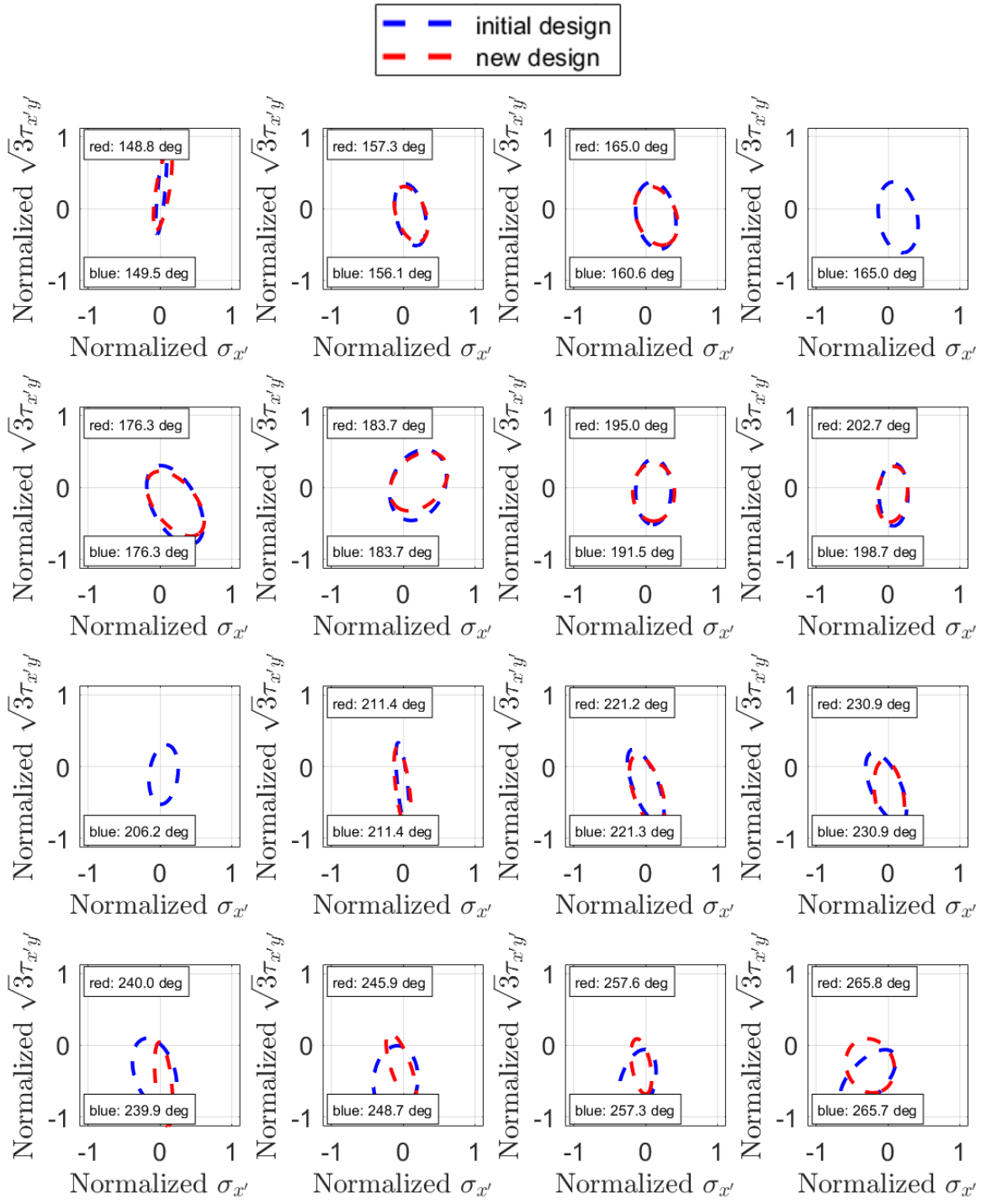

Figure 96: Comparison of the 2-dimensional stress space representation for the shell elements around the tower base from approximately 140 to 270 degrees in the initial and modified internal structure for FLS DLC D with no wind/wave misalignment.

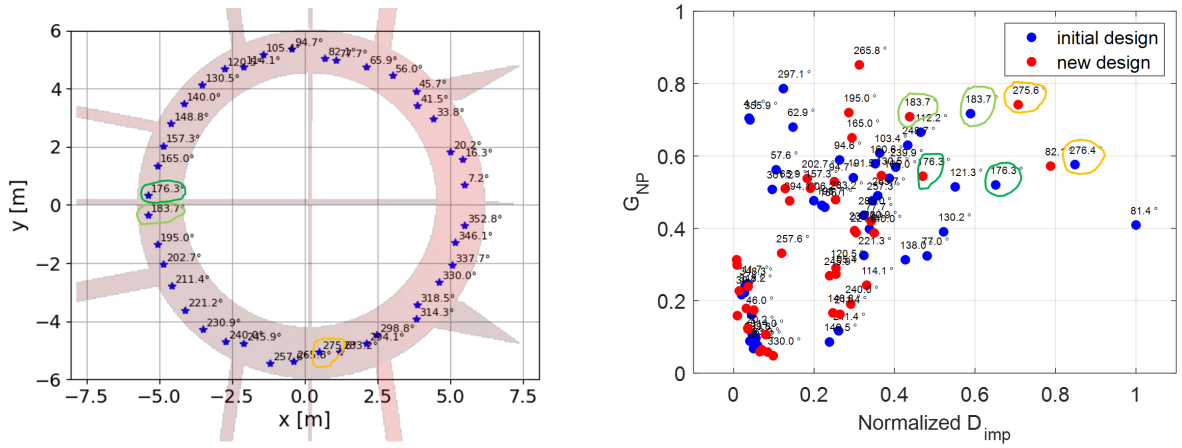

(a) Angle of shell elements around the tower base.

(b) G_{NP} vs. normalized D_{imp}.

Figure 97: Identification of high fatigue damage importance and non-proportionality around the tower base in the initial and modified internal structure.

The introduction of the extra bulkheads changed the stress response of the elements. At around $\theta = 180$ degrees, the fatigue damage importance was slightly decreased, and the level of non-proportionality remained almost the same or increased. At $\theta = 114.1$ degrees, a few degrees before the new bulkhead is placed, the level of non-proportionality decreased, as at $\theta = 120.5$ degrees, a few degrees after the new bulkhead. The minor axis of the ellipse is smaller, therefore, the level of non-proportionality is smaller.

At $\theta = 240$ degrees, before another bulkhead is placed, the level of non-proportionality was also decreased, as at $\theta = 245.9$ degrees, after the bulkhead. The maximum stress range remained almost the same. At $\theta = 275.6$ and $\theta = 265.8$ degrees, the maximum stress range was decreased.

Overall, the extra bulkheads lead to a smaller maximum fatigue damage importance and level of non-proportionality, but the changes differ from element to element. The elements before and after the new bulkheads have a lower level of non-proportionality than before.

4.2.6 Multiaxial screening with double plate thickness

The 2-dimensional stress space representation for the shell elements around the tower base at the deck, with the initial and double the thickness of the upper deck plate around the tower, is shown in Figure 98, with the rest in Appendix D. The level of non-proportionality G_{NP} over the normalized fatigue damage importance D_{imp} for all angles around the tower is compared in Figure 99.

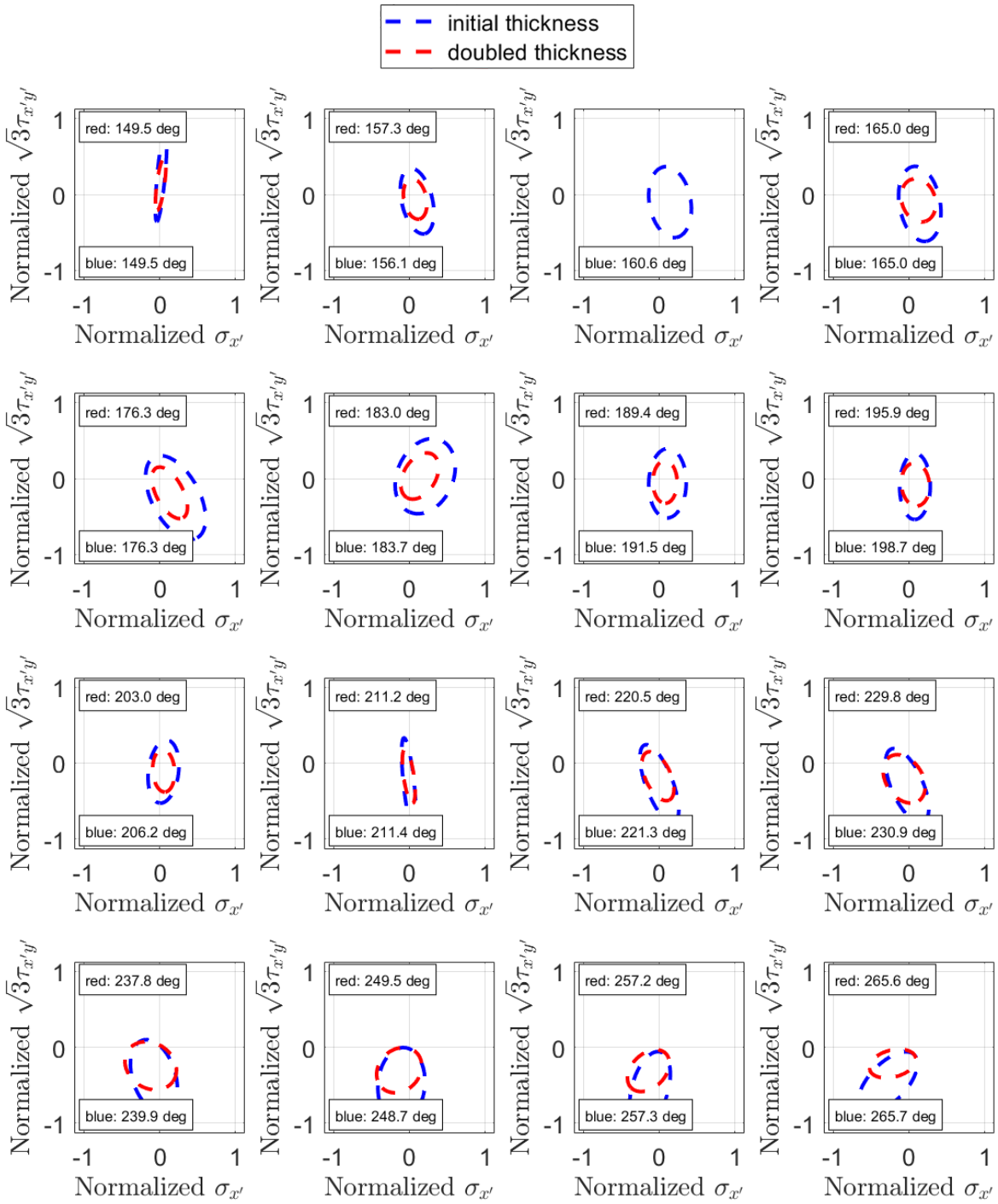

Figure 98: Comparison of the 2-dimensional stress space representation for the shell elements around the tower base from approximately 140 to 270 degree with the initial and a doubled plate thickness at the tower base for FLS DLC D with no wind/wave misalignment.

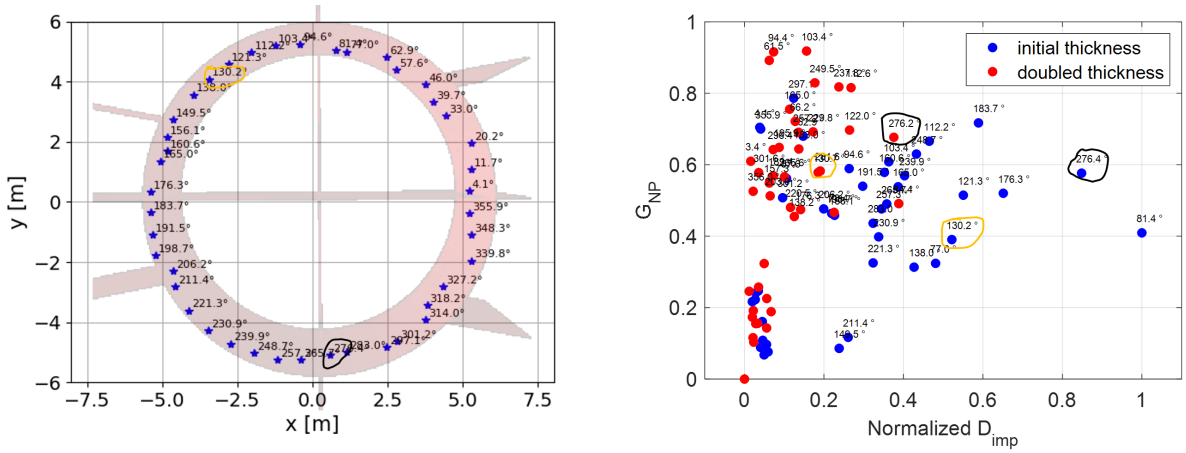

(a) Angle of shell elements around the tower base.

(b) G_{NP} vs. normalized D_{imp}.

Figure 99: Identification of high fatigue damage importance and non-proportionality around the tower base with the initial and a doubled plate thickness.

The increased thickness reduces the maximum stress ranges and, therefore, the fatigue damage importance is lower, especially for angles from $\theta = 50$ to 300 degrees. However, the level of non-proportionality is in general similar or increased, for example, at around $\theta = 130$ and 275 degrees.

The length of the major axis of the ellipses is decreased with an increased thickness more than the length of the minor axis, therefore, maintaining or increasing the level of non-proportionality.

4.2.7 Multidirectional fatigue damage at the tower side

For the hot spot plate and hot spot plate multidirectional methods, a hot spot patch with mesh size txt is required, where t is the thickness of the structure at the examined location. The tower and upper deck have been meshed accordingly, as shown in Figure 100. However, for the plate, a 2tx2t mesh size was implemented, as the small thickness of the plate was crashing the software when creating the hot spot patches. Nevertheless, it is assumed acceptable, as the plate thickness is smaller than the tower thickness, and the mesh size is already significantly small. Different FEM models were created for each mesh size. The stresses are read at 0.5t and 1.5t from the intersection, and they are extrapolated to calculate the hot spot stresses.

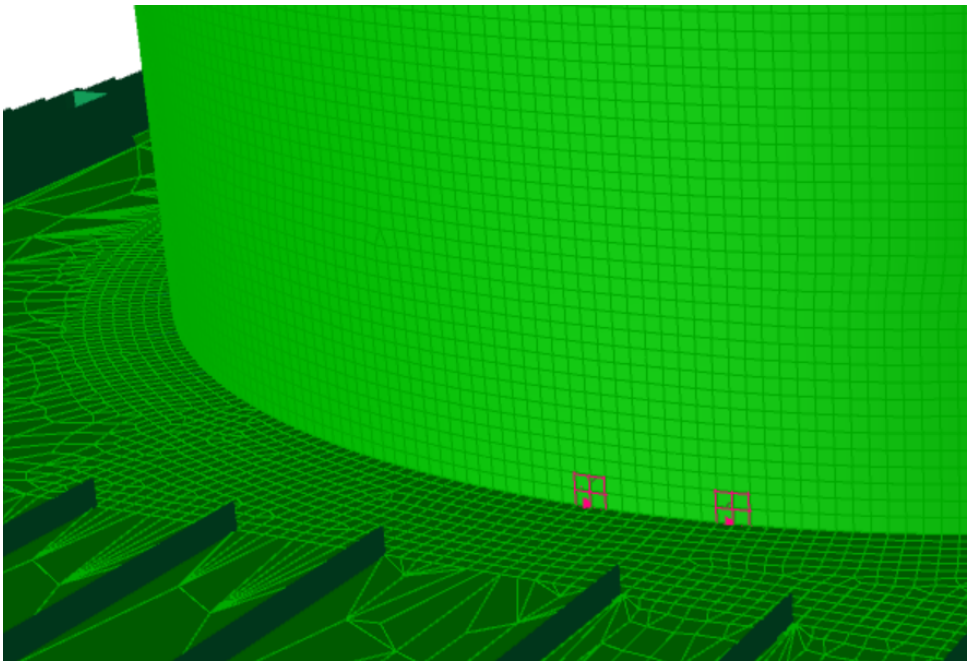

(a) Patches txt at the tower.

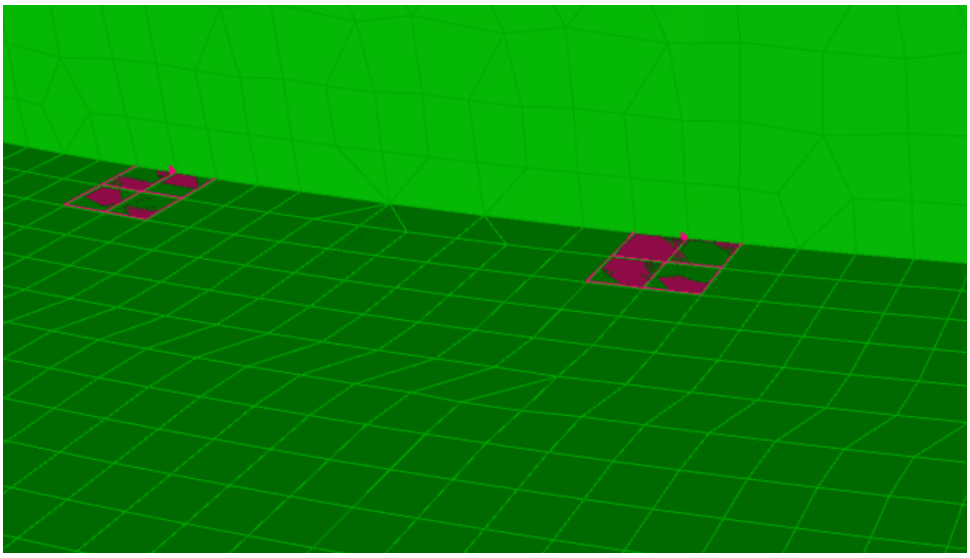

(b) Patches 2tx2t at the deck.

Figure 100: Hot spot patches at the tower and deck at the tower base interface.

The fatigue damage for DLC C at different angles around the tower base, but on the tower side, is presented in Figure 101, based on the nominal uniaxial, hot spot plate, and hot spot plate multidirectional approach. A high fatigue damage is observed when comparing the hot spot plate fatigue with the nominal uniaxial fatigue at angles $\theta = 0, 90, 180$ and 270 degrees. This can be attributed to the

local geometry, as bulkheads are inside the barge at these locations, so many plates intersect. This leads to a numerical singularity with high stresses that don't appear in reality. Therefore, these points are excluded, and nearby locations are examined instead.

Also, the hot spot plate fatigue and hot spot plate multidirectional perpendicular fatigue are the same at $\theta = 0, 90, 180$ and 270 degrees. This means that the perpendicular direction about the weld is the critical stress direction.

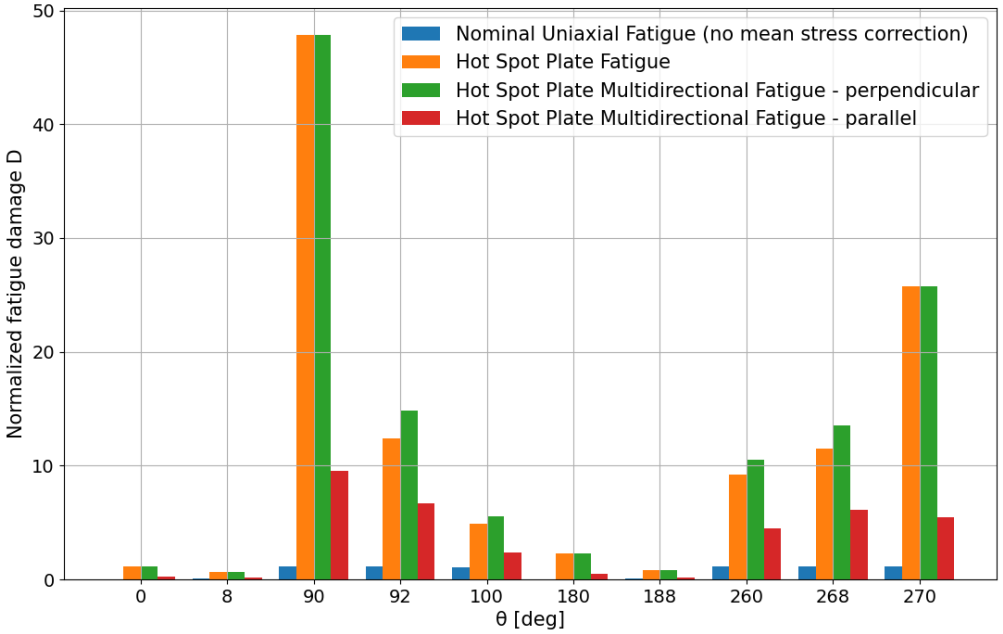

Figure 101: Comparison of the fatigue damage with the nominal uniaxial, hot spot plate, and hot spot plate multidirectional approach at different angles around the tower at the tower base and on the tower side for FLS DLC C, without its probability, and for no wind/wave misalignment.

In Figure 102, the fatigue damage is compared at angles $\theta = 8, 100, 188$ and 260 degrees at the tower base and on the tower side. As already seen from the nominal uniaxial fatigue calculation, the fatigue-sensitive locations are at $\theta = 90$ (or 100) and 270 (or 260) degrees. This is also observed with the hot spot plate fatigue and hot spot multidirectional perpendicular fatigue calculations. However, due to the geometry changes, the stresses are further increased with the hot spot plate methods, and therefore, the fatigue damage is also higher. Some modifications can be applied to the structure to reduce the stresses, such as the following:

- remove part of the bulkhead at the intersection locations to avoid artificial stresses.
- include stiffeners (rings) at the tower part exceeding the barge, as were already included in the internal part of the tower from the provided model.
- include external brackets from the tower to the upper deck to distribute the load path to more locations.

Moreover, it is seen that at $\theta = 260$ degrees, the damage is higher than at $\theta = 100$ degrees (only 10 degrees away from the critical locations at $\theta = 270$ and 90 degrees, respectively). This result was not predicted from the nominal uniaxial fatigue calculation.

The hot spot plate fatigue and hot spot multidirectional perpendicular fatigue are identical at $\theta = 8$ and 188 degrees. This suggests that the main principal direction, normal to the weld line, contributes more to the fatigue damage at these locations. At $\theta = 100$ and 260 degrees, the hot spot multidirectional

perpendicular fatigue is higher, suggesting that there is a different critical stress angle θ'_{cp} at which the perpendicular damage is higher. The worst parallel damage is, in all cases, smaller.

The fatigue damage for DLC C is also compared in Figure 103, when the wind/wave misalignment is considered. The same results are derived for this load case as well and the fatigue damage is higher.

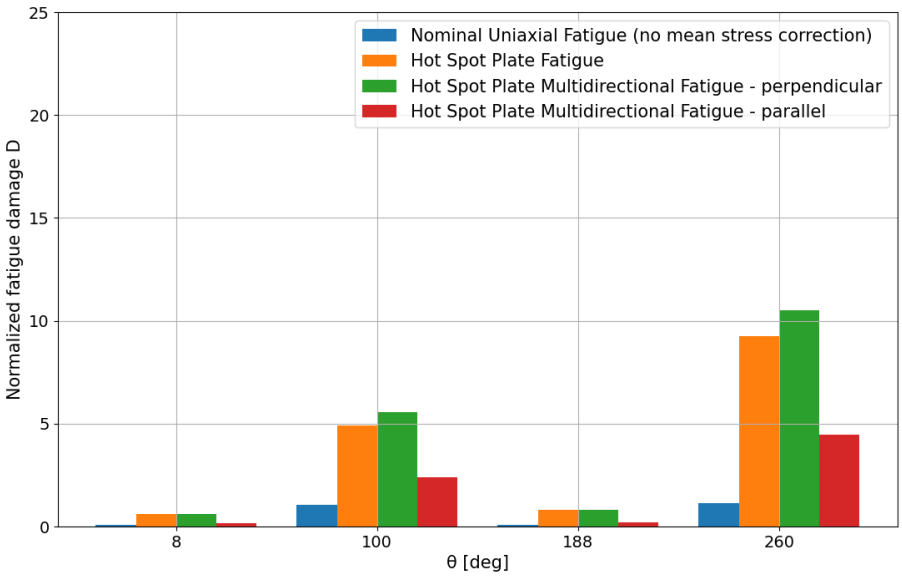

Figure 102: Comparison of the fatigue damage with the nominal uniaxial, hot spot plate, and hot spot plate multidirectional approach at $\theta = 8, 100, 188$ and 260 degrees at the tower base and on the tower side for FLS DLC C, without its probability, and for no wind/wave misalignment.

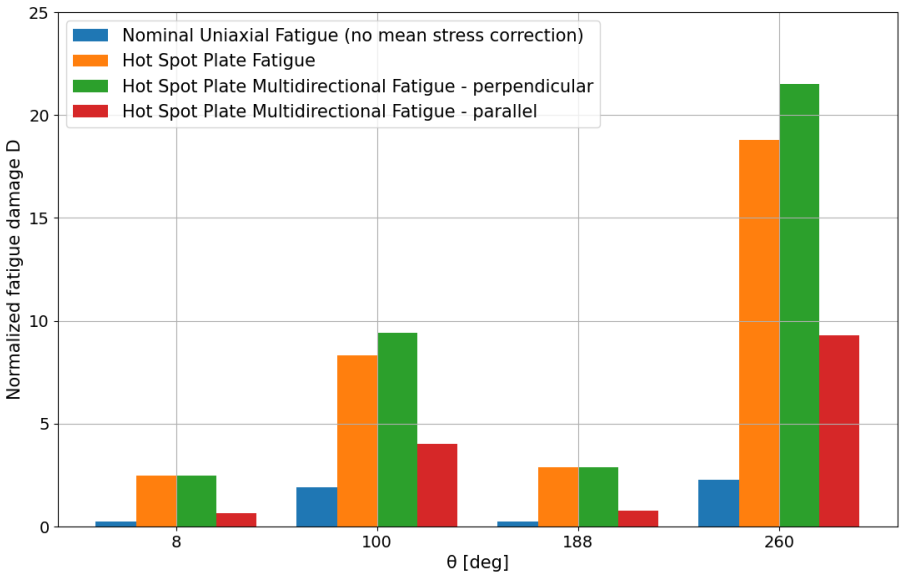

Figure 103: Comparison of the fatigue damage with the nominal uniaxial, hot spot plate, and hot spot plate multidirectional approach at $\theta = 8, 100, 188$ and 260 degrees at the tower base and on the tower side for FLS DLC C, without its probability, and for a 30 degrees wind/wave misalignment.

The fatigue damage based on the different methods is further compared for all DLCs in the following figures (from Figure 104 to Figure 107). The results with the hot spot plate and hot spot plate multi-directional methods follow the same pattern as the nominal uniaxial approach, but with higher stresses and, therefore, higher fatigue damage. It is noted that the same SN-curve type D is used in all cases, apart from the parallel damage, where an SN-curve type C2 is used, according to the relevant standard.

The parallel damage is always the smallest among the DLCs. At $\theta = 100$ and 260 degrees, the hot spot plate multidirectional perpendicular fatigue is always higher, whereas at $\theta = 8$ and 188 degrees, they are always the same. At $\theta = 260$ degrees, the fatigue damage is higher than at $\theta = 100$ degrees with both hot spot plate methods.

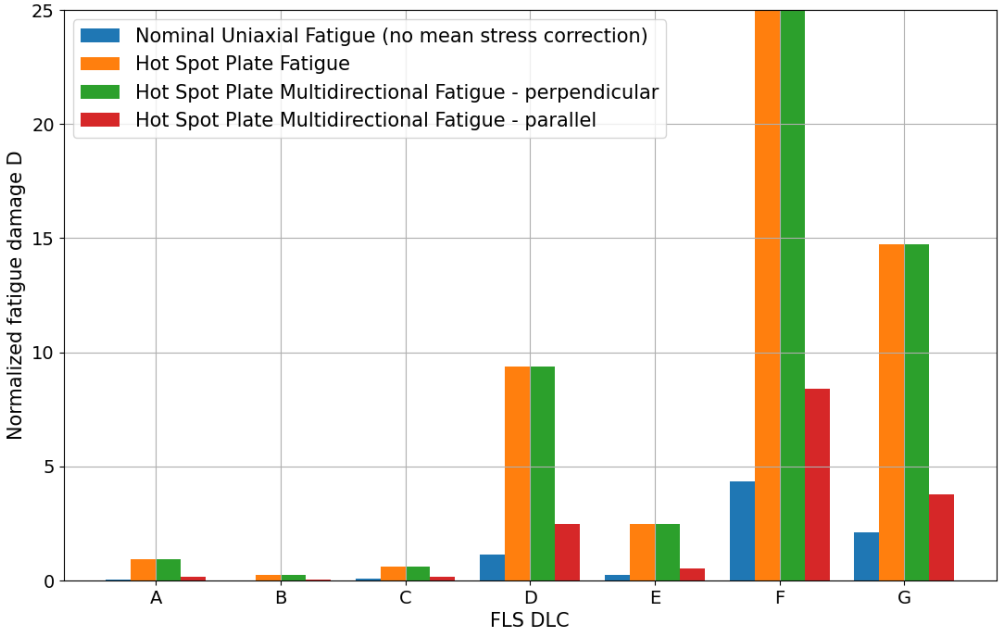

Figure 104: Comparison of the fatigue damage with the nominal uniaxial, hot spot plate, and hot spot plate multidirectional approach at $\theta = 8$ degrees at the tower base and on the tower side for all DLCs, without the probability of each DLC, and for no wind/wave misalignment.

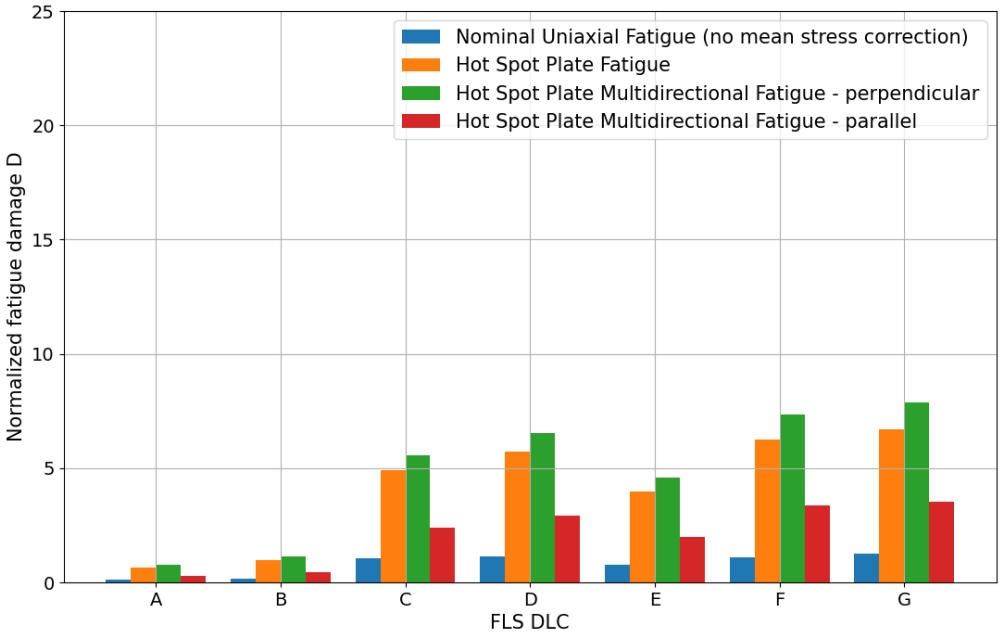

Figure 105: Comparison of the fatigue damage with the nominal uniaxial, hot spot plate, and hot spot plate multidirectional approach at $\theta = 100$ degrees at the tower base and on the tower side for all DLCs, without the probability of each DLC, and for no wind/wave misalignment.

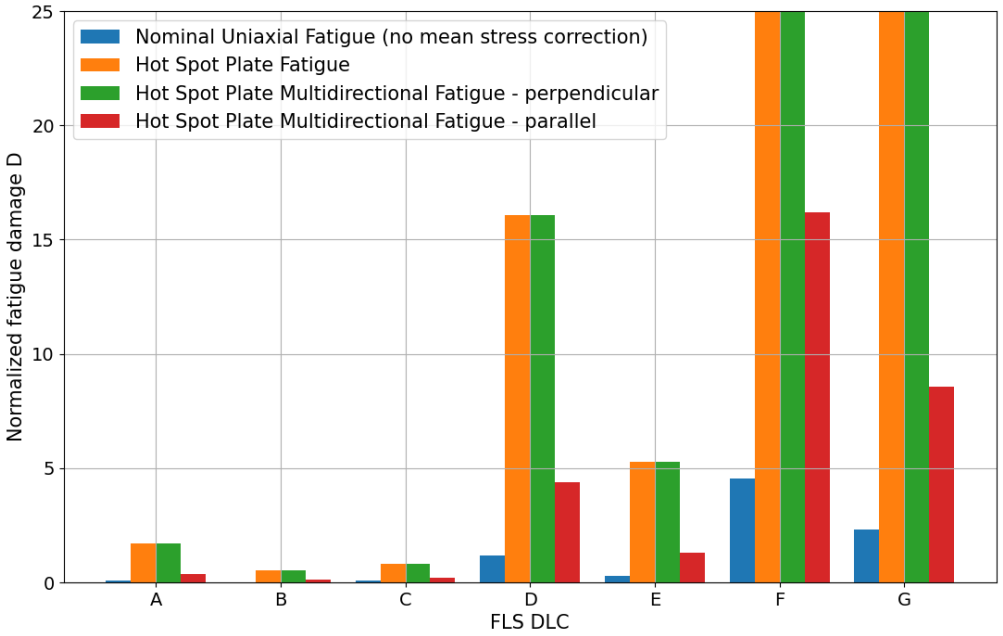

Figure 106: Comparison of the fatigue damage with the nominal uniaxial, hot spot plate, and hot spot plate multidirectional approach at $\theta = 188$ degrees at the tower base and on the tower side for all DLCs, without the probability of each DLC, and for no wind/wave misalignment.

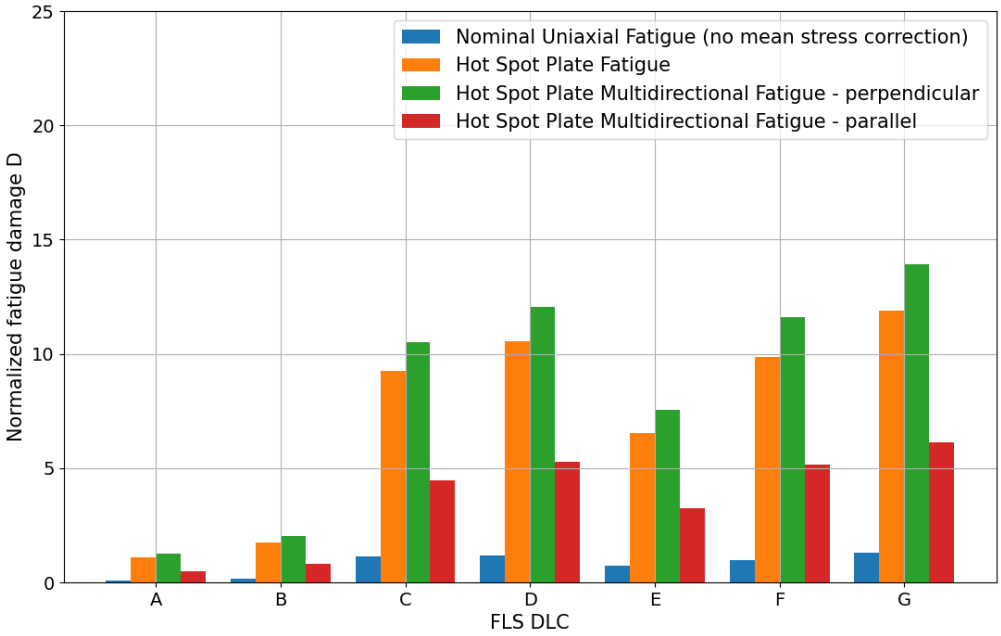

Figure 107: Comparison of the fatigue damage with the nominal uniaxial, hot spot plate, and hot spot plate multidirectional approach at $\theta = 260$ degrees at the tower base and on the tower side for all DLCs, without the probability of each DLC, and for no wind/wave misalignment.

4.2.8 Multidirectional fatigue damage at the deck side

In Figure 108, the fatigue damage based on the two hot spot plate methods is presented around the tower base, but on the deck side, at selected locations, considering the 2-dimensional stress space screening. Once more, at angles close to many intersecting plates ($\theta = 182$ and 269 degrees), the stresses are artificially high, therefore, these locations are not examined.

At $\theta = 15$ and 321 degrees, the fatigue damage is smaller compared to the other angles, as was expected from the screening. For the rest, the hot spot plate fatigue damage is usually higher. This is due to the principal stress that is used as the effective stress $\Delta\sigma_{\text{Eff}}$ in Equation 19, with the constant a equal to 0.90. However, when comparing the results from the hot spot plate method based on $\Delta\sigma_{\text{Eff}} = \sqrt{\Delta\sigma_{\perp}^2 + 0.81\Delta\tau_{\parallel}^2}$ rather then the principal stresses, then the hot spot plate multidirectional method, which is based on the same equation, has a higher fatigue damage, meaning that there is an other critical plane, apart from the one perpendicular to the weld, for which this effective stress is higher.

However, the fatigue damage based on the principal stresses is more critical and is the one displayed. A lower value for the constant a, though, that depends on the weld detail, can lead to smaller fatigue damage. Moreover, as the principal stress direction changes, it refers to different planes at the same time when calculating fatigue damage, therefore, it might be overestimating fatigue damage. With the hot spot plate multidirectional fatigue approach, only one plane is examined at a time, therefore leading to smaller cumulative fatigue damage.

According to the screening, one of the most critical location for multiaxiality seems to be at around $\theta = 180$ degrees. Indeed, the hot spot plate perpendicular damage is higher around this angle. Also, at $\theta = 150$ degrees, the perpendicular damage is higher, as this location is close to bulkhead A. Therefore, it is seen that wherever there is another bulkhead, the critical plane changes. Nevertheless, the hot spot plate fatigue based on the principal stresses is higher in other locations.

Moreover, the screening based on the 2-d stress space representation is only highlighting the existence of multiaxial conditions. The fatigue damage is not equivalent to the fatigue damage importance shown

before, as no counting method was applied. In contrast, only the level of non-proportionality and its effect on the maximum stress range are shown. For example, at around $\theta = 80$ degrees, the fatigue damage importance was the highest. However, applying a cycle counting method shows that this is not the case.

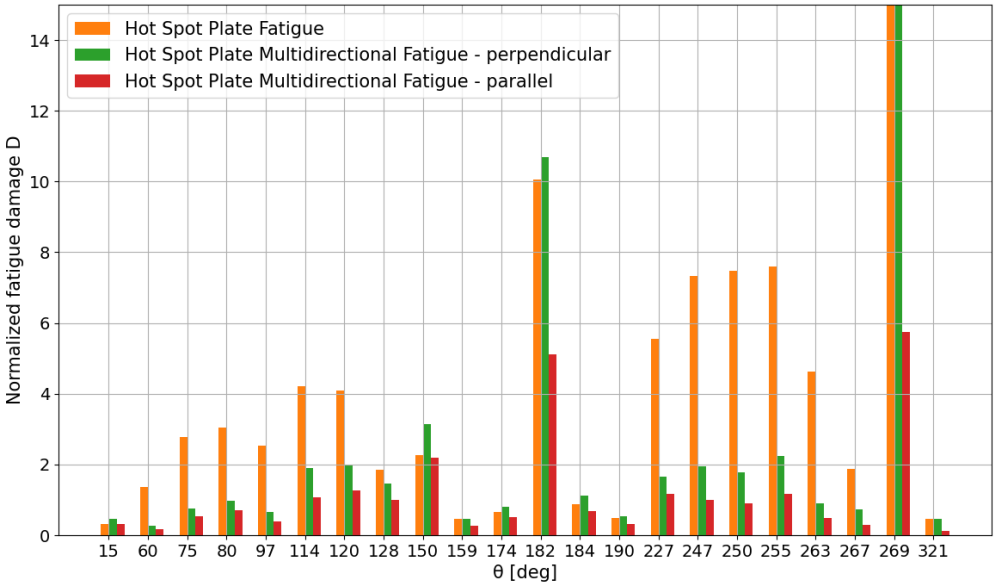

Figure 108: Comparison of the fatigue damage with the hot spot plate and hot spot plate multidirectional approach at different angles around the tower base, but on the deck side, for FLS DLC D, without its probability, and for no wind/wave misalignment.

In the following figures (from Figure 109 to Figure 112), the fatigue damage with the two hot spot plate methods is compared for all DLCs. A similar pattern to the DLC D is observed for all the other DLCs as well.

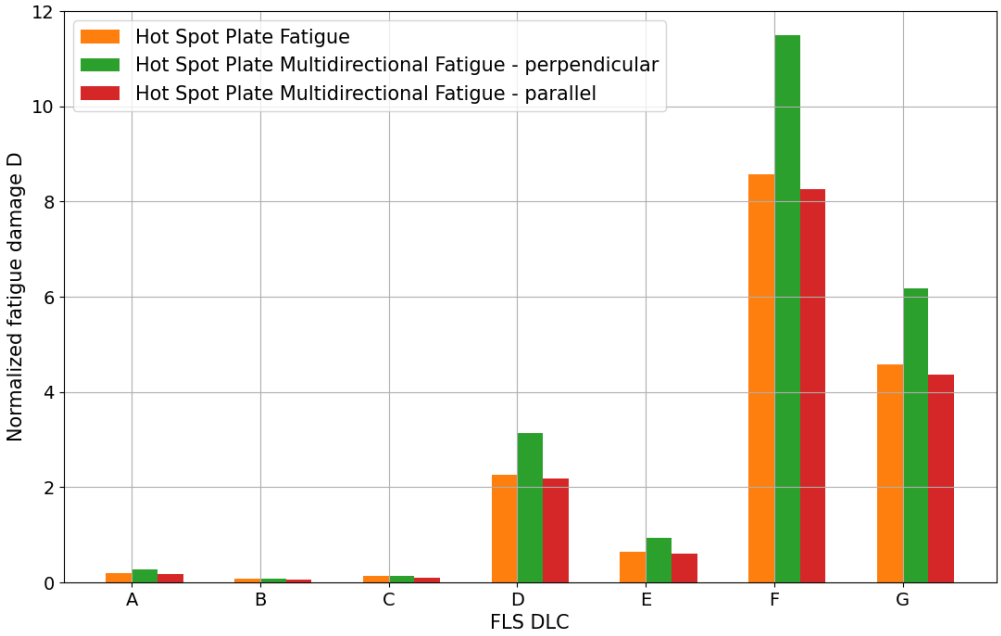

Figure 109: Comparison of the fatigue damage with the hot spot plate and hot spot plate multidirectional approach at $\theta = 150$ degrees on the deck side, for all DLCs, without the probability of each DLC, and for no wind/wave misalignment.

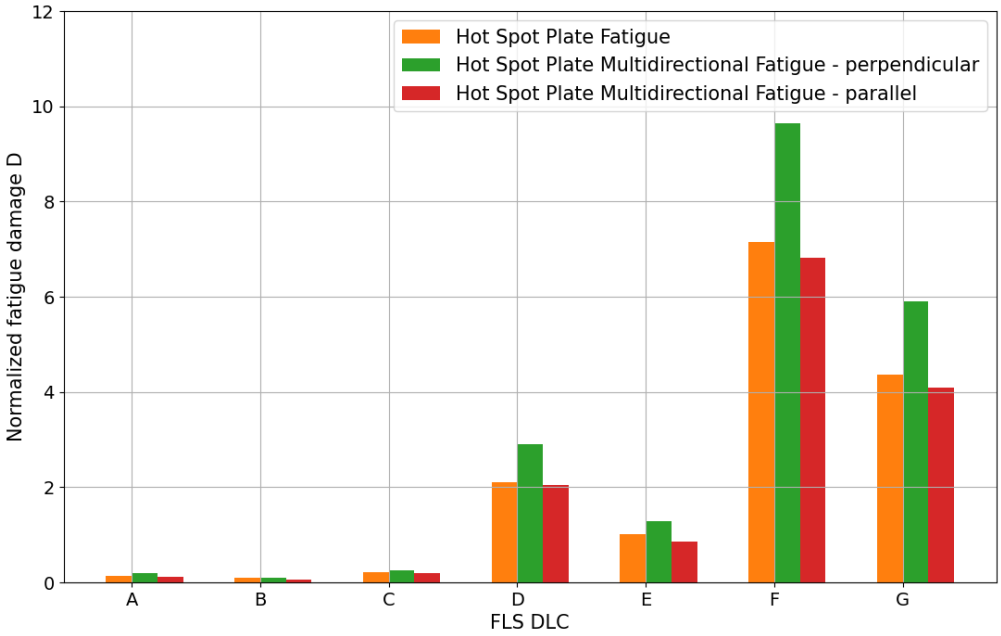

Figure 110: Comparison of the fatigue damage with the hot spot plate and hot spot plate multidirectional approach at $\theta = 150$ degrees on the deck side, for all DLCs, without the probability of each DLC, and with 30 degrees wind/wave misalignment.

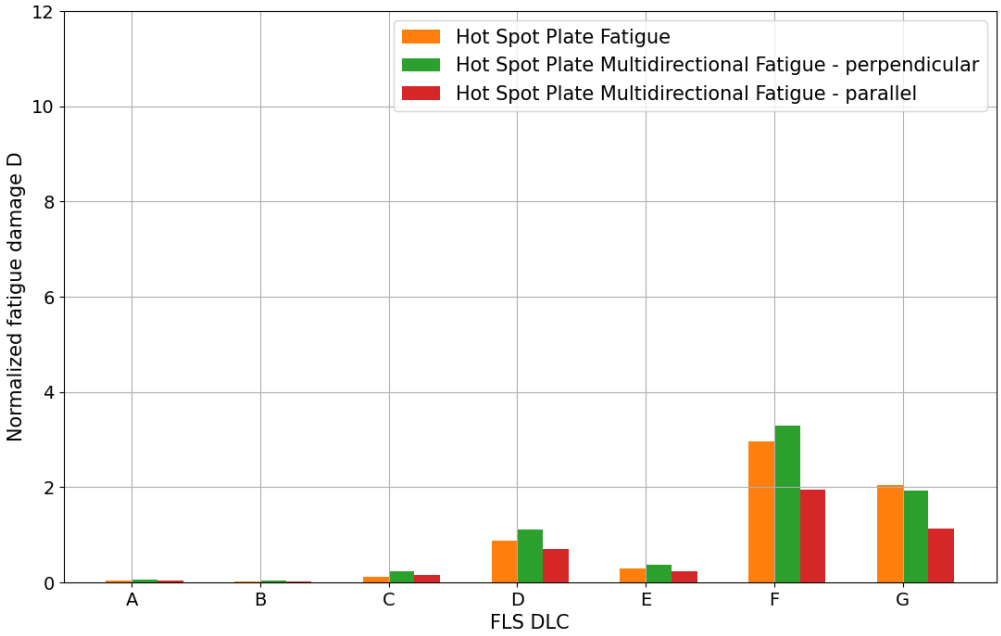

Figure 111: Comparison of the fatigue damage with the hot spot plate and hot spot plate multidirectional approach at $\theta = 184$ degrees on the deck side, for all DLCs, without the probability of each DLC, and for no wind/wave misalignment.

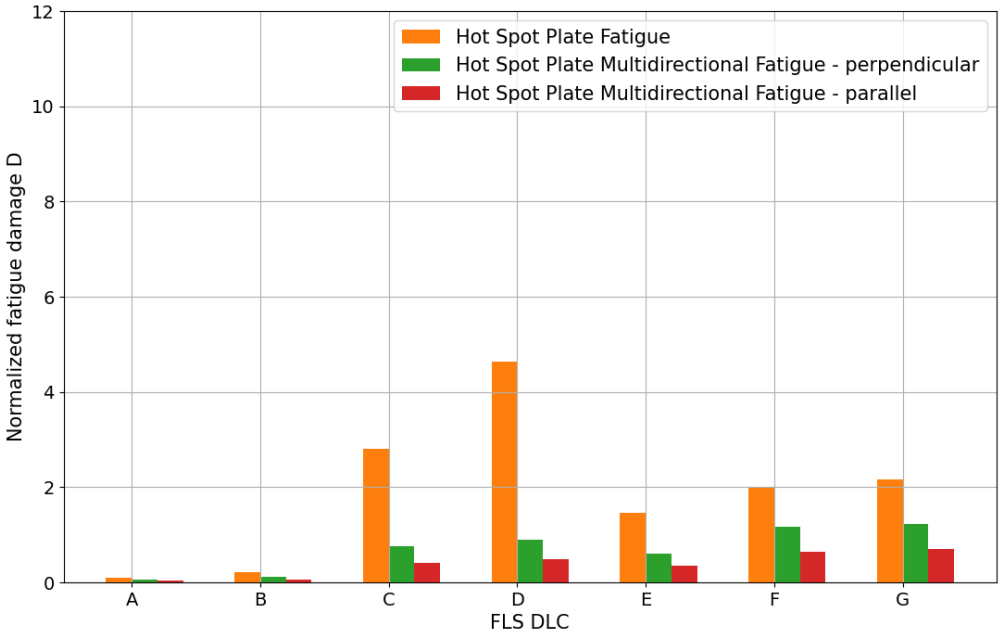

Figure 112: Comparison of the fatigue damage with the hot spot plate and hot spot plate multidirectional approach at $\theta = 263$ degrees on the deck side, for all DLCs, without the probability of each DLC, and for no wind/wave misalignment.

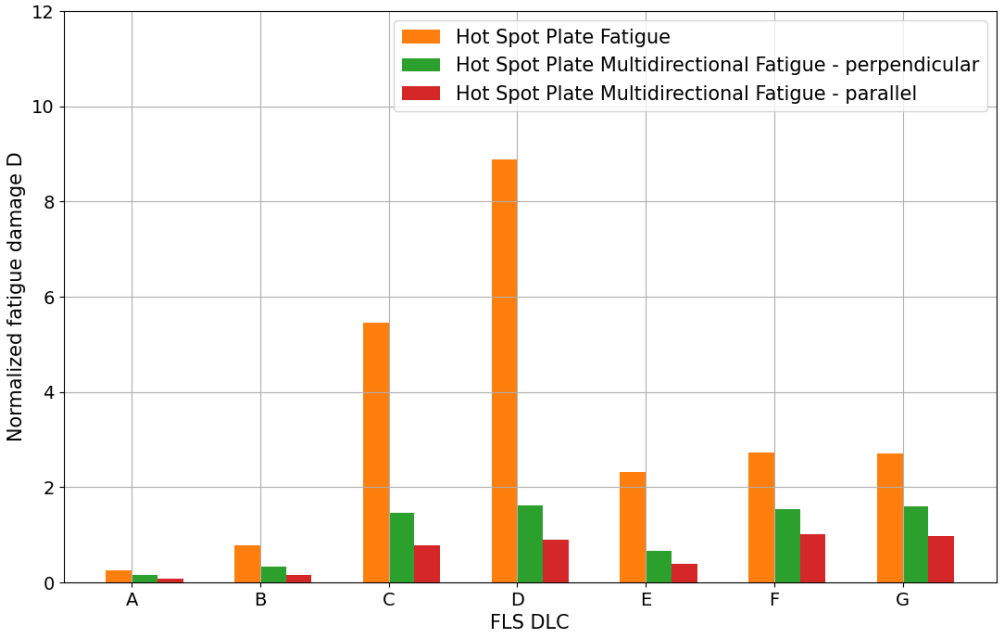

Figure 113: Comparison of the fatigue damage with the hot spot plate and hot spot plate multidirectional approach at $\theta = 263$ degrees on the deck side, for all DLCs, without the probability of each DLC, and with 30 degrees wind/wave misalignment.

In conclusion, the difference between the effective stress due to the principal stress from the hot spot plate method and the effective stress from the hot spot plate multidirectional method is higher on the deck side than the tower side, suggesting that a stress state with a significant normal stress component, parallel to the weld, and shear stress component is present at the deck, and that the principal stress direction changes. The effective stress from the hot spot plate multidirectional method is in general higher than the effective stress from the hot spot plate method based on $\sqrt{\Delta\sigma_{\perp}^2 + 0.81\Delta\tau_{\parallel}^2}$, but the resulting fatigue damage is only calculated by the worst damage, which in this case is due to the principal stress.

Decreasing the constant a, with a less sensitive weld detail, can lead to smaller fatigue damage. Also, it is noted that when considering the principal stress, which is the maximum stress, the plane is different at every timestep for a multiaxial non-proportional stress state. This further justifies the fact that a smaller fatigue damage is seen at the deck with the hot spot plate multidirectional approach, where only one plane is examined at a time.

Comparing the normalized fatigue damage from the different methods and for different angles and DLCs, a higher damage is seen on the tower side. Therefore, steps can be taken to decrease the difference with the introduction of stiffeners at the part of the tower exceeding the barge, or with additional brackets from the tower to the upper deck to distribute the loads to more locations, as previously discussed.

4.2.9 Comparison of stresses at the tower and deck side

In addition to the fatigue damage plots, the different stress components and the principal stress P1 are presented in the following figures for an example element at $\theta = 230.9$ degrees, at both the tower and deck side, for FLS DLC D and for the coarse mesh during screening.

In Figure 114, it can be seen that $\sqrt{\Delta\sigma_{\perp}^2 + 0.81\Delta\tau_{\parallel}^2}$ is slightly larger than $0.9 * |P1|$ at the tower side. In contrary, on the deck side, $0.9 * |P1|$ has higher stress ranges, therefore leading to higher fatigue damage.

Looking at the stress components in Figure 116 and Figure 117, which are on the tower and deck side respectively, the following conclusions are derived:

- The shear stress component at the tower is very small, as already seen from the nominal shear stress equation with the forces/moments from SIMA. In contrary, the shear stress component at the deck is significant, as seen from the multiaxial screening with the 2-d stress space plots.
- The parallel stress component has almost the same magnitude with the perpendicular stress component at the deck, whereas at the tower, it is smaller. In combination with the increased shear stress at the deck, the ranges of the resulting principal stress P1 are higher at the deck, therefore leading to higher fatigue damage.

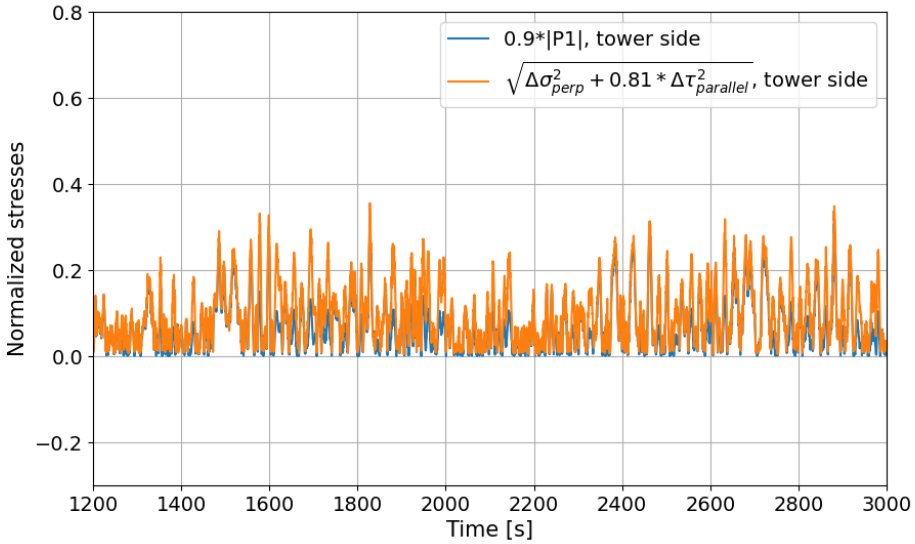

Figure 114: Comparison of the effective stresses in the hot spot plate fatigue method for FLS DLC D and the element at $\theta = 230.9$ degrees at the tower side (coarse mesh).

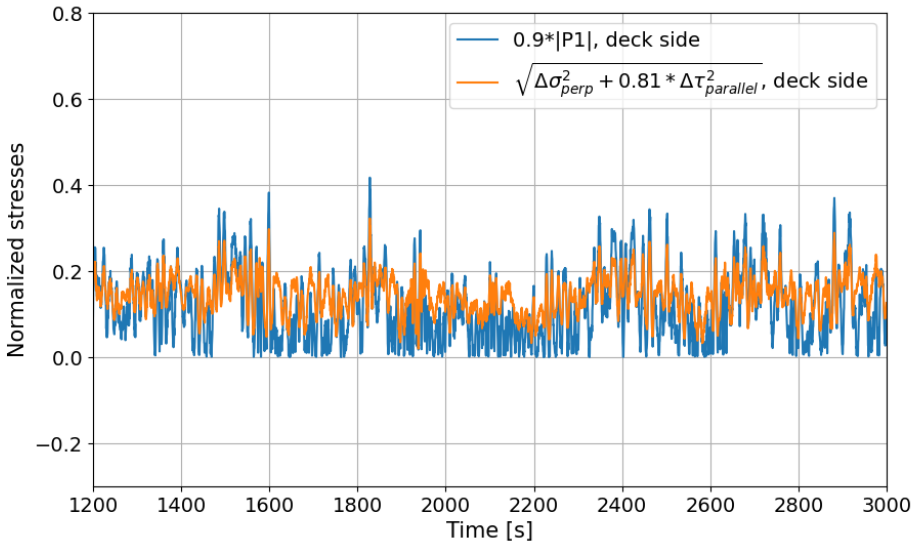

Figure 115: Comparison of the effective stresses in the hot spot plate fatigue method for FLS DLC D and the element at $\theta = 230.9$ degrees at the deck side (coarse mesh).

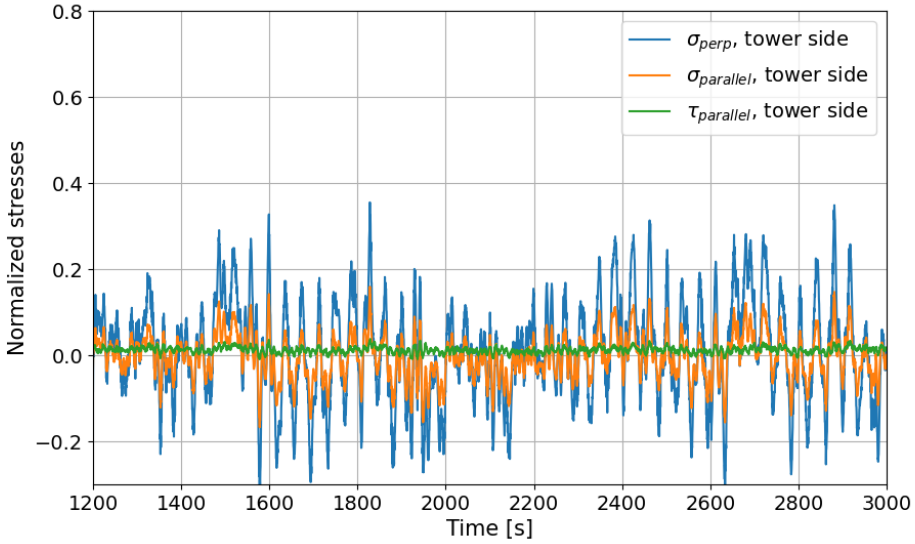

Figure 116: Comparison of the stresses components in the hot spot plate fatigue method for FLS DLC D and the element at $\theta = 230.9$ degrees at the tower side (coarse mesh).

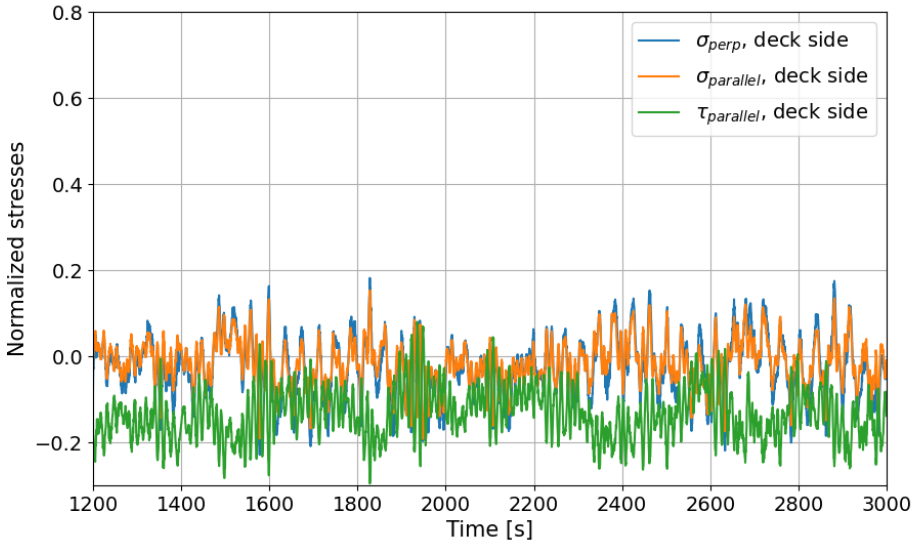

Figure 117: Comparison of the stresses components in the hot spot plate fatigue method for FLS DLC D and the element at $\theta = 230.9$ degrees at the tower side (coarse mesh).

5 Conclusions and Future Work

5.1 Conclusions

A thorough study was carried out in this thesis with the first design iteration of the WindBarge, a barge-type floater from Green Floating Marine Structures (GFMS), with a 15 MW wind turbine and a single mooring line layout with redundancy. The focus areas were the internal structure of the floater and the tower transition region. The main research topics included describing the stress distribution from the tower to the internal structure and the hull, screening the model for multiaxial conditions at the tower base, and fatigue damage calculation. A modification of the internal structure was proposed and studied, and the fatigue damage was assessed with different approaches. Therefore, the provided shell model of the floater was extended to include part of the tower.

At first, several offshore standards and recommended practices were identified and reviewed or referred to for guidelines about the design and simulation of offshore wind turbines, which are summarized in the following list:

- **DNV-OS-J101**: Design of Offshore Wind Turbine Structures (OFFSHORE STANDARD)
- **IEC 61400-1**: Wind turbines – Part 1: Design requirements (INTERNATIONAL STANDARD)
- **IEC 61400-3-2**: Wind energy generation systems – Part 3-2: Design requirements for floating offshore wind turbines (INTERNATIONAL STANDARD)
- **DNVGL-RP-C205**: Environmental conditions and environmental loads (RECOMMENDED PRACTICE)
- **DNVGL-ST-0437**: Loads and site conditions for wind turbines (STANDARD)
- **DNV-OS-J103**: Design of Floating Wind Turbine Structures (OFFSHORE STANDARD)
- **DNV-ST-0119**: Floating wind turbine structures (OFFSHORE STANDARD)
- **DNVGLRP-C203**: Fatigue design of offshore steel structures (OFFSHORE STANDARD)
- **LIFES50+**: Qualification of innovative floating substructures for 10MW wind turbines and water depths greater than 50m, Deliverable D7.2 Design Basis.

Also, background material from the WindBarge project was studied and utilized. For the simulations, DNV's software suite SESAM was used.

The wind and wave environment of the examined location was studied in combination with modeling techniques. The necessary design load cases from standards were identified and a selection was carried out for the most representative ones for this study. The internal structure was studied with the selected ultimate limit state (ULS) design load cases (DLCs), including operating and parked conditions.

Regarding the internal structure, the following general conclusions are derived:

- The loads from the tower and wind turbine are the main contributors to the stress response of the floater. The closer to the tower, the higher the stress levels. The pressure induced from the waves is not important, especially near the tower base.
- The dominating frequency in the stress time series of this innovative barge-type floater is mainly the roll eigenfrequency and secondary the wave peak frequency. For parked conditions, the pitch eigenfrequency becomes more relevant than the roll eigenfrequency. This is expected to be similar with other concepts, more or less, but somewhat different as it also depends on the eigenfrequencies of the design, the mooring lines configuration, and the stiffness of the whole system.
- The port side of the floater internally is more loaded than the starboard side during operation. This can be foreseen from the positive mean bending moment M_{x} and negative force F_{y}. In general, the stress components $(\sigma_{\mathrm{x}}, \sigma_{\mathrm{y}}, \tau_{\mathrm{xy}})$ can be associated with the external loads and the local shell element axes. For the parked condition, the longitudinal bulkheads are loaded more, as the pitch motion becomes more significant.

- By introducing additional bulkheads in the lateral direction of the floater, the stress level is reduced. The more loaded bulkhead is towards the port and stern side and can be associated with the positive mean bending moment M_x and M_y, respectively, and the negative and positive forces F_y and F_x as well. Therefore, the structure internally is not loaded uniformly. The outcomes of this study can be generally considered when designing similar floaters.

Moreover, a multiaxial screening based on a 2-dimensional representation of the stress space was carried out along the perimeter of the tower base for the shell elements at the deck of the floater. The following general conclusions are derived:

- A significant level of non-proportionality appears at the deck along the circumference of the tower. Around $\theta = 180, 270$ and 90 degrees, the fatigue damage importance and level of non-proportionality are the most critical. However, in other angles, the fatigue damage importance and non-proportionality can also be important, with or without the bulkheads inside, therefore, a combination of the external loading and the design defines them.
- A study was carried out to find out whether the direct shear contributing loads (torsion M_z and shear forces F_x and F_y) affect the multiaxial stress response. It is seen that the external loading affects the response, but it is not the main cause of non-proportionality, as the geometry is the most important factor.
- The extra bulkheads lead to a smaller maximum fatigue damage importance and level of non-proportionality, but overall, the changes differ from element to element. At the locations where the bulkheads were added, the level of non-proportionality reduced significantly.
- The increased plate thickness at the deck reduces the maximum stress ranges and, therefore, the fatigue damage importance. However, the level of non-proportionality is generally the same or increased. The length of the major axis of the ellipses is decreased with an increased thickness more than the length of the minor axis, therefore, maintaining or increasing the level of non-proportionality.

It is noted that the results depend on the mesh, which was relatively coarse in this study. Nevertheless, it is expected to still be representative of the stress state regarding multiaxiality. If the nodal forces and moments were available output from SESTRA, the mesh-insensitive structural stress would have been calculated instead.

In addition, it is highlighted that the applied screening does not include any cycle counting, therefore, the multiaxial fatigue damage importance does not represent the actual fatigue damage. It displays, though, the stress state.

The following approaches were considered for the fatigue damage assessment:

- **Nominal uniaxial fatigue**: the forces and moments at the tower base from the beam model in SIMA are used to calculate the nominal uniaxial stress and estimate fatigue damage, with and without a mean stress correction, using the rainflow algorithm.
- **Hot spot plate fatigue**: the effective stress $\Delta\sigma_{\text{Eff}} = \max\left\{\sqrt{\Delta\sigma_{\perp}^2 + 0.81\Delta\tau_{\parallel}^2}, \quad \alpha|\Delta\sigma_1|, \quad \alpha|\Delta\sigma_2|\right\}$ is calculated at the deck and tower side based on the stresses from the shell model.
- **Hot spot plate multidirectional fatigue**: the effective stress $\Delta\sigma_{\text{Eff}} = \gamma\sqrt{\Delta\sigma_{\perp}^2 + 0.81\Delta\tau_{\parallel}^2}$ is calculated at the deck and tower side based on the stresses from the shell model for different stress directions, therefore, different crack planes to identify the critical plane.

The derived conclusions are the following:

- The fatigue damage varies significantly along the circumference, with the most critical locations at $\theta = 90$ and 270 degrees, based on the nominal uniaxial fatigue approach.
- As the tower is under compression for an extensive period of time, the inclusion of a mean stress correction reduces the fatigue damage estimation at critical locations. Therefore, it is important to include it to avoid conservatism. At $\theta = 270$ degrees, the correction is more effective due to the positive mean bending moment Mx.

- The dominating frequency that causes fatigue is the roll eigenfrequency (the roll motion is increased due to the coupling with the yaw motion). Increasing primarily the roll damping and secondarily the yaw damping, reduces significantly the fatigue damage difference along the perimeter of the tower. Otherwise, a thickness (or diameter) increase of the tower would have been necessary. Alternatively, the roll stiffness may be increased to reduce roll motions, as discussed in Appendix E.
- The stresses from the actual design of the tower base, taken from the shell model with a txt mesh size, where t is the thickness of the plates, lead to a higher fatigue damage estimation at the tower side. At $\theta = 270$ degrees, it is now seen as more critical than at $\theta = 90$ degrees, which can be related to the higher stresses on the port side of the floater and signifies the importance of examining the actual design and not only the tower as a beam model. It is also seen that the multidirectional approach leads to a higher fatigue damage estimation at the tower than the hot spot plate fatigue approach.
- At the deck side, the hot spot plate fatigue damage is larger than the hot spot plate multidirectional fatigue damage because the principal stress $\Delta\sigma_1$ is more dominant there than at the tower side. Otherwise, the hot spot plate multidirectional fatigue damage would always lead to the same or larger fatigue damage estimation for some critical crack plane. As the normal stress component $\sigma_\perp$ mainly drives the crack, whether the estimation from the principal stress should be considered needs to be further assessed, as it changes orientation, therefore, considers different crack planes at the same time when calculating fatigue damage. Nevertheless, an important observation is that a parallel to the weld line stress component $\sigma_\parallel$ and shear stress appears on the deck side that increases the principal stress induced fatigue damage. In contrast, on the tower side, the principal stress induced fatigue damage is lower than the multidirectional approach.
- The critical fatigue locations from the multiaxial screening do not correspond completely to the actual fatigue critical locations on the deck side, as no cycle counting is applied. The most critical locations are towards the port side of the floater.

The above-mentioned conclusions highlight the importance of examining fatigue damage from all angles around the tower and considering the actual design. Damping can be increased with larger keels or by introducing fins. Advanced control strategies is another approach that can be considered with a floater-turbine coupled control. Feedback signals regarding the floater motions and position can be used to control the blade pitch angle or generator torque levels, as mentioned in DNV-ST-0119 [28]. An increased roll stiffness can be considered, but further studies are needed.

Supplementary studies were also carried out in Appendix E regarding the cause of roll motion. The following conclusions are derived:

- There is a coupling between the roll and yaw motion of the floater. They oscillate with the same frequency equal to the roll eigenfrequency. This coupling was also found in spar-type wind turbines [80]. In general, though, the yaw eigenfrequency depends on the pretension.
- An artificial yaw stiffness leads to no oscillations in roll. An artificial pitch stiffness also reduces roll motion, but less effectively than yaw stiffness. The roll/yaw coupling seems to be the main cause of the increased roll motions. Reducing yaw motions can reduce roll motions, therefore, lead to lower fatigue damage.
- Increasing the quadratic roll damping reduces roll motion more effectively than linear roll damping or yaw damping, but all of these changes are effective.
- The introduction of a yaw controller reduces the roll motion and increases the power output, signifying the importance of control strategies in such a dynamic system.
- A direct increase in the roll stiffness, which reduces the roll eigenperiod, can decrease the roll and yaw motion.

Finally, it is concluded that the design of such an innovative concept, a barge-type 15 MW floating wind turbine with a single mooring line layout, is mostly fatigue driven, as a potential thickness increase is not required by the yield strength of the material, but due to fatigue. Nevertheless, there are several measures to reduce the roll motion, which is the main contributor to fatigue, so that there is a smaller difference in fatigue damage along the perimeter of the tower base.

5.2 Future Work

The objectives of this study were achieved through specific tasks, as described in section 1.5. The multiaxiality has been investigated at the tower transition region for a barge-type floating wind turbine and the stress response of the internal structure has been associated with the external loading and the eigenfrequencies of the FOWT for ultimate limit state load cases. Moreover, the design of such a floating structure has been identified to be fatigue-driven.

Regarding the study of the internal structure, further studies are suggested for the future that can lead to additional design considerations:

- Simulation of additional design load cases, including operational or parked conditions with faults, start-up, and shutdown (normal and emergency), to study the response of the internal structure for all possible scenarios.
- Apart from the yield strength of the material and fatigue, the structure could also fail due to buckling. Therefore, a buckling analysis is needed for all structural members to make sure that they don't buckle and to identify buckling mode shapes.
- The stress response (and buckling) of the stiffeners may be also studied, as in this study only the plates were analyzed.

Regarding fatigue, an updated design iteration of the WindBarge may be studied with modifications that will reduce the roll motions, therefore, fatigue damage variation along the periphery of the tower base. Then, additional studies are also recommended for fatigue and multiaxiality, as follows:

- The selection of an appropriate SN curve seems to be challenging. It must account for both a multiaxial stress state and the actual connection of the tower and the barge. Different standards provide different SN curves and methodologies. The necessity of fatigue data from an experiment (e.g., with a scaled model of the FOWT or a prototype model) is highlighted in order to estimate fatigue damage with a more appropriate SN curve and to verify or improve fatigue damage estimation methods.
- The fatigue screening based on the 2-dimensional stress space representation and the MVEE is not representative of the actual fatigue damage, as no counting method is utilized. The screening procedure with DNV SESAM Core may be used and compared with the actual fatigue damage. However, this approach assumes a proportional stress state and the rainflow counting algorithm is used. A new methodology may be developed that accounts for the multiaxial stress state and utilizes a cycle counting method.
- Additional locations at the barge may be examined regarding multiaxiality. For example, at the locations of the stiffeners and the connection of the bulkheads with the tower internally and in the rest of the hull.
- From the literature review, it is seen that the Path Dependent Maximum Range Method considering the moment of load path (MLP-PDMR) is a promising fatigue damage accumulation method for a non-proportional stress state. This algorithm may be developed and compared with the hot spot plate multidirectional fatigue from DNV, which is based on the critical plane theory. For that purpose, the use of another software is also recommended (e.g., ANSYS, Abaqus) to derive the mesh-insensitive structural stress, instead of the element stresses.
- The artificial stress at the intersection of the tower with the bulkheads can be reduced by removing a small part of the bulkhead at the intersection with the tower. Also, the inclusion of stiffeners (rings) at the part of the tower exceeding the barge can be investigated regarding it influence on the stress levels. Moreover, additional external brackets from the tower to the upper deck may be studied regarding the new stress response, as the load path will be distributed to more locations.
- A comprehensive fatigue analysis would require additional load cases with more wind speeds and wave parameters, accounting for the joint probability density function (PDF) for the wind speed, significant wave height, and peak period. Also, simulating additional seeds can reduce statistical uncertainty.

References

[1] *Grammarly*. 2025. URL: https://www.grammarly.com/.

[2] Emilio Faraggiana, Giuseppe Giorgi, Massimo Sirigu, Alberto Ghigo, Giovanni Bracco, and Giuliana Mattiazzo. "A review of numerical modelling and optimisation of the floating support structure for offshore wind turbines". In: *Journal of Ocean Engineering and Marine Energy* 8.3 (2022), pp. 433–456. ISSN: 2198-6444. DOI: 10.1007/s40722-022-00241-2.

[3] Emma C. Edwards, Anna Holcombe, Scott Brown, Edward Ransley, Martyn Hann, and Deborah Greaves. "Evolution of floating offshore wind platforms: A review of at-sea devices". In: *Renewable and Sustainable Energy Reviews* 183 (2023), p. 113416. ISSN: 1364-0321. DOI: https://doi.org/10.1016/j.rser.2023.113416.

[4] Erin Bachynski-Polić. "Lecture notes and slides TMR03 - Integrated dynamic analysis of wind turbines". In: *NTNU* (). (Accessed: 11.10.2024).

[5] BW Ideol. *Ideol's floating foundation : construction methods*. Screenshot from YouTube video. Accessed: 01.03.2025. 2020. URL: https://www.youtube.com/watch?v=mqGLe0fMG8A&ab_channel=BWIdeol.

[6] Beridi. *Our Technology*. Accessed: 01.03.2025. URL: https://www.beridi.com/our-technology/.

[7] Rover Grupo. *Triwind*. Accessed: 01.03.2025. URL: https://www.rovergrupo.com/en/triwind.

[8] Beridi Maritime. *MEET TRIWIND (FULL VERSION)*. Screenshot from YouTube video. Accessed: 01.03.2025. 2021. URL: https://www.youtube.com/watch?v=zcMfF25N7Ig&ab_channel=BERIDIMARITIME.

[9] Beridi. *Design of a new Hexagonal Platform (Flowin Floater)*. Accessed: 01.03.2025. URL: https://www.beridi.com/design-of-a-new-hexagonal-platform/.

[10] *GFMS website*. (Accessed: 21.09.2024). URL: https://www.gfms.no/.

[11] Magne T. Bolstad and Jørgen R. Krokstad. "Functional Specification". In: *unpublished* (June 2023). (Report from the WindBarge project).

[12] Tor Huse Knudsen Jørgen R. Krokstad Arun Kamath and Erin Bachynski-Polić. "Design Basis Summary". In: *unpublished* (October 2024). (ID:RP M1.1.7 - Report from the WindBarge project).

[13] *SIMA DOCUMENTATION*. SINTEF. URL: https://www.sima.sintef.no/doc/4.6.0/sima/index.html.

[14] Tor Huse Knudsen. "Tower and floater assembly". In: *unpublished* (November 2023). (Report from the WindBarge project).

[15] Javier López-Queija, Eider Robles, Josu Jugo, and Santiago Alonso-Quesada. "Review of control technologies for floating offshore wind turbines". In: *Renewable and Sustainable Energy Reviews* 167 (2022), p. 112787. ISSN: 1364-0321. DOI: https://doi.org/10.1016/j.rser.2022.112787.

[16] C R Dos Santos, R Stenbro, L E Stieng, Ø W Hanseen-Bauer, F Wendt, N Psichogios, and A B Aardal. "Active control of yaw drift of single-point moored wind turbines". In: *Journal of Physics: Conference Series* 2767.3 (2024), p. 032014. ISSN: 1742-6588. DOI: 10.1088/1742-6596/2767/3/032014.

[17] T J Larsen and T D Hanson. "A method to avoid negative damped low frequent tower vibrations for a floating, pitch controlled wind turbine". In: *Journal of Physics: Conference Series* 75.1 (July 2007), p. 012073. DOI: 10.1088/1742-6596/75/1/012073.

[18] DNV. *Design of Offshore Wind Turbine Structures*. (OFFSHORE STANDARD DNV-OS-J101). May 2014.

[19] IEC. *Wind turbines – Part 1: Design requirements*. (INTERNATIONAL STANDARD IEC 61400-1). Aug. 2005.

[20] IEC. *Wind energy generation systems – Part 3-2: Design requirements for floating offshore wind turbines*. (INTERNATIONAL STANDARD IEC 61400-3-2). Jan. 2025.

[21] László Arany, Subhamoy Bhattacharya, John Macdonald, and S. John Hogan. "Simplified critical mudline bending moment spectra of offshore wind turbine support structures". In: *Wind Energy* 18.12 (2015), pp. 2171–2197. DOI: https://doi.org/10.1002/we.1812.

[22] DNV GL. *Environmental conditions and environmental loads*. (RECOMMENDED PRACTICE DNVGL-RP-C205). Aug. 2017.

[23] DNV GL. *Loads and site conditions for wind turbines*. (STANDARD DNVGL-ST-0437). Nov. 2016.

[24] N.D. Kelley and B.J. Jonkman. *Overview of the TurbSim Stochastic Inflow Turbulence Simulator*. NREL: National Renewable Energy Laboratory. Feb. 2007.

[25] Tiago Duarte, Sébastien Gueydon, Jason Jonkman, and António Sarmento. "Computation of Wave Loads Under Multidirectional Sea States for Floating Offshore Wind Turbines". In: *Proceedings of the International Conference on Offshore Mechanics and Arctic Engineering - OMAE* 9 (June 2014). DOI: 10.1115/OMAE2014-24148.

[26] Antonia Krieger, Gireesh Ramachandran, Luca Vita, Pablo Alonso, Joannès Berque, and Goren Aguirre. *LIFES50+ Qualification of innovative floating substructures for 10MW wind turbines and water depths greater than 50m, Deliverable D7.2 Design Basis*. Nov. 2015.

[27] DNV. *Design of Floating Wind Turbine Structures*. (OFFSHORE STANDARD DNV-OS-J103). June 2013.

[28] DNV. *Floating wind turbine structures*. (OFFSHORE STANDARD DNV-ST-0119). June 2021.

[29] Haoran Li, Zhiqiang Hu, Jin Wang, and Xiangyin Meng. "Short-term fatigue analysis for tower base of a spar-type wind turbine under stochastic wind-wave loads". In: *International Journal of Naval Architecture and Ocean Engineering* 10.1 (2018), pp. 9–20. ISSN: 2092-6782. DOI: https://doi.org/10.1016/j.ijnaoe.2017.05.003.

[30] IEC TC88-MT. "Iec 61400-3: Wind turbines–part 1: Design requirements". In: *International Electrotechnical Commission, Geneva* 64 (2005).

[31] *Joint Probability Distribution of Environmental Conditions for Design of Offshore Wind Turbines*. Vol. Volume 10: Ocean Renewable Energy. International Conference on Offshore Mechanics and Arctic Engineering. June 2017, V010T09A068. DOI: 10.1115/OMAE2017-61451.

[32] *Xtract User Manual*. DNV. URL: https://sesam.dnv.com/download/userdocumentation/xtract_um.pdf.

[33] "Lecture notes TMR 4190 Finite Element Methods in Structural Analysis". In: *NTNU* (). (Accessed: 03.02.2025).

[34] P. Dong. "A structural stress definition and numerical implementation for fatigue analysis of welded joints". In: *International Journal of Fatigue* 23.10 (2001), pp. 865–876. ISSN: 0142-1123. DOI: https://doi.org/10.1016/S0142-1123(01)00055-X.

[35] Hiroko Kyuba and Pingsha Dong. "Equilibrium-equivalent structural stress approach to fatigue analysis of a rectangular hollow section joint". In: *International Journal of Fatigue* 27.1 (2005), pp. 85–94. ISSN: 0142-1123. DOI: https://doi.org/10.1016/j.ijfatigue.2004.05.008.

[36] Pingsha Dong, Zhigang Wei, and Jeong K. Hong. "A path-dependent cycle counting method for variable-amplitude multi-axial loading". In: *International Journal of Fatigue* 32.4 (2010), pp. 720–734. ISSN: 0142-1123. DOI: https://doi.org/10.1016/j.ijfatigue.2009.10.010.

[37] DNV GL. *Fatigue design of offshore steel structures*. (RECOMMENDED PRACTICE DNVGL-RP-C203). Apr. 2016.

[38] *Fracture mechanics*. (Accessed: 27.04.2025). URL: https://en.wikipedia.org/wiki/Fracture_mechanics.

[39] M Janssen, J Zuidema, and RJH Wanhill. *Fracture Mechanics - 2nd Edition.* Vol. 2nd edition. Delft University Press, 2002. ISBN: 90-407-2221-8.

[40] J.H. den Besten. "fatigue resistance of welded joints in aluminium high-speed craft: A TOTAL STRESS CONCEPT". PhD thesis. Delft University of Technology, 2015.

[41] Paula van Lieshout, Henk den Besten, and Miroslaw Kaminski. "Multiaxial fatigue assessment of welded joints in marine Structures: Literature overview of progress in academia and engineering practice". In: *International Shipbuilding Progress* 65 (Dec. 2017), pp. 1–43. DOI: 10.3233/ISP-170141.

[42] Piotr Janiszewski. *rainflow 3.2.0*. Released: 17.4.2023. URL: https://pypi.org/project/rainflow/#description.

[43] ASTM. "Standard practices for cycle counting in fatigue analysis". In: *ASTM* (Reapproved 2011). Designation: E1049 − 85.

[44] G. J. Hayman. *MLife Theory Manual for Version 1.00*. NREL: National Renewable Energy Laboratory. Oct. 2012.

[45] Erin Elizabeth Bachynski. "Design and Dynamic Analysis of Tension Leg Platform Wind Turbines". PhD thesis. Norwegian University of Science and Technology, 2014.

[46] Marit I. Kvittem and Torgeir Moan. "Time domain analysis procedures for fatigue assessment of a semi-submersible wind turbine". In: *Marine Structures* 40 (2015), pp. 38–59. ISSN: 0951-8339. DOI: https://doi.org/10.1016/j.marstruc.2014.10.009.

[47] Xiaoming Ran and Erin E. Bachynski-Polić. "Time-domain simulation, fatigue and extreme responses for a fully flexible TLP floating wind turbine". In: *Marine Structures* 101 (2025), p. 103778. ISSN: 0951-8339. DOI: https://doi.org/10.1016/j.marstruc.2025.103778.

[48] Carlos Eduardo Silva de Souza and Erin E. Bachynski-Polić. "Design, structural modeling, control, and performance of 20 MW spar floating wind turbines". In: *Marine Structures* 84 (2022), p. 103182. ISSN: 0951-8339. DOI: https://doi.org/10.1016/j.marstruc.2022.103182.

[49] Helen Ege. "Investigation of the Tower Design for the Offshore Wind Turbine Concept OO-Star Wind Floater". MA thesis. Norwegian University of Science and Technology, 2019.

[50] Chin Tze Ng, Cetin Morris Sonsino, and Luca Susmel. "Multiaxial fatigue assessment of welded joints: A review of Eurocode 3 and International Institute of Welding criteria with different stress analysis approaches". In: *Fatigue & Fracture of Engineering Materials & Structures* 47.7 (2024), pp. 2616–2649. DOI: https://doi.org/10.1111/ffe.14319.

[51] Rick Donk. "Multi-axial fatigue strength assessment of a turret in a FPSO". MA thesis. Norwegian University of Science and Technology, 2019.

[52] J.L. Woudstra. "Multiaxial stress response in TLP-type FOWT substructures". MA thesis. Delft University of Technology, 2024.

[53] Traian I. Marin. "Fatigue Analysis of the Column-Pontoon Connection in a Semi-Submersible Floating Wind Turbine". MA thesis. Delft University of Technology, Norwegian University of Science and Technology, 2014.

[54] Nima Moshtagh. "Minimum volume enclosing ellipsoid". In: *http://www.mathworks.com/matlabcentral/fileexchange/9542* (Jan. 2006).

[55] Leonid G. Khachiyan. "Rounding of Polytopes in the Real Number Model of Computation". In: *Mathematics of Operations Research* 21.2 (1996), pp. 307–320. ISSN: 0364765X, 15265471. URL: http://www.jstor.org/stable/3690235 (visited on 03/25/2025).

[56] *Sesam Core TECHNICAL DOCUMENTATION*. DNV. URL: C:%5CProgram%20Files%5CDNV%5CSesam%20Core%20V4.0-00%5CDoc%5CSesamCoreTD.pdf.

[57] DNV GL. *Fatigue design of offshore steel structures*. (RECOMMENDED PRACTICE DNVGL-RP-C203) Amended September 2021. Sept. 2019.

[58] Mikkel Løvenskjold Larsen, Jörg Baumgartner, Henrik Bisgaard Clausen, and Vikas Arora. "Multiaxial fatigue assessment of welded joints using a principal component-based measure for non-proportionality". In: *International Journal of Fatigue* 158 (2022), p. 106731. ISSN: 0142-1123. DOI: https://doi.org/10.1016/j.ijfatigue.2022.106731.

[59] Jifa Mei and Pingsha Dong. "A new path-dependent fatigue damage model for non-proportional multi-axial loading". In: *International Journal of Fatigue* 90 (2016), pp. 210–221. ISSN: 0142-1123. DOI: https://doi.org/10.1016/j.ijfatigue.2016.05.010.

[60] Paula van Lieshout, Henk den Besten, and Miroslaw Kaminski. "Comparative study of multiaxial fatigue methods applied to welded joints in marine structures". In: *Frattura ed Integrità Strutturale* 10 (July 2016), pp. 173–192. DOI: 10.3221/IGF-ESIS.37.24.

[61] Zhen Gao, Daniel Merino, Kai-Jia Han, Haoran Li, and Stian Fiskvik. "Time-domain floater stress analysis for a floating wind turbine". In: *Journal of Ocean Engineering and Science* 8.4 (2023). Ocean Engineering for Future Marine Structures and Applications, pp. 435–445. ISSN: 2468-0133. DOI: https://doi.org/10.1016/j.joes.2023.08.001.

[62] Shuaishuai Wang, Torgeir Moan, and Zhen Gao. "Methodology for global structural load effect analysis of the semi-submersible hull of floating wind turbines under still water, wind, and wave loads". In: *Marine Structures* 91 (2023), p. 103463. ISSN: 0951-8339. DOI: https://doi.org/10.1016/j.marstruc.2023.103463.

[63] Andreas Landa. "Optimize structure based on dynamic analysis ULS and FLS". In: *unpublished* (August 2024). (Report from the WindBarge project).

[64] *HYDROD DOCUMENTATION*. DNV. URL: C:/Program%20Files/DNV/HydroD%20V7.1-01/Doc/UserManual/UserManual.html.

[65] DNV. *New Fast Time Domain Methods for Floating Offshore Wind Substructures*. (Accessed: 11.04.2025). 2024. URL: https://mysoftware.dnv.com/knowledge-centre/sesam-workflows/webinars/sesam-workflows-td/.

[66] *Sesam Wind Manager: Time History Fatigue Analysis using Response Reconstruction on a Floating OWT structure*. DNV. URL: https://mysoftware.dnv.com/knowledge-centre/sesam-workflows/help-library/tutorials/td-tutorials/.

[67] *SESAM MANAGER: Managing Sesam Workflow*. DNV. URL: https://sesam.dnv.com/download/userdocumentation/sesammanager-um.pdf.

[68] *SESTRA: Finite element analysis solver*. DNV. URL: https://sesam.dnv.com/download/userdocumentation/sestra-um.pdf.

[69] Fotios Theodorakis. *Structural assessment methods for a barge-type floating wind turbine*. Tech. rep. Norwegian University of Science and Technology, 2024.

[70] Evan Gaertner, Jennifer Rinker, Latha Sethuraman, Frederik Zahle, Benjamin Anderson, Garrett Barter, Nikhar Abbas, Fanzhong Meng, Pietro Bortolotti, Witold Skrzypinski, George Scott, Roland Feil, Henrik Bredmose, Katherine Dykes, Matt Shields, Christopher Allen, and Anthony Viselli. *Definition of the IEA 15-Megawatt Offshore Reference Wind Turbine*. English. National Renewable Energy Laboratory (NREL), 2020.

[71] C. Allen, A. Viscelli, H. Dagher, A. Goupee, E. Gaertner, N. Abbas, M.D. Hall, and G. Barter. *Definition of the UMaine VolturnUS-S Reference Platform Developed for the IEA Wind 15-Megawatt Offshore Reference Wind Turbine: IEA Wind TCP Task 37*. National Renewable Energy Laboratory (NREL), 2020.

[72] National Renewable Energy Laboratory (NREL). *IEA-15-240-RWT*. 2020. URL: https://github.com/IEAWindTask37/IEA-15-240-RWT.

[73] National Renewable Energy Laboratory (NREL). *ROSCO*. Version 0.1.0. 2019. URL: https://github.com/NREL/rosco.

[74] SP Mulders and JW van Wingerden. "Delft Research Controller: an open-source and community-driven wind turbine baseline controller". In: *Journal of Physics: Conference Series* 1037.3 (June 2018), p. 032009. DOI: 10.1088/1742-6596/1037/3/032009.

[75] Arun Kamath, Tor Huse Knudsen, and Idar Barstad. "Metocean design basis". In: *unpublished* (November 2023). (Report from the WindBarge project).

[76] Steven Winterstein, T.C. Ude, C.A. Cornell, P. Bjerager, and Sverre Haver. "Environmental parameters for extreme response: inverse FORM with omission factors". In: *Proc. of Intl. Conf. on Structural Safety and Reliability (ICOSSAR93)* (Jan. 1993).

[77] Jørgen R. Krokstad. "Establish load cases (DLCs)". In: *unpublished* (December 2024). (WindBarge technical note from GFMS).

[78] Arun Kamath. *NORA3 Scat Hs Tp Wsp7*. (Excel Spreadsheet for the WindBarge, accessed: 27.02.2025).

[79] Peter Welch. "The use of fast Fourier transform for the estimation of power spectra: A method based on time averaging over short, modified periodograms". In: *IEEE Transactions on audio and electroacoustics* 15.2 (2003), pp. 70–73.

[80] Herbjørn Haslum, Mathias Marley, Sachin Tejwant Navalkar, Bjørn Skaare, Nico Maljaars, and Haakon S. Andersen. "Roll–Yaw Lock: Aerodynamic Motion Instabilities of Floating Offshore Wind Turbines". In: *Journal of Offshore Mechanics and Arctic Engineering* 144.4 (Mar. 2022), p. 042002. ISSN: 0892-7219. DOI: 10.1115/1.4053697. URL: https://doi.org/10.1115/1.4053697.

[81] Erin E. Bachynski et al. *Marine Dynamics*. Department of Marine Technology, 2024.

[82] Martin O.L. Hansen. *AERODYNAMICS OF WIND TURBINES (THIRD EDITION)*. Routledge, 2015.

[83] Zhen Gao. "Lecture notes - Time-domain equations of motions with convolution terms and their replacement techniques". In: *NTNU* (2017). (Accessed: 11.10.2024).

[84] Xinmeng Zeng, Yanlin Shao, Xingya Feng, Kun Xu, Ruijia Jin, and Huajun Li. "Nonlinear hydrodynamics of floating offshore wind turbines: A review". In: *Renewable and Sustainable Energy Reviews* 191 (2024), p. 114092. ISSN: 1364-0321. DOI: 10.1016/j.rser.2023.114092.

[85] Maria Alonso Reig, Antonio Pegalajar-Jurado, Iñigo Mendikoa, Victor Petuya, and Henrik Bredmose. "Accelerated second-order hydrodynamic load calculation on semi-submersible floaters". In: *Marine Structures* 90 (2023), p. 103430. ISSN: 0951-8339. DOI: 10.1016/j.marstruc.2023.103430.

[86] Erin E. Bachynski and Torgeir Moan. "Ringing loads on tension leg platform wind turbines". In: *Ocean Engineering* 84 (2014), pp. 237–248. ISSN: 0029-8018. DOI: 10.1016/j.oceaneng.2014.04.007.

[87] Ying Tu, Zhengshun Cheng, and Michael Muskulus. "A review of slamming load application to offshore wind turbines from an integrated perspective". In: *Energy Procedia* 137 (2017), pp. 346–357. ISSN: 1876-6102. DOI: 10.1016/j.egypro.2017.10.359.

[88] Amin Ghadirian, Fabio Pierella, and Henrik Bredmose. "Calculation of slamming wave loads on monopiles using fully nonlinear kinematics and a pressure impulse model". In: *Coastal Engineering* 179 (2023), p. 104219. ISSN: 0378-3839. DOI: 10.1016/j.coastaleng.2022.104219.

[89] Wei-Liang Chuang. "On the fluid kinematics of common types of greenwater events: An experimental study". In: *Applied Ocean Research* 153 (2024), p. 104235. ISSN: 0141-1187. DOI: 10.1016/j.apor.2024.104235.

[90] Y. El khchine and M. Sriti. "Tip Loss Factor Effects on Aerodynamic Performances of Horizontal Axis Wind Turbine". In: *Energy Procedia* 118 (2017). 2017 2nd International Conference on Advances on Clean Energy Research (ICACER 2017), Berlin, Germany April 7-9, 2017, pp. 136–140. ISSN: 1876-6102. DOI: https://doi.org/10.1016/j.egypro.2017.07.028.

[91] DET NORSKE VERITAS. *STRENGTH ANALYSIS OF HULL STRUCTURES IN TANKERS*. (CLASSIFICSTIOIN NOTES). Jan. 1999.

[92] Lloyd's Register. *Procedure for Ship Units*. (ShipRight procedures). Feb. 2022.

[93] ABS. *SafeHull Finite Element Analysis of Hull Structures*. (GUIDANCE NOTES). July 2024.

[94] DNV AS. *Structural design of offshore units*. OFFSHORE STANDARDS. July 2024.

[95] DNV AS. *Finite element analysis*. (CLASS GUIDELINE). Aug. 2021.

[96] Haoyuan Gu and Hamn-Ching Chen. "Numerical simulation of a semi-submersible FOWT platform under calibrated extreme and irregular waves". In: *Ocean Engineering* 311 (2024), p. 118847. ISSN: 0029-8018. DOI: https://doi.org/10.1016/j.oceaneng.2024.118847.

[97] John Marius Hegseth, Erin Bachynski-Polić, and Madjid Karimirad. "Comparison and Validation of Hydrodynamic Load Models for a Semi-Submersible Floating Wind Turbine". In: June 2018, V010T09A075. DOI: 10.1115/OMAE2018-77676.

[98] Zhixin Zhao, Wenhua Wang, Wei Shi, Shengwenjun Qi, and Xin Li. "Effect of floating substructure flexibility of large-volume 10 MW offshore wind turbine semi-submersible platforms on dynamic response". In: *Ocean Engineering* 259 (2022), p. 111934. ISSN: 0029-8018. DOI: https://doi.org/10.1016/j.oceaneng.2022.111934.

[99] Michael Borg, Anders Hansen, and Henrik Bredmose. "Floating substructure flexibility of large-volume 10MW offshore wind turbine platforms in dynamic calculations". In: *Journal of Physics: Conference Series* 753 (Sept. 2016), p. 082024. DOI: 10.1088/1742-6596/753/8/082024.

Appendix

A Hydro-aero and dynamic time domain analysis of FOWT

At first, the hydrodynamic loads are examined, linear and nonlinear. Most of the theory regarding these loads is based on [81], except otherwise mentioned. Then, the aerodynamic loads are presented, for steady and dynamic wind and turbine conditions according to [82]. Finally, the dynamic time domain analysis procedure is presented according to [13] and [83].

Existing simulation tools do not account for the interaction between hydrodynamic and aerodynamic loads when calculating RAOs and QTFs [84]. An integrated tool that couples hydro-aero-servo-elastic loads is important to be developed for more accurate loads and responses. For this work, SIMA is used for the integrated analysis of the WindBarge, WADAM for the frequency domain analysis, and WASIM for the time domain analysis.

A.1 Hydrodynamic loads

A structure in the sea is subject to various loads from the water. In calm sea conditions, hydrostatic forces act on the floating structure, providing buoyancy to counteract the gravitational forces, and restoring forces to equilibrium. The excitation from the waves consists of one wave period (regular waves) or a number of wave periods that are summed up (irregular waves). These loads are called hydrodynamic loads because they vary with time. Currents are the continuous movement of water, however, they can induce a dynamic response due to vortex shedding around the structure.

Navier-Stokes equations

There are a few theories that model hydrodynamic loads. The Navier-Stokes equations are governing regarding fluid motions. The equations are:

$$\frac{\partial \boldsymbol{u}}{\partial t} + \boldsymbol{u} \cdot \nabla \boldsymbol{u} = -\frac{1}{\rho_{\mathrm{w}}} \nabla p + g + \nu \nabla^2 \boldsymbol{u} \tag{46}$$

where ρ_{w} is the density of the water, g is the acceleration of gravity, μ is the dynamic viscosity, ν is the kinematic viscosity ($\nu = \frac{\mu}{\rho_{\mathrm{w}}}$), p is the pressure, $\boldsymbol{u} = (u, v, w)$ is the velocity vector of the fluid and $\nabla = (\partial/\partial x, \partial/\partial y, \partial/\partial z)$ is the vector of partial derivatives.

Moreover, the continuity equation is considered to solve the problem:

$$\nabla \cdot \boldsymbol{u} = 0 \tag{47}$$

Computational Fluid Dynamics (CFD) is required to solve the Navier-Stokes equation, which is computationally intensive.

Potential flow theory

Some simplifications can be made to reduce the computational time, which form the potential flow theory:

- The fluid is inviscid ($\nu = 0$), so there are no shear forces.
- The flow is irrotational ($\nabla \times \boldsymbol{u}$).

The velocity potential ϕ is introduced, so that $\boldsymbol{u} = (u, v, w) = \nabla\phi$. Therefore:

$$u = \frac{\partial \phi}{\partial x}, \qquad v = \frac{\partial \phi}{\partial y}, \qquad w = \frac{\partial \phi}{\partial z}, \tag{48}$$

The limitation of the potential flow theory is that the flow separation is not modeled, so no vortices are considered and damping due to the flow separation is not accounted for. This has an impact especially in roll damping due to the bilge keels.

Bernoulli equation

Based on these assumptions, the Bernoulli equation is derived:

$$p = -\rho_{\mathrm{w}} \frac{\partial \varphi}{\partial t} - \frac{\rho_{\mathrm{w}}}{2} \nabla\varphi \cdot \nabla\varphi - \rho_{\mathrm{w}} g z + C(t) \tag{49}$$

where the first term on the right-hand side is the dynamic pressure, the second is the quadratic pressure, the third is the hydrostatic pressure and the fourth is a constant equal to the atmospheric pressure.

Also, the Laplace equation is derived from the continuity of mass as:

$$\nabla\phi^2 = 0 \tag{50}$$

By solving for the unknown velocity potential ϕ, we can then calculate the velocity field $\boldsymbol{u}$ and the pressure p.

Boundary value problem (BVP)

This problem is called the boundary value problem (BVP) and requires numerical methods. WADAM (Wave Analysis by Diffraction and Radiation Analysis Method) by DNV GL and WAMIT (Wave Analysis by the Method of Integral Equations) are two computational tools for the BVP. The numerical method, called the Boundary Element Method (BEM), requires discretizing the body's wetted surface. Therefore, these codes are also called panel codes.

Both the second order problem and the first order problem (linearized BVP) can be solved with these codes, whereas the former takes significantly more time. Kinematics and dynamic free-surface conditions are applied by utilizing Taylor expansion. The first-order BVP is solved based on the mean wetted body surface, however, higher-order BVP requires knowledge of the instantaneous free surface and wetted body surface [84]. The second-order BVP utilizes the linear velocity potential and introduces products of it to account for the sum- and difference-frequency nonlinear terms. For more information about the linearization procedure and the boundary conditions applied, the reader can refer to [81] or any other hydrodynamics book.

Linear wave theory

The linear wave theory doesn't consider any stucture present. The solution to the linearized BVP provides the following equations for shallow water depth:

$$\varphi(x, y, z, t) = \frac{g\zeta_\alpha}{\omega} \frac{\cosh k(z+h)}{\cosh kh} \cos(\omega t - kx) \tag{51}$$

$$\zeta(x, y, t) = \zeta_\alpha \sin(\omega t - kx) \tag{52}$$

$$\omega^2 = gk \tanh kh \tag{53}$$

where ζ is free-surface elevation, ζ_α is the wave amplitude, $\omega = 2\pi/T_{\mathrm{w}}$ is the wave frequency, T_{w} is the wave period, h is the water depth, $k = 2\pi/\lambda_{\mathrm{w}}$ is the wave number, λ_{w} is the wavelength, x refers to the horizontal position and z refers to the vertical position. The last equation relates the wave frequency ω with the wave number k and is called the dispersion relation.

In the case of deep water depth, the solution to the BVP provides the following equations:

$$\varphi(x, y, z, t) = \frac{g\zeta_a}{\omega} e^{kz} \cos(\omega t - kx) \tag{54}$$

$$\zeta(x, y, t) = \zeta_a \sin(\omega t - kx) \tag{55}$$

$$\omega^2 = gk \tag{56}$$

The WindBarge is designed for water depths up to 80 m, therefore the equations for the shallow/intermediate water depth are applicable.

Frequency and time domain

Since the problem is linear, it is possible to solve for the steady-state response for each wave frequency. This frequency domain approach produces the Response Amplitude Operators (RAOs), which provide the amplitude and phase for each degree of freedom for all relevant wave frequencies. RAOs are an output from WADAM or WAMIT.

The restoring, added mass, and damping coefficients, as well as additional second-order elements and loads, can be used as input for the dynamic equations of the system, which are then solved in the time domain to obtain the responses. This can be done in SIMA (Simulation of Marine Applications). This approach is necessary to account for transient and higher-order phenomena that can lead to large system responses.

Wave diffraction

When the structure disturbs the flow, the waves are diffracted. For a small body compared to the wavelength, there is no wave diffraction, only locally, since the flow cannot go through the body. It is often used in practice the following limit: if $\lambda_w/D > 5$, where D is the horizontal dimension, then there is no wave diffraction [81]. When the dimensions are considerable, the water surface is disturbed and causes wave diffraction. For the WindBarge, it is $D = 30m$ and for a water depth at $h = 40m$ (Creyke Beck) and a wave period $T_w = 6s$, then we get from Equation 53 that $\lambda_w = 56m$, therefore the ratio $\lambda_w/D = 1.87 < 5$ and the wave diffraction is significant.

In general, shorter waves are more easily diffracted than long waves. The diffraction forces are included in the Morison equation with the strip theory approach. However, Morison's equation doesn't account for the free-surface diffraction, as, for example, in the MacChamy-Fuchs solution for vertical cylinders. As a result, the wave loads are overestimated in large-volume structures when free-surface diffraction is significant. With the BEM approach, the diffraction is inherently accounted for with the discretization of the wetted body (panel model) and the potential flow theory.

Velocity potentials

Since the problem is linear, the total velocity potential ϕ can be expressed as a sum of the following potentials (super-position): the incident wave velocity potential, the diffraction velocity potential, and the radiation velocity potentials for the six degrees of freedom (DOFs) of rigid bodies. When the structure is moving in a calm sea, waves are generated in all DOFs and this is called radiation.

The different problems are solved separately. The diffraction problem provides the wave excitation forces and the radiation problem provides the added mass and damping coefficients. The second-order BVP problem provides sum- and difference-frequency terms for the loads. They are necessary for large-volume structures with mooring systems to account for the low-frequency motions in irregular waves [81].

Wave excitation loads

The wave excitation loads are derived from the diffraction problem. The dynamic pressure is multiplied by the normal of each degree of freedom n_j and integrated along the mean wetted body surface S_0:

$$F_j^{\text{exc}} = \rho_w \int_{S_0} \frac{\partial \varphi_{\text{incident}}}{\partial t} n_j dS + \rho_w \int_{S_0} \frac{\partial \varphi_{\text{diffraction}}}{\partial t} n_j dS \tag{57}$$

The first term is the Froude-Kriloff force (due to the motion of water particles), and the last is the diffraction force. The $\varphi_{\text{incident}}$ is calculated based on the linear wave theory, and the $\varphi_{\text{diffraction}}$ is derived numerically according to [81].

Restoring, added mass and damping coefficients

The hydrostatic pressure ($-\rho g z$) in the Bernoulli equation provides the buoyancy and the restoring forces to counteract the gravitational forces when the structure is not in equilibrium. The hydrostatic forces and moments are calculated by integrating along the instantaneous wetted surface S_B:

$$\mathbf{F}_{\text{hs}} = \int_{S_{\text{B}}} \rho_{\text{w}} g z \mathbf{n} dS \tag{58}$$

$$\mathbf{M}_{\text{hs}} = \int_{S_{\text{B}}} \rho_{\text{w}} g z (\mathbf{r} \times \mathbf{n}) dS \tag{59}$$

They provide the hydrostatic coefficients C_{ij}, which give the hydrostatic forces in DOF i due to a displacement in DOF j.

The dynamic pressure $\rho \frac{\partial \varphi}{\partial t}$ in the Bernoulli equation, multiplied with the normal of each degree of freedom n_j, is integrated along the wetted surface S_0:

$$\mathbf{F}_{jk}^{hd} = \rho_{\text{w}} \int_{S_0} \frac{\partial \varphi_k}{\partial t} n_j \text{dS} \tag{60}$$

The hydrodynamic load can be expressed in the following form:

$$\mathbf{F}_{jk}^{hd} \equiv -A_{jk}(\omega)\ddot{\eta}_j - B_{jk}(\omega)\dot{\eta}_j \tag{61}$$

where $A_{jk}(\omega)$ are the added mass coefficients, $B_{jk}(\omega)$ are the damping coefficients, which are frequency dependent, and $\dot{\eta}_j, \ddot{\eta}_j$ are the velocity and acceleration of DOF j.

All these coefficients are necessary to form the dynamic equations of the system in order to simulate it in SIMA.

Morison equation

Since the viscous effects were neglected in the potential flow theory, it is now necessary to include the viscous damping. This is implemented in 2D with the Morison equation:

$$F_{\text{m}}(t) = \rho_{\text{w}} \frac{\pi}{4} C_{\text{f}} a_{\text{w}}(t) + \rho_{\text{w}} \frac{\pi}{4} C_{\alpha} a_{\text{r}}(t) + \frac{1}{2} \rho_{\text{w}} D C_{\text{D}} u_{\text{r}}(t) u_{\text{r}}(t) \tag{62}$$

where C_{α} is the added mass coefficient, D is a characteristic dimension of the body, C_{D} is the drag coefficient, $\alpha_{\text{w}}(t)$ is the acceleration of the water, and $u_{\text{r}}(t)$ is the relative velocity of the water. The drag coefficient C_{D} is determined with experiments in the water. The strip theory is used, where the body is divided vertically into strips, upon which the loads are calculated and then summed up.

The first term in the equation is the Froude-Kriloff force, the second is the diffraction and radiation forces and the last is the viscous drag. The viscous term contributes to the damping of the system and it is important to include it in order not to overestimate the loads. This damping term can be described by a quadratic term as $B_{jj}^{(2)} \eta_j |\eta_j|$ for a non-coupled DOF j. The quadratic damping coefficient $B_{jj}^{(2)}$ can be found from experiments or CFD.

Combining the potential flow theory and the Morison equation is the standard procedure to model the hydrodynamic loads [81]. The nonlinear hydrodynamic effects are significant in the design of floating structures, as they can influence the wave-frequency and low-frequency responses [84].

Wave drift forces and ringing or springing

The second-order dynamics introduce squared wave amplitude and sum- and difference-frequencies in the loads and responses [84]. The difference-frequency loads, also called low-frequency or slow-drift loads, contribute significantly to horizontal motion. It is important to include them to avoid underestimation of the responses of the floating offshore wind turbines (FOWTs) and the mooring loads.

Newman's approximation, Pinkster's approximation, and the full Quadratic Transfer Function (QTF) can be used to solve the second-order problem, as presented in [85] and mentioned in [84]. Moreover, CFD can be used to tune engineering models to achieve higher fidelity [84].

Ringing refers to high-frequency responses from extreme, transient waves that cause structural resonance. Springing refers to second-order sum-frequency wave responses in steady-state. TLPs are susceptible to these resonances because they have high eigenfrequencies (in heave and pitch) compared to the other FOWTs (e.g. barge) [86].

Wave slamming

A wave with a large amount of energy that breaks upon a structure generates a high slamming load for a short time in a small area (plunging breaking wave) [87]. The Morison equation does not include the forces from breaking waves. An additional term can be added, formulated as:

$$F_{\mathrm{S}} = \int_{l} C_{\mathrm{s}}(z) \frac{1}{2} \rho_{\mathrm{w}} U(z)^2 W(z)\, dz \tag{63}$$

where C_{s} is the slamming coefficient, U is the water velocity, W is the effective width of the structure and l is the impact height. According to [87], there are different criteria and calculation methods that can be used (with an engineering problem or CFD).

In simulation tools, the slamming load can be added indirectly via an extra inertial or drag term in Morison's equation, except otherwise defined. In [88], they proposed a pressure impulse-based slamming model with nonlinear wave kinematics and validated it experimentally with a cylinder in extreme wave conditions. In SIMA [13], the slamming force is related to the change of added mass with time.

The slamming forces are significant and must be considered in the design process of a structure based on ULS, to be within safe stress limits.

Greenwater

Greenwater is the phenomenon where seawater goes over the structure, propagates, and breaks. In [89], different types of greenwater are investigated experimentally, and numerical simulation methods are summarized. The velocity field of different types were acquired, and the different phases and behaviours of the flow were identified. The greenwater is important to be investigated for the safety of personnel on the deck and any equipment there.

A.2 Aerodynamic loads

The aerodynamic loads are presented for steady conditions (constant wind speed, rotational speed, pitch angle) and unsteady conditions (dynamic wind inflow, varying pitch angle and rotational speed).

One-dimensional momentum theory

A simple disk is considered for an infinite-blade wind turbine with steady-state, incompressible, frictionless, and non-rotating flow. The control volume of Figure 118 is then utilized.

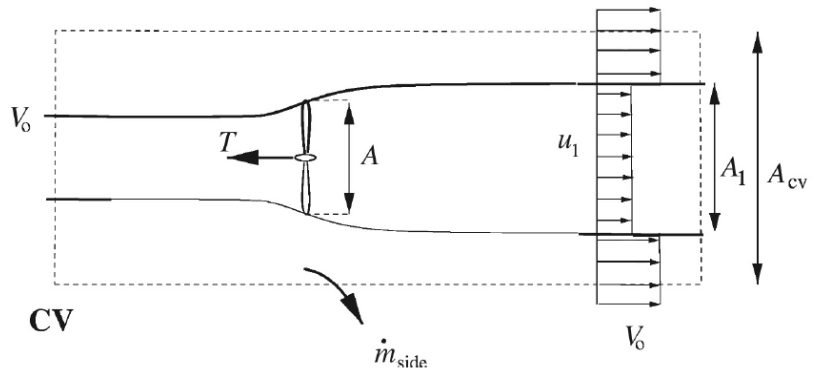

Figure 118: Control volume of wind turbine [82].

Applying Bernoulli's equation, axial momentum in the control volume, and the conservation of mass, the following equations are derived:

$$u = (1 - a)V_o \tag{64}$$

$$P = 2\rho V_o^3 A a(1 - a)^2 \tag{65}$$

$$T = 2\rho V_o^2 A a(1 - a) \tag{66}$$

$$C_P = \frac{P}{\frac{1}{2}\rho V_o^3 A} = 4a(1 - a)^2 \tag{67}$$

$$C_T = \frac{T}{\frac{1}{2}\rho V_o^2 A} = 4a(1 - a) \tag{68}$$

where α is the axial induction factor defined in Equation 64 (see Figure 119), ρ is the density of the air, P s the power output, T is the thrust, A is the area of the rotor, C_P is the power coefficient, and C_T is the thrust coefficient. The maximum power coefficient is $C_{P,max} = 16/27 = 59\%$ (Betz limit) for $a = 1/3$.

However, there is some rotation of the wake, and the tangential induction factor a' is now introduced. The velocity triangles are commonly used to present the velocities in a section of the blade, as shown in Figure 119.

The flow angle ϕ (angle between the relative velocity and the rotational plane) is defined as:

$$tan\phi = \frac{a'\omega r}{aV_o} = \frac{(1 - a)V_o}{(1 + a')\omega r} \tag{69}$$

where r is the radial position of the blade section and ω is the turbine's rotational speed.

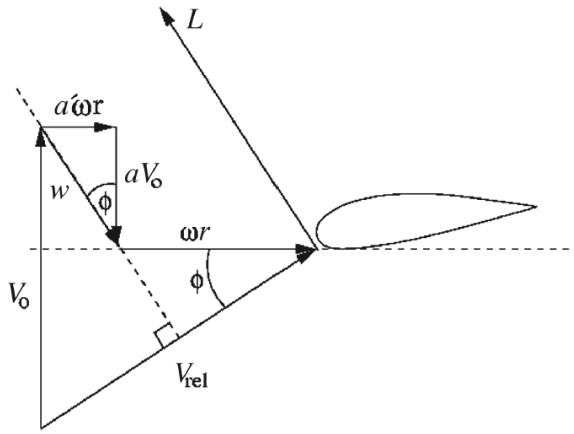

Figure 119: Velocity triangles of a blade section [82].

Blade element momentum theory

A streamtube is utilized in the blade element momentum (BEM) method with annular elements to derive the formulas for the thrust, power, and torque. As presented in Figure 120, the angle θ is the angle between the rotor plane and the chord, and it's called pitch angle, whereas the angle α is the angle between the relative velocity and the chord, and it's called the angle of attack. Therefore, it is $\alpha = \phi - \theta$.

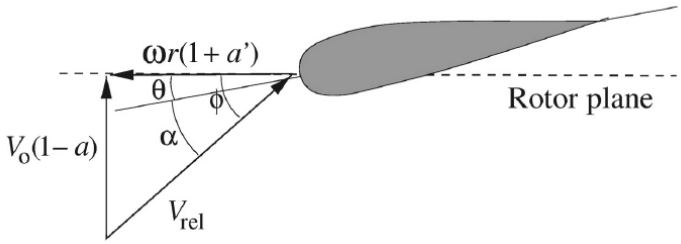

Figure 120: Blade section velocities [82].

The lift l and drag d force per length in a blade section are depicted in Figure 121 and expressed as:

$$l = \frac{1}{2}\rho V_{\text{rel}}^2 c C_{\text{l}} \tag{70}$$

$$d = \frac{1}{2}\rho V_{\text{rel}}^2 c C_{\text{d}} \tag{71}$$

where c is the chord length, C_{l} is the lift coefficient, C_{d} is the drag coefficient, and V_{rel} is the relative wind velocity.

The normal p_{N} and tangential p_{T} forces are also introduced along with the normal C_{n} and tangential C_{t} force coefficients:

$$p_{\text{N}} = l cos\phi + d sin\phi \tag{72}$$

$$p_{\text{T}} = l sin\phi - d cos\phi \tag{73}$$

$$C_{\text{N}} = C_{\text{l}} cos\phi + C_{\text{d}} sin\phi \tag{74}$$

$$C_T = C_{\text{l}} sin\phi - C_{\text{d}} cos\phi \tag{75}$$

$$C_{\mathrm{n}} = \frac{p_{\mathrm{N}}}{\frac{1}{2}\rho V_{\mathrm{rel}}^2 c} \tag{76}$$

$$C_{\mathrm{t}} = \frac{p_{\mathrm{T}}}{\frac{1}{2}\rho V_{\mathrm{rel}}^2 c} \tag{77}$$

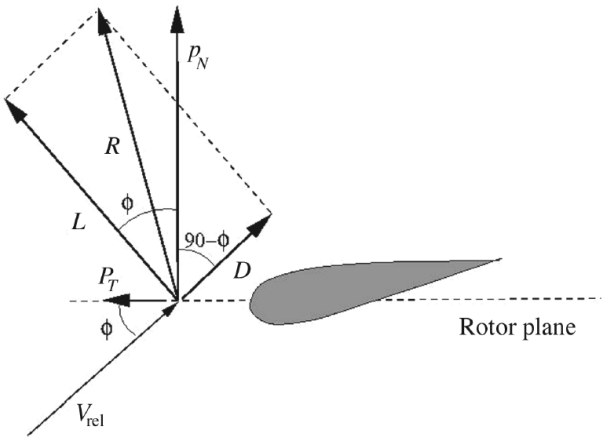

Figure 121: Blade section loads [82].

The variable σ is defined, which is called solidity, and it is expressed as:

$$\sigma(r) = \frac{c(r)B}{2\pi r} \tag{78}$$

where B is the number of blades.

Then, the normal force dT and the torque dM per strip dr are expressed as:

$$dT = \frac{1}{2}\rho B \frac{V_{\mathrm{o}}^2(1-a)^2}{sin^2\phi} c C_{\mathrm{n}} dr \tag{79}$$

$$dM = \frac{1}{2}\rho B \frac{V_{\mathrm{o}}(1-a)\omega r(1+a')}{sin\phi cos\phi} c C_{\mathrm{t}} r dr \tag{80}$$

The axial a and tangential a' induction factors are finally expressed as:

$$a = \frac{1}{\frac{4sin^2\phi}{\sigma C_{\mathrm{n}}} + 1} \tag{81}$$

$$a' = \frac{1}{\frac{4sin\phi cos\phi}{\sigma C_{\mathrm{t}}} + 1} \tag{82}$$

The BEM algorithm is solved for each strip dr, which are considered independent. An iteration is required to identify the axial a and tangential a' induction factors, starting with an initial guess, calculating the flow angle ϕ and the angle of attack α, and then the normal C_{n} and tangential C_{t} force coefficients. The lift C_{l} and drag C_{t} force coefficients are predefined and read from look-up tables. The induction factors are calculated and the process is repeated until convergence, over a specified tolerance. Finally, the loads on the blade sections can be calculated.

BEM corrections

Prandtl's tip loss factor F

The BEM theory considers an infinite number of blades. Prandtl's tip loss factor F is used as a correction to account for the finite number of blades, considering that the helical vortex wake modeled as vortex sheets has no effect on the wake and is conveyed by the flow [90]. F is expressed as follows:

$$F = \frac{2}{\pi} cos^{-1}[exp(-\frac{B}{2}\frac{R-r}{rsin\phi})] \tag{83}$$

where R is the wind turbine radius. The calculation of F in the BEM algorithm is required at each iteration.

The axial a and tangential a' induction factors are then corrected and expressed as:

$$a = \frac{1}{\frac{4Fsin^2\phi}{\sigma C_\mathrm{n}} + 1} \tag{84}$$

$$a' = \frac{1}{\frac{4Fsin\phi cos\phi}{\sigma C_\mathrm{t}} + 1} \tag{85}$$

Induction factors

For induction factors higher than 0.4, the relation between the thrust coefficient C_T and axial induction factor a is inaccurate. Different empirical equations correct this, such as Wilson and Walker, and Glauert correction [82].

In SIMA, the following relation by Burton et al is used:

$$a = \frac{C_\mathrm{T}/F - C_\mathrm{T1}}{C_\mathrm{T2} - C_\mathrm{T1}}(a_2 - a_1) - a_1 \tag{86}$$

where $a_2 = 1$, $C_\mathrm{T2} = 1.82$, $a_1 = 1 - 0.5\sqrt{C_\mathrm{T2}}$, and $C_\mathrm{T1} = 4a_1(1 - a_1)$.

Both Equation 84 and Equation 86 must be satisfied and they are solved iteratively in the BEM algorithm until convergence is achieved.

The 15 MW NREL wind turbine [70] is used in the WindBarge concept as the reference wind turbine. The tip speed ratio $\lambda = \frac{\omega R}{V_\mathrm{o}}$ and pitch angle θ_p can be adjusted to obtain the optimal values for the power C_P and thrust C_T coefficients, as shown in Figure 122. In this case, the optimal values are $\lambda = 9$ and $\theta_\mathrm{p} = 0\,\mathrm{deg}$. Common tip speed ratios λ are around 8-10.

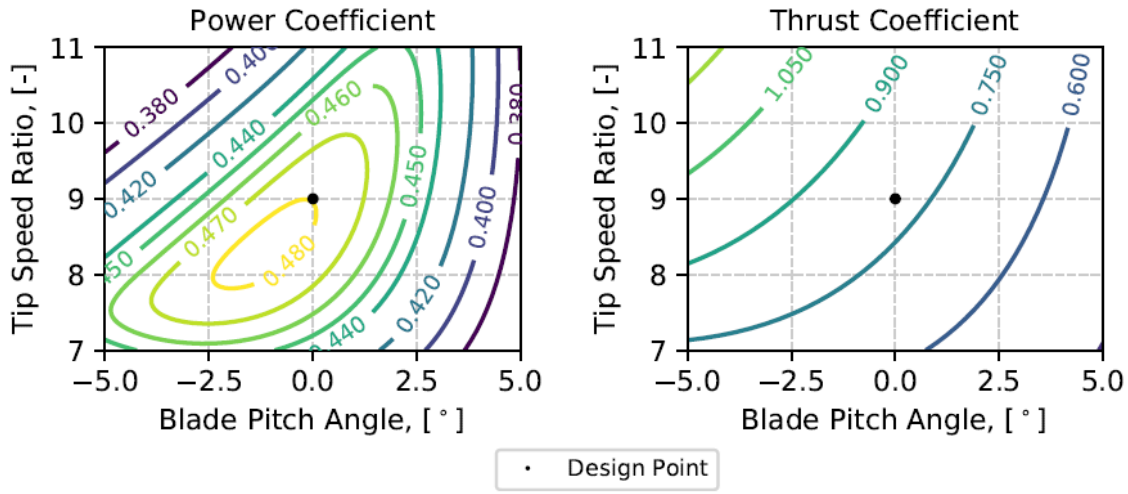

Figure 122: Power coefficient C_P and thrust coefficient C_T dependence on pitch angle θ_p and tip speed ratio λ [70].

Dynamic inflow (wake and stall)

Dynamic wake

The BEM method considers quasi-static conditions. However, the wind speed and direction is varying with time, the blades are pitching, and the tower is moving. Therefore, there is a time delay in the induced velocities due to the vorticity being convected downstream. A commonly used filter for the dynamic wake is from Stig Øye with the following differential equations:

$$W_{\text{int}} + \tau_1 \frac{dW_{\text{int}}}{dt} = W_{\text{qs}} + k \cdot \tau_1 \frac{dW_{\text{qs}}}{dt} \tag{87}$$

$$W + \tau_2 \frac{dW}{dt} = W_{\text{int}} \tag{88}$$

where W_{qs} is the quasi-static induced velocity, W_{int} in an intermediate induced velocity, τ_1 and τ_2 are time constants, k is a parameter equal to 0.6, and W is the filtered induced velocity.

Dynamic stall

Also, the angle of attack changes dynamically and the response depends on the boundary level attachment. When there is separation at the trailing edge of the airfoil, a dynamic stall model is used for the changing lift and drag coefficients. In SIMA, the Stig Øye model is considered as a filter according to the following equation:

$$C_{\text{l}} = f_{\text{s}} C_{\text{l,inv}}(\alpha) + (1 - f_{\text{s}}) C_{\text{l,fs}}(\alpha) \tag{89}$$

where f_{s} is the degree of stall, $C_{\text{l,inv}}$ is the lift coefficient without separation, and $C_{\text{l,fs}}$ is the lift coefficient for full separation.

The reader can refer to [82] and [13] for more information about the wake and stall model.

Additional corrections

Yaw/tilt

For a rotor tilt angle and a yaw angle between the rotor and the incoming wind, the induced velocities vary at different locations of the blade. The induction factor a is then corrected according to the following Glauert formula [13]:

$$a_{\text{skew}} = a[1 + tan(\frac{\chi}{2})(\frac{r}{R})cos(\Psi)] \tag{90}$$

where χ is the wake skew angle (angle between the rotation axis and the wind velocity), and Ψ is the azimuth angle, which equal to zero at the at the most downwind point. The yaw/tilt model is necessary to be included to account for the restoring yaw moment from the upstream blades.

Tower shadow

Also, the local inflow is modified due to the tower's presence and a velocity deficit is developed upwind of the tower. The potential flow model is corrected using the following formulas to calculate the velocity factors x_{infl} and y_{infl}:

$$x_{\text{w}} = \frac{2x}{D_{\text{tow}}} \tag{91}$$

$$y_{\text{w}} = \frac{2y}{D_{\text{tow}}} \tag{92}$$

$$x_{\text{infl}} = \left[1 - \frac{(x_{\text{w}} + b)^2 - y_{\text{w}}^2}{\left((x_{\text{w}} + b)^2 + y_{\text{w}}^2\right)^2} + \frac{C_{\text{D}}}{2\pi} \frac{x_{\text{w}} + b}{(x_{\text{w}} + b)^2 + y_{\text{w}}^2} \right] \tag{93}$$

$$y_{\text{infl}} = -2\left[\frac{(x_{\text{w}}+b)\,y_{\text{w}}}{\left((x_{\text{w}}+b)^2+y_{\text{w}}^2\right)^2}+\frac{C_{\text{D}}}{2\pi}\frac{y_{\text{w}}}{(x_{\text{w}}+b)^2+y_{\text{w}}^2}\right] \tag{94}$$

where D_{tow} is the local tower diameter, and b is the Bak coefficient. The wind speed is multiplied with these factors and the The reader can refer to SIMA documentation [13] for more information about these equations.

A.3 Dynamic time domain analysis

In SIMA, SIMO is used for the simulation of motions of complex floating systems. It simulates nonlinearities in the time domain from waves and low frequency forces. RIFLEX is used for flexible risers and slender structures (tower, blades, mooring line).

SIMO

The dynamic equations of the system according to SIMA documentation [13] can be expressed as:

$$\mathbf{M}\ddot{\mathbf{x}} + \boldsymbol{C}\dot{\mathbf{x}} + \mathbf{D}_1\dot{\mathbf{x}} + \mathbf{D}_2\dot{\mathbf{x}}|\dot{\mathbf{x}}| + \mathbf{K}(\mathbf{x})\mathbf{x} = \mathbf{q}(t,\mathbf{x},\dot{\mathbf{x}}) \tag{95}$$

with

$$\mathbf{M} = \mathbf{m} + \mathbf{A}(\omega) \tag{96}$$
$$\mathbf{A}(\omega) = \mathbf{A}_\infty + \alpha(\omega) \tag{97}$$
$$\mathbf{C}(\omega) = \mathbf{C}_\infty + \mathbf{c}(\omega) \tag{98}$$

where $\mathbf{M}$ is the frequency-dependent mass matrix, $\mathbf{m}$ is the body mass matrix, A is the frequency-dependent added-mass ($\mathbf{A}_\infty = \mathbf{A}(\omega = \infty)$), $\mathbf{C}$ is the frequency-dependent potential damping matrix ($\mathbf{C}_\infty = \mathbf{C}(\omega = \infty) = 0$), $\mathbf{D}_1$ is the linear damping matrix, $\mathbf{D}_2$ is the quadratic damping matrix, $\mathbf{K}$ is the hydrostatic stiffness matrix, $\mathbf{x}$ is the position vector, and $\mathbf{q}$ is the excitation force vector (wind and current drag, first and second order wave excitation forces, wave drift damping).

In the frequency domain, the equation becomes:

$$(\omega^2\mathbf{A}(\omega) + i\omega\mathbf{C}(\omega))\mathbf{X}(\omega) = \mathbf{F}(\omega) \tag{99}$$

where $\mathbf{F}(\omega)$ contains all non frequency-dependent terms.

Based on the previous expressions, the equations of the system by the inverse Fourier transform are:

$$(\mathbf{m}+\mathbf{A}_\infty)\ddot{\mathbf{x}} + \mathbf{D}_1\dot{\mathbf{x}} + \mathbf{D}_2\dot{\mathbf{x}}|\dot{\mathbf{x}}| + \mathbf{K}\mathbf{x} + \int_0^t h(t-\tau)\dot{\mathbf{x}}(\tau)d\tau = \mathbf{q}(t,\mathbf{x},\dot{\mathbf{x}}) \tag{100}$$

where $h(\tau)$ is the retardation function with the following expression:

$$h(\tau) = \frac{1}{2\pi}\int_{-\infty}^{\infty}(c(\omega) + i\omega\alpha(\omega))e^{i\omega t}d\omega \tag{101}$$

The retardation function accounts for the wave radiation forces. This force has a memory effect which is conveyed by the convolution term. Therefore, the force appears even when the floater stops moving [83].

Equation 100 is solved in the time domain. Alternatively, the motions can be calculated separately for the high and low frequency terms. The high frequency response is calculated in the frequency domain, whereas the low frequency response is calculated in the time domain. The reader can refer to SIMA documentation [13] for more information.

RIFLEX

The general dynamic equations of the system can be expressed as:

$$(\mathbf{M}^{\mathrm{S}} + \mathbf{M}^{\mathrm{H}})\ddot{\mathbf{r}} + (\mathbf{C}^{\mathrm{S}} + \mathbf{C}^{\mathrm{H}})\dot{\mathbf{r}} + \mathbf{K}\mathbf{r} = \mathbf{R}^{\mathrm{E}} \tag{102}$$

where $\mathbf{M}^{\mathrm{S}}$ is the structural mass matrix, $\mathbf{M}^{\mathrm{H}}$ is the hydrodynamic mass (added mass) matrix, $\mathbf{C}^{\mathrm{S}}$ is the structural damping matrix, $\mathbf{C}^{\mathrm{H}}$ is the hydrodynamic damping matrix, $\mathbf{K}$ is the hydrostatic stiffness matrix, $\mathbf{R}^{\mathrm{E}}$ is the external force vector, and $\mathbf{r}, \dot{\mathbf{r}}, \ddot{\mathbf{r}}$ are the displacement, velocity, acceleration vectors.

A nonlinear time domain analysis is executed to calculate the motions of the finite element model (FEM) in SIMA. The Rayleigh structural damping is introduced for the energy dissipation in the structures as $\mathbf{C}^{\mathrm{S}} = a_1\mathbf{M}_{\mathrm{t}} + a_2\mathbf{K}_{\mathrm{t}}$, where $\mathbf{M}_{\mathrm{t}}$ is the tangential mass matrix and $\mathbf{K}_{\mathrm{t}}$ is the tangential stiffness matrix. Usually, the mass-proportional coefficient a_1 is omitted for large structures to avoid having unrealistic damping [13].

The numerical integration is carried out with a Newton-Raphson iteration procedure for the tangential mass, damping, and stiffness matrices and it is based on the Newmark $\beta-$family and the Wilson $\theta-$method. The reader can refer to SIMA documentation [13] for more information about the integration procedure.

B Methods for internal loads in offshore platforms and FOWTs

B.1 Structural analysis guidelines

In [91], guidelines are provided for the strength analysis of hull structures in tankers by DET NORSKE VERITAS which are recommended for class approval. The following points, that could also be applicable for a barge floater, are noted:

- The openings in the girders can either be modeled by a reduced thickness or the actual opening when they affect the stress distribution. Small openings can be neglected.
- Shell elements with four nodes may be used for the plates and beam elements with two nodes for stiffeners and longitudinals. An overlap between the beams and the shell elements is suggested to avoid hinge-like behavior, when connecting to only one node in the shell element, to achieve better load distribution.
- At least three elements shall be used on the shortest side of the girders.
- At least two elements shall be used between transverse girders.
- At least one element shall be used between longitudinals for accurate load transfer.
- The flange from brackets shall not be connected to the plating to avoid stress concentrations.

Similar mesh requirements are noted from Lloyd's Register regarding the design and construction procedures for ship units [92]. For example, at least one element between longitudinal, vertical or web stiffeners shall be used. The stiffener spacing is acceptable as a mesh size, however, high stress locations (e.g. bracket toes, openings) require finer mesh for accurate stresses. Moreover, the following points are noted:

- The aspect ratio of the elements shall not exceed three and be as close to one.
- The triangular elements shall be avoided, especially in high stress locations.
- The fine mesh shall consist of at least ten elements towards all directions (mesh size smaller than 50 mm), as presented in Figure 123.
- The element centroid is to be used for averaging stresses.
- The inertia of the combined plating and stiffener is to be accounted for the out of plane bending of beam elements. Half the stiffener spacing from each side is to be accounted for the plating contribution.

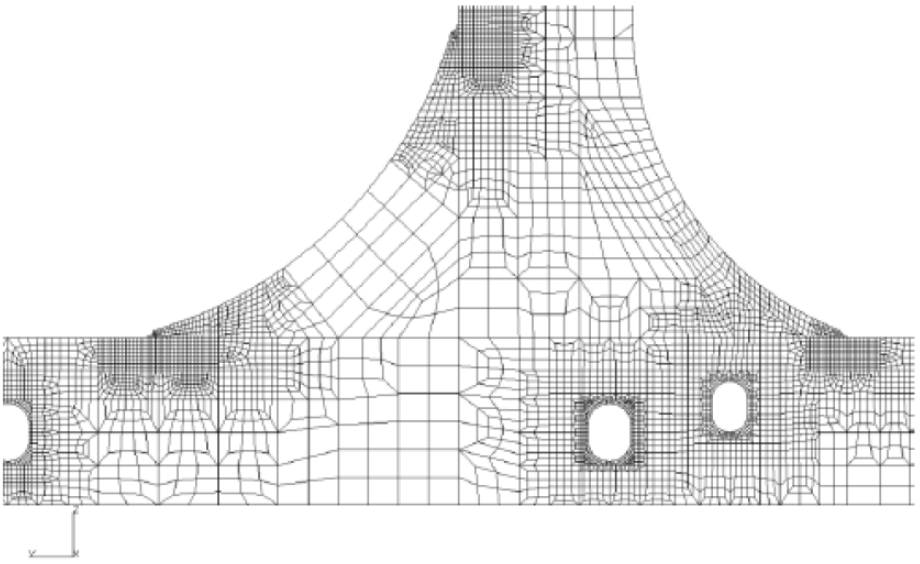

Figure 123: Example fine mesh of a vertical web frame [92].

The guidance notes for the FEA of hull structures from ABS [93] refer similar recommendations. The following additional points are noted:

- The eccentricity of the neutral axis of the beam elements has to be modeled.
- The internal angle of the elements shall be more than 30 degrees.
- The taper shall be less than ten.
- The warping of the elements shall be less than five degrees.

The standard from DNV AS regarding the structural design of offshore units [94] refers to the FEA guidelines from DNV AS [95]. Again, similar practices are described. The following points are noted:

- For linear elements with four or three nodes, the shape functions shall include the incompatible modes for accurate bending representation.
- The global assessment shall be based on membrane or in-plane stresses of the shell/plate elements.
- The fatigue assessment shall be based on the surface stresses of the shell/plate elements.
- The shear, in-plane and von-Mises stresses, and the axial stress for beam elements shall be examined.
- The buckling analysis of plates and stiffened panels shall be carried out.
- The boundary conditions shall be away from locations of interest and could be placed in the centerline close to the aft and fore end of the vessel.
- The curvature of the free edge of large brackets shall be modeled to avoid extreme stresses.
- The stiffeners shall be modeled with shell elements in locations with fine mesh.

B.2 Literature study

Several studies were found, regarding the structural analysis of FOWTs, of which the more insightful are discussed in the following paragraphs. Different approaches and FOWTs are presented which can guide towards additional research questions.

Coupled time-domain analysis

In [61], a time-domain analysis is carried out using DNV's software suite (WADAM, WASIM, SIMA, SESTRA). The irregular waves and motions of the floater are taken from a global analysis in SIMA and the hydrostatic and hydrodynamic pressures are regenerated on the wet surface of the floater with WASIM and a MATLAB code. The pressures are transferred to a shell finite element model and a linear structural analysis is conducted in SESTRA.

The IEA 15 MW wind turbine and the UMaine semi-sumersible are studied. The stresses at selected points in the structure are compared with two approaches: the frequency-domain method using WADAM and SESTRA, where stress transfer functions are produced for these locations, and the time-domain method proposed with WASIM. A good agreement was observed for the examined wave conditions.

In [62], the same approach for the coupled analysis is followed for the DTU 10 MW reference wind turbine and semi-submersible floater. The total hydrodynamic loads produced from WASIM and SIMA are compared and a good agreement is shown. The importance of including all global loads is highlighted, as the combination of loads can lead to a reduction. The misalignment between the wind and the waves was observed to have a small impact on the von mises stress in the structure. The response in parked conditions was found important and the inertia loads from the wind turbine were studied regarding their dynamic effect. The second-order wave loads are seen to have a small impact on the internal forces in the structure.

Coupled CFD-FEM

In [96], a coupled CFD-FEM (FANS-MOORING3D) method is utilized to simulate the response of a semi-submersible FOWT under extreme wave conditions. An iterative wave adjustment method increased the accuracy of the simulated waves and the OC5 project experimental data were used for verification of the method. It is highlighted that the wave configuration greatly affects the low-frequency pitch morion of the floater and a short-duration wave was better calibrated.

Even though CFD is not to be used in this study, it is important to highlight that it is an alternative method where more accurate responses are achieved with the cost of an increased computational time.

Distributed hydrodynamic loads

In [97], an approach for distributed hydrodynamic loads is proposed for large volume structures to get the internal loads in the hull and it is applied on a 5 MW semi-submersible FOWT. Instead of utilizing the whole hull as the panel to derive the added mass coefficients, damping coefficients, and excitation loads from potential theory, the hull is split into sections and these terms are calculated separately for these bodies. The substructures are linked to the nodes of a beam element model that accounts for the hull's stiffness.

The structure was considered rigid, however the hull flexibility could be examined with this approach too. In wave-only conditions, this method agreed well with the experimental results regarding the column bending moment, but it's underestimated when the wind is included and the mean angle of the floater is not considered. The global motions were exactly foreseen for all load cases.

Floater flexibility

In [98], the flexibility of a semi-submersible substructure for the DTU 10 MW wind turbine is studied with an OpenFAST code. In extreme sea states, a significant difference is found in the wave loads in surge and pitch between flexible and rigid body. Also, the response in surge, pitch, and heave motion is increased near the corresponding eigenfrequencies. In normal sea states, the flexibility of the structure highly impacts the fatigue damage in the tower and mooring system.

In [99], the flexibility of a spar-type floater is examined for a 10 MW wind turbine. HAWC2 and WAMIT are utilized, the eigenmodes are calculated in HAWC2, and the added mass is updated from WAMIT based on the new shape. It was found that the first bending moment was coupled to the pitch motion.

The importance of flexibility on a barge-type floater shall be examined too. It is expected to have a significant impact on the motions and loading of the structure, but the extent of this effect must be quantified.

Difference-frequency second order wave loads

In [48], three different 20 MW spar-type FOWT are examined regarding extreme stresses and fatigue life at the tower base and at sea water level (SWL). Hydroelasticity was accounted for by modeling the spar in SIMA with RIFLEX elements as beams. The difference between the spar models was in the static pitch angle of the floater at rated wind speed. High static pitch angle was associated with larger fatigue damage. It is shown that the difference-frequency second-order wave loads have an insignificant impact concerning fatigue (less than 1 %) and a small impact on extreme stresses (less than 4 %). This effect shall be examined and compared with a barge-type FOWT.

B.3 Software

There are two different approaches for the coupled analysis of FOWT regarding the hydrodynamic loads [84]:

- Time-domain models using the impulse response function (IRF), or else retardation function, and the frequency-dependent hydrodynamic coefficients (added mass, damping).
- CFD models with accurate turbulence modeling.

For the CFD approach, OpenFoam, Star CCM+, and ANSYS Fluent are most commonly used. For the IRF approach, OpenFAST, OrcaFlex, SIMA, Bladed, HAWC2, Qblade, and Ashes are usually utilised.

Regarding the hydrodynamic coefficients (added mass, damping), the following hydrodynamic codes are commonly used, which are based on potential theory: WAMIT, ANSYS AQWA, WADAM, HAMS, NEMOH, MOSES, Hydrostar, and WAFDUT.

For the structural analysis with finite element method (FEM), the following software can be used: ANSYS, ABAQUS, and SESTRA.

C Power spectral density of uniaxial stress

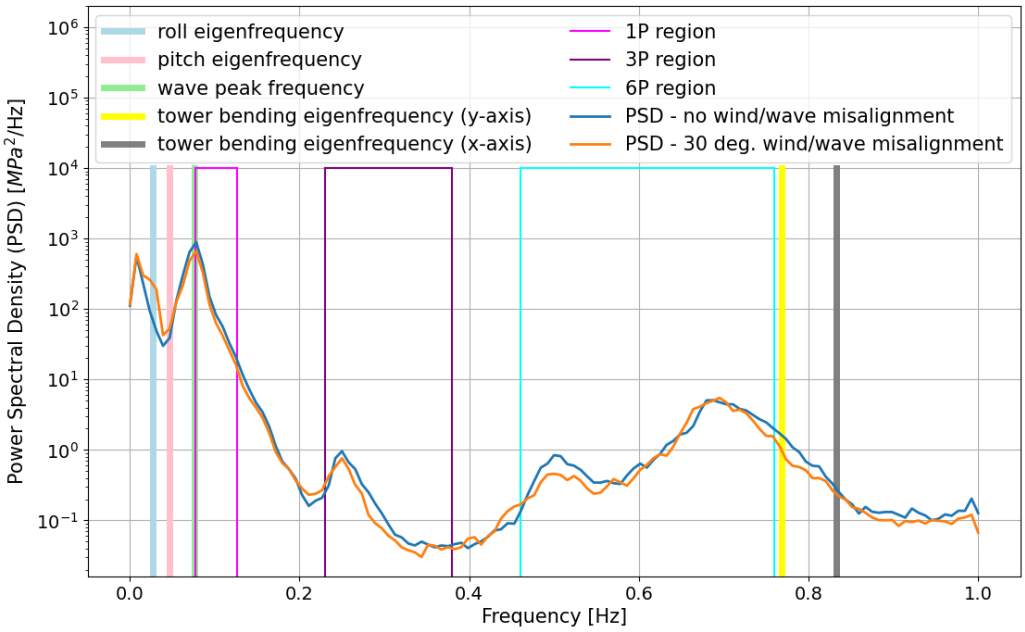

Figure 124: Power spectral density (PSD) of axial stress at the tower base with polar coordinate $\theta = 0$ degrees for mean wind speed $U_w = 7$ m/s in combination with the eigenfrequency of pitch and roll, the wave peak frequency, the tower bending eigenfrequency over the y-axis and x-axis, and the 1P, 3P, and 6P regions.

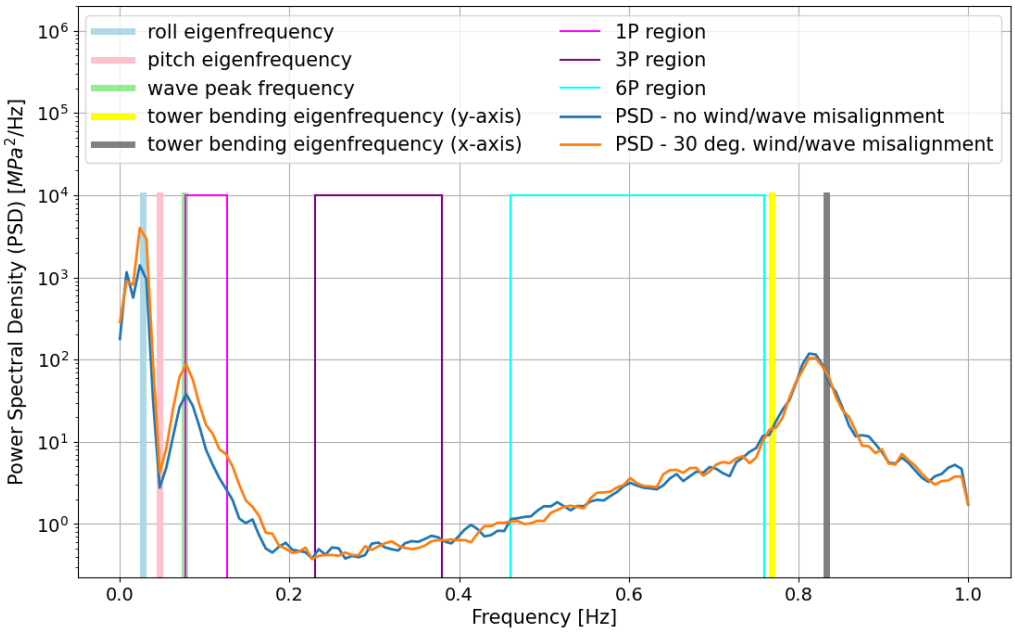

Figure 125: Power spectral density (PSD) of axial stress at the tower base with polar coordinate $\theta = 90$ degrees for mean wind speed $U_w = 7$ m/s in combination with the eigenfrequency of pitch and roll, the wave peak frequency, the tower bending eigenfrequency over the y-axis and x-axis, and the 1P, 3P, and 6P regions.

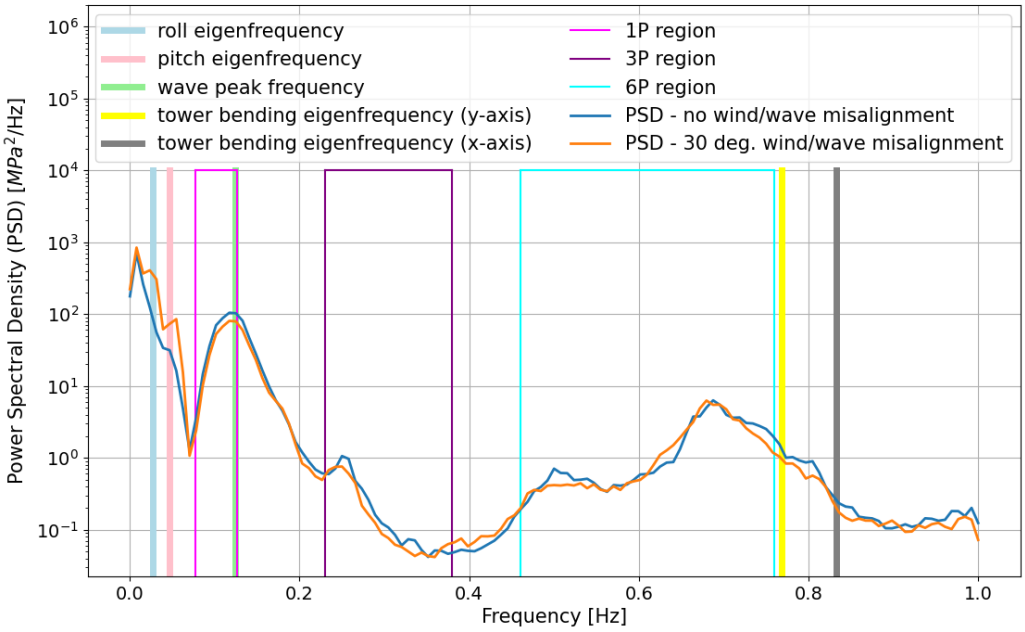

Figure 126: Power spectral density (PSD) of axial stress at the tower base with polar coordinate $\theta = 0$ degrees for mean wind speed $U_w = 7.6$ m/s in combination with the eigenfrequency of pitch and roll, the wave peak frequency, the tower bending eigenfrequency over the y-axis and x-axis, and the 1P, 3P, and 6P regions.

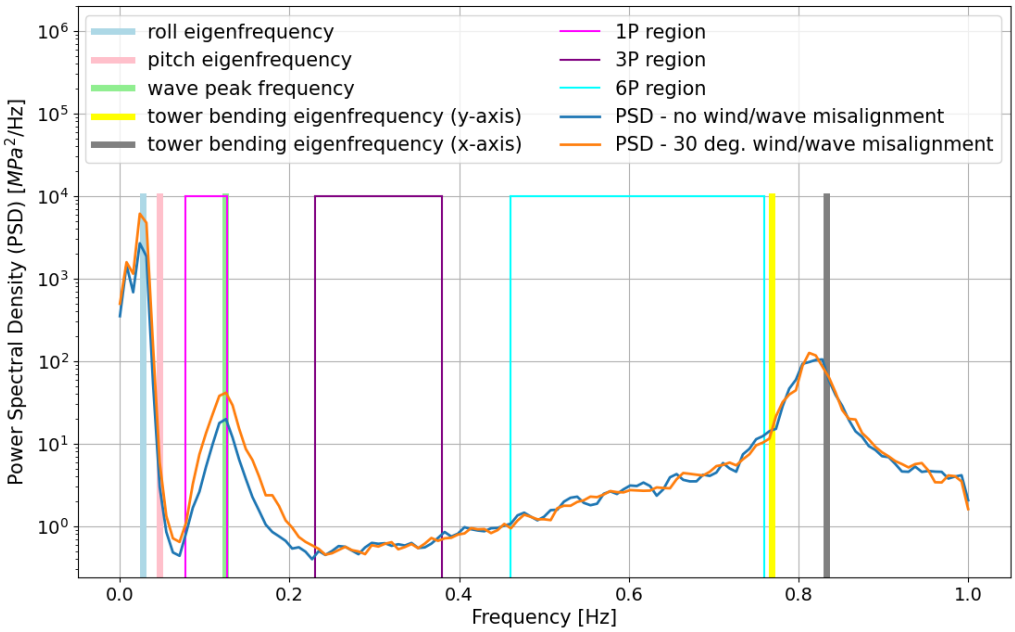

Figure 127: Power spectral density (PSD) of axial stress at the tower base with polar coordinate $\theta = 90$ degrees for mean wind speed $U_w = 7.6$ m/s in combination with the eigenfrequency of pitch and roll, the wave peak frequency, the tower bending eigenfrequency over the y-axis and x-axis, and the 1P, 3P, and 6P regions.

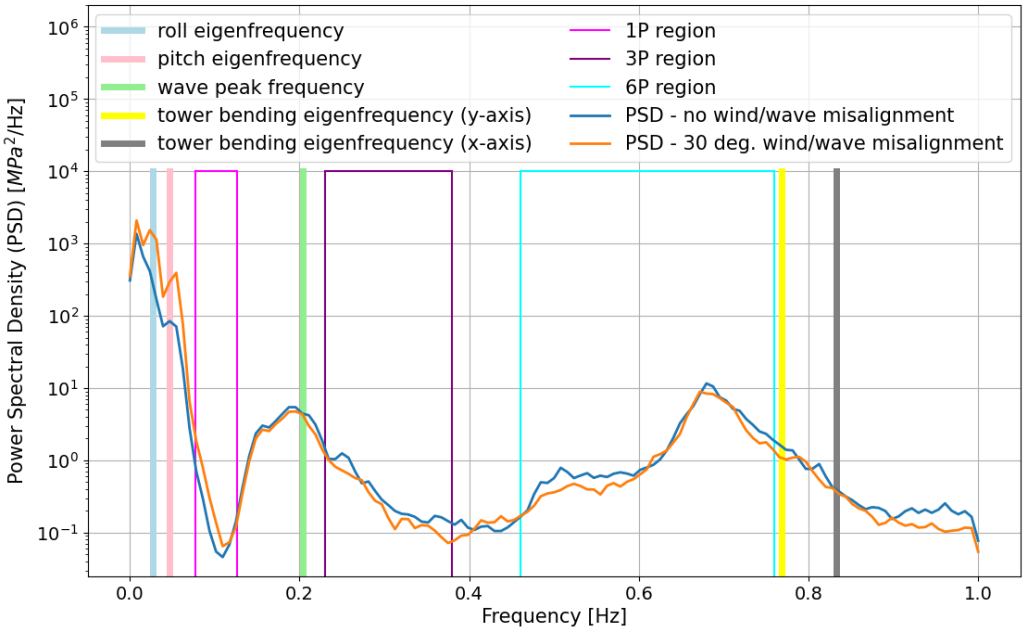

Figure 128: Power spectral density (PSD) of axial stress at the tower base with polar coordinate $\theta = 0$ degrees for mean wind speed $U_w = 9.1$ m/s in combination with the eigenfrequency of pitch and roll, the wave peak frequency, the tower bending eigenfrequency over the y-axis and x-axis, and the 1P, 3P, and 6P regions.

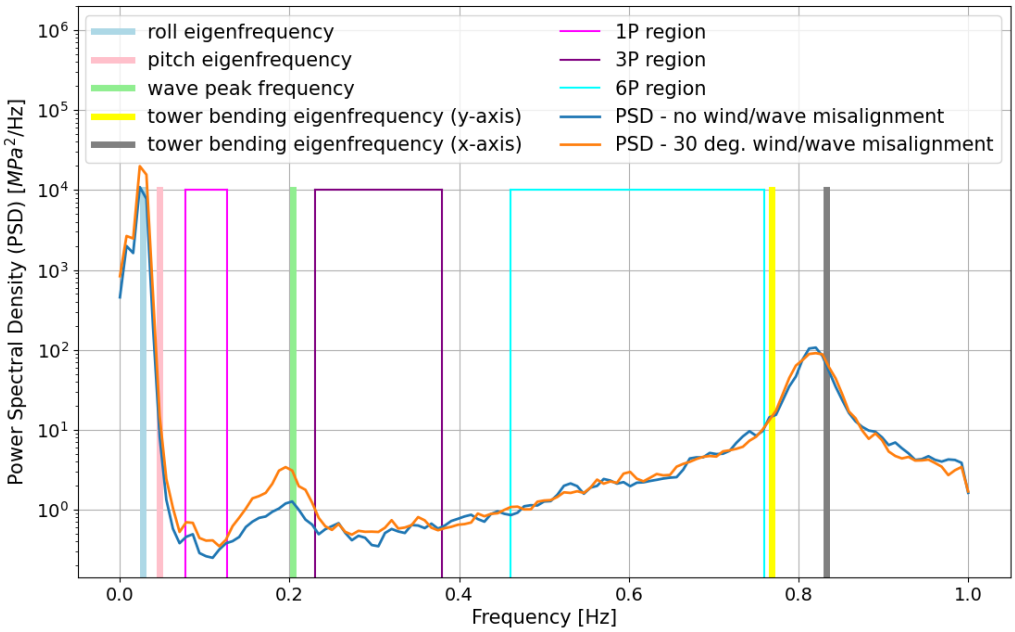

Figure 129: Power spectral density (PSD) of axial stress at the tower base with polar coordinate $\theta = 90$ degrees for mean wind speed $U_w = 9.1$ m/s in combination with the eigenfrequency of pitch and roll, the wave peak frequency, the tower bending eigenfrequency over the y-axis and x-axis, and the 1P, 3P, and 6P regions.

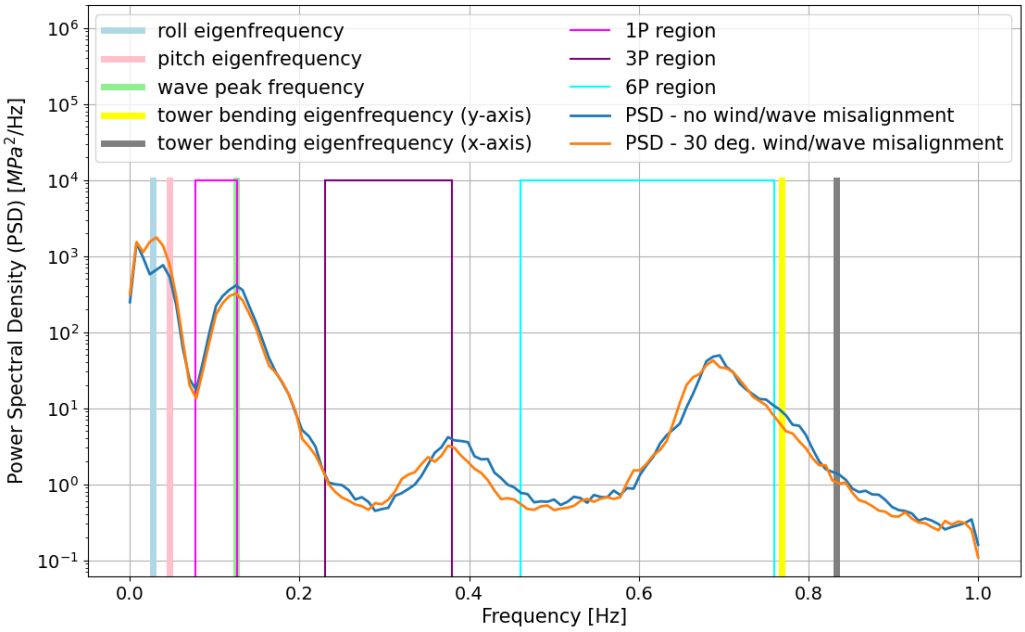

Figure 130: Power spectral density (PSD) of axial stress at the tower base with polar coordinate $\theta = 0$ degrees for mean wind speed $U_w = 15.3$ m/s in combination with the eigenfrequency of pitch and roll, the wave peak frequency, the tower bending eigenfrequency over the y-axis and x-axis, and the 1P, 3P, and 6P regions.

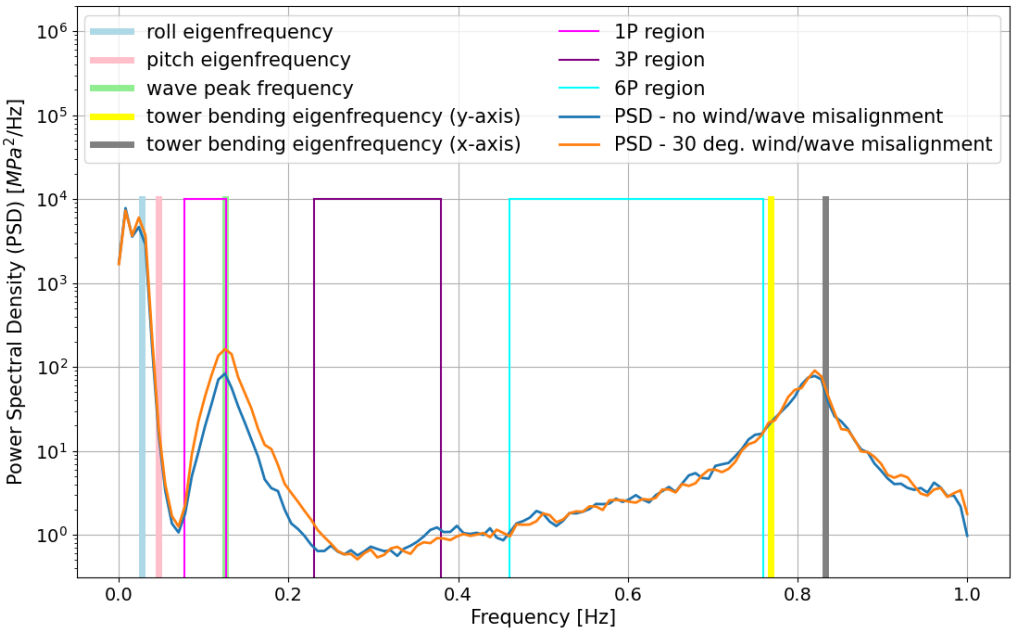

Figure 131: Power spectral density (PSD) of axial stress at the tower base with polar coordinate $\theta = 90$ degrees for mean wind speed $U_{\mathrm{w}} = 15.3$ m/s in combination with the eigenfrequency of pitch and roll, the wave peak frequency, the tower bending eigenfrequency over the y-axis and x-axis, and the 1P, 3P, and 6P regions.

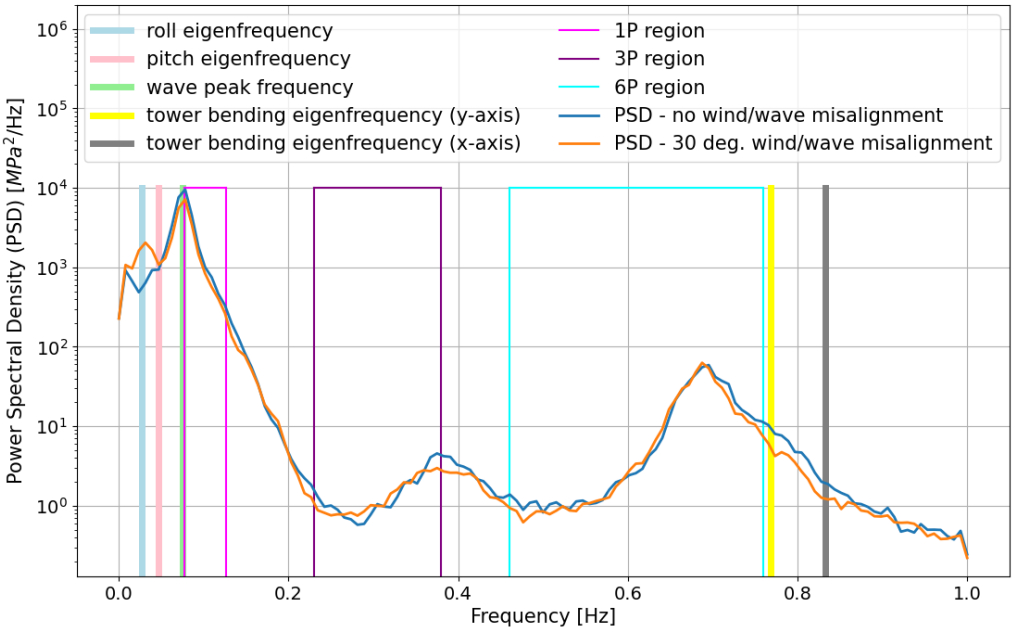

Figure 132: Power spectral density (PSD) of axial stress at the tower base with polar coordinate $\theta = 0$ degrees for mean wind speed $U_{\mathrm{w}} = 18.9$ m/s in combination with the eigenfrequency of pitch and roll, the wave peak frequency, the tower bending eigenfrequency over the y-axis and x-axis, and the 1P, 3P, and 6P regions.

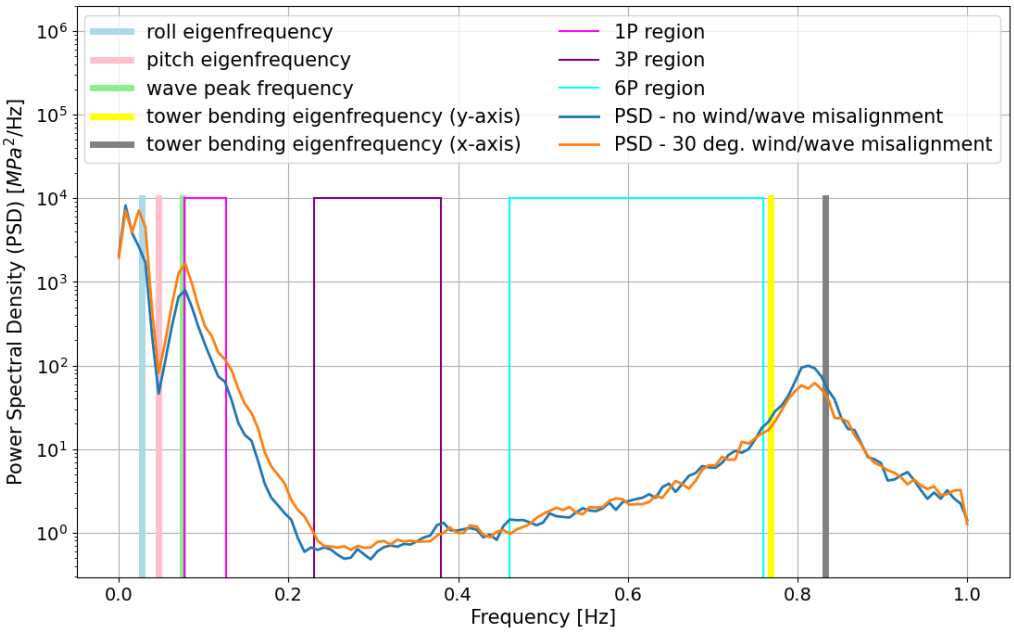

Figure 133: Power spectral density (PSD) of axial stress at the tower base with polar coordinate $\theta = 90$ degrees for mean wind speed $U_{\mathrm{w}} = 18.9$ m/s in combination with the eigenfrequency of pitch and roll, the wave peak frequency, the tower bending eigenfrequency over the y-axis and x-axis, and the 1P, 3P, and 6P regions.

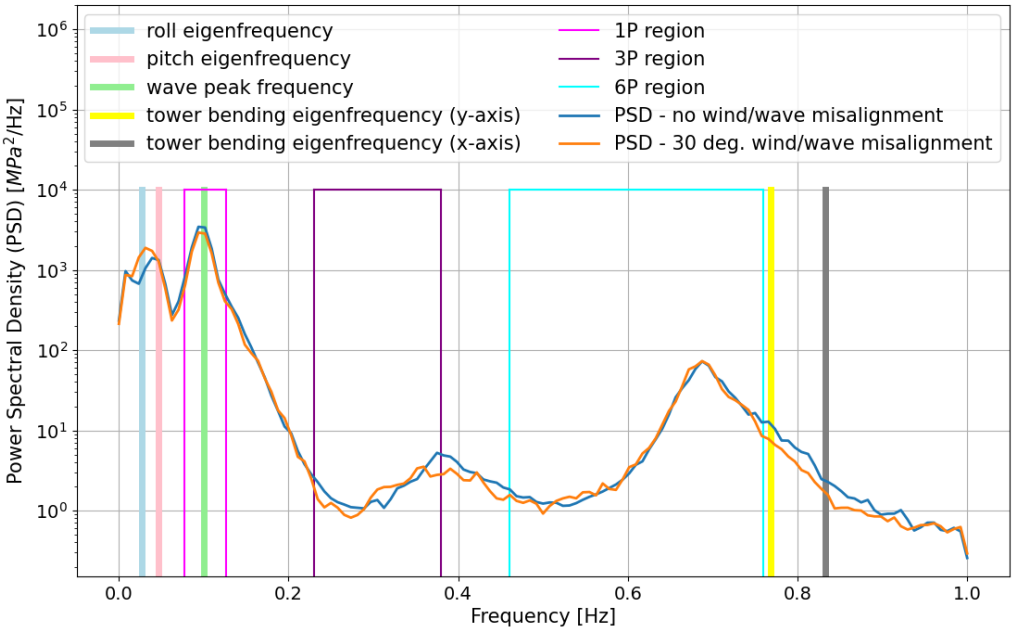

Figure 134: Power spectral density (PSD) of axial stress at the tower base with polar coordinate $\theta = 0$ degrees for mean wind speed $U_{\mathrm{w}} = 21.9$ m/s in combination with the eigenfrequency of pitch and roll, the wave peak frequency, the tower bending eigenfrequency over the y-axis and x-axis, and the 1P, 3P, and 6P regions.

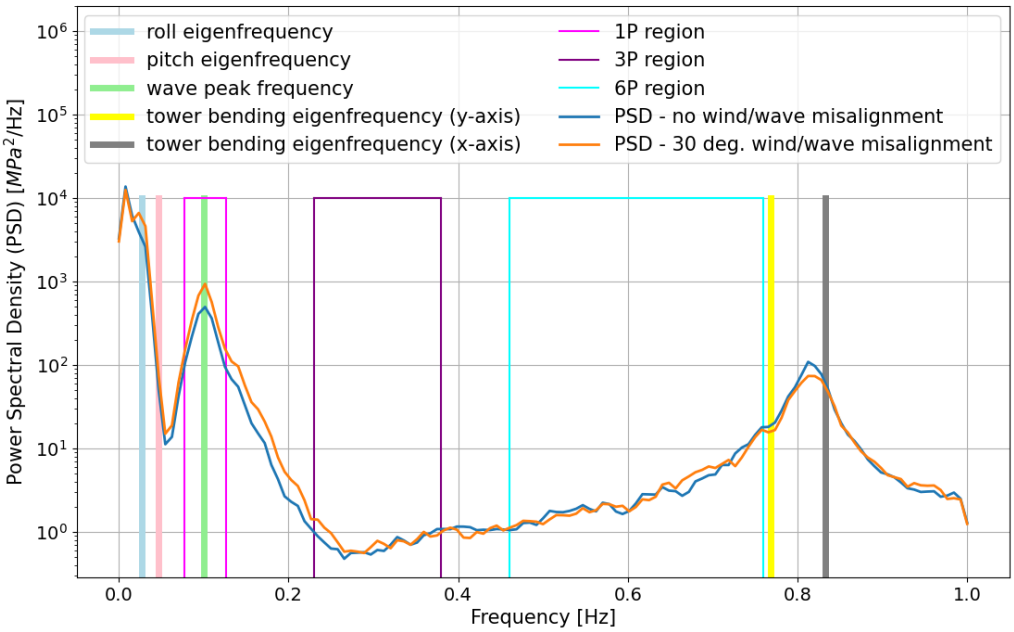

Figure 135: Power spectral density (PSD) of axial stress at the tower base with polar coordinate $\theta = 90$ degrees for mean wind speed $U_{\mathrm{w}} = 21.9$ m/s in combination with the eigenfrequency of pitch and roll, the wave peak frequency, the tower bending eigenfrequency over the y-axis and x-axis, and the 1P, 3P, and 6P regions.

D Multiaxial screening

D.1 Multiaxial screening without shear

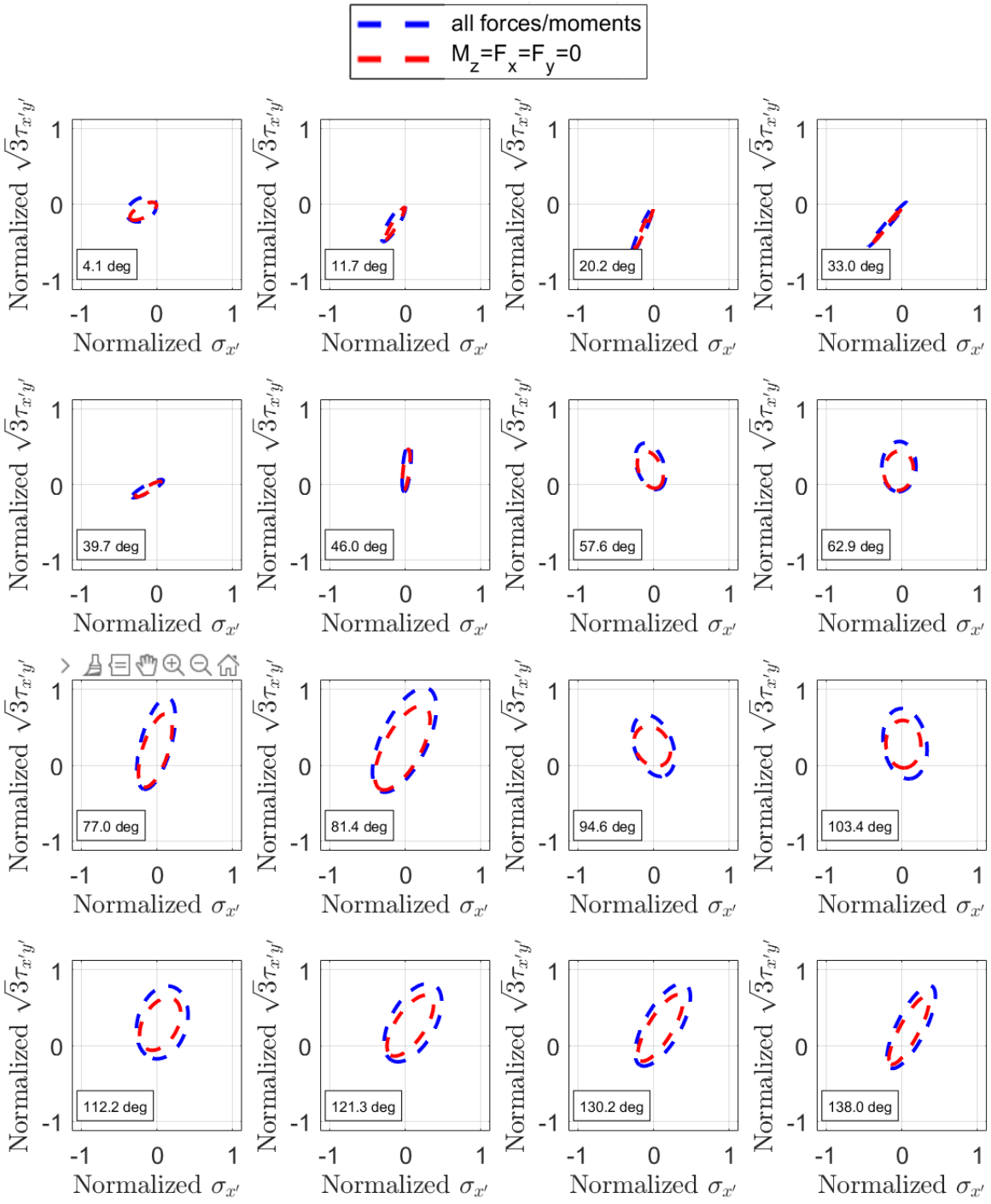

Figure 136: Comparison of the 2-dimensional stress space representation for the shell elements around the tower base from approximately 0 to 140 degrees with and without shear contributing forces and moments for FLS DLC D with no wind/wave misalignment.

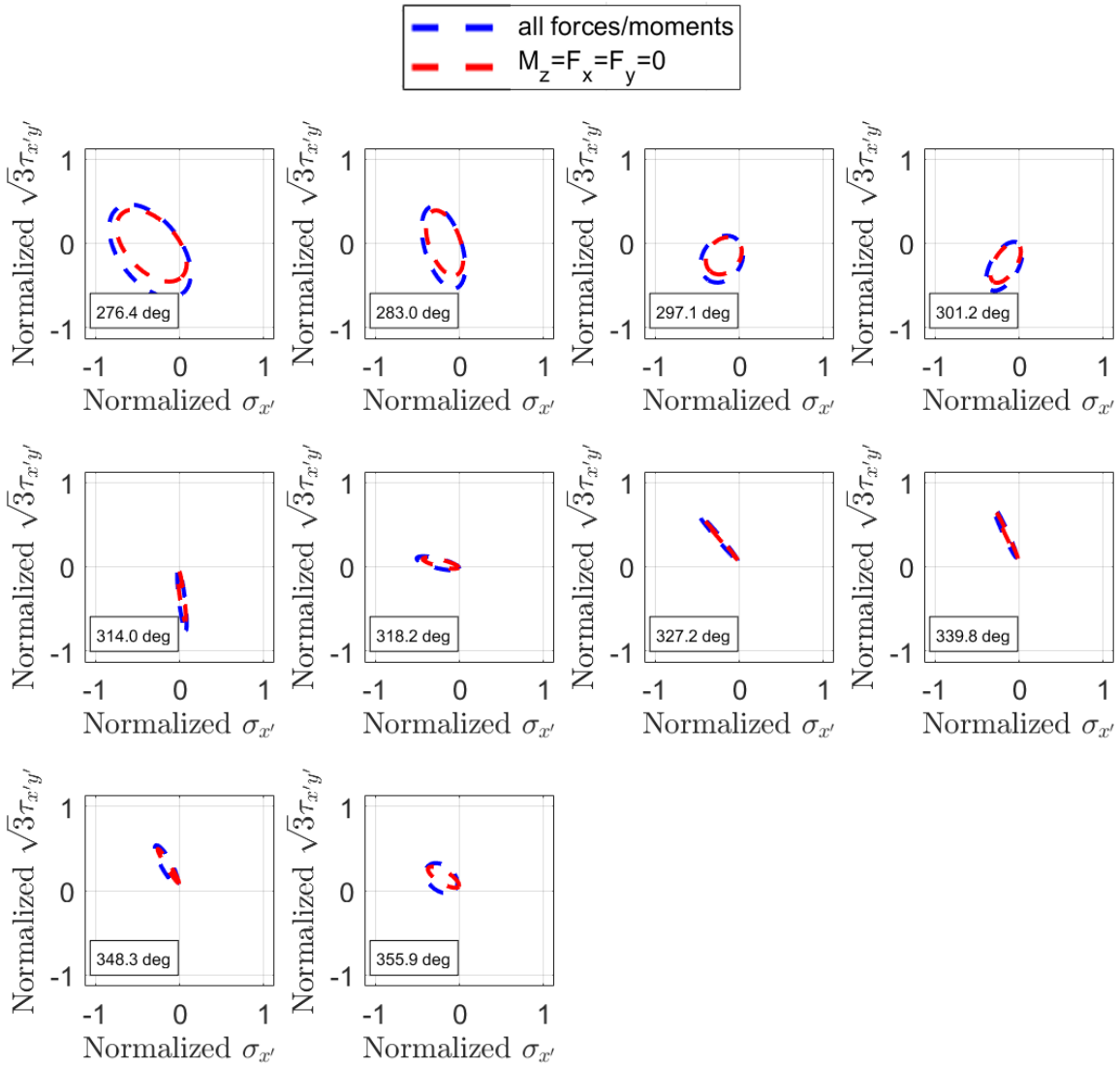

Figure 137: Comparison of the 2-dimensional stress space representation for the shell elements around the tower base from approximately 270 to 360 degrees with and without shear contributing forces and moments for FLS DLC D with no wind/wave misalignment.

D.2 Multiaxial screening of new design

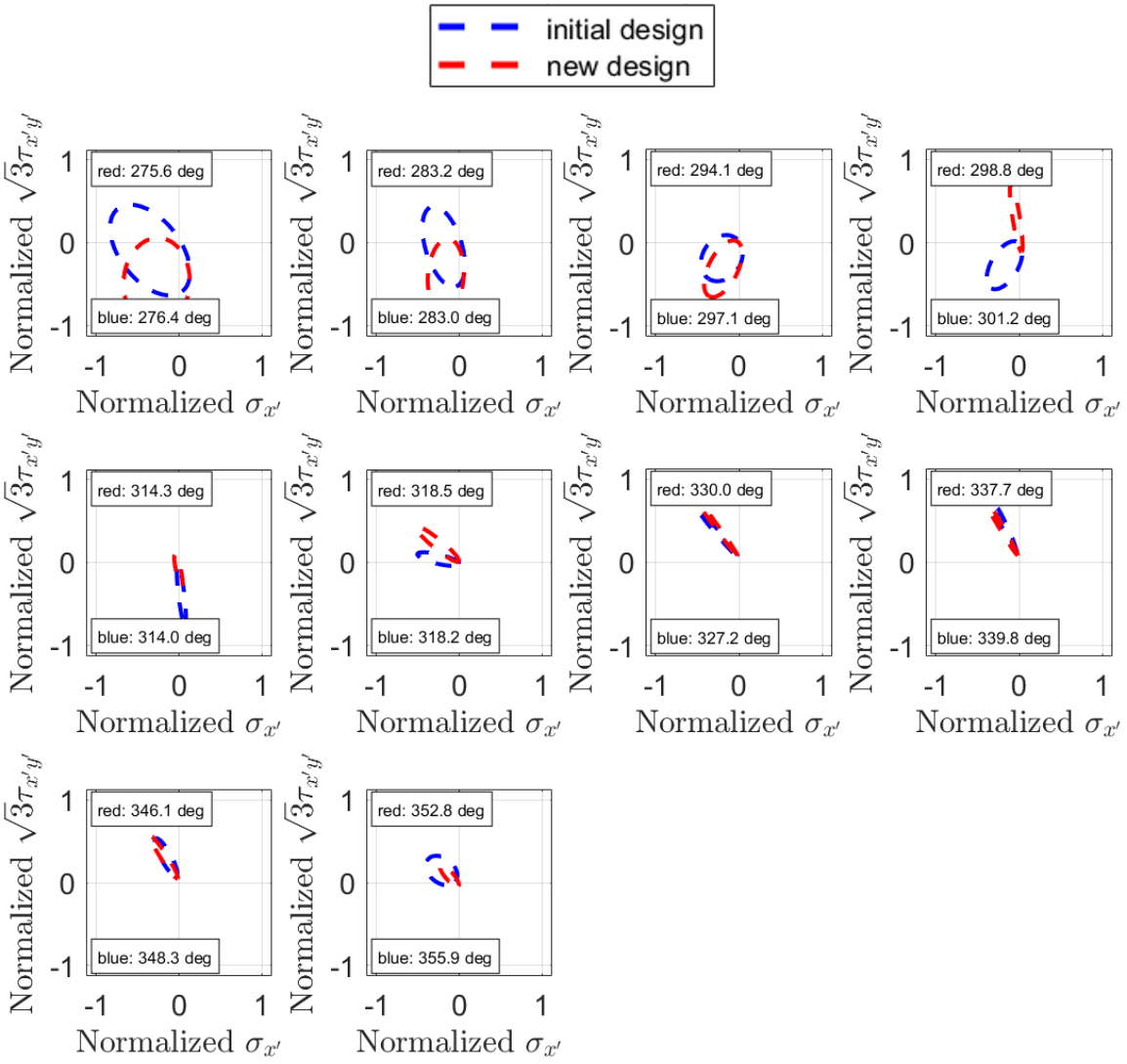

Figure 138: Comparison of the 2-dimensional stress space representation for the shell elements around the tower base from approximately 270 to 360 degrees in the initial and modified internal structure for FLS DLC D with no wind/wave misalignment.

D.3 Multiaxial screening with double plate thickness

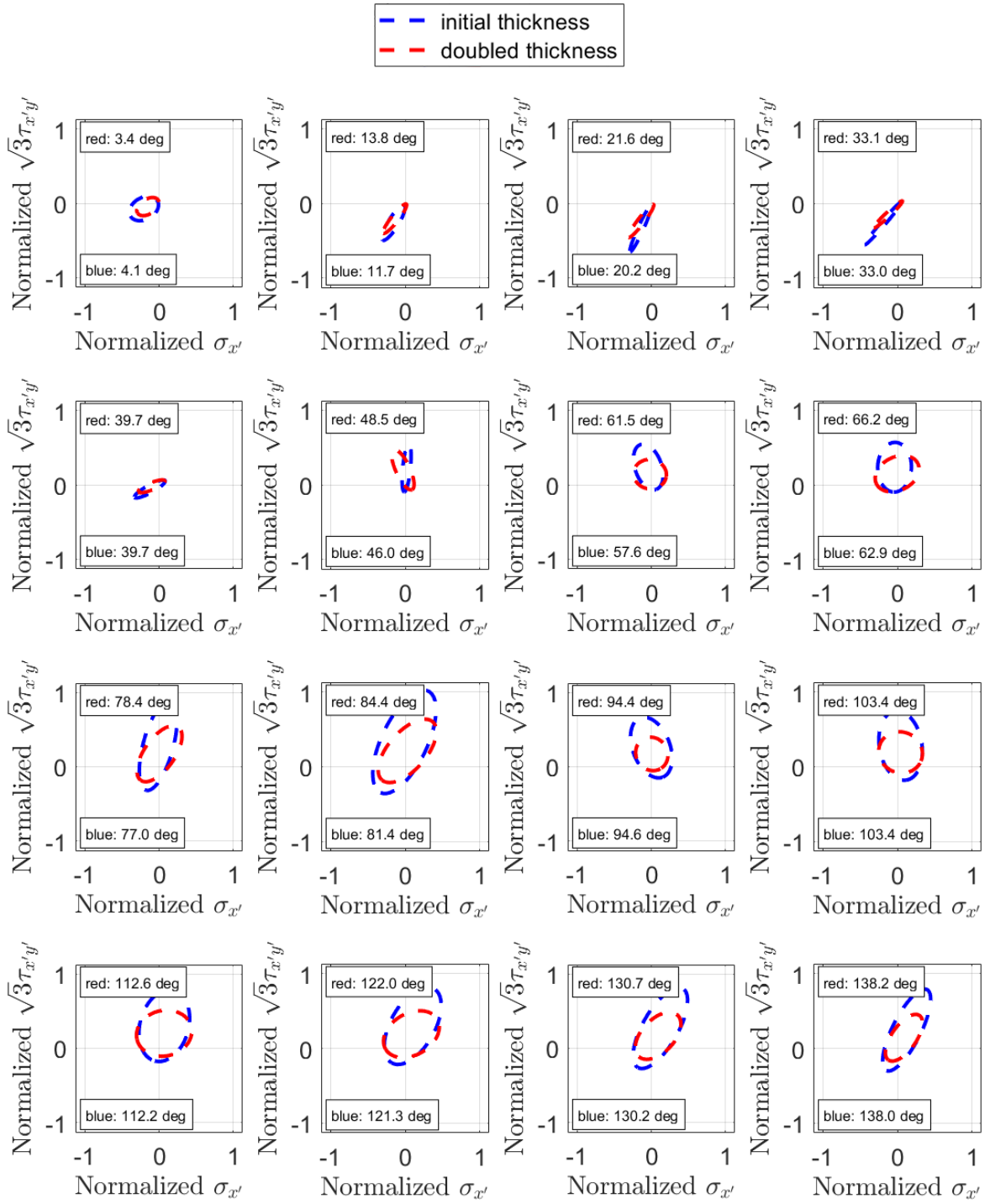

Figure 139: Comparison of the 2-dimensional stress space representation for the shell elements around the tower base from approximately 0 to 140 degrees with the initial and a doubled plate thickness at the tower base for FLS DLC D with no wind/wave misalignment.

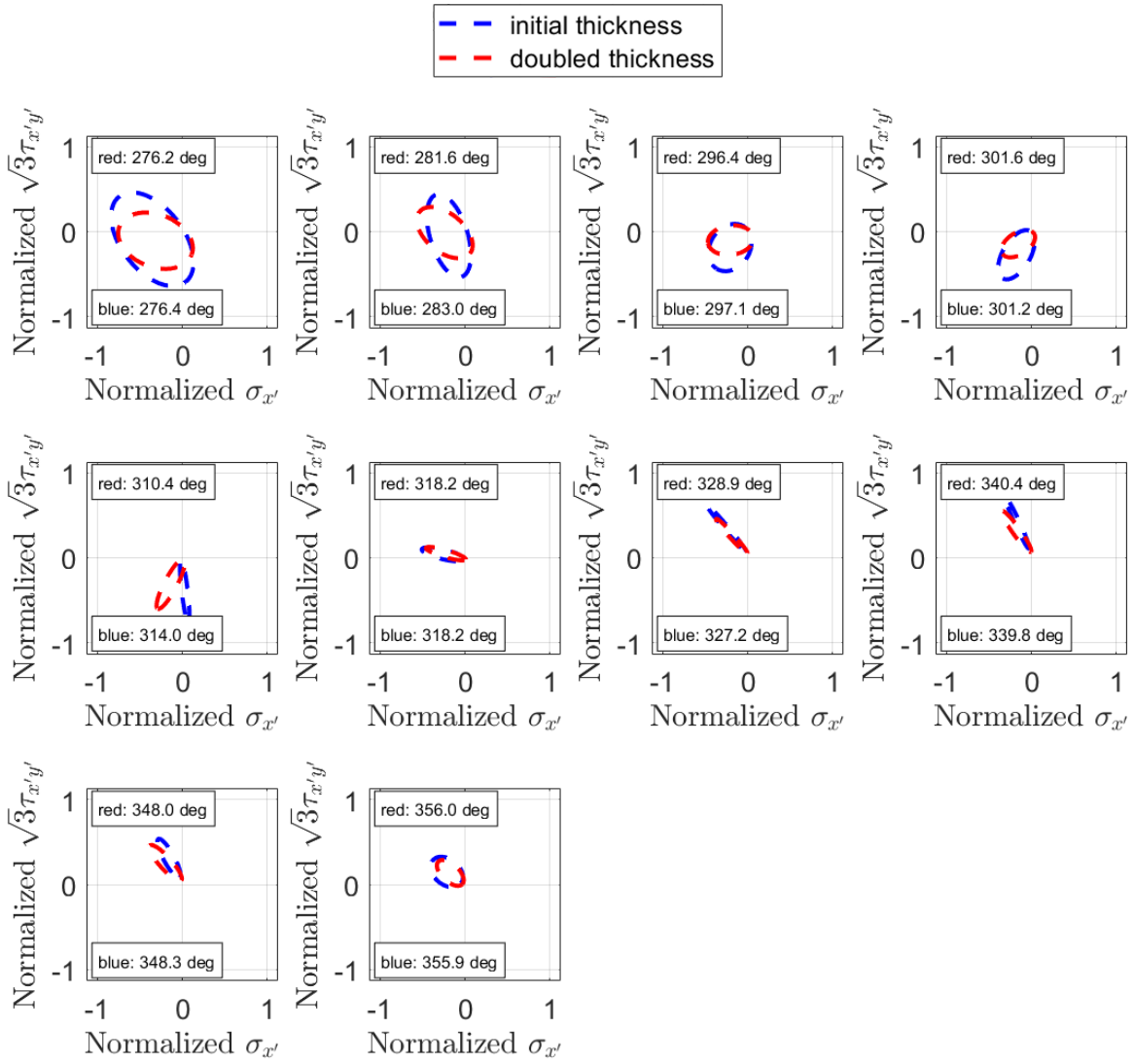

Figure 140: Comparison of the 2-dimensional stress space representation for the shell elements around the tower base from approximately 270 to 360 degrees with the initial and a doubled plate thickness at the tower base for FLS DLC D with no wind/wave misalignment.

E Supplementary studies for the roll motions

As it was seen from both the ultimate and the fatigue limit state study, the roll eigenfrequency is dominating in the stress response. The cause of the roll motion and the coupling with the other degrees of freedom are investigated with the following simulations and plots.

In Figure 141, the roll and pitch motion of the floater are presented for different wind speeds in a calm sea, as well as the rotor speed and blade 1 pitch angle. There is no pitch motion for wind speeds lower than the rated wind speed, only a positive mean angle, and for higher wind speeds, it is still small. However, the roll motion is more dominant, oscillating at about 2 - 3 degrees from a positive mean roll angle that is appearing from the operating wind turbine, which rotates clockwise. It is concluded that the roll motion is caused by the wind and the rotating wind turbine, and not from the waves.

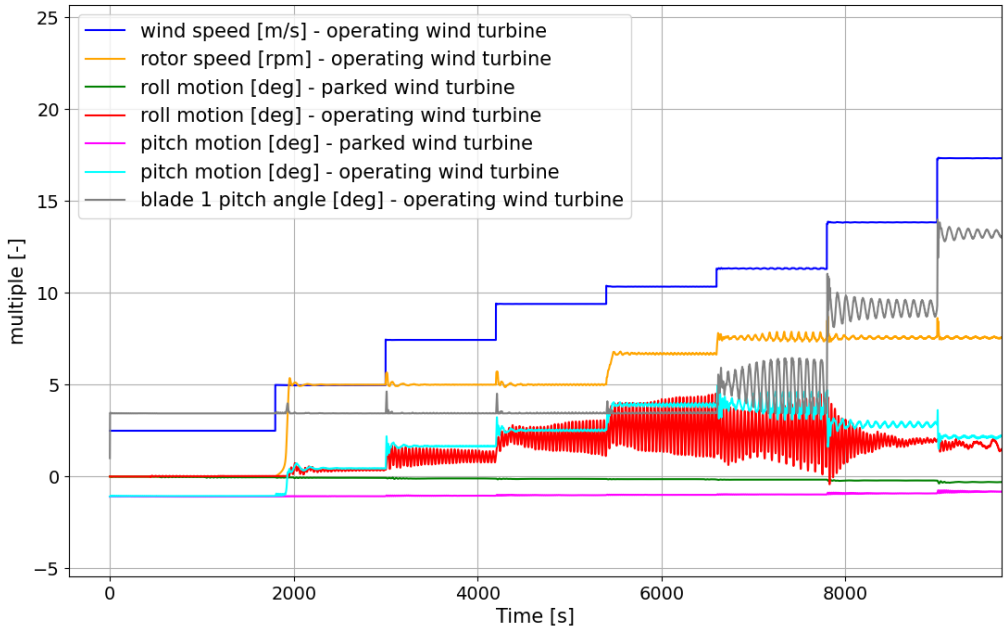

Figure 141: Comparison of the roll and pitch motion in a parked and an operating wind turbine for different wind speeds in a calm sea; also, the rotor speed and blade 1 pitch angle variation are presented.

In Figure 142, the roll and yaw motion are presented for the same environment, and in Figure 143, the time series are zoomed to look at the period. It is seen that both motions have the same period for the most part, which is the roll eigenperiod. Therefore, there is a coupling between the two motions. The impact of this coupling in the roll motion is further investigated by introducing an artificial yaw and pitch stiffness separately and together in Figure 144. By restraining the barge in yaw, the roll motion disappears. An artificial pitch stiffness also decreases the roll motion, but not as significantly as the yaw stiffness. Therefore, an indirect way to further decrease the roll motion is to increase the stiffness in yaw.

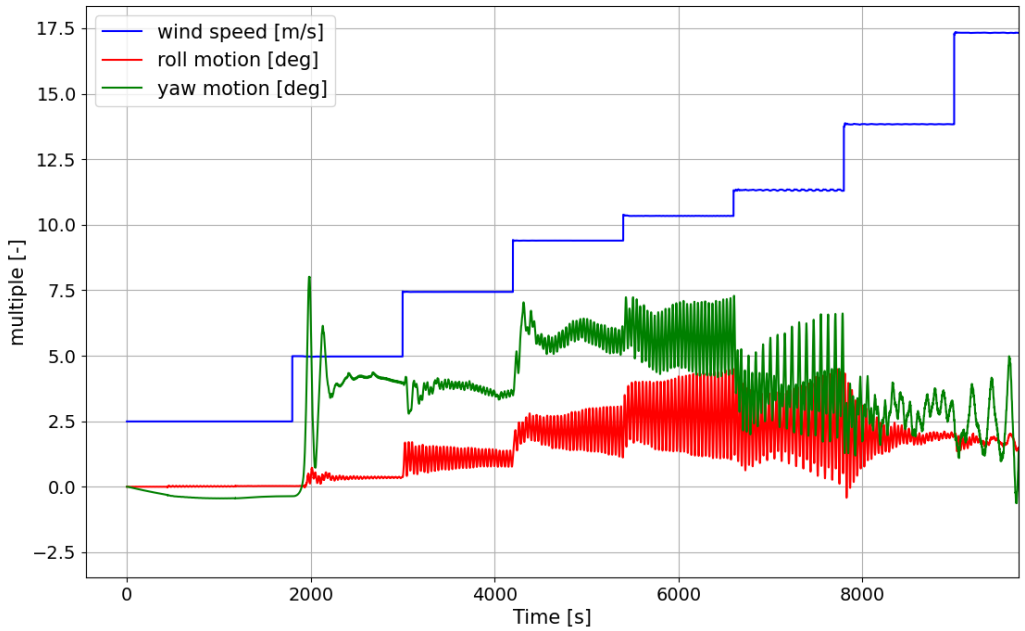

Figure 142: Comparison of the roll and yaw motion in an operating wind turbine for different wind speeds in a calm sea.

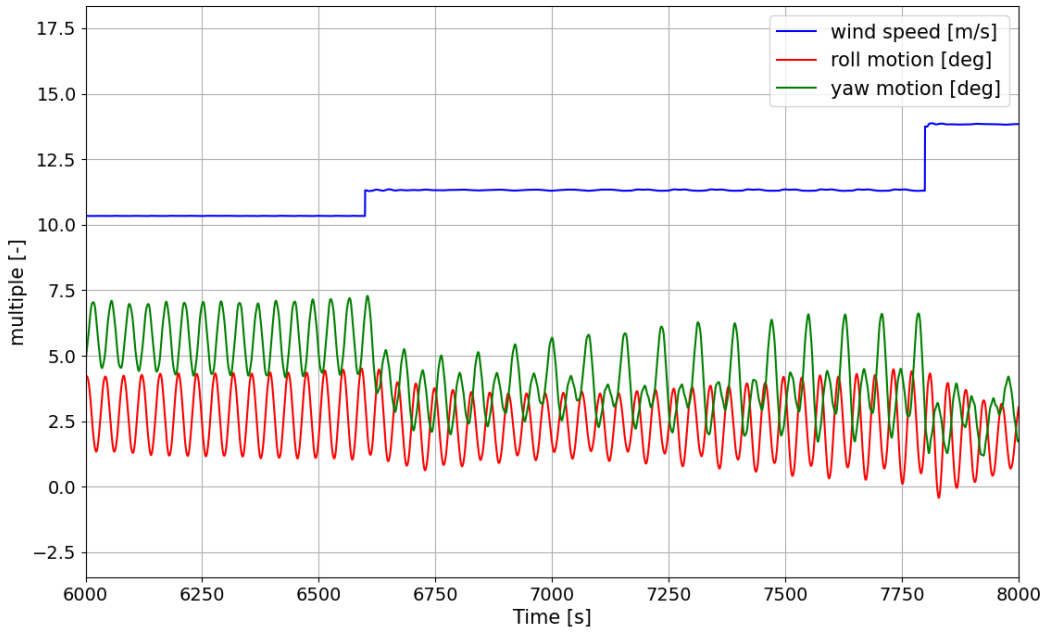

Figure 143: Zoomed comparison of the roll and yaw motion in an operating wind turbine for different wind speeds in a calm sea.

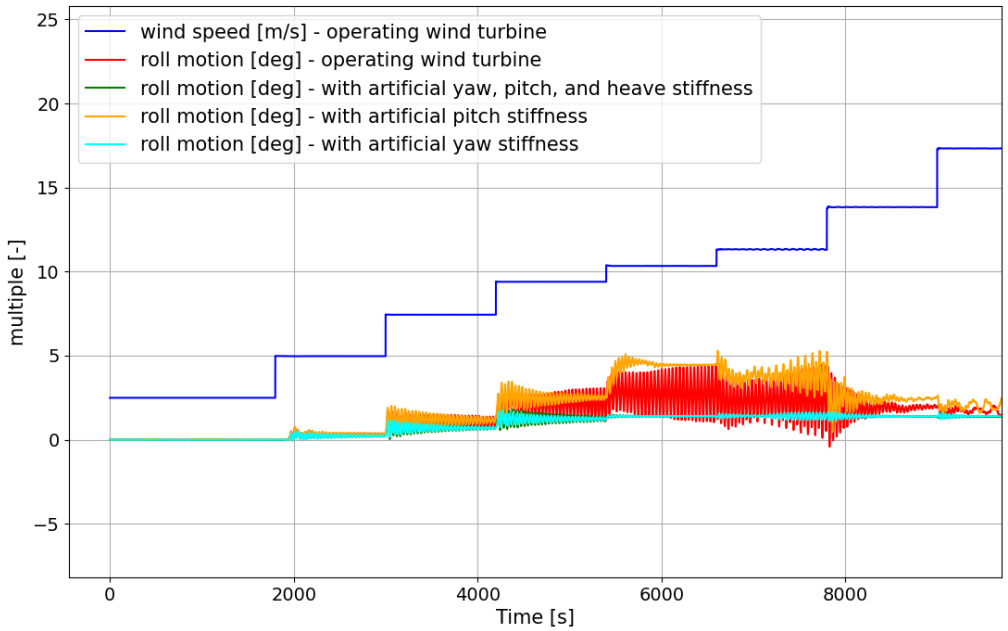

Figure 144: Comparison of the roll motion in an operating wind turbine for different wind speeds in a calm sea with artificial stiffness in yaw, pitch, and heave.

Damping effect

Damping is another means to reduce the roll motion. Since restricting the yaw motion has a direct impact on roll, an increase in yaw damping was also studied. The increased damping can be achieved with an increased length of the keel or by introducing fins, among other ways. In Figure 145, the linear and quadratic roll damping are doubled separately, and in Figure 146, the linear yaw damping is doubled, and the quadratic yaw damping is set to a large value. The doubled quadratic roll damping decreases the roll motion more effectively than the doubled linear roll damping, suggesting that higher frequencies are apparent in this design. The increased yaw damping did not contribute as much in the roll motion reduction.

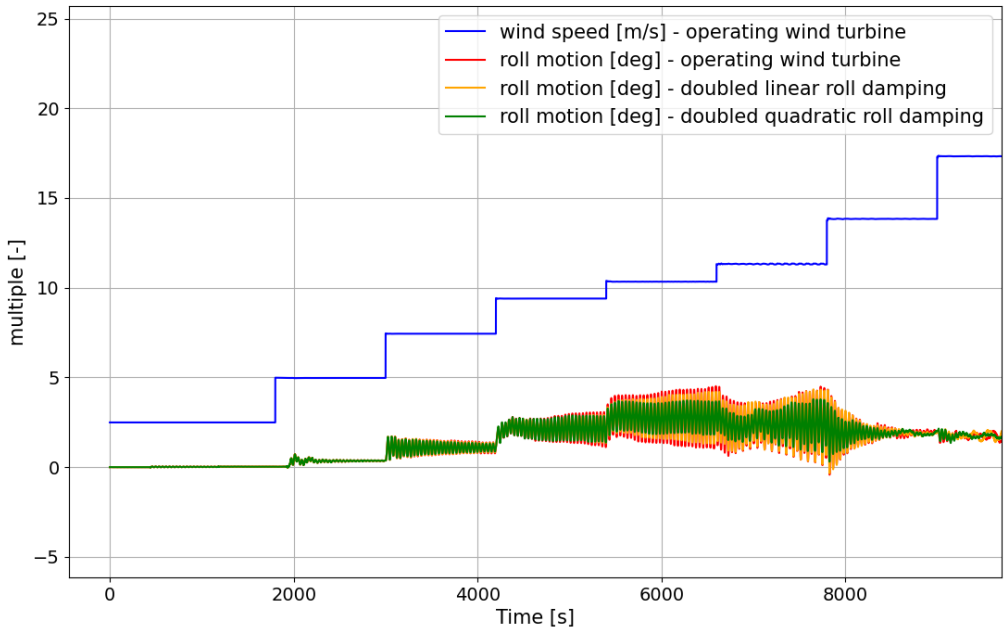

Figure 145: Comparison of the roll motion in an operating wind turbine for different wind speeds in a calm sea with doubled linear and quadratic roll damping.

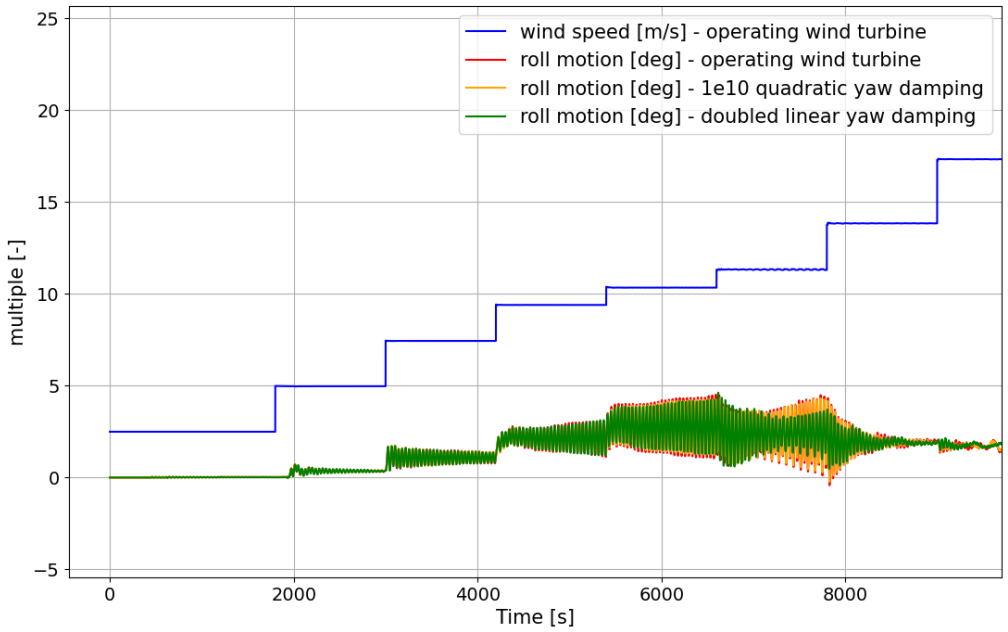

Figure 146: Comparison of the roll motion in an operating wind turbine for different wind speeds in a calm sea with doubled linear and increased quadratic yaw damping.

Roll stiffness effect

A change in the roll stiffness is also briefly studied, as depicted in Figure 147. When the roll stiffness is increased, the roll eigenperiod decreases, and when the roll stiffness is decreased, the roll eigenperiod increases. Both examples in the figure highlight that the roll motions can be reduced, but the softer floater causes a high static angle, which is not wanted. However, a stiffer floater causes smaller roll motions with a static angle close to zero.

In Figure 148, the yaw motion is also compared. A static angle in yaw is observed in a softer floater, but with the stiffer floater, there is no significant yaw motion. This study shows that a change in the roll stiffness can reduce the roll motion, however, further studies are needed in that direction.

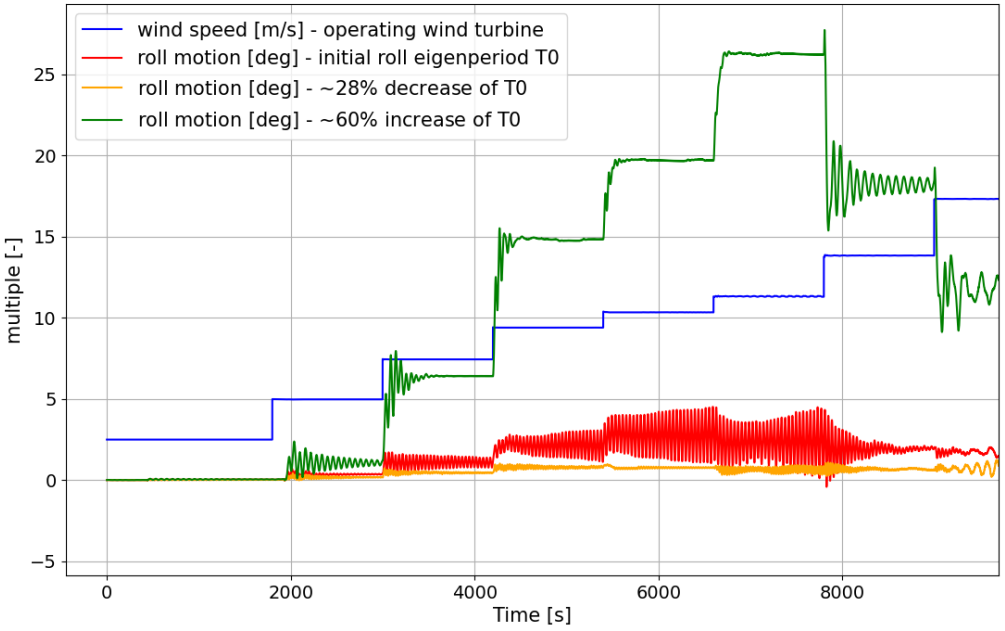

Figure 147: Comparison of the roll motion in an operating wind turbine for different wind speeds in a calm sea with increased and increased roll stiffness.

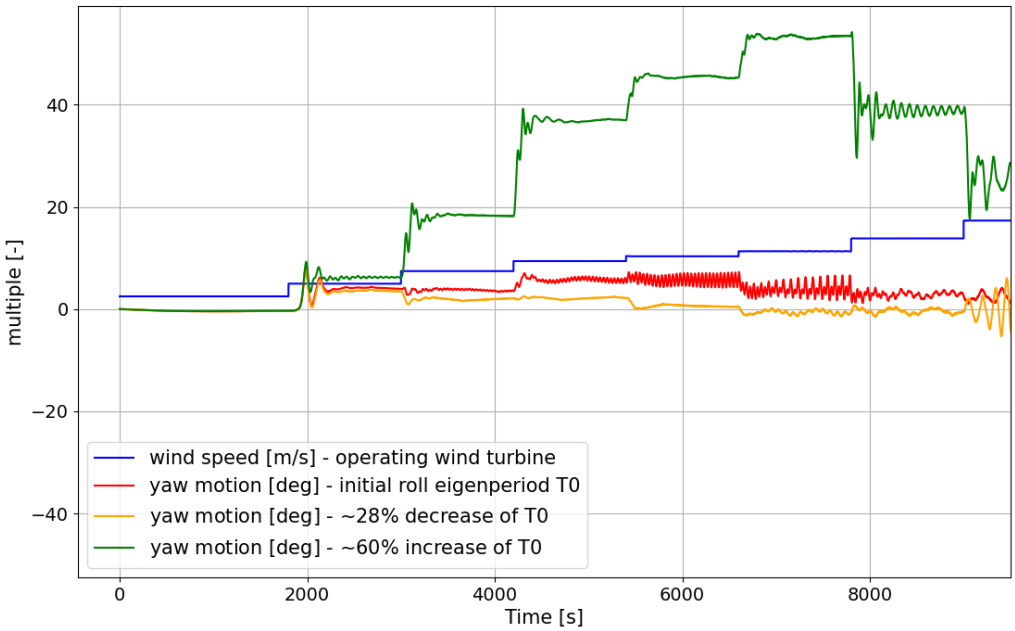

Figure 148: Comparison of the yaw motion in an operating wind turbine for different wind speeds in a calm sea with increased and increased roll stiffness.

Yaw controller effect

The introduction of the yaw controller is examined regarding both the roll motion and the power output. In Figure 149, it is shown that with the yaw controller, a significant reduction in the roll motion was achieved. Also, in Figure 150, the power output was increased, reaching its optimum expected output with the yaw controller.

The importance of such a controller is shown with the presented plots. Further tuning the controller or using an individual blade pitch controller could further reduce the roll motion and increase performance.

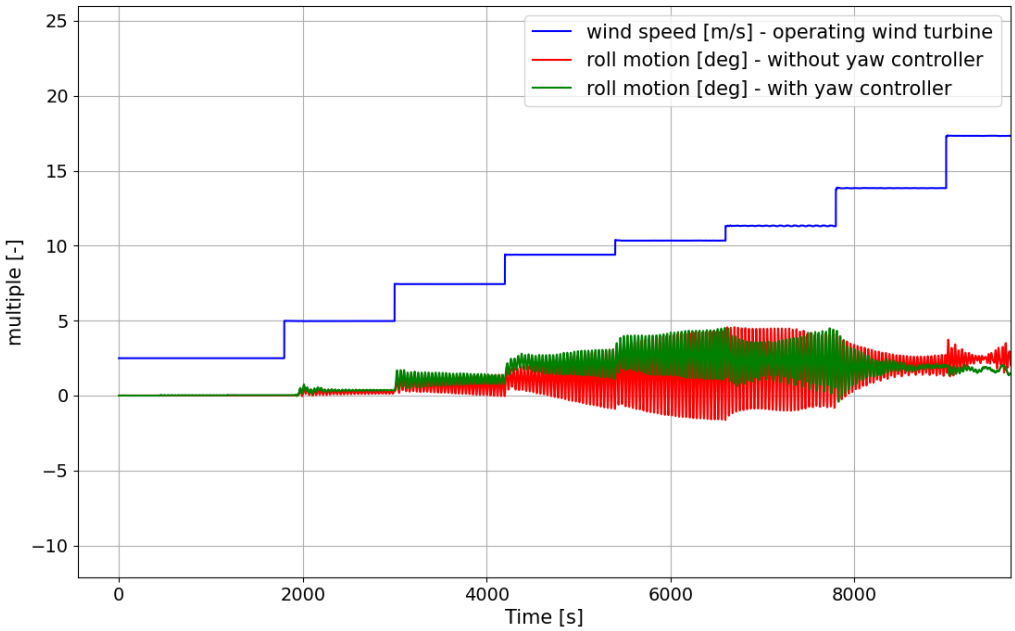

Figure 149: Comparison of the roll motion in an operating wind turbine for different wind speeds in a calm sea with and without the yaw controller.

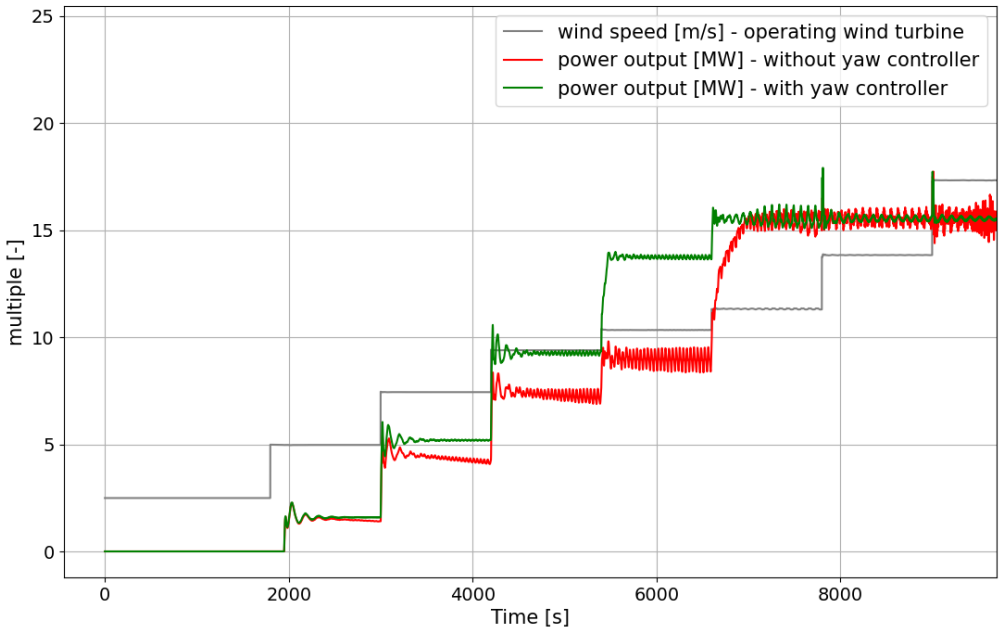

Figure 150: Comparison of the power output in an operating wind turbine for different wind speeds in a calm sea with and without the yaw controller.